

WAVELETS ON NON-EUCLIDEAN MANIFOLDS

THÈSE N^o 3409 (2005)

PRÉSENTÉE À LA FACULTÉ SCIENCES ET TECHNIQUES DE L'INGÉNIEUR

Institut de traitement des signaux

SECTION DE GÉNIE ÉLECTRIQUE ET ÉLECTRONIQUE

ÉCOLE POLYTECHNIQUE FÉDÉRALE DE LAUSANNE

POUR L'OBTENTION DU GRADE DE DOCTEUR ÈS SCIENCES

PAR

Iva BOGDANOVA

M.Sc. in Applied Mathematics,
M.Sc. in Telecommunication Techniques and Technologies, Université Technique de Sofia, Bulgarie
et de nationalité bulgare

acceptée sur proposition du jury:

Prof. P. Vandergheynst, directeur de thèse
Prof. S.T. Ali, rapporteur
Prof. J.-P. Antoine, rapporteur
Prof. M. Kunt, rapporteur

Lausanne, EPFL
2006

Acknowledgments

I would like to sincerely thank Prof. Murat Kunt for giving me the opportunity to join the Signal Processing Institute (ITS) at EPFL along with the freedom in acquiring knowledge all these years at ITS. In the same time, I am "hyperbolically" thankful to the supervisor of my dissertation, Prof. Pierre Vandergheynst, for the guidance, understanding and support during my PhD studies. I would also like to acknowledge the grant of the Swiss National Science Foundation dedicated to this research.

It was a great pleasure and honor for me to have on my examination committee Prof. Syed Twareque Ali, Prof. Jean-Pierre Antoine and Prof. Murat Kunt. I would like to thank them all for accepting to read and review this dissertation, for all the comments and questions I received during the evaluation process. Also, I am thankful to Prof. Jean-Philippe Thiran, who presided the committee.

I am deeply thankful to Prof. Jean-Pierre Gazeau for the many discussions we had concerning the hyperboloid.

I would like to thank all my colleagues who created and maintained a nice working ambiance. Special thanks are due to Yves Wiaux whose friendly criticism helped me a lot while writing this dissertation and who in addition read the first version. Thanks to Laurent Jacques and Xavier Bresson for sharing ideas and a lot of interesting discussions.

Another important acknowledgment goes to Kafedzhiisky family for all the constant support.

I am grateful to my parents - without them this dissertation could not have come into existence.

December 2005,

Lausanne, Switzerland

Contents

| | |
|---|-------------|
| Acknowledgments | iii |
| Contents | v |
| Abstract | ix |
| Version Abrégé | xi |
| List of Figures | xiii |
| List of Tables | xvii |
| Introduction | 1 |
| 1 Manifolds, Signals and Wavelets | 5 |
| 1.1 The notion of manifold | 5 |
| 1.1.1 Riemannian manifold | 6 |
| 1.2 Non-Euclidean manifolds | 7 |
| 1.3 Non-Euclidean manifolds as a geometric model for data | 9 |
| 1.4 Signals and harmonic analysis | 11 |
| 1.4.1 A broad definition for signal | 11 |
| 1.4.2 Signal analysis in frequency domain | 11 |
| 1.4.3 Time-frequency signal analysis | 13 |
| 1.5 General set-up: wavelets on a manifold | 14 |
| 1.5.1 Wavelet construction based on group theory | 14 |
| 1.5.2 Wavelet construction based on convolution | 15 |
| 1.6 Wavelets on the real line: 1-D wavelets | 16 |
| 1.6.1 Group of affine transformation on the real line | 16 |
| 1.6.2 1-D wavelet admissibility condition | 17 |
| 1.6.3 Examples of 1-D wavelets | 18 |
| 1.7 Wavelets on the Euclidean plane: 2-D wavelets | 19 |
| 1.7.1 Similitude group on the Euclidean plane | 20 |
| 1.7.2 2-D wavelet admissibility condition | 21 |
| 1.7.3 Examples of 2-D wavelets | 22 |

| | | |
|----------|---|-----------|
| 1.8 | Discrete Wavelet Frames | 23 |
| 1.8.1 | Classical frames | 23 |
| 1.8.2 | Continuous and half-continuous frames | 24 |
| 1.8.3 | Controlled and weighted frames | 24 |
| 1.8.4 | 2-D wavelet frames | 26 |
| 1.9 | Summary | 28 |
| 2 | Wavelets and Frames on the Sphere | 29 |
| 2.1 | Spherical Geometry | 29 |
| 2.1.1 | Spherical coordinates | 29 |
| 2.1.2 | Stereographic projection of the sphere | 30 |
| 2.2 | Harmonic analysis on the sphere | 30 |
| 2.2.1 | Fourier transform on the sphere | 31 |
| 2.2.2 | Wigner transform | 32 |
| 2.2.3 | Convolution on the sphere | 32 |
| 2.2.4 | Correlation on the sphere | 33 |
| 2.3 | Wavelets on the sphere | 34 |
| 2.3.1 | Affine transformations on the sphere and their group theory | 34 |
| 2.3.2 | The continuous wavelet transform on the sphere | 37 |
| 2.3.3 | An example of wavelets on the sphere | 39 |
| 2.3.4 | Wavelets on the sphere based on convolution | 40 |
| 2.4 | Discrete wavelet transform on the sphere | 40 |
| 2.4.1 | Half-continuous spherical frames | 40 |
| 2.4.2 | Discrete spherical frames | 47 |
| 2.5 | Laplacian pyramid on the sphere | 51 |
| 2.5.1 | Euclidean Laplacian pyramid | 52 |
| 2.5.2 | Analysis spherical Laplacian pyramid | 53 |
| 2.5.3 | Synthesis spherical Laplacian pyramid | 53 |
| 2.6 | Summary | 56 |
| 3 | Wavelets on the Hyperboloid | 57 |
| 3.1 | Motivation | 57 |
| 3.2 | Geometry of the two-sheeted hyperboloid | 58 |
| 3.2.1 | Hyperbolic coordinates | 58 |
| 3.2.2 | Projective structures | 58 |
| 3.3 | Affine transformations on the 2-hyperboloid | 59 |
| 3.3.1 | Rotations and motions on the hyperboloid | 59 |
| 3.3.2 | Dilations on the hyperboloid | 60 |
| 3.4 | Harmonic analysis on the 2-hyperboloid | 66 |
| 3.4.1 | Fourier-Helgason Transform | 66 |
| 3.5 | Continuous Wavelet Transform on the Hyperboloid | 67 |
| 3.5.1 | Convolution on the hyperboloid | 68 |
| 3.6 | Wavelets on the 2-hyperboloid | 71 |
| 3.6.1 | The hyperbolic wavelet admissibility condition | 71 |
| 3.6.2 | An example of hyperbolic wavelet | 77 |
| 3.6.3 | An example of continuous wavelet transform on the hyperboloid | 78 |
| 3.7 | The hyperbolic wavelet L^1 -normalized transform | 78 |
| 3.7.1 | L^1 -normalized hyperbolic admissibility condition | 84 |

| | | |
|----------|---|------------|
| 3.8 | Euclidean limit | 85 |
| 3.9 | Summary | 85 |
| 4 | On Processing Non-Euclidean Images | 87 |
| 4.1 | Plenoptic function | 87 |
| 4.1.1 | Catadioptric sensors and omni-directional images | 88 |
| 4.1.2 | Central catadioptric sensors | 89 |
| 4.1.3 | Mapping of a hyperbolic image onto the sphere | 91 |
| 4.1.4 | Mapping of a parabolic image onto the sphere | 92 |
| 4.2 | Processing of non-Euclidean images | 93 |
| 4.2.1 | Scale-space analysis for non-Euclidean images | 93 |
| 4.2.2 | Active contours on non-Euclidean manifolds | 102 |
| 4.2.3 | Motion estimation in spherical omnidirectional images | 107 |
| 4.3 | Summary | 111 |
| | Conclusions | 113 |
| | Appendix A | 115 |
| | Bibliography | 119 |
| | Curriculum Vitae | 125 |

Abstract

This dissertation investigates wavelets as a multiscale tool on non-Euclidean manifolds. The growing importance of using non-Euclidean manifolds as a geometric model for data comes from the diversity of the data collected. In this work we mostly deal with the sphere and the hyperboloid. First, given the recent success of the continuous wavelet transform on the sphere a natural extension is to build discrete frames. Then, from a more theoretical perspective, having already wavelets on the sphere, which is a non-Euclidean manifold of constant positive curvature, it is interesting and even challenging to build and prove the existence of wavelets on its dual manifold-the hyperboloid as non-Euclidean manifold of constant negative curvature.

This dissertation starts with detailing the construction of one- and two-dimensional Euclidean wavelets in both continuous and discrete versions. Next, it continues with details on the construction of wavelets on the sphere. In the three cases (line, plane and sphere) the group theoretical approach for constructing wavelets is used.

We develop discrete wavelet frames on the sphere by discretizing the existing spherical continuous wavelet transform. First, half-continuous wavelet frames are derived. Second, we show that a controlled frame may be constructed in order to get an easy reconstruction of functions from their decomposition coefficients. Finally we completely discretize the continuous wavelet transform on the sphere and give examples of frame decomposition of spherical data. As a close parent of the wavelet transform we also implement the Laplacian Pyramid on the sphere.

Another important part of this dissertation is dedicated to the hyperboloid. We build a total family of functions, in the space of square-integrable functions on the hyperboloid, by picking a probe with suitable localization properties, applying on it hyperbolic motions and supplemented by appropriate dilations. Based on a minimal set of axioms, we define appropriate dilations for the hyperbolic geometry. Then, the continuous wavelet transform on the hyperboloid is obtained by convolution of the scaled wavelets with the signal. This transform is proved to be a well-defined invertible map, provided the wavelets satisfy an admissibility condition.

As a final part in this dissertation, we discuss one possible application of non-Euclidean wavelets - the processing of non-Euclidean images. This leads to implementing some other basic non-Euclidean image processing techniques, for example scale-space analysis and active contour, that we apply to catadioptric image processing.

Version Abrégé

Cette dissertation étudie la transformée en ondelettes en tant que technique multirésolution sur des variétés non-Euclidiennes. L'importance grandissante de ces variétés comme modèle géométrique est motivée par la pluralité et la complexité de nouvelles formes de données. Dans ce travail, nous nous concentrons principalement sur la sphère et l'hyperboloïde. Tout d'abord, au vu des récents succès de la transformée continue en ondelettes sur la sphère, une extension naturelle consiste à construire des repères discrets associés. Un second problème, de nature plus théorique, consiste à étendre le formalisme sphérique au cas de la variété duale à la sphère: l'hyperboloïde de courbure constante négative.

Notre travail démarre avec un exposé des transformées euclidiennes en dimension un et deux, dans leurs versions continues et discrètes. Ensuite, nous détaillons la construction des ondelettes sur la sphère. Dans ces trois cas, droite, plan et sphère, nous procédons au moyen de l'approche par théorie des groupes.

Nous développons ensuite des repères sur la sphère en discrétisant la transformée continue. D'abord, nous introduisons les repères dits quasi-continus. Ensuite nous prouvons que ces repères peuvent être contrôlés par un opérateur borné et à inverse borné, ce qui nous permet de reconstruire aisément une fonction à partir de ses coefficients dans le repère. Enfin, nous procédons à une discrétisation complète et donnons des illustrations pratiques sur des signaux naturels. La pyramide laplacienne sur la sphère, un parent proche des ondelettes, est également discutée.

Une autre partie importante de cette dissertation concerne l'hyperboloïde. Nous introduisons une nouvelle famille totale de fonctions dans l'espace des fonctions de carré intégrable sur cette variété en sélectionnant une forme génératrice à laquelle nous appliquons des rotations hyperboliques, supplémentées de dilatations spécialement définies. Ces dernières sont construites sur base d'un ensemble minimum d'axiomes adaptés à la géométrie hyperbolique. Ensuite nous définissons la transformée continue en ondelettes au moyen de la convolution entre un signal et la famille explicitée plus haut. Nous prouvons que cette transformée est bien définie et possède un inverse stable si la forme génératrice de départ satisfait une condition d'admissibilité.

Dans la dernière partie de cette dissertation, nous discutons des applications des ondelettes à des images non-Euclidiennes. Ceci nous amène à introduire d'autres outils de traitement d'images sur des variétés, comme les notions d'espace-échelle et de contours actifs. Enfin nous montrons des applications pratiques aux images catadioptriques.

List of Figures

| | | |
|-----|---|----|
| 1.1 | Examples of non-Euclidean manifolds: (a) 2-sphere, (b) one-sheeted 2-hyperboloid, (c) two-sheeted 2-hyperboloid. | 8 |
| 1.2 | The hyperboloid model of the hyperbolic plane. | 9 |
| 1.3 | Examples of non-Euclidean manifolds: (a) ellipsoid,(b) elliptic paraboloid, (c) hyperbolic paraboloid. | 9 |
| 1.4 | Examples of non-Euclidean signals: (a) CMB temperature anisotropies full sky image, (b) spherical omni-directional image, (c) diffusion spectrum magnetic resonance image, (d)high-dimensional data. | 10 |
| 1.5 | Examples of 1-D Euclidean wavelets: (a) Mexican hat wavelet, (b)real part of the Morlet wavelet, $\omega_0 = 7$ | 19 |
| 1.6 | Examples of 2-D Euclidean wavelets: (a) 2-D Mexican hat wavelet, $\sigma = 1.7$, (b) 2-D DOG wavelet, $\alpha = 0.5$ | 22 |
| 2.1 | Spherical geometry: (a) spherical coordinates, (b)cross-section of a stereographic projection through the South Pole. | 30 |
| 2.2 | Spherical DOG wavelet for $\alpha = 1.25$: (a) $a = 0.03$,(b) $a = 0.09$ | 39 |
| 2.3 | The function $S(l)$ for $l \in [0, 31)$ and $K = 1, 2, 3$. First Approach. | 42 |
| 2.4 | The function $S(l)$ for $l \in [0, 31[$ and $K = 1, 2, 3$. Second Approach. | 44 |
| 2.5 | Behavior of $\hat{\psi}_a(l, 0)$ as a function of the scale a . If $a = 0.01$, the bandwidth of the dilated wavelet exceeds the limit fixed by the discretization. | 44 |
| 2.6 | Spherical frame decomposition of Mars map: (a) original data (Mars map) (512×512 equi-angular grid), (b) $\mathcal{W}_2[p, q]$, (c) $\mathcal{W}_3[p, q]$, (d) $\mathcal{W}_5[p, q]$, (e) $\mathcal{W}_7[p, q]$, (f) $\mathcal{W}_8[p, q]$. . . | 50 |
| 2.7 | Spherical frame reconstruction of the Mars map: (a) approximate reconstruction (by inverse spherical wavelet frames), (b)amplitude of the error of the reconstruction, (c) by spherical conjugate algorithm, (d) difference between the original and reconstructed signal $s^{(2)}$ obtained by 2 iterations of the conjugate gradient algorithm. | 51 |
| 2.8 | Decomposition step of 2 level Spherical Laplacian Pyramid, 512 × 512-Mars surface map. The finished pyramid consists of two hight-pass bands (h_0, h_1) and the low-pass band (f_2). | 54 |
| 2.9 | Reconstruction step for 2 level Spherical Laplacian Pyramid. The process begins with the two hight-pass bands (h_0, h_1) and the low-pass band (f_2), and then perfectly reconstructs the starting sphere f_0 | 55 |
| 3.1 | Geometry of the 2-hyperboloid. | 58 |
| 3.2 | Projective structure on the hyperboloid: conic projection | 59 |

| | | |
|------|---|-----|
| 3.3 | Cross-section of a conic projection of the hyperboloid and the action of the dilation through it. | 61 |
| 3.4 | Action of a dilation a on the hyperboloid H_+^2 by “flattening”. | 62 |
| 3.5 | Conic projection and flattening. | 63 |
| 3.6 | Cross-section of conic projection for different parameter p | 63 |
| 3.7 | Analysis of the distance (3.9) as a function of dilation a , with x_N being the North Pole and using conic projection for different parameter p | 64 |
| 3.8 | Action of a dilation a on the hyperboloid H_+^2 through a stereographic projection. . . | 65 |
| 3.9 | Visualization of the dilation on a hyperboloid H_+^2 | 65 |
| 3.10 | The hyperbolic DOG wavelet f_ψ^β , for $\beta = 2$ at different scales a and positions (χ, φ) . . . | 79 |
| 3.11 | Action of a dilation on the hyperbolic DOG wavelet f_ψ^β , for $\beta = 2$ at $\chi = 0, \varphi = 0$; up: $a = 0.01$, middle: $a = 0.125$, bottom: $a = 0.5$ | 80 |
| 3.12 | Action of a hyperbolic translation on the hyperbolic DOG wavelet f_ψ^β , for $\beta = 2$ at $a = 0.3, \varphi = \pi$; up: $\chi = 0.75$, middle: $\chi = 1.25$, bottom: $\chi = 2.75$ | 81 |
| 3.13 | Action of a rotation on the hyperbolic DOG wavelet f_ψ^β , for $\beta = 2$ at $a = 0.3, \chi = 1.25$; up: $\varphi = \pi/2$, middle: $\varphi = \pi/4$, bottom: $\varphi = 3\pi/2$ | 82 |
| 3.14 | Continuous wavelet transform of a hyperbolic triangle at different scales a , using hyperbolic DOG wavelet with $\beta = 2$ | 83 |
| 4.1 | Notion of plenoptic function: (a) The plenoptic function describes the information available to an observer at any point in space and time, (b) the image information available from a single viewing point is described by the pencil of light rays passing through the eye; the rays are parameterized in spherical coordinates and so is represented the full sphere of optical information impinging on a point in space. . . . | 88 |
| 4.2 | Examples of non-Euclidean images: (a) hyperbolic, (b) parabolic. | 89 |
| 4.3 | Geometric configuration of catadioptric sensor with hyperbolic mirror: the camera center coincides with the focal point of the mirror F_C and the rays reflected from the mirror intersect in F_M | 90 |
| 4.4 | Geometric configuration of catadioptric sensor with parabolic mirror: an (orthographic) camera with a parabolic mirror assembled so that rays of the camera are parallel to the mirror symmetry axis and the reflected rays intersect in F_M | 91 |
| 4.5 | Plenoptic sphere centered at the hyperbolic mirror focus F_M | 91 |
| 4.6 | Cross-section of mapping the parabolic image on the sphere [35]. | 93 |
| 4.7 | Scale-space stack of non-Euclidean images. | 94 |
| 4.8 | Scale-space on a hyperbolic image: (a) original, (b) $t = 10$, (c) $t = 100$, (d) $t = 300$. . | 98 |
| 4.9 | Gradient of a hyperbolic image: (a) original image, (b) gradient in direction of x , (c) gradient in direction of y , (d) magnitude of the gradient. | 99 |
| 4.10 | Scale-space on a spherical image: (a) original image, (b) $t = 10$, (c) $t = 100$, (d) $t = 300$ | 101 |
| 4.11 | Gradient of a real spherical image: (a) original image, (b) spherical gradient. | 101 |
| 4.12 | Active contour on a Euclidean image: (a) original image (b) associated edge detecting function $f(I_0)$, (c) the contour at the beginning of the evolution process, (d) the contour at the end of the evolution process. | 102 |
| 4.13 | Evolution of geometric active contour on the hyperboloid: (a) initial contour on the hyperboloid, (b) initial contour viewed on the unit disk, (c) the contour at final state of evolution on the hyperboloid, (d) the contour at final state of evolution, viewed on the unit disk | 105 |

| | |
|--|-----|
| 4.14 Segmentation in a synthetic hyperbolic image: (a) original image, (b) edge detection function, (c) segmented image | 106 |
| 4.15 Evolution of the geometric active contour on the sphere: (a) the initial state of the contour on the sphere, (b) the initial state of the contour projected on the disk, (c) the contour in a further state of its evolution on the sphere, (d) the contour in a further state of its evolution projected on the disk | 106 |
| 4.16 Algorithm for local motion estimation on the sphere. | 107 |
| 4.17 Parabolic image mapped on the sphere of view, level $l = 1$ | 109 |
| 4.18 Level 0 of the motion estimation algorithm: (a) first original unfolded sphere S_0 , (b) second original unfolded sphere G_0 | 109 |
| 4.19 Motion predicted image \widetilde{G}_0 | 109 |
| 4.20 Motion predicted error E_0 | 110 |
| 4.21 Motion field at resolution level 3. | 110 |
| 4.22 Relative energy of the prediction error, for different block and search window sizes ($L = 5$). | 110 |

List of Tables

| | | |
|-----|--|----|
| 2.1 | Estimation of the bounds A and B as a function of the extremum of $S(l)$ for some values of K . First approach. | 42 |
| 2.2 | Estimation of the bounds A and B as a function of the extremum of $S(l)$ for some values of K . Second approach. | 44 |
| 2.3 | Evaluation of K_0 , K_1 and δ on the functions $f \in L^2(S^2)$ at bandwidth 128. | 48 |

Introduction

The wavelet analysis is a particular time-scale or space-scale representation of signals. Its applications run from signal and image processing to data analysis.

The Fourier Transform (FT) converts a function f that depends on time, into a new function \hat{f} which depends on frequency. In contrast, the wavelet transform uses approximating functions that are localized in both time and frequency space. It is this unique characteristic that makes it particularly useful.

Although wavelets represent a departure from Fourier analysis, they are also a natural extension of it. Thus the history of wavelets begins with the history of Fourier analysis. Before 1975, many researchers had pondered over the idea of Windowed Fourier Analysis (for instance Gabor in [32]) and this idea allowed to consider things in terms of both time and frequency. Windowed FT dealt with studying the frequencies of a signal piece by piece, i.e. window by window. This windows helped to make the time variable discrete or fixed. The different oscillating functions of varying frequencies could be looked at in these windows. While Morlet worked with windowed Fourier analysis he discovered that keeping the window fixed was the wrong approach. He did exactly the opposite. He kept the frequency of the function (number of oscillations) constant and changed the window. He discovered that stretching the window stretched the function and squeezing the window compressed the function. Morlet and Grossman worked on an idea that Morlet discovered while experimenting on a basic calculator - that is, a signal could be transformed into wavelet form and then transformed back into the original signal without any information being lost. Since wavelets deal with both time and frequency, they thought a double integral would be needed to transform wavelet coefficients back into the original signal. However, in 1984, Grossman found that a single integral was all that was needed [36]. While working on this idea, they also discovered another interesting thing: making a small change in the wavelets only causes a small change in the original signal.

The next two important contributors to the field of wavelets were by Meyer and Mallat [56, 55]. They gave rise to the multiresolution analysis. Using wavelets as a tool for multiresolution analysis was a big step in the research of wavelets. It was where the scaling function of wavelets was first mentioned, and it allowed researchers and mathematicians to construct their own family of wavelets using its criteria. Around 1988, Daubechies created her own family of wavelets [26] based on the same idea. Daubechies wavelet family satisfies a number of wavelet properties. They have compact support, orthogonality, regularity, and continuity.

However, data analysis has undergone deep changes recently and the field faces new exciting challenges. On one hand the volume of data is exploding due to the ubiquity of digital sensors(think of a camera). The first challenge resides in extracting information from very high dimensional data. On the other hand, the type of data has also evolved tremendously over the past few decades, from images or volumetric data to non-scalar valued signals. As a first example comes tensor

diffusion imaging, a new modality in medical imaging; or multi-modal signals, i.e. signals obtained when the same physical scene is observed through different sensors. The representation and analysis of signals in non-Euclidean geometry is a recurrent problem in many scientific domains. Not only certain data are constrained by nature on curved surfaces, but a lot of detectors collect information via interfaces which are geometrically complicated. Because of these demands, in 1998 Antoine and Vandergheynst built wavelets on the sphere that are coherent states associated to the conformal group of the sphere [9, 10].

Having already wavelets on the sphere, which is a non-Euclidean manifold of constant positive curvature, it is interesting and even challenging to build and prove the existence of wavelets on its dual manifold - the hyperboloid as a non-Euclidean manifold but of constant negative curvature.

Another recurrent problem connected to these non-Euclidean wavelets is processing of omnidirectional images obtained from catadioptric imaging sensors. The advantages of the latter over the (classical) cameras comes from shooting a 360^0 -scene with a camera and a curved mirror. This mirror could be hyperbolic, or spherical, or parabolic, and images obtained are governed by the corresponding mirror's geometry, the non-Euclidean ones. It is challenging to implement some image processing techniques. As main examples stand scale-space analysis, active contour and motion estimation.

Organization of the Dissertation

This dissertation articulates around harmonic analysis on non-Euclidean manifolds. It is realized in four main chapters. The first three chapters are theoretical. They concern the wavelet transform on Euclidean manifolds, on the sphere and on the hyperboloid, respectively. The fourth one is application oriented. The state of the art is described in the whole first chapter and in a part of the second one. In a little more detail:

- **Chapter 1: Manifolds, signals and wavelets**

This chapter focuses on the concept of manifold, including both Euclidean and non-Euclidean ones. It recalls the basic Fourier transform and gives the basic notion of construction of wavelets together with the corresponding wavelet transform on Euclidean manifolds. In general, two main approaches for building wavelets on a manifold are distinguished: one based on group-theory and the other based on convolution. Two particular Euclidean cases are explored: wavelets on the line and wavelets on the plane. It finishes with discretization of the continuous wavelet transform for both one- and two-dimensional Euclidean cases.

- **Chapter 2: Wavelets and frames on the sphere**

In this chapter we enter into the non-Euclidean world and concentrate on the sphere. It starts with recalling the group-theoretical construction of wavelets on the sphere. Then we discretize it and construct the stereographic frames on the sphere.

- **Chapter 3: Wavelet on the hyperboloid**

We enter deeper into the non-Euclidean world and, in this chapter, we focus on the hyperboloid. The difference between the sphere and hyperboloid, even though both non-Euclidean manifolds, is just the curvature: the first has positive, while the latter negative. One important ingredient for wavelet is the dilation operation. Based on a minimal set of axioms, we define appropriate dilations for the hyperbolic geometry. We then define the corresponding continuous wavelet transform based on convolution theorem and prove that this is an invertible map.

- **Chapter 4: On processing non-Euclidean images**

This chapter present some processing techniques for non-Euclidean images. These are scale-space and active contour. All are based on the usual Euclidean one, but taking into account the respective geometry and its influence on the image, we derive their non-Euclidean counterparts. Motion estimation algorithm on the sphere is developed as well.

This division allows an easy access to particular wavelets construction viewed from the prism of manifold's geometry.

Main Contributions of the Dissertation

- Derivation of half-continuous and fully discretized stereographic wavelet frames on the sphere.
- Construction of Laplacian pyramid on the sphere.
- Construction of wavelets on the hyperboloid. This includes: proof of the convolution theorem in Fourier-Helgason domain, derivation of hyperbolic wavelet admissibility condition for different schemes of hyperbolic dilation.
- Derivation of image processing techniques for non-Euclidean images obtained by central catadioptric sensors. These are: scale-space, active contour on the sphere and hyperboloid; multiresolution motion estimation on the sphere.

Manifolds, Signals and Wavelets

1

In this introductory chapter, we give a basic idea for signals and their relation to flat or curved manifolds, i.e. Euclidean or non-Euclidean. Signals are analyzed better in frequency domain and the Fourier transform is the tool which transforms a signal as a function of time to a function of frequency. It is the basic tool for harmonic analysis but not the most efficient. The idea behind the wavelet transform is to decompose a signal locally into contributions living at different scales and thus it stands ahead the Fourier transform. Obviously, the signal analysis is more efficient in time-frequency domain. Thus wavelets on the line and plane are described as two particular cases of wavelets on Euclidean manifolds. It finishes with exposing different aspects of the discretization of continuous wavelet transform for both one- and two-dimensional Euclidean cases.

1.1 The notion of manifold

Euclid has formulated the first geometric theory in his "*Elements*", the *Euclidean geometry*, based on axioms justified by physical experience and the perception of space. This step seemed natural: a mathematical theory, whatever its abstraction is, presents more or less a link with the physical reality. The difficulties which affront the mathematicians interested in the fundamentals of geometry, come not only from the confusion between metrical and topological concepts, but as well from the concept of the grandeur of the objects in multiple dimensions.

A *manifold* is a topological space that is locally Euclidean [50, 65], i.e. around every point, there is a neighborhood that is topologically the same as the open unit ball in \mathbb{R}^n . To illustrate this idea, let consider the ancient belief that the Earth was flat as contrasted with the modern evidence that it is round. The discrepancy arises essentially from the fact that on the small scales that we see, the Earth does look flat. In general, any object that is nearly "flat" on small scales is a manifold, and so manifolds constitute a generalization of objects we could live on in which we could encounter the round/flat "Earth problem".

The basic example of a manifold is *Euclidean space*, i.e. n -dimensional real linear space \mathbb{R}^n , and many of its properties carry over to manifolds. In particular, \mathbb{R} is the real line and \mathbb{R}^2 is the

Euclidean plane. A manifold is *symmetric* with respect to a given operation, if this operation (when applied on it) does not change it. Actually, the Euclidean plane is a symmetric surface*. The basic operations of symmetry are:

- Translation is an affine transformation of Euclidean space which moves every point by a fixed distance in the same direction. It can also be interpreted as the addition of a constant vector to every point, or as shifting the origin of the coordinate system;
- Rotation: a counterclockwise rotation of the plane about the origin;
- Reflexion (mirror view): "flips" the plane over a line.

A manifold may be endowed with more structure than a locally Euclidean topology. For instance, it could be smooth. A smooth manifold with a metric is a *Riemannian manifold* [13, 59].

1.1.1 Riemannian manifold

Certainly we should be able to measure lengths of curves on the manifold in order to do geometry. For a surface $M^2 \subset \mathbb{R}^3$, we can measure the length of a curve $\gamma : [0, 1] \rightarrow M$ by the usual formula

$$l(\gamma) = \int_0^1 |\gamma'(t)| dt \quad (1.1)$$

Notice that the basic ingredients is the measure of the length of the tangent vector $\gamma'(t) \in T_{\gamma(t)}M$, where $T_{\gamma(t)}M$ is the tangent space of the curve $\gamma(t)$ on the manifold M . We can also use this formula for any manifold embedded in \mathbb{R}^n , which covers the classical cases in algebraic geometry and analysis where manifolds appear as the zero set of constraint equations.

Definition 1. A Riemannian manifold (M, g) is a smooth manifold M with a family of smoothly varying positive definite inner products $g = g_x$ on T_xM for each $x \in M$. The family g is called a Riemannian metric. Two Riemannian manifolds (M, g) and (N, h) are called isometric if there exists a smooth diffeomorphism $f : M \rightarrow N$ such that

$$g_x(X, Y) = h_{f(x)}(dfX, dfY)$$

for all $X, Y \in T_xM$, for all $x \in M$.

Given a Riemannian metric we can set the length of a curve $\gamma : [0, 1] \rightarrow M$ to be

$$l(\gamma) = \int_0^1 g_x \sqrt{(\gamma'(t), \gamma'(t))} dt. \quad (1.2)$$

On \mathbb{R}^n , the standard Riemannian metric is given by the standard inner product $g_x(v, w) = v \cdot w$ for all $u, w \in T_x\mathbb{R}^n$, for all $x \in \mathbb{R}^n$. Of course, we call \mathbb{R}^n with this Riemannian metric *Euclidean space*. If M is a sub-manifold of Euclidean space, then M has a natural Riemannian metric given by $g_x(v, w) = v \cdot w$. This so called *induced metric* is the metric used in the classical theory of curves and surfaces in Euclidean three-space. By this same construction, a sub-manifold of a Riemannian manifold always inherits an induced metric.

To compute with Riemannian metric, we must be able to analyze it in a local coordinate chart. If $v, w \in T_xM$ and (x_1, x_2, \dots, x_n) are coordinates near x , then there exist α_i, β_i such that

$$v = \sum \alpha_i \frac{\partial}{\partial x_i}, \quad w = \sum \beta_i \frac{\partial}{\partial x_i}. \quad (1.3)$$

*a surface is a two-dimensional manifold

We have

$$g_x(v, w) = g_x\left(\sum_i \alpha_i \partial_{x_i}, \sum_j \beta_j \partial_{x_j}\right) \quad (1.4)$$

$$= \sum_{i,j} \alpha_i \beta_j g_x(\partial_{x_i}, \partial_{x_j}), \quad (1.5)$$

where $\partial_{x_i} = \frac{\partial}{\partial x_i}$. Thus, g_x is determined by the symmetric, positive definite matrix $(g_{ij}(x)) = (g_x(\partial_{x_i}, \partial_{x_j}))$. Note that while the metric g is defined on all of M , the $g_{ij}(x)$ are defined only in a coordinate chart, where we can write

$$g = \sum_{i,j} g_{ij} dx_i \otimes dx_j. \quad (1.6)$$

Here g_{ij} is called metric tensor and g is known as linear element, or first fundamental form.

Therefore, Riemannian manifolds permit to understand and visualize the concepts and fundamental results of the *non-Euclidean geometry*.

Let us develop the metric (1.6) in three-dimensional Euclidean space with orthogonal coordinate system x_0, x_1, x_2 . We note it as $ds^2 \equiv g$. It is defined by the relation:

$$ds^2 = dx_0^2 + dx_1^2 + dx_2^2. \quad (1.7)$$

Inside this space, another manifolds exist. They are two-dimensional manifolds imbedded in three-dimensional Euclidean space. For instance, the plane can be viewed as a two-dimensional Euclidean manifold in the three-dimensional Euclidean space.

1.2 Non-Euclidean manifolds

In the three-dimensional Euclidean space, the set of all points equidistant from a point (called a center) forms a sphere (Figure 1.1(a)). Each point x on this surface can be described by three-dimensional vector in polar coordinates $\theta \in [0, \pi]$ and $\varphi \in [0, 2\pi]$ as $x = (\cos \theta, \sin \theta \sin \varphi, \sin \theta \cos \theta) \equiv (x_0, x_1, x_2)$. In this particular case, we assumed the distance between each point and the center to be 1. Based on these coordinates we can see that the metric on this surface is $ds^2 = d\theta^2 + \sin^2 \theta d\varphi^2$. What first distinguishes the sphere from the Euclidean plane is that the sphere is not flat and the *curvature* is the amount by which it deviates from being flat. A manifold which bulges out in all directions, such as the sphere, is positively curved. A rough test for positive curvature is that if one takes any point on the manifold, there is some plane touching it at that point so that the manifold lies all on one side except at that point.

The negative curvature analogue of the n -sphere is the *hyperbolic n -space* [68]. Two-dimensional hyperbolic surface $H^2 \in \mathbb{R}^3$ can be thought of a sphere of imaginary radius. Figure 1.1(b) shows the one-sheeted hyperboloid, while Figure 1.1(c) shows the two-sheeted hyperboloid. Every plane through a point on such a manifold actually cuts it in two or more pieces.

What distinguishes the three surfaces - the plane, sphere and hyperboloid, is the fact that they satisfy all the standard postulate of the Euclidean geometry [23], except the subtle fifth postulate which concerns the existence and uniqueness of straight lines passing by a point and parallel to a given another straight line. It is remarkable that these geometries are characterized by their behavior according this postulate.

The geometries of the plane and of the sphere are connected by the fact that each one can be represented in a three-dimensional Euclidean space. Their symmetries result from the ones of the three-dimensional Euclidean geometry, which facilitates their visualization. But this pleasant fact

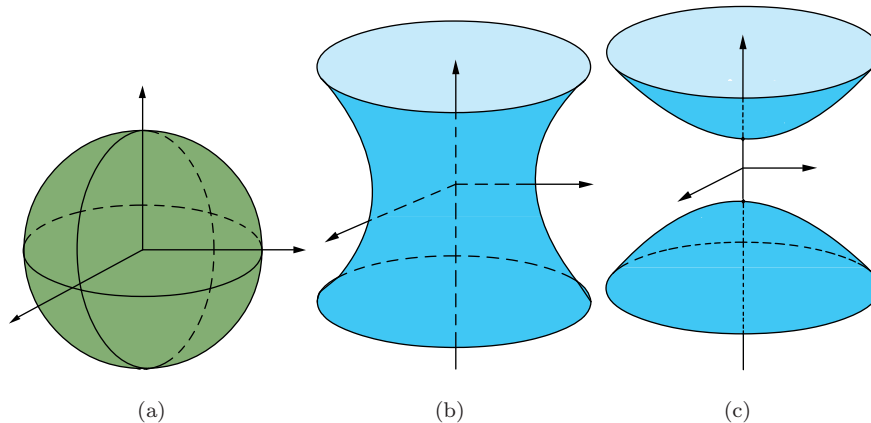


Figure 1.1: Examples of non-Euclidean manifolds: (a) 2-sphere, (b) one-sheeted 2-hyperboloid, (c) two-sheeted 2-hyperboloid.

is not valid for the hyperbolic plane. One could represent some aspects of the hyperbolic plane in the Euclidean geometry, but some other aspects of it will be lost.

The non-Euclidean geometry, elaborated by Lobatchevsky is known as *hyperbolic geometry*[20]. It is obtained as the fifth postulate in the Euclidean geometry:

"In the plane, it exists one and only one straight line passing through a point and parallel to another straight line which does not contain the given point",

is replaced by

"Given a straight line in the plane and a point, not on the line, there are more than one straight lines parallel to the given line and passing through the given point".

In other words, in the geometry of Lobatchevsky, there exist an infinity of lines passing through same point and parallel to a straight line, which does not contain this point.

There are many representations of the hyperbolic plane studied and known. Such are the upper half of the Euclidean plane, the Poincaré disk, Beltrami pseudo sphere, Klein's model or hemisphere model [68]. But the most popular model among all of them is the *hyperboloid model* shown on Figure 1.2. This model represents the surface of revolution of a hyperbola. The bottom of the hyperboloid is at distance 1 (North Pole) from the origin O. Though the model is actually stretched up to infinity, it is cut for easy observation and visualization. We put a disk at the origin and draw sweeping rays from -1 (the South Pole) of the axis of revolution* to the red straight line on the hyperboloid and thus we get the so called arc, on the Poincaré's disk. Actually, the simplest representation of the hyperbolic plane, from the Riemannian geometry viewpoint, is as one sheet of a two sheeted hyperboloid.

It is important to note that the sphere and the hyperboloid are not the only examples of non-Euclidean manifolds, but they are the canonical ones. Roughly speaking, each manifold which is not flat is already non-Euclidean one. Such are, for instance, the ellipsoid or the paraboloid [59, 23]. In the three-dimensional Euclidean space, each point on the ellipsoid can be described by the vector $x = (a \cos \theta, b \sin \theta \sin \varphi, c \sin \theta \cos \varphi)$, $\theta \in [0, \pi]$, $\varphi \in [0, 2\pi]$ and a, b, c are fixed positive real numbers determining the shape of the ellipsoid. In fact, if two of those numbers are equal, the ellipsoid is a spheroid; if all three are equal, then we have a sphere. On the other hand, there are two kinds

*a straight line about which some line or plane is revolved, so that the several points of the line or plane shall describe circles with their centers in the fixed line, and their planes perpendicular to it, the line describing a surface of revolution, and the plane a solid of revolution.

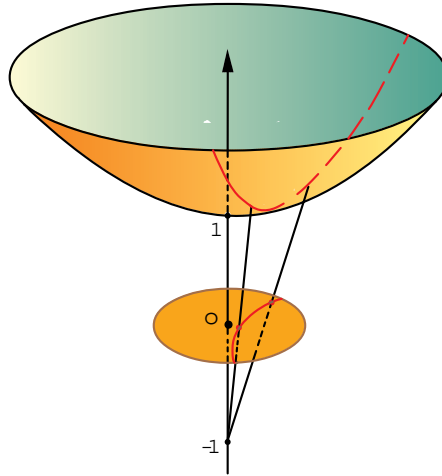


Figure 1.2: The hyperboloid model of the hyperbolic plane.

of paraboloid: elliptic and hyperbolic as shown on Figures 1.3(b) and 1.3(c), respectively. The elliptic paraboloid is shaped like a cup and can have a maximum or minimum point. The hyperbolic paraboloid is shaped like a saddle and can have a critical point called a saddle point.

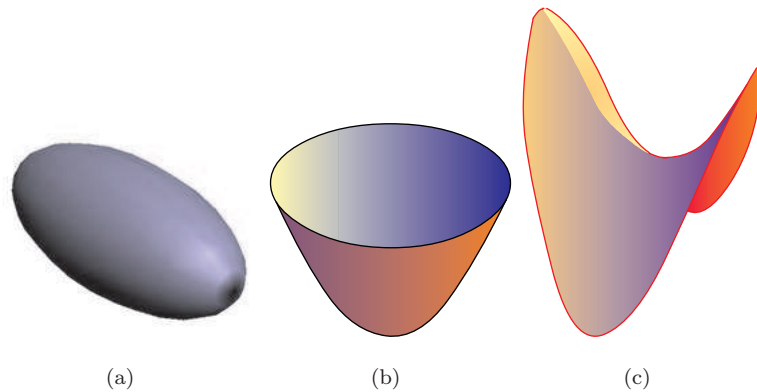


Figure 1.3: Examples of non-Euclidean manifolds: (a) ellipsoid, (b) elliptic paraboloid, (c) hyperbolic paraboloid.

In this dissertation, we mostly work on the sphere and on the hyperboloid. The elliptic paraboloid will also appear in the last chapter. For simplicity, it is called paraboloid. But first we explain what is the use of non-Euclidean manifolds in data analysis.

1.3 Non-Euclidean manifolds as a geometric model for data

Let us think of a specific case: we measure minute changes in temperature, produced by an infra-red radiation. For this purpose a thermal sensor is used for detecting the temperature differences. These temperatures are peaked up in an electronic circuit and stored on computer. In addition, if these are measurements performed by a satellite then we obtain an image of this temperature fluctuations in the full sky. Obviously, the set of data obtained is somehow spherical since the satellite is in

the center of the sphere and it measures the data all around. Clearly, there is data collected on curved manifolds. Actually, not only certain data is constrained by nature on curved surfaces, but a lot of detectors collect information via interfaces which are geometrically complicated. A natural example is the human eye. In the same manner, if we have a spherical mirror, in it we can see the reflection of the scene around. In addition, having a camera which points at that mirror we obtain a spherical image. Respectively, by using a hyperbolic mirror instead of the spherical one, we obtain a hyperbolic image. Therefore, from geometrical point of view, these signals are *non-Euclidean (multidimensional) signals*. Concrete examples are shown on Figure 1.4. What we see on Figures 1.4(a) and 1.4(b) is that these are somehow 2-D (flat) images. Actually, it is so because the non-Euclidean data they contain was adapted to the Euclidean space, so that it would be possible to represent them. This "adaptation" is a projection of the non-Euclidean data to a manifold which is usually in the Euclidean world.

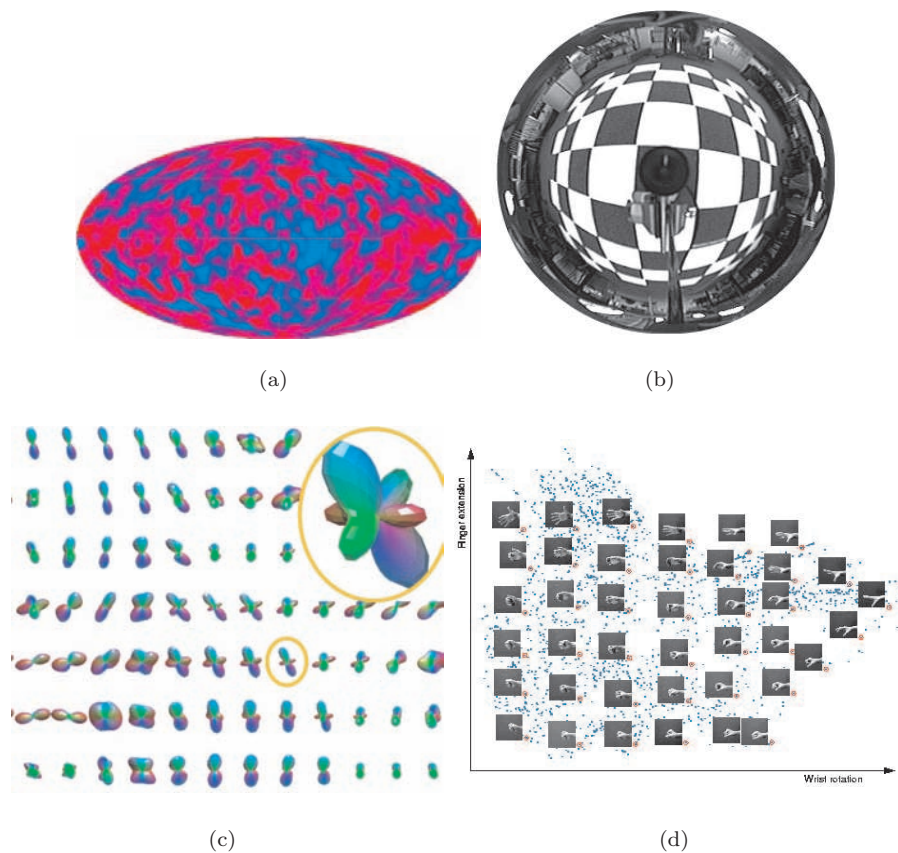


Figure 1.4: Examples of non-Euclidean signals: (a) CMB temperature anisotropies full sky image, (b) spherical omni-directional image, (c) diffusion spectrum magnetic resonance image, (d) high-dimensional data.

The current "data deluge" inundating science and technology is remarkable not merely for the often-mentioned *volumes* of data, but also for the rapid proliferation in new data types. In addition to the old standby of simple numerical arrays, we are starting to see arrays where the entries have highly structured values obeying nonlinear constraints [66, 17].

Clearly, a given feature shared by all these complex data is the importance of geometry and we can distinguish three different occurrences of the non-Euclidean geometry in data processing:

- (i) Data on non-Euclidean manifold: for instance-Cosmic Microwave Background (CMB) temperature anisotropies full sky image (Figure 1.4(a)); non-Euclidean (omnidirectional) images (Figure 1.4(b));
- (ii) Data with non-scalar values, i.e. manifold-valued signals: for instance, diffusion tensor MRI [37] - at each point \vec{x} of a sampled volume in \mathbb{R}^3 is assigned a function $P_{\vec{x}}(\theta, \varphi)$ that describes the probability with which a water molecule at \vec{x} diffuses in direction (θ, φ) (Figure 1.4(c));
- (iii) Euclidean data (in \mathbb{R}^n) but mostly clustered around a lower dimensional non-Euclidean manifold i.e. data arrays of the form $s(t), s(x, y), s(x, y, z)$ with t, x, y, z run through equi-spaced values in a cartesian grid, and s takes values in a manifold M (Figure 1.4(d)): for instance high dimensional data sets; document databases.

1.4 Signals and harmonic analysis

1.4.1 A broad definition for signal

It is difficult, and even it might be impossible to give a unique definition of a signal, since it varies from one to another domain of application. Even though, a signal is a "representation" of a variable of a physical system meant to provide "information" on that given system. Most signals of interest can be modelled as functions of time or position [63, 49] or they can be of different dimensions:

- Since a sound is a vibration of a medium (such as air), a sound signal associates a pressure value to every value of time. This is 1-D continuous time signal.
- A picture assigns a color value to each of a set of points. Since the points lie on a plane, the domain is two-dimensional. A painting, being a physical object, is a continuous signal.
- A video is a series of images. A point in a video is identified by its position (two-dimensional) and by the time at which it occurs, so the video is a three-dimensional signal.

One of the fundamental distinctions between different types of signals is between continuous-time, as the sound is, and discrete-time. In the mathematical language, the domain of a continuous-time (CT) signal is the set of real numbers, whereas the domain of a discrete-time (DT) signal is the set of integers (or some interval)[49]. It is the nature of the signal that determines what these integers represent. Computers and other digital devices are restricted to discrete time. For instance, CDs contain discrete signals representing sound, recorded at 44,100 samples per second. Or, digital images are 2-D digital signals. It is often convenient to represent color as the sum of the intensities of three primary colors, so that this kind of signal is vector-valued with dimension three.

1.4.2 Signal analysis in frequency domain

A time-domain graph shows how a signal changes over time, whereas a frequency domain graph shows how much of the signal lies within each given frequency band over a range of frequencies. When we analyze a signal(function) with respect to frequency, then we work in the *frequency domain*. A frequency domain representation also includes information on the phase shift that must be applied to each frequency in order to be able to recombine the frequency components to recover the original time signal.

It is remarkably useful to analyze the *frequency spectrum* of a signal, which is a representation of a signal or other function in terms of frequency. A frequency spectrum contains both amplitude

(non-negative scalar measure of a wave's magnitude of oscillation) and phase (relates the position of a feature to that same feature in another part of the waveform) information. The power spectrum describes how much of the "energy" (loosely defined) of the function or signal lies in any given frequency band, without regard for the phase. This technique is applicable to all signals, both continuous and discrete. For instance, if a signal is passed through a linear time-invariant system, the frequency spectrum of the resulting output signal is the product of the frequency spectrum of the original input signal and the frequency response of the system.

Fourier transform

Actually, the *Fourier transform* of a signal $f(t)$ can be thought of as that signal in the frequency domain. It is the operation which transforms the signal from a function of time $f(t)$ to a function of frequency $\hat{f}(\omega)$; it is a decomposition of a function into harmonics of different frequencies [43, 48].

Suppose f is a complex-valued Lebesgue-integrable function, i.e. $f \in L^1(\mathbb{R})$. We then define its *continuous Fourier transform* \hat{f} to be also a complex-valued function:

$$\hat{f}(\omega) = \frac{1}{\sqrt{2\pi}} \int_{-\infty}^{\infty} f(t)e^{-i\omega t} dt, \quad \forall \omega \in \mathbb{R}. \quad (1.8)$$

We think of ω as a frequency and $\hat{f}(\omega)$ as the complex number which is the amplitude and phase of the component of the signal $f(t)$ at that frequency.

The Fourier transform is close to a self-inverse mapping: if $\hat{f}(\omega)$ is defined as above, and f is sufficiently smooth, then

$$f(t) = \frac{1}{\sqrt{2\pi}} \int_{-\infty}^{\infty} \hat{f}(\omega)e^{i\omega t} d\omega, \quad \forall t \in \mathbb{R} \quad (1.9)$$

The factor $\frac{1}{\sqrt{2\pi}}$ before each integral are normalization factors. These factors are arbitrary as long as their product is equal to $\frac{1}{2\pi}$. The values chosen above are referred to as unitary normalization constants. Another common choice is 1 and $\frac{1}{2\pi}$ for the forward and inverse transforms, respectively. In addition, the Fourier coordinate ω is sometimes replaced by $2\pi\nu$, integrating over all frequencies ν , in which case the unitary normalization constants are both equal to unity.

The Fourier transform can be extended to n -dimensional space in a straightforward manner. If $f(\vec{x}) \in \mathbb{R}^n$ and \vec{k} is the corresponding vector in the transform space, then

$$\hat{f}(\vec{k}) = \left(\frac{1}{\sqrt{2\pi}}\right)^n \int_{\mathbb{R}^n} f(\vec{x})e^{-i\vec{k}\cdot\vec{x}} d\vec{x}, \quad (1.10)$$

where $d\vec{x}$ is an n -dimensional infinitesimal volume element in the space and the product in the exponential is the dot product. Using the n -dimensional orthogonality relationship:

$$\delta(\vec{k} - \vec{k}') = \left(\frac{1}{2\pi}\right)^n \int_{\mathbb{R}^n} e^{\pm i(\vec{k} - \vec{k}')\cdot\vec{x}} d\vec{x} \quad (1.11)$$

yields the inverse transform:

$$f(\vec{x}) = \left(\frac{1}{\sqrt{2\pi}}\right)^n \int_{\mathbb{R}^n} \hat{f}(\vec{k})e^{i\vec{k}\cdot\vec{x}} d\vec{k}. \quad (1.12)$$

The Fourier transform translates between convolution and multiplication of functions. If $f(t)$ and $g(t)$ are integrable functions with Fourier transforms $\hat{f}(\omega)$ and $\hat{g}(\omega)$, respectively, and if the convolution of f and g exists and is integrable, then the Fourier transform of the convolution is given by the product of the Fourier transforms $\hat{f}(\omega)\hat{g}(\omega)$:

$$(f * g)(t) = \int_{-\infty}^{+\infty} f(\tau)g(t - \tau)d\tau \quad (1.13)$$

and consequently

$$\widehat{(f * g)}(\omega) = \hat{f}(\omega)\hat{g}(\omega). \quad (1.14)$$

That is, convolution in the time domain is the equivalent of multiplication in the frequency domain. The same is true in the inverse - convolution in frequency is the equivalent of multiplication in the time domain. The equation (1.14) is the *convolution theorem*. In signal processing language, the convolution is the time-domain equivalent of the *filtering* in the frequency domain. Highly used in data processing is the correlation, even though it is viewed as special case of the convolution. In general, the correlation is used to compare similarities of two sets of data and is written as:

$$\widehat{(f \star g)}(\omega) = \overline{\hat{f}(\omega)}\hat{g}(\omega), \quad (1.15)$$

where $\overline{(\cdot)}$ denotes the complex conjugate. A detailed proof of these two fundamental theorems can be found in [63, 62] for the continuous and discrete case, respectively.

Naturally, for scientific computations and digital signal processing, one must have functions x_k that are defined over discrete instead of continuous domains, again finite or periodic. In this case, one uses the *discrete Fourier transform*, which represents x_k as the sum of sinusoids:

$$x_k = \frac{1}{N} \sum_{j=0}^{N-1} f_j e^{\frac{2\pi i j k}{N}}, \quad k = 0, \dots, N-1, \quad (1.16)$$

where f_j are the Fourier amplitudes. Although applying this formula directly would require $\mathcal{O}(N^2)$ operations, it can be computed in only $\mathcal{O}(N \log N)$ operations using a fast Fourier transform (FFT) algorithm, which makes the FT a fundamental operation.

1.4.3 Time-frequency signal analysis

Most real-life signals are not just complex and influenced by a specific geometry but it is a fact that they are non-stationary, i.e. their statistical properties change with time, and they usually cover a wide range of frequencies. Many signals contain transient components, whose appearance and disappearance are physically very significant. In addition, there is often a direct correlation between the characteristic frequency of a given segment of the signal and the time duration of that segment. Clearly, a generalization of signal processing is needed and the Fourier transform alone is not enough. Strictly speaking, it applies only to stationary signals, and it loses all information about the time localization of a given frequency component. Moreover, it is highly unstable with respect to perturbation, because of its global character. Regarding this problems, the signal analysis turned out to be more efficient in *time-frequency* representation. The idea is that one needs two parameters: one, called a , characterizes the frequency, the other, b , indicates the position in the signal. Indeed, the basic idea of the *wavelet transform*, as we will see later, is to decompose a signal locally into contributions living at different scales. This makes the contrast with the Fourier coefficients, which are sinusoidal waves repeating themselves indefinitely. But taking into account that many signals are in non-Euclidean geometry, new time-frequency analyzing tools are needed. In particular, wavelet transforms are of great interest.

It must be clear that wavelets on the line or on the plane are two particular cases of *Euclidean wavelets*, in particular, in the space $L^2(\mathbb{R})$ or in $L^2(\mathbb{R}^2)$. Naturally, there exist a generalization of these Euclidean wavelet transforms to n -dimensional Euclidean space \mathbb{R}^n . We need to specify that we cannot use any of this constructions as wavelets on the sphere or the hyperboloid or any other curved manifold, even though they are manifolds in the Euclidean space. The most particular feature of such manifolds is their curvature. In other words, these are non-Euclidean manifolds and the wavelets which "live" on them are going to be *non-Euclidean wavelets*.

1.5 General set-up: wavelets on a manifold

There are two approaches to wavelet analysis. The first is geometric: a generalization of time-frequency analysis which results in *continuous wavelet transform (CWT)* [27]. The second approach is functional and it gives a rise to *wavelet orthonormal basis* [26, 28]. In both approaches, though, wavelets are a family of elementary signals built by suitably translating and dilating a single *mother wavelet* [3, 8, 25]. The main advantages of the wavelet transform over the classical Fourier transform is its microscopic nature: zooming in and out the signal.

In general, for constructing a continuous wavelet transform on a manifold, few basic requirements should be satisfied

- wavelets and signals must “live” on the manifold;
- the transform must involve dilations of some kind; and
- in case of curved manifold: the CWT should reduce locally to the usual CWT in the tangent plane.

For such a construction, we distinguish two main techniques: the one is based on group theory and the other is based on a convolution theorem.

1.5.1 Wavelet construction based on group theory

One basic method for building wavelets on any manifold is based on group theory. In this technique the wavelets coincide with, so called in the physical literature, the *coherent states (CS)* associated to a group representation of affine transformations. Let us expose here some details for this construction. Most of this discussion is borrowed and adopted from [4].

Let M be a manifold. For instance, M could be the n -dimensional Euclidean space \mathbb{R}^n , the 2-sphere S^2 , space-time $\mathbb{R} \times \mathbb{R}$ or $\mathbb{R}^2 \times \mathbb{R}$, the hyperboloid H^2 , etc. In order to construct coherent states on M , one needs two ingredients:

- the class of finite energy signals living on M , i.e. the space $L^2(M, d\mu) \equiv \mathcal{H}$ for a suitable measure μ ; and
- a (locally compact) group G of transformations acting (transitively) on M , i.e., $m \mapsto g[m]$, $\forall g, g' \in G$ with $g[g'[m]] = gg'[m]$, $e[m] = m$, where e is the neutral element, and for any pair $m, m' \in M$, there is at least one $g \in G$ such that $g[m] = m'$.

From this, one obtains a natural unitary representation of G in the space $L^2(M, d\mu)$:

$$[U(g)f](m) = f(g^{-1}m). \quad (1.17)$$

Then, the system of CS on M associated to G may be defined if U is a *square integrable* representation of G ; that is, U is irreducible and there exists a nonzero vector $\psi \in L^2(M, d\mu)$, called *admissible*, such that the matrix element $\langle U(g)\psi | \psi \rangle$ is square integrable as a function on G , with respect to the (left or right) invariant Haar measure on G . When this is the case, the corresponding CS, indexed by G , are obtained as the elements in the orbit of an admissible vector ψ under U :

$$\psi_g = U(g)\psi, \quad g \in G. \quad (1.18)$$

Quite often, however, the representation U is not square integrable in the strict sense just described. However, it may become square integrable when restricted to a homogeneous space $X = G/H$, for

some closed subgroup H . By this the following is meant. Let $\sigma : X \rightarrow G$ be a Borel section. Then the nonzero vector $\psi \in L^2(M, d\mu)$ is said to be *admissible* mod(H, σ), and the representation U square integrable mod(H, σ), if the following condition holds:

$$\int_X |\langle U(\sigma(x))\psi | \phi \rangle|^2 d\nu(x) < \infty, \forall \phi \in \mathcal{H}, \quad (1.19)$$

where ν is a (quasi)invariant measure on X .

Then CS indexed by X may be defined as

$$\psi_{\sigma(x)} = U(\sigma(x))\psi, \quad x \in X, \quad (1.20)$$

and they form a total (overcomplete) set S_σ in \mathcal{H} , with essentially the same properties as in the restricted case described before.

The condition (1.19) may also be written as

$$0 < \int_X |\langle \psi_{\sigma(x)} | \phi \rangle|^2 d\nu(x) = \langle \phi | A_\sigma \phi \rangle < \infty, \quad \forall \phi \in \mathcal{H}, \quad (1.21)$$

where A_σ is a positive, bounded, invertible operator. If the operator A_σ^{-1} is also bounded, the family $S_\sigma = \psi_{\sigma(x)}, x \in X$ is called a *frame*, and a *tight frame* if $A_\sigma = \lambda I$, for some $\lambda > 0$.

Here are some familiar examples of this construction:

- (1) The $ax + b$ group acting on \mathbb{R} yields the usual 1-D continuous wavelets [36].
- (2) The similitude group of \mathbb{R}^n , consisting of translations $b \in \mathbb{R}^n$, rotations $R \in SO(n)$, and dilations $a > 0$, yields the n -dimensional wavelets [61]. For an axisymmetric wavelet ψ , the isotropy group $H \equiv SO(n-1)$, is quotient out and so $X = \mathbb{R}^n \cdot \mathbb{R}_*^+ \cdot S^{n-1} \sim \mathbb{R}^{2n}$.

In any of these examples one has $A_\sigma = 1$. The admissible vector ψ is normalized by $c(\psi) = \langle \psi | A_\sigma \psi \rangle = 1$ and it generates a frame; that is, A_σ^{-1} is bounded. The linear map $W_\psi : \mathcal{H} \rightarrow L^2(X, d\nu)$ defined by

$$(W_\psi \phi)(x) = \langle \psi_{\sigma(x)} | \phi \rangle, \quad \phi \in \mathcal{H}, \quad (1.22)$$

is called the *CS map* or the *wavelet transform* associated to ψ . Clearly, the vectors $\psi_g = U(g)\psi \in \mathcal{H}$ are the *coherent states (CS)* of the representation $U(g)$. Its range, \mathcal{H}_ψ , is complete with respect to the scalar product $\langle \Phi | \Psi \rangle_\psi \equiv \langle \Phi | W_\psi A_\sigma^{-1} W_\psi^{-1} \Psi \rangle$ and W_ψ is unitary from \mathcal{H} onto \mathcal{H}_ψ . As a consequence, the map W_ψ may be inverted on its range by the adjoint operator, which yields the reconstruction formula

$$\psi = W_\psi^{-1} \Phi = \int_X \Phi(x) A_\sigma^{-1} \psi_{\sigma(x)} d\nu(x), \quad \Phi \in \mathcal{H}_\psi. \quad (1.23)$$

In other words, the signal ϕ is expanded in terms of CS $A_\sigma^{-1} \psi_{\sigma(x)}$, the (wavelet) coefficients being $\Phi(x) = (W_\psi \phi)(x)$.

The technique for building a family of wavelets on a manifold based on group theory is not the only one. Another possible construction of wavelets is based on convolution. This apparatus for constructing wavelets is more practical.

1.5.2 Wavelet construction based on convolution

This technique is more practical and for realizing it one needs:

- a function on a given manifold (let us call it ψ),

- a set of affine transformations, i.e. dilations, rotations and translations, and
- a convolution theorem valid for square-integrable functions on the manifold.

The construction consists of the following. First, the "mother wavelet" ψ , to which affine operations may be applied, is defined as a localized function on the manifold. Second, the wavelet transform of a signal is defined as the convolution of the signal with the rotated and dilated version of the mother wavelet. Thus the wavelet coefficients are obtained. Finally, an admissibility condition is imposed on the mother wavelet by explicitly requiring the exact reconstruction formula of the signal from its wavelet coefficients.

We next put into details the group theoretical construction of one- and two-dimensional Euclidean wavelets. Being an elegant construction, it as well leads naturally toward extensions of the wavelet transform. For instance wavelets on the sphere are first constructed based on the group theory, but this will be exposed in Chapter 2. Note that from signal processing perspective, this result can also be obtained by considering wavelet transform as a convolution with a particular family of filters.

1.6 Wavelets on the real line: 1-D wavelets

1.6.1 Group of affine transformation on the real line

We are interested in finite energy signals $f \in L^2(\mathbb{R}, dx)$. Let us consider the group of affine transformations on \mathbb{R} , defined by the following semi-direct product:

$$G_{Aff} = \mathbb{R} \rtimes \mathbb{R}_*. \quad (1.24)$$

Any element of this group is represented by a couple $(b; a) \circ (b'; a') = (b + ab'; aa')$. The neutral and inverse elements are respectively

$$e = (0; 1), \quad (b; a)^{-1} = \left(-\frac{b}{a}; a^{-1}\right). \quad (1.25)$$

The form (1.24) permits to supply \mathbb{R} with a transitive action

$$\begin{aligned} \sigma_{(b;a)} &: \mathbb{R} \rightarrow \mathbb{R} \\ x &\mapsto ax + b \end{aligned}$$

which makes it a G -space. This action can be separated in two operations

- Translation :

$$T^b : \mathbb{R} \rightarrow \mathbb{R} \quad (1.26)$$

$$x \mapsto x + b, b \in \mathbb{R}. \quad (1.27)$$

- Dilation :

$$D^a : \mathbb{R} \rightarrow \mathbb{R} \quad (1.28)$$

$$x \mapsto ax, a \in \mathbb{R}_*. \quad (1.29)$$

In order to build wavelets on the line using the transformations contained in G we need to specify a representation in $L^2(\mathbb{R}, dx)$ and to verify that it is square integrable. The following theorem summarizes these results.

1.6.2 1-D wavelet admissibility condition

Theorem 1. (Grossmann-Morlet [36]).

(i) Up to a unitary equivalence, G_{Aff} has one and only one unitary irreducible representation (UIR) acting in $L^2(\mathbb{R}, dx)$

$$(U(b, a)f)(x) = \frac{1}{\sqrt{a}}f\left(\frac{x-b}{a}\right) \equiv f_{b,a}, \quad a \neq 0, b \in \mathbb{R}, \quad (1.30)$$

or in the Fourier domain

$$(\hat{U}(b, a)\hat{f})(\omega) = \sqrt{a}e^{-i\omega b}\hat{f}(a\omega). \quad (1.31)$$

(ii) U is square-integrable and $\psi \in L^2(\mathbb{R}, dx)$ is said to be admissible if and only if

$$C_\psi = 2\pi \int_{-\infty}^{+\infty} d\omega \frac{|\hat{\psi}(\omega)|^2}{|\omega|} < \infty. \quad (1.32)$$

The square integrability is a basic step in the process of constructing a family of wavelets. We show the corresponding formal calculations for this case here:

$$\begin{aligned} \int_{G_{Aff}} |\langle \hat{U}(b, a)\hat{\psi} | \hat{\psi} \rangle|^2 \frac{da db}{a^2} &= \iiint e^{ib(\xi-\xi')} \overline{\hat{\psi}(a\omega)} \hat{\psi}(a\omega') \overline{\hat{\psi}(\omega)} \hat{\psi}(\omega') d\omega d\omega' \frac{da}{|a|} d\omega \\ &= 2\pi \iint |\hat{\psi}(a\omega)|^2 |\hat{\psi}(\omega)|^2 \frac{da}{|a|} d\omega \\ &= 2\pi \|\psi\|^2 \int_{-\infty}^{+\infty} |\hat{\psi}(\omega)|^2 \frac{d\omega}{|\omega|} < \infty, \end{aligned}$$

where Fubini's theorem was applied for interchanging the integrals.

Let us note that in equation (1.24) we have imposed $a \in \mathbb{R}, a \neq 0$. In most of the cases we choose only positive dilations. With this new definition, the representation (1.30) or (1.31) is not anymore irreducible on $L^2(\mathbb{R}, dx)$. It is decomposed into two parts

$$U = U_+ \oplus U_-,$$

which are irreducible on the Hardy-spaces $\mathbf{H}_+^2(\mathbb{R})$ and $\mathbf{H}_-^2(\mathbb{R})$ defined by

$$\mathbf{H}_\pm^2(\mathbb{R}) = \{f \in L^2(\mathbb{R}, dx) | \hat{f}(\omega) = 0 \quad \omega \lessgtr 0\}$$

and which are called spaces of progressive signals (or of analytical signals). With these restrictions, the admissibility condition equation (1.32) becomes

$$C_\psi^+ = 2\pi \int_0^{+\infty} d\omega \frac{|\hat{\psi}(\omega)|^2}{\omega} < \infty$$

over $\mathbf{H}_+^2(\mathbb{R})$ and similarly over $\mathbf{H}_-^2(\mathbb{R})$. The wavelet analysis on $L^2(\mathbb{R}, dx)$ is possible if it is imposed either a strict equality of wavelets contributions of \mathbf{H}_+^2 and \mathbf{H}_-^2

$$0 < C_\psi^+ = C_\psi^- < +\infty,$$

or a symmetry of the positive and negative frequencies of the wavelet

$$0 < C_\psi = \int_{-\infty}^{+\infty} d\omega \frac{|\hat{\psi}(\omega)|^2}{|\omega|} < +\infty.$$

The condition (1.32) imposes only small restrictions on the convergence of $\hat{\psi}$ at infinity, but asks for rapid annulation in $\omega = 0$. The following corollary gives precise meaning of this remark.

Corollary 2. (Necessary admissibility condition).

If $\psi \in L^1(\mathbb{R}, dx) \cap L^2(\mathbb{R}, dx)$ is admissible, then $\hat{\psi}(0) = 0$.

The last condition means that ψ has a zero mean.

$$\int_{-\infty}^{+\infty} \psi(x) dx = 0. \quad (1.33)$$

According to this, an admissible wavelet is a sufficiently oscillating function.

Following equation (1.22), we can explicitly define the 1-D continuous wavelet transform now.

Definition 2. A function $\psi \in L^2(\mathbb{R})$ with $\int \psi = 0$ is called wavelet. The wavelet transform of a function $f \in L^p(\mathbb{R}), 1 \leq p \leq \infty$, is defined as

$$\mathcal{W}_f(b, a) = \langle \psi_{b,a} | f \rangle = \int_{-\infty}^{+\infty} dx \frac{1}{\sqrt{a}} \overline{\psi\left(\frac{t-b}{a}\right)} f(x), b \in \mathbb{R}, a > 0. \quad (1.34)$$

The numbers $\mathcal{W}_f(b, a)$ will be often called the *wavelet coefficients* of f (with respect to the wavelet ψ).

Notice that a different normalization is often used, namely, replacing $\frac{1}{\sqrt{a}}$ by $\frac{1}{|a|}$ in (1.34), which has the effect of enhancing small scales in transforms, we obtain the so called L^1 -normalization. It ensures that L^1 norm is conserved under dilation. However, the L^2 -normalization given in (1.34) is the only one that comes from a unitary representation of G_{Aff} .

In practice, one often imposes on the analyzing wavelet ψ a number of additional properties, for instance, restrictions on the support of ψ and of $\hat{\psi}$. Or we might have requirements on ψ to have certain number $N \geq 1$ of *vanishing moments*: $\int_{-\infty}^{+\infty} x^n \psi(x) dx = 0, n = 0, 1, \dots, N$. This property improves its efficiency at detecting singularities in the signal. Indeed, the transform (1.34) does not "see" the smoothest part of the signal, that is polynomial of degree up to N (and, in general, less interesting). Only the sharper part remains, including all singularities. For instance, if the first moment ($n = 1$) vanishes, the transform will erase any linear trends in the signal.

For completing the picture of 1-D Euclidean wavelets, we next provide two basic examples.

1.6.3 Examples of 1-D wavelets

Example 1. (The 1-D Mexican hat (or Marr) wavelet)

$$\psi_{mex}(x) = (1 - x^2)e^{-\frac{x^2}{2}} \quad (1.35)$$

$$\hat{\psi}_{mex}(\omega) = \omega^2 e^{-\frac{\omega^2}{2}}. \quad (1.36)$$

This simply is the second derivative of a Gaussian and is shown on Figure 1.5(a). It is a real wavelet with two vanishing moments ($n = 0, n = 1$). If a higher derivative of the Gaussian is taken, similar wavelets but with more vanishing moments are obtained.

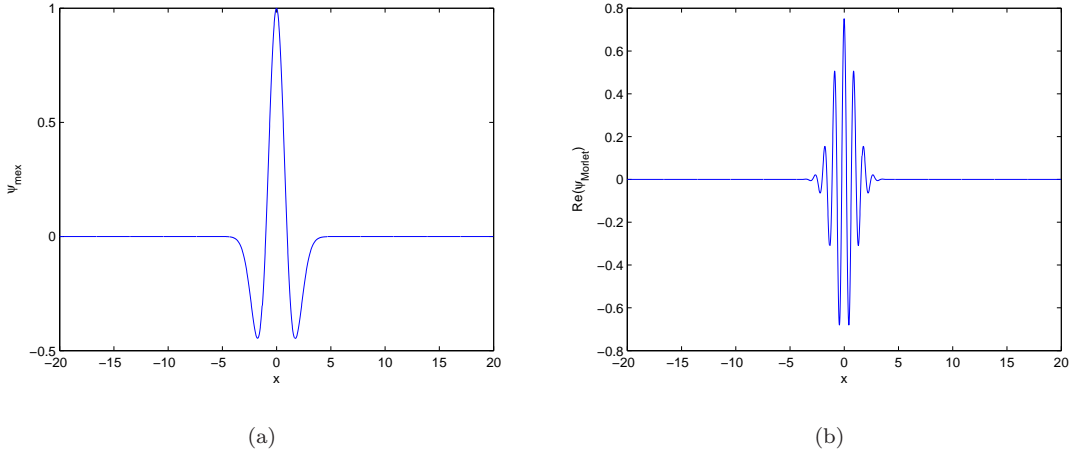


Figure 1.5: Examples of 1-D Euclidean wavelets: (a) Mexican hat wavelet, (b) real part of the Morlet wavelet, $\omega_0 = 7$

Example 2. (*The 1-D Morlet wavelet*)

$$\psi(x) = \pi^{-1/4} (e^{i\omega_0 x} - e^{-\omega_0^2/2}) e^{-x^2/2} \quad (1.37)$$

$$\widehat{\psi}(\omega) = \pi^{-1/4} [e^{-(\omega-\omega_0)^2/2} - e^{-\omega^2/2} e^{-\omega_0^2/2}]. \quad (1.38)$$

Actually, this is just a modulated Gaussian. The first term alone does not satisfy the admissibility condition and so a correction term is needed. For ω_0 large enough, however, this term is numerically negligible. This wavelet is complex, and so is the corresponding transform, which enables one to deal separately with the phase and the modulus of the transform. In applications, such as feature detection, the phase turns out to be a crucial ingredient, and this property of the Morlet wavelet makes it efficient and highly used there [51]. This wavelet is shown on Figure 1.5(b).

Finally, the continuous wavelet transform is covariant with respect to the group $ax + b$:

$$f(x - b_0) \mapsto \mathcal{W}_f(b - b_0, a), b_0 \in \mathbb{R}, \quad (1.39)$$

$$a_0^{-1/2} f(a_0^{-1}x) \mapsto \mathcal{W}_f(a_0^{-1}b, a_0^{-1}a), a_0 > 0. \quad (1.40)$$

The properties (1.39) and (1.40), especially with the translation, are one of the reasons why the CWT is extremely useful for detecting particular features in signals. Indeed, the translation covariance is lost in the discrete time WT, which is one of the drawbacks of the discrete wavelet scheme based on multiresolution which we will meet later in this chapter.

1.7 Wavelets on the Euclidean plane: 2-D wavelets

In 1-D, the CWT amounts to projecting the signal onto the wavelet $\psi_{b,a}$, obtained by translation and dilation of the mother wavelet ψ . Thus, the transform is fully determined by these elementary operations of the line. Consequently, in order to derive the CWT for 2-D Euclidean case, it is normal to consider first the elementary operations which one wants to apply to the 2-D signal. The wavelet construction has been generalized to two and higher dimensions [60, 61]. Actually, as it will be shown later, considering the affine transformations first, allows one to extend the CWT to much more general situations - in higher dimensions and curved spaces.

1.7.1 Similitude group on the Euclidean plane

For extending wavelet analysis to 2-D, Murenzi defined a group which contains translations, dilations and rotations [61]. To illustrate this we take as a model a two-dimensional image. This is a finite energy signal $f \in L^2(\mathbb{R}^2, d^2\vec{x})$. The operations applied to f are translations in the Euclidean plane ($\vec{b} \in \mathbb{R}^2$), global dilations (zooming in and out by $a > 0$) and rotations around the origin ($\theta \in [0, 2\pi)$). Together these transformation constitute a four-parameter group, called the *similitude group* on the Euclidean plane and denoted by $SIM(2)$. The last two operations (dilations and rotation) are commutative and the only possibility for expressing this group remains

$$G = \mathbb{R}^2 \times (\mathbb{R}_*^+ \times SO(2)) \sim SIM(2). \quad (1.41)$$

The action on the plane is

$$\vec{x} = (\vec{b}, a, \theta)\vec{y} = ar_\theta\vec{y} + \vec{b}, \quad (1.42)$$

where r_θ is the 2×2 rotation matrix.

A generic element of this group is written as $g = (\vec{b}; (a, \theta))$. There is a realization of $SIM(2)$ by means of 3 non-singular matrices

$$g = \begin{pmatrix} ar_\theta & \vec{b} \\ 0 & 1 \end{pmatrix}, \quad (1.43)$$

where

$$r_\theta = \begin{pmatrix} \cos \theta & -\sin \theta \\ \sin \theta & \cos \theta \end{pmatrix}, \quad (1.44)$$

is the classical realization of the rotation group $SO(2)$.

The three operations which compose $SIM(2)$ are realized in terms of unitary operators on $L^2(\mathbb{R}^2, d^2x)$:

- translations: $(T^{\vec{b}}f)(\vec{x}) = f(\vec{x} - \vec{b})$,
- dilations : $(D^a f)(\vec{x}) = \frac{1}{a}f(\frac{\vec{x}}{a})$,
- rotations : $(R^\theta f)(\vec{x}) = f(r_\theta\vec{x})$.

The natural action of the similitude group on the Euclidean plane is

$$\sigma[g] : \mathbb{R}^2 \rightarrow \mathbb{R}^2, \quad (1.45)$$

$$\sigma[(\vec{b}; (a, \theta))f]\vec{x} = ar_\theta\vec{x} + \vec{b}, \quad (1.46)$$

whose product makes a unitary representation of the similitude group in $L^2(\mathbb{R}^2, d^2\vec{x})$ as

$$[\mathcal{U}(\vec{b}; (a, \theta))f](\vec{x}) = (T^{\vec{b}}D^aR^\theta f)(\vec{x}) \quad (1.47)$$

$$= \frac{1}{a}f(a^{-1}r_{-\theta}(\vec{x} - \vec{b})). \quad (1.48)$$

This representation is irreducible on $L^2(\mathbb{R}^2, d^2\vec{x})$. It is as well square-integrable and offers a more general admissibility condition as shown in the following theorem.

1.7.2 2-D wavelet admissibility condition

Theorem 3. Let $\psi \in L^2(\mathbb{R}^2, d^2\vec{x})$ such that

$$0 < C_\psi = \int \int_{\mathbb{R}^2} d^2\vec{k} \frac{|\hat{\psi}(\vec{k})|^2}{|\vec{k}|^2} < +\infty. \quad (1.49)$$

Then all the elements $f \in L^2(\mathbb{R}^2, d^2\vec{x})$ admit the decomposition

$$f = \frac{1}{C_\psi} \int_{SIM(2)} d^2\vec{b} d\theta \frac{da}{a^3} \langle \mathcal{U}(\vec{b}; (a, \theta)) \psi | f \rangle \mathcal{U}(\vec{b}; (a, \theta)) \psi \quad (1.50)$$

in $f \in L^2(\mathbb{R}^2, d^2\vec{x})$.

If we impose that the wavelet belongs to $L^1(\mathbb{R}^2)$, the Fourier transform is continuous and we obtain a simpler condition

Corollary 4. An element $\psi \in L^1(\mathbb{R}^2, d^2\vec{x}) \cap L^2(\mathbb{R}^2, d^2\vec{x})$ is admissible only if it satisfies

$$\hat{\psi}(0) = 0, \quad (1.51)$$

which means

$$\int_{\mathbb{R}^2} d^2\vec{x} \psi(\vec{x}) = 0. \quad (1.52)$$

This corollary shows that in order one wavelet to be admissible, its mean must be zero. Consequently, such an wavelet can be used as a band-pass filter. The associated wavelet transform based on so described family of wavelets is the corresponding:

Definition 3. Let $f \in L^2(\mathbb{R}^2, d^2\vec{x})$ and ψ is an admissible wavelet. The 2-D wavelet transform of f with respect to ψ is said to be the function $\mathcal{W}_f \in L^2(SIM(2), d\mu_L)$.

$$\mathcal{W}_f(\vec{b}; (a, \theta)) = \langle \mathcal{U}(\vec{b}; (a, \theta)) \psi | f \rangle \quad (1.53)$$

$$= a^{-1} \int_{\mathbb{R}^2} d^2\vec{x} \psi(a^{-1}r_{-\theta}(\vec{x} - \vec{b})) f(\vec{x}) \quad (1.54)$$

$$= a \int_{\mathbb{R}^2} d^2\vec{k} e^{i\vec{b}\vec{k}} \overline{\hat{\psi}(a r_{-\theta}(\vec{k}))} \hat{s}(\vec{k}). \quad (1.55)$$

From the above definition it is clear that the CWT on the Euclidean plane \mathcal{W}_f is the scalar product of f with the transformed wavelet $\psi_{\vec{b}, a, \theta}$, considered as a function of (\vec{b}, a, θ) .

Let us rewrite the 2-D wavelet transform from Definition 3 as

$$\mathcal{W}_f(\vec{b}; (a, \theta)) = \langle \psi_{(\vec{b}; (a, \theta))} | f \rangle \quad (1.56)$$

$$= \frac{1}{a} \int_{\mathbb{R}^2} d^2\vec{x} \psi\left(\frac{r_{-\theta}(\vec{x} - \vec{b})}{a}\right) f(\vec{x}). \quad (1.57)$$

If we denote

$$\tilde{\psi}_{(a, \theta)}(\vec{x}) = \frac{1}{a} \psi\left(-\frac{r_{-\theta}\vec{x}}{a}\right), \quad (1.58)$$

we can see that equation (1.57) can be expressed as

$$\mathcal{W}_f(\vec{b}; (a, \theta)) = (f * \overline{\tilde{\psi}_{(a, \theta)}})(\vec{b}), \quad (1.59)$$

which is a convolution of the signal with the wavelet ψ , to which it is previously applied a rotation of angle θ and a dilation by a factor a .

1.7.3 Examples of 2-D wavelets

Example 3. (*The 2-D Mexican hat wavelet*)

$$\psi(\vec{x}) = -\Delta \exp\left(-\frac{1}{2}|\vec{x}|^2\right) = (2 - |\vec{x}|^2) \exp\left(-\frac{1}{2}|\vec{x}|^2\right), \quad \Delta = \partial_x^2 + \partial_y^2. \quad (1.60)$$

This is real, rotation invariant wavelet, with vanishing moments of order up to 1, also known as LOG wavelet* This particular wavelet is, for instance, efficient for a fine point-wise analysis, but not for detecting directions. In some applications it might be useful to introduce additional parameter, namely, the width σ of the Gaussian. Thus the wavelet (1.60) becomes:

$$\psi(\vec{x}) = -\Delta \exp\left(-\frac{\sigma^2|\vec{x}|^2}{2}\right), \quad (1.61)$$

$$\hat{\psi}(\vec{\omega}) = \frac{|\vec{\omega}|^2}{\sigma^2} \exp\left(-\frac{|\vec{\omega}|^2}{2\sigma^2}\right). \quad (1.62)$$

This wavelet is shown on Figure 1.6(a).

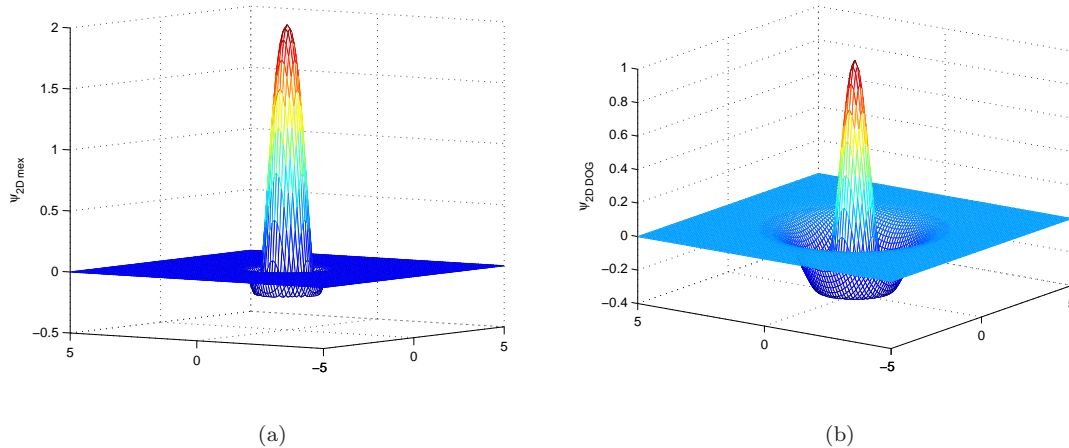


Figure 1.6: Examples of 2-D Euclidean wavelets: (a) 2-D Mexican hat wavelet, $\sigma = 1.7$, (b) 2-D DOG wavelet, $\alpha = 0.5$.

Example 4. (*"Difference-of-Gaussian" (DOG) wavelet*):

$$\psi_{DOG}(\vec{x}) = \frac{1}{2\alpha^2} \exp\left(-\frac{1}{2\alpha^2}|\vec{x}|^2\right) - \exp\left(-\frac{1}{2}|\vec{x}|^2\right), \quad (0 < \alpha < 1) \quad (1.63)$$

This is another interesting class of wavelets obtained as the difference of two positive functions. In order to get an isotropic wavelet in this way, the only possibility is to take the difference between a single isotropic function ψ and a contracted version of the latter. A typical example of this class of wavelets, shown on Figure 1.6(b).

There are many other particular examples. In all cases, the main use of the 2-D wavelets is for the analysis of images. In particular, the 2-D CWT can be used for the detection or determination of specific features, such as hierarchical structure, edges, filaments, contours, etc. Of course, the type of wavelet chosen depends on the precise aim.

*It was initially introduced by Marr and Hildreth, in their work on vision, because it is obtained by applying an isotropic differential operator of second order to the Gaussian.

We must note that the reconstruction formula in the continuous wavelet transform cannot be used in practice. This problem is corrected in the discrete version of the wavelet transform which we now describe.

1.8 Discrete Wavelet Frames

In this section we reveal the meaning of discretization of the continuous wavelet transform. We start the discussion with the classical frames in Section 1.8.1. Then we continue with continuous and half-continuous frames in Section 1.8.2, and controlled and weighted frames in Section 1.8.3. We conclude with 2-D Euclidean frames in Section 1.8.4.

1.8.1 Classical frames

Let \mathfrak{H} be a Hilbert space with scalar product $\langle \cdot | \cdot \rangle$ and the associated norm $\|f\| = \sqrt{\langle f | f \rangle}$, $f \in \mathfrak{H}$. We start with a precise definition adopting the terminology introduced by Duffin and Schaefer [30]:

Definition 4. *Let Γ be a countable set. A family of vectors $\Psi = \{\psi_n \in \mathfrak{H} : n \in \Gamma\}$ is a discrete frame in \mathfrak{H} if there exist two constants $0 < A \leq B < \infty$ such that*

$$A\|f\|^2 \leq \sum_{n \in \Gamma} |\langle \psi_n | f \rangle|^2 \leq B\|f\|^2, \quad \forall f \in \mathfrak{H}. \quad (1.64)$$

The frame is called *tight* if $A = B$. When $A = B = 1$ and $\|\psi_n\| = 1, \forall n \in \Gamma$, the frame is just an orthonormal basis. Given a frame Ψ , the associated *frame operator* L is defined as

$$Lf = \sum_{n \in \Gamma} \langle \psi_n | f \rangle \psi_n. \quad (1.65)$$

This is, of course, a bounded operator. Indeed [72]:

Proposition 5. *If Ψ is a frame of \mathfrak{H} , the associated frame operator L is bounded and verifies*

$$A\mathbf{1} \leq L \leq B\mathbf{1}, \quad (1.66)$$

where $\mathbf{1}$ denotes the unit operator and $P \leq Q$ means $\langle g | Pg \rangle \leq \langle g | Qg \rangle, \forall g \in \mathfrak{H}$, for two given operators P and Q .

It follows that the frame operator L is not only bounded, it also has a bounded inverse, that is, it belongs to the set $GL(\mathfrak{H})$ [2]. We emphasize that $GL(\mathfrak{H})$ is the natural class of operators in the context of frame theory. Indeed, (1.64) means that the norm $\|\cdot\|$ and the set of coefficients $\{\langle \psi_n | \cdot \rangle\}$ define the same Hilbertian topology on \mathfrak{H} . And the elements of $GL(\mathfrak{H})$ are precisely the natural isomorphisms for such a Hilbertian structure, exactly as unitary operators are the isomorphisms for the Hilbert space structure defined by a given inner product $\langle \cdot | \cdot \rangle$ (note the difference between a *Hilbert space* and a *Hilbertian space*: the former is attached to a given inner product, the latter to an equivalence class of inner products).

It is possible to reconstruct a function from its frame coefficients. Let us introduce first a related family of vectors $\tilde{\Psi} = \{\tilde{\psi}_n : n \in \Gamma\}$ defined by

$$\tilde{\psi}_n = L^{-1}\psi_n. \quad (1.67)$$

Then, we have the following result:

Proposition 6. [25] *The family $\tilde{\Psi}$ is a frame with bounds $0 < B^{-1} \leq A^{-1} < \infty$, called the dual frame of Ψ . Any $f \in \mathfrak{H}$ can be reconstructed from its frame coefficients through*

$$f = \sum_{n \in \Gamma} \langle \psi_n | f \rangle \tilde{\psi}_n = \sum_{n \in \Gamma} \langle \tilde{\psi}_n | f \rangle \psi_n. \quad (1.68)$$

The proof of this proposition can be found in [25]. Note that if the frame is tight then $\tilde{\psi}_n = \frac{1}{A} \psi_n$, and the same vectors are used for the decomposition and for the reconstruction. In fact, $\langle Lf | f \rangle = A \|f\|^2$ for every $f \in \mathfrak{H}$, so $L = A \mathbf{1}$ and $L^{-1} = A^{-1} \mathbf{1}$. This is the most attractive property of a tight frame.

Finally, when $A \simeq B$ we can have a good approximation of the element f by setting

$$f \simeq \frac{2}{A+B} Lf = \frac{2}{A+B} \sum_{n \in \Gamma} \langle \psi_n | f \rangle \psi_n, \quad (1.69)$$

since in this case $\frac{2}{A+B} L \simeq \mathcal{I}$.

1.8.2 Continuous and half-continuous frames

Several variations on the original frame concept have been studied. For instance, it is possible to extend the original definition to the case of continuous decompositions [72], as follows. Let \mathcal{C} be a measurable space with measure $d\mu(\nu)$. Given a family $\Psi = \{\psi_\nu \in \mathfrak{H}, \nu \in \mathcal{C}\}$, we define the frame operator

$$L : f \in \mathfrak{H} \mapsto Lf = \int_{\mathcal{C}} d\mu(\nu) \langle \psi_\nu | f \rangle \psi_\nu. \quad (1.70)$$

The set Ψ is called a *continuous* frame if L is a bounded operator. This guarantees that $L \in GL(\mathfrak{H})$, and thus also the reconstruction of f from its wavelet coefficients $\{\langle \psi_\nu | f \rangle\}$.

It is also possible to have a mixed set of indices where some of them are continuous while the rest are discrete. If we note by $\nu \in \mathcal{C}$ the continuous set and by $n \in \mathcal{D}$ the discrete one, then we say that the family $\Psi = \{\psi_{\nu,n} \in \mathfrak{H} : \nu \in \mathcal{C}, n \in \mathcal{D}\}$ is a frame if there exist two constants $0 < A \leq B < \infty$ such that, $\forall f \in \mathfrak{H}$,

$$A \|f\|^2 \leq \sum_{n \in \mathcal{D}} \int_{\mathcal{C}} d\mu(\nu) |\langle \psi_{\nu,n} | f \rangle|^2 \leq B \|f\|^2. \quad (1.71)$$

In that case, the family Ψ is called a *half-continuous* frame.

1.8.3 Controlled and weighted frames

We introduce in this section a slight variation on the definition of frames, called *controlled frames*. It helps tuning the frame bounds in order to obtain a better approximation of f by Lf (as in (1.69)) [40, 54, 27].

Controlled frames

Definition 5. *Let $O \in GL(\mathfrak{H})$. A frame controlled by the operator O is a family of vectors $\Psi = \{\psi_n \in \mathfrak{H} : n \in \Gamma\}$ such that there exist two constants $A, B \in \mathbb{R}_+^*$ verifying*

$$A \|f\|^2 \leq \sum_{n \in \Gamma} \langle \psi_n | f \rangle \langle f | O \psi_n \rangle \leq B \|f\|^2, \quad (1.72)$$

for all $f \in \mathfrak{H}$.

In that case, the frame operator is given by

$$L_o f = OLf = \sum_{n \in \Gamma} \langle \psi_n | f \rangle O \psi_n. \quad (1.73)$$

Proposition 7. *The family Ψ is a frame of \mathfrak{H} controlled by $O \in GL(\mathfrak{H})$ iff Ψ is a (classical) frame of \mathfrak{H} .*

This result is obtained by projecting $L_o f$ on f and noting that $L_o = OL$. Therefore, if Ψ is controlled by O , there are two constants $A, B \in \mathbb{R}_+^*$ such that

$$A\mathcal{I} \leq L_o \leq B\mathcal{I} \quad (1.74)$$

$$\Leftrightarrow$$

$$AO^{-1} \leq L \leq BO^{-1}, \quad (1.75)$$

with L the classical frame operator defined in (1.65). Since there are two constants $A_o, B_o \in \mathbb{R}_+^*$ such that $A_o \leq O \leq B_o$, we see that a frame controlled by O with frame bounds $A, B \in \mathbb{R}_+^*$ is a genuine frame with frame bounds AB_o^{-1} and BA_o^{-1} . Conversely, if $A' \leq L \leq B'$ for $A', B' \in \mathbb{R}_+^*$, then $A'O \leq L_o \leq B'O$ and $A'A_o \leq L_o \leq B'B_o$, which proves (1.72).

As a consequence, given a controlled frame Ψ , every function $f \in \mathfrak{H}$ may be reconstructed as in (1.68) without using the operator O . But when $A \simeq B$ in (1.74), $\frac{2}{A+B}L_o$ is close to the identity and we obtain a new approximation for f

$$f \simeq \frac{2}{A+B} L_o f = \frac{2}{A+B} \sum_{n \in \Gamma} \langle \psi_n | f \rangle O \psi_n. \quad (1.76)$$

Thus, if $|B_o/A_o| < |B/A|$, Eq. (1.76) gives a better approximation to f than the one obtained using the frame operator L in (1.69). If, in addition, it turns out that $O \psi_n$ is easily computed, then we have a simple and good reconstruction of f , as desired. Thus, while a controlled frame is equivalent to a classical frame in the mathematical sense, as stated in Proposition 7, they can have very different numerical properties.

Weighted frames

A particular case of controlled frame occurs when the operator O is diagonal with respect to the elements ψ_n of the frame Ψ , i.e., if $O \psi_n = w_n \psi_n$ for $w_n \in \mathbb{R}$. Notice that, since O is positive, we have necessarily $w_n > 0$. This diagonalization of the operator O leads to the concept of *weighted frames*.

Definition 6. *Let $\Psi = \{\psi_n : n \in \Gamma \subset \mathbb{Z}\}$ be a family of elements of \mathfrak{H} and $\{w_n \in \mathbb{R}_+^* : n \in \Gamma\}$ a sequence of strictly positive weights. We say that this family is a w -frame of \mathfrak{H} , if there exist two constants $0 < A \leq B < \infty$ such that, for every $f \in \mathfrak{H}$,*

$$A\|f\|^2 \leq \sum_{n \in \Gamma} w_n |\langle \psi_n | f \rangle|^2 \leq B\|f\|^2. \quad (1.77)$$

In fact, if $w_n > 0$ for all $n \in \Gamma$, a w -frame $\{\psi_n\}$ corresponds to the classical frame $\{\sqrt{w_n} \psi_n\}$. But it will be useful to make these weights more explicit later on. It is interesting to note that the notion of weighted frames was already present in the beginnings of frame theory, as developed by Duffin and Schaeffer [30], in the context of the reconstruction of band-limited signals. They have

shown that if $\text{supp}(\widehat{f}) \subset [-\frac{\pi}{T}, \frac{\pi}{T}]$, then it is possible to reconstruct the continuous function f from an irregular sampling $\{f(t_n)\}_{n \in \mathbb{Z}}$, by using the frame

$$\left\{ \sqrt{\frac{t_{n+1} - t_{n-1}}{2}} h_T(t - t_n) : n \in \mathbb{Z} \right\}, \quad (1.78)$$

where $h_T(t) = \text{sinc}(\frac{\pi t}{T})$. We see that in this case some strictly positive weights $w_n = \sqrt{\frac{t_{n+1} - t_{n-1}}{2}}$ appear, which reflect the particular sampling geometry. We will see in the next chapter, section 2.4.1, similar considerations are needed for an equi-angular spherical sampling.

Even if a weighted frame may also be expressed as a classical frame, we point out that it is possible to define a w -frame operator $L_w : \mathfrak{H} \rightarrow \mathfrak{H}$ in this context by

$$L_w f = \sum_{n \in \Gamma} w_n \langle \psi_n | f \rangle \psi_n, \quad (1.79)$$

for every $f \in \mathfrak{H}$. This is an invertible operator and the reconstruction formula for f reads

$$f = L_w^{-1} L_w f = L_w^{-1} \sum_{n \in \Gamma} w_n \langle \psi_n | f \rangle \psi_n = \sum_{n \in \Gamma} w_n \langle \psi_n | f \rangle \widetilde{\psi}_n, \quad (1.80)$$

where $\widetilde{\psi}_n = L_w^{-1} \psi_n$.

Half-continuous controlled frames

To conclude this section, let us remark that we can define half continuous frames controlled by an operator from $GL(\mathfrak{H})$. In that case, taking the same notations as in Section 1.8.2, a family $\Psi = \{\psi_{\nu, n} \in \mathfrak{H} : \nu \in \mathcal{C}, n \in \mathcal{D}\}$ constitutes such a frame if, for two constants $A, B \in \mathbb{R}_+^*$,

$$A \|f\|^2 \leq \sum_{n \in \mathcal{D}} \int_{\nu \in \mathcal{C}} d\mu(\nu) \langle \psi_{\nu, n} | f \rangle \langle f | O \psi_{\nu, n} \rangle \leq B \|f\|^2, \quad (1.81)$$

for all $f \in \mathfrak{H}$ and a given $O \in GL(\mathfrak{H})$. As before, it is easy to see that a half-continuous controlled frame is equivalent to a classical half-continuous frame on \mathfrak{H} . A particular case arises when O can be factorized in

$$O \psi_{\nu, n} = w_n \widetilde{O} \psi_{\nu, n}, \quad (1.82)$$

where $\widetilde{O} \in GL(\mathfrak{H})$ and w_n are positive weights. Then, (1.81) becomes

$$A \|f\|^2 \leq \sum_{n \in \mathcal{D}} w_n \int_{\nu \in \mathcal{C}} d\mu(\nu) \langle \psi_{\nu, n} | f \rangle \langle f | \widetilde{O} \psi_{\nu, n} \rangle \leq B \|f\|^2. \quad (1.83)$$

1.8.4 2-D wavelet frames

Proceeding as in 1-D, one first obtains the following natural discretization scheme.

- for the dilations: a logarithmic scale $a_j = a_0 \lambda^{-j}$, $j \in \mathbb{Z}$, for some $\lambda > 1$. We put $a_0 = 1$.
- for the rotations: uniformly subdivision of the interval $[0, 2\pi)$ into L_0 pieces. For some natural number $L_0 \in \mathbb{N}$, that is, $\theta_l = l\theta$, $\theta = \frac{2\pi}{L_0}$, $l \in \mathbb{Z}_{L_0} = \{0, \dots, L_0 - 1\}$.
- for the translations: the two previous discretization are taken into account, putting

$$\vec{b}_m \equiv \vec{b}_{j l m_0 m_1} = \lambda^{-j} r_{l\theta_0}(\vec{u}_{m_0 m_1}), \quad (1.84)$$

with

$$\vec{u}_{m_0 m_1} \equiv (m_0 \beta_0, m_1 \beta_1), \quad m_0, m_1 \in \mathbb{Z}_0, \quad \beta_0, \beta_1 \geq 0. \quad (1.85)$$

Thus the discretization grid reads:

$$\Lambda = \Lambda(\lambda, L_0, \beta_0, \beta_1) = \left\{ (\lambda^{-j}, l \frac{2\pi}{L_0}, \vec{b}_{jlm_0m_1}), (j, l, m_0, m_1) \in \mathbb{Z} \times \mathbb{Z}_{L_0} \times \mathbb{Z}^2 \right\}. \quad (1.86)$$

The resulting discretized wavelet transform, which is a map from $L^2(\mathbb{R}^2, d^2\vec{x})$ to $l^2(\mathbb{Z} \times \mathbb{Z}_{L_0} \times \mathbb{Z}^2)$, reads now:

$$S_{jlm_0m_1} \equiv S(\vec{b}_m, \lambda^{-j}, l\theta_0) = \langle \psi_{jlm_0m_1} | s \rangle \quad (1.87)$$

$$= \lambda^j \int_{\mathbb{R}^2} d^2\vec{x} \overline{\psi(\lambda^j r_{-l\theta_0}(\vec{x}) - \vec{u}_{m_0, m_1})} f(\vec{x}) \quad (1.88)$$

$$= \lambda^{-j} \int_{\mathbb{R}^2} d^2\vec{k} e^{i\vec{b}_{m_0, m_1} \cdot \vec{k}} \overline{\hat{\psi}(\lambda^{-j} r_{-l\theta_0}(\vec{k}))} \hat{f}(\vec{k}), \quad (1.89)$$

with wavelet coefficients

$$\left\{ S_{jlm_0m_1}, (j, l, m_0, m_1) \in \mathbb{Z} \times \mathbb{Z}_{L_0} \times \mathbb{Z}^2 \right\}. \quad (1.90)$$

It remains to be found conditions on the grid $\Lambda(\lambda, L_0, \beta_0, \beta_1)$, that is, on the parameters $\lambda, L_0, \beta_0, \beta_1$, such that the family of wavelets $\{\psi_{jlm_0m_1}, (j, l, m_0, m_1) \in \mathbb{Z} \times \mathbb{Z}_{L_0} \times \mathbb{Z}^2\}$ is a frame. This was worked out in [61] and here we provide just the following theorem:

Theorem 8. *Assume the wavelet ψ satisfies the following conditions:*

$$(i) \quad s(\lambda, L_0, \psi) = \operatorname{ess\,inf}_{\vec{k} \in \mathbb{R}^2} \sum_{j=-\infty}^{\infty} \sum_{l=0}^{L_0} |\hat{\psi}(\lambda^{-j} r_{-l\theta_0}(\vec{k}))|^2 \quad (1.91)$$

$$= \operatorname{ess\,inf}_{(|\vec{k}|, \theta) \in [0, \lambda) \times [0, 2\pi)} \sum_{j=-\infty}^{\infty} \sum_{l=0}^{L_0} |\hat{\psi}_p(\lambda^{-j} |\vec{k}|, \varphi - l\theta_0)|^2 > 0, \quad (1.92)$$

where $\vec{k} = |\vec{k}|(\cos \varphi, \sin \varphi)$ and $\hat{\psi}_p$ is the Fourier transform of ψ in polar coordinates.

$$(ii) \quad S(\lambda, L_0, \psi) = \sup_{\vec{k} \in \mathbb{R}^2} \sum_{j=-\infty}^{\infty} \sum_{l=0}^{L_0} |\hat{\psi}(\lambda^{-j} r_{-l\theta_0}(\vec{k}))|^2 \quad (1.93)$$

$$= \sup_{(|\vec{k}|, \theta) \in [0, \lambda) \times [0, 2\pi)} \sum_{j=-\infty}^{\infty} \sum_{l=0}^{L_0} |\hat{\psi}_p(\lambda^{-j} |\vec{k}|, \varphi - l\theta_0)|^2 < \infty. \quad (1.94)$$

$$(iii) \quad \sup_{\vec{u} \in \mathbb{R}^2} (1 + |\vec{u}|)^{1+\epsilon} \alpha(\vec{u}) < \infty, \quad (1.95)$$

where $\epsilon > 0$ and

$$\alpha(\vec{u}) = \sup_{\vec{k} \in \mathbb{R}^2} \sum_{j=-\infty}^{\infty} \sum_{l=0}^{L_0} |\hat{\psi}(\lambda^{-j} r_{-l\theta_0}(\vec{k})) + \vec{u}|^2 |\hat{\psi}(\lambda^{-j} r_{-l\theta_0}(\vec{k}))|^2. \quad (1.96)$$

Then there exist constants $\beta_0^c, \beta_1^c > 0$ such that:

(1) $\forall \beta_0 \in (0, \beta_0^c), \beta_1 \in (0, \beta_1^c)$, the family $\{\psi_{ljm_0m_1}\}$ associated to $(\lambda, L_0, \beta_0, \beta_1)$ is a frame of $L^2(\mathbb{R}^2, d^2\vec{x})$;

(2) $\forall \delta > 0$, there exist $\beta_0 \in (\beta_0^c, \beta_0^c + \delta), \beta_1 \in (\beta_1^c, \beta_1^c + \delta)$, such that the family $\{\psi_{ljm_0m_1}\}$ associated to $(\lambda, L_0, \beta_0, \beta_1)$ is not a frame of $L^2(\mathbb{R}^2, d^2\vec{x})$.

The proof of this theorem can be found in [8].

Clearly, the discretization of the CWT leads to the theory of frames. For many practical purposes of signal processing, a tight frame is almost as good as an orthonormal basis. If one remains with the standard wavelets, one could not do better since wavelets does not generate any orthonormal basis. There are cases in which such basis are required, for instance in data compression. For this operation, consisting in removing all wavelet expansion coefficients below a fixed threshold, would be ideal an orthonormal basis. The reason for this is that we need wavelet coefficients to be as de-correlated as possible in order to not introduce any bias in this operation.

Fortunately, it turns out that one can design wavelets that do generate such bases. This leads to discrete-time WT and the key point was the discovery that almost all examples of orthonormal bases of wavelets can be associated to multiresolution analysis [57, 55].

We restrict our presentation to this but further information on constructing orthonormal wavelet bases can be found in [54].

1.9 Summary

- Signals are constrained on flat (Euclidean) or on curved (non-Euclidean) manifolds.
- The signal analysis turns to be more efficient in time-frequency representation. The basic idea of the wavelet transform is to decompose a signal locally into contributions living at different scale.
- One basic method for construction wavelets on a manifold is based on the group theory. In this case the wavelets coincide with the coherent states associated to a group representation. But the WT defined as the scalar product of the signal with the transformed wavelet can also be seen as the convolution of the signal with the scaled flipped and conjugated wavelet. In order to call a dilated and translated(rotated) function a wavelet, it must satisfy a particular admissibility condition.
- The CWT on the line is derived from the natural unitary representation of the $ax + b$ group in the space of finite energy signals $L^2(\mathbb{R}, dx)$, while the 2-D wavelets are derived from the similitude group $SIM(2)$ on the Euclidean plane.
- For numerical implementation of great use is the discrete wavelet transform

Wavelets and Frames on the Sphere

2

Now it is time to enter the proper subject of this dissertation, namely, the wavelet analysis on non-Euclidean manifolds. We start first by the sphere, a non-Euclidean manifold of positive curvature. We recall the group theoretical construction of wavelets on the sphere.

Then we turn toward discretization of the continuous spherical wavelets and start with building half-continuous spherical frames. The first approach toward them stems from a straightforward generalization of the classical Euclidean construction but we show that it cannot yield a tight frame (a property rooted in the fact that the continuous version of the wavelet transform is not an isometry). In the second approach we start from the Plancherel relation and determine under which conditions we can obtain controlled frames. We then show that a controlled frame may be constructed in order to get an easy reconstruction of functions from their decomposition coefficients. We completely discretize the CWT on the sphere and give an example of frame decomposition of spherical data. As a final step in this chapter, we construct spherical Laplacian pyramid.

2.1 Spherical Geometry

2.1.1 Spherical coordinates

The 2-sphere ($S^2 \in \mathbb{R}^3$) of radius r is a compact manifold of constant positive curvature ($\kappa = 1$) and equation $x_1^2 + x_2^2 + x_3^2 = r^2$. In polar coordinates (Figure 2.1(a)), we write:

$$\begin{aligned}x_0 &= r \cos \theta \\x_1 &= r \sin \theta \sin \varphi, \quad r \in (0, \infty), \quad \theta \in [0, \pi], \quad \varphi \in [0, 2\pi) \\x_2 &= r \sin \theta \cos \varphi\end{aligned}$$

In the following discussion, we are working with the two-dimensional sphere but for simplicity we call it just sphere.

In order to visualize the sphere (or any other non-Euclidean manifold) in the plane one needs to perform a projection.

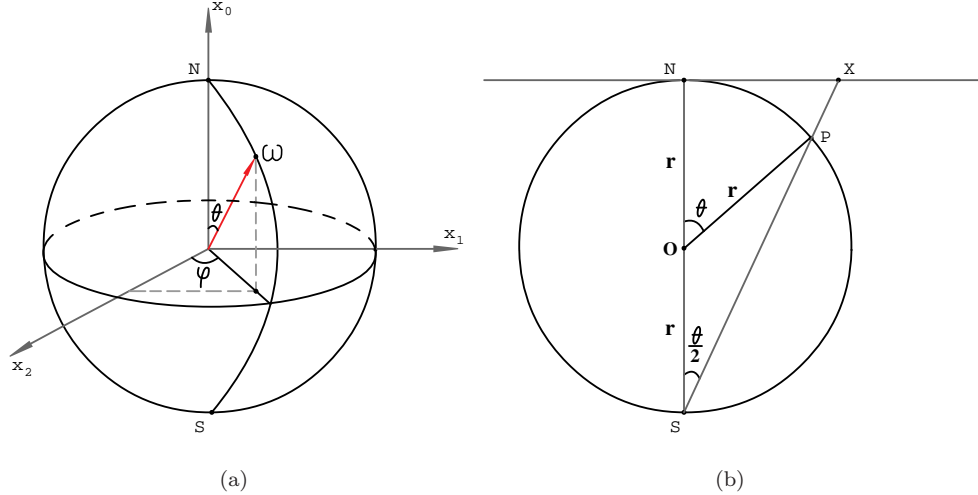


Figure 2.1: Spherical geometry: (a) spherical coordinates, (b) cross-section of a stereographic projection through the South Pole.

2.1.2 Stereographic projection of the sphere

The *stereographic projection* from the South Pole maps any point of the surface of the sphere onto a point of the tangent plane at the North Pole, as depicted on Figure 2.1(b). In $\triangle SOP$ we have:

- $\angle SOP = 180^\circ - \theta$,
- $OS = OP = r$
- $\angle OSP = \angle OPS = \psi$.

Then, for the angles in $\triangle SOP$ we get: $180^\circ - \theta + 2\psi = 180^\circ$, from where we obtain $\psi = \frac{\theta}{2}$. From $\triangle NSX$ we have $NX = 2r \tan \frac{\theta}{2}$, which is the stereographic projection. Thus, the stereographic projection $\Phi : S^2 \mapsto \mathbb{C}$ (here S^2 is taken as the Riemann sphere and the tangent plane at the North Pole as the complex plane \mathbb{C}) is a bijection given by

$$\Phi(\omega) = \zeta = 2 \tan \frac{\theta}{2} e^{i\varphi}, \quad \omega \equiv (\theta, \varphi), \quad \theta \in [0, \pi], \quad \varphi \in [0, 2\pi]. \quad (2.1)$$

2.2 Harmonic analysis on the sphere

Let us first introduce the basic Fourier analysis on the sphere and then some numerical implementation aspects concerning the discrete version of the spherical Fourier transform. We will use this background to build discrete frames on the sphere (in Section 2.4) and the Laplacian pyramid on the sphere (in Section 2.5).

2.2.1 Fourier transform on the sphere

Before entering into the details of the continuous wavelet transform on the 2-sphere, we need to have a basic notion of the Fourier analysis on this non-Euclidean manifold [29, 39]. Let $L^2(S^2, d\mu(\theta, \varphi))$ denote the Hilbert space of square integrable functions on S^2 with the invariant measure on the sphere $d\mu(\omega) = \sin\theta d\theta d\varphi$ where ω, θ, φ are as defined in (2.1). A function on the sphere is an *axisymmetric function* (or zonal function) if it is invariant under rotation on itself, i.e. such a function is independent of the angle φ , $f(\theta)$. Any non-axisymmetric function is given as a general function $f(\theta, \varphi) \in L^2(S^2, d\mu(\theta, \varphi))$.

Let us recall that a rotation $\rho \in SO(3)$ may be parameterized by its Euler angles $\varphi, \theta, \vartheta \in S^1$ in the following way

$$\rho = \rho(\varphi, \theta, \vartheta) = R_\varphi^{x_0} R_\theta^{x_1} R_\vartheta^{x_0}, \quad (2.2)$$

where ρ stands for three-dimensional rotation matrix acting on the coordinates $\omega \equiv (\theta, \varphi)$ and R_γ^u denotes a rotation by an angle γ around the u axis. If g is an axisymmetric function, then $R_\rho g = R_{[\omega]} g$, where $[\omega] = \rho(\varphi, \theta, 0)$. In this way, if g is localized around the North Pole, then $R_{[\omega]} g$ is localized around $\omega = (\theta, \varphi) \in S^2$.

In polar coordinates, the usual inner product is given by

$$\langle f, g \rangle = \int_0^\pi \int_0^{2\pi} d\varphi \sin\theta d\theta f(\theta, \varphi) \overline{g(\theta, \varphi)} \quad (2.3)$$

$$= \int_{S^2} d\mu(\omega) f(\omega) \overline{g(\omega)}. \quad (2.4)$$

As it is known from [74], the *spherical harmonics* provide an orthonormal basis for $L^2(S^2)$. For any non-negative integer l and an integer m such that $|m| \leq l$, the (l, m) -spherical harmonic Y_l^m is a harmonic homogeneous polynomial of degree l . The harmonics of degree l span a subspace of $L^2(S^2)$ of dimension $2l + 1$ which is invariant under the relations of the sphere. The expansion of any function $f \in L^2(S^2)$ in terms of spherical harmonics is written

$$f = \sum_{l \geq 0} \sum_{|m| \leq l} \hat{f}(l, m) Y_l^m \quad (2.5)$$

and $\hat{f}(l, m)$ denotes the (l, m) -Fourier coefficients, equal to $\langle f, Y_l^m \rangle$. In coordinates (θ, φ) , Y_l^m has the factorization

$$Y_l^m(\theta, \varphi) = k_{l,m} P_l^m(\cos\theta) e^{im\varphi}, \quad (2.6)$$

where P_l^m is the associated Legendre function of degree l and order m , and $k_{l,m} = \left[\frac{2l+1}{4\pi} \frac{(l-m)!}{(l+m)!} \right]^2$ is a normalization constant. The orthonormality and completeness relations respectively read:

$$\int_0^\pi \int_0^{2\pi} d\varphi d\theta \sin\theta \overline{Y_l^m(\theta, \varphi)} Y_{l'}^{m'}(\theta, \varphi) = \delta_{ll'} \delta_{mm'}, \quad (2.7)$$

and

$$\sum_{l \in \mathbb{N}} \sum_{|m| \leq l} \overline{Y_l^m(\theta', \varphi')} Y_l^m(\theta, \varphi) = \delta(\cos\theta' - \cos\theta) \delta(\varphi' - \varphi), \quad (2.8)$$

where $\overline{(\cdot)}$ denotes the complex conjugate.

Consequently, separating variables according to (2.6) shows that the computation of the spherical harmonic transform can be reduced to a regular Fourier transform in the longitudinal coordinate φ followed by a projection onto the associated Legendre functions

$$\hat{f}(l, m) = \langle f, Y_l^m \rangle = k_{l,m} \int_0^\pi \int_0^{2\pi} d\varphi d\theta \sin\theta e^{-im\varphi} f(\theta, \varphi) P_l^m(\cos\theta). \quad (2.9)$$

2.2.2 Wigner transform

The Wigner D -functions $D_{mn}^l(\rho)$ for $\rho = (\varphi, \theta, \phi) \in SO(3)$ as defined in (2.2), and with $l \in \mathbb{N}$, $m, n \in \mathbb{Z}$, and $|m|, |n| \leq l$, are the matrix elements of the irreducible unitary representation of weights l of the rotation group $SO(3)$ in $L^2(SO(3), d\rho)$. Any function $g(\rho) \in L^2(SO(3), d\rho)$ is uniquely given as a linear combination of Wigner D -functions (inverse Wigner transform):

$$g(\rho) = \sum_{l \in \mathbb{N}} \frac{2l+1}{8\pi^2} \sum_{|m|, |n| \leq l} \widehat{g}(l, m, n) \overline{D_{mn}^l(\rho)}, \quad (2.10)$$

for the Wigner coefficients (direct Wigner transform)

$$\widehat{g}(l, m, n) = \int_{\rho \in SO(3)} d\rho D_{mn}^l(\rho) g(\rho), \quad (2.11)$$

with $|m|, |n| \leq l$.

2.2.3 Convolution on the sphere

In general, the convolution on the sphere is well defined and has many properties in common with its equivalent in \mathbb{R}^n . It is useful to treat the convolution by the means of axisymmetric functions, i.e. $\varphi = 0$. Let us consider the elements of $L^2([-1, +1], d\cos\theta)$, for which the Fourier series are developed in Legendre polynomials:

$$\widehat{\psi}(l) = \sqrt{\frac{4\pi}{2l+1}} \int_{-1}^{+1} d\cos\theta \psi(\cos\theta) P_l(\cos\theta), \quad (2.12)$$

$$\psi(\cos\theta) = \sum_{l=0}^{\infty} \sqrt{\frac{2l+1}{4\pi}} \widehat{\psi}(l) P_l(\cos\theta). \quad (2.13)$$

Therefore, for two measurable functions on S^2 , f and g , if g is axisymmetric, the convolution of both reads [73]:

$$(g * f)(\gamma) = \int_{S^2} d\mu(\omega) g(\omega) f(\vec{\omega} \cdot \vec{\gamma}), \quad (2.14)$$

where $\vec{\omega} \cdot \vec{\gamma}$ is the scalar product in \mathbb{R}^3 of unitary vectors in the direction of ω and γ .

Of great importance for us is the following convolution theorem.

Theorem 9. (Spherical Convolution Theorem) [29] *For functions $f, g \in L^2(S^2)$, the transform of the convolution is a point-wise product of the transforms:*

$$\widehat{(g * f)}(l, m) = \sqrt{\frac{4\pi}{2l+1}} \widehat{g}(l, 0) \widehat{f}(l, m). \quad (2.15)$$

Therefore, a popular method to perform spherical convolution is to first project the discretized spherical function and filter onto the span of spherical harmonics and perform the convolution in the Fourier domain via simple multiplication. We must note that the convolution theorem is independent of the sampling. Hence, as long as we can project our samples onto the span of spherical harmonics accurately, we can perform convolution via the Fourier domain accurately, regardless of the sampling grid.

2.2.4 Correlation on the sphere

The correlation on the sphere is defined as the scalar product between a function f and an arbitrary another function g rotated on itself in a direction $\psi \in [0, 2\pi)$, and translated at any point $\omega_0 \equiv (\theta_0, \varphi_0)$ on the sphere.

For a rotation $\rho \in SO(3)$ as defined in (2.2), the correlation on the sphere can be decomposed in Wigner D-functions [76]. The Wigner coefficients $\langle \widehat{R_\rho g | f} \rangle(l, m, n)$ of the correlation $\langle R_\rho g | f \rangle$ are given as the point-wise product of the scalar spherical harmonics coefficients $\hat{f}(l, m)$ and $\hat{g}(l, n)$. The following correlation holds:

$$\langle R_\rho g | f \rangle = \sum_{l \in \mathbb{N}} \frac{2l+1}{8\pi^2} \sum_{|m|, |n| \leq l} \langle \widehat{R_\rho g | f} \rangle(l, m, n) \overline{D_{mn}^l(\rho)}, \quad (2.16)$$

with the Wigner coefficients on $SO(3)$ given as

$$\langle \widehat{R_\rho g | f} \rangle(l, m, n) = \frac{8\pi^2}{2l+1} \overline{\hat{g}(l, n)} \hat{f}(l, m). \quad (2.17)$$

The following proposition shows that the correlation has a simple expression in the Fourier domain. When reduced to axisymmetric function, the correlation on the sphere is equivalent to the convolution on the sphere:

Proposition 10. (Spherical Correlation) *Let $f \in L^2(S^2)$ and let $g \in L^2(S^2)$ be axisymmetric. Then*

$$\widehat{(g \star f)}(l, m) = \sqrt{\frac{4\pi}{2l+1}} \overline{\hat{g}(l, 0)} \hat{f}(l, m), \quad \forall (l, m) \in \mathcal{N}, \quad (2.18)$$

where \hat{h} denotes the Fourier transform of h on S^2 and $\mathcal{N} = \{(l, m) : l \in \mathbb{N}, m \in \mathbb{Z}, |m| \leq l\}$.

A proof of this classical result can be found in [29].

Equations (2.18) suggests a fast implementation of the FT in the Fourier domain. We will use this later, in Section 2.4, for discretization of the continuous wavelet transform on the sphere.

We say that a function $f \in L^2(S^2)$ is *band-limited of bandwidth* $\beta \in \mathbb{N}$ if

$$f \in \mathcal{B}_\beta = \{g \in L^2(S^2) : \hat{g}(l, m) = 0, \forall (l, m) \in \mathcal{N} \text{ such that } l \geq \beta\}. \quad (2.19)$$

We will work with data discretized on the *equi-angular grid* \mathcal{G}_β defined by:

$$\mathcal{G}_\beta := \{(\theta_p, \varphi_q) : p, q \in \mathbb{Z}[2\beta]\}, \quad (2.20)$$

with $\mathbb{Z}[N] = \{0, \dots, N-1\}$, $\theta_p = (2p+1)\frac{\pi}{4\beta}$ and $\varphi_q = q\frac{\pi}{\beta}$. Actually, $\{\theta_p\}$ constitutes a *pseudo-spectral* grid, localized on the zeros of a Chebishev polynomial of order 2β [15, 29]. The next result, proved in [29], will be of great importance in what follows. It shows that there is a quadrature formula for calculating the Fourier coefficients of band-limited functions.

Proposition 11. (Spherical Sampling) *Let $g \in \mathcal{B}_\beta$ with $\beta \in \mathbb{N}^0$. Then there exist weights $w_p^\beta \in \mathbb{R}_+^*$ such that*

$$\hat{g}(l, m) = \int_{S^2} d\mu(\theta, \varphi) \overline{Y_l^m(\theta, \varphi)} g(\theta, \varphi) \quad (2.21)$$

$$= \sum_{p, q \in \mathbb{Z}[2\beta]} w_p^\beta \overline{Y_l^m(\theta_p, \varphi_q)} g(\theta_p, \varphi_q), \quad (2.22)$$

for all $(l, m) \in \mathcal{N}_\beta = \{(l, m) \in \mathcal{N} : l < \beta\}$ and $(\theta_p, \varphi_q) \in \mathcal{G}_\beta$. Explicitly

$$w_p^\beta = \frac{2\pi}{\beta^2} \sin(\theta_p) \sum_{k \in \mathbb{Z}[\beta]} \frac{1}{2k+1} \sin((2k+1)\theta_p), \quad (2.23)$$

with $\sum_{p \in \mathbb{Z}[2\beta]} \sum_{q \in \mathbb{Z}[2\beta]} w_p^\beta = 4\pi$.

This sampling theorem ensures that the discretization of the spherical functions is reversible (i.e. no aliasing). Equation (2.22) is in fact a *Discrete Fourier Transform* on the sphere. The Inverse Discrete Fourier Transform is obtained as

$$g(\theta_p, \varphi_q) = \sum_{(l, m) \in \mathcal{N}_\beta} \widehat{g}(l, m) Y_l^m(\theta_p, \varphi_q), \quad p, q \in \mathbb{Z}[2\beta]. \quad (2.24)$$

For l and m fixed, the evaluation of (2.22) needs $\mathcal{O}(\beta^2)$ operations. Then for $(l, m) \in \mathcal{N}_\beta$, i.e., β^2 elements, $\mathcal{O}(\beta^4)$ operations are needed. The same estimate is valid for the computation of the inverse Fourier transform. The performance of this evaluation may be greatly improved if one notes that the spherical harmonic function $Y_l^m(\theta_p, \varphi_q)$, as defined in equation (2.6), is a separable function in terms of the variables θ and φ , which automatically implies $\mathcal{O}(\beta^3)$ [76]. Then a discrete Fourier transform on S^1 may be applied on the longitude φ_q in (2.22), which yields

$$\widehat{g}(l, m) = \sum_{p, q \in \mathbb{Z}[2\beta]} w_p^\beta g(\theta_p, \varphi_q) \overline{Y_l^m(\theta_p, \varphi_q)} \quad (2.25)$$

$$= \sum_{p \in \mathbb{Z}[2\beta]} w_p^\beta n_{lm} \check{g}(\theta_p, m) P_l^m(\cos \theta_p), \quad (2.26)$$

with $\check{g}(\theta_p, m) = \sum_{q \in \mathbb{Z}[2\beta]} g(\theta_p, \varphi_q) e^{-im\varphi_q}$.

2.3 Wavelets on the sphere

Antoine and Vandergheynst built the theory of wavelets on the sphere [10, 9, 11]. They started by exploring the geometry of the problem, which led them to considering the conformal group of the sphere and this permitted them to construct a spherical dilation in a purely algebraic way. The problem then was brought to the study of coherent states associated to this conformal group, i.e. the Lorentz group $SO_0(3, 1)$. After isolating a suitable representation from the principle series, they showed that it is square integrable in the generalized sense of Ali, Antoine and Gazeau [3], which means that the associated coherent states are indexed by a homogeneous space of the whole conformal group. Moreover, they showed that this theory satisfies an Euclidean limit, in other words, CWT on the sphere locally converges to the usual theory in the tangent plane, or for big radius of curvature as imposed by geometry.

2.3.1 Affine transformations on the sphere and their group theory

The spherical CWT, as in 1-D and 2-D Euclidean cases, is based on affine transformations. Consequently, the first step toward constructing a CWT on S^2 is to identify the appropriate transformations [10]. These are of two types, *motions*(displacements) and *dilations*:

- (i) Motions are given by elements of the rotation group $SO(3)$, which indeed act transitively on S^2 , and $S^2 \equiv SO(3)/SO(2)$.
- (ii) Dilations are obtained in two ways:

- dilations around the North Pole, D_N , are obtained by considering usual dilations in the tangent plane at the North Pole and lifting them to S^2 by inverse stereographic projection from the South Pole;
- dilation around any other point $\omega \in S^2$ is obtained by moving ω to the North Pole by a rotation $\gamma \in SO(3)$, performing a dilation D_N and going back by inverse rotation.

What follows next is to identify a group of affine transformations on S^2 . The rotation group $SO(3)$ is mapped onto $SU(2)$, with homographic action on \mathbb{C} :

$$\zeta \mapsto \frac{a\zeta + b}{c\zeta + d}, \quad \begin{pmatrix} a & b \\ c & d \end{pmatrix} \in SU(2). \quad (2.27)$$

A dilation $\zeta \mapsto a\zeta, a > 0$ is represented by the diagonal matrix $diag(a^{\frac{1}{2}}, a^{-\frac{1}{2}})$. Combining these two transformations we obtain the full group $SL(2, \mathbb{C})$, and a simply transitive action on S^2 by $SL(2, \mathbb{C})/\mathbb{Z}_2 \simeq SO_0(3, 1)$, the Lorentz group. We note that $SO(3, 1)$ is the conformal group of the tangent plane \mathbb{R}^2 and that of S^2 as well. All these considerations can be translated in a straightforward group-theoretical language by considering the *Iwasawa decomposition* of the Lorentz group $SO_0(3, 1)$. In other words, like any connected semi-simple Lie group, the latter admits a decomposition into three closed subgroups, namely $G = KAN$, where K is the maximal compact subgroup, A is Abelian, and N is nilpotent, and both are simply connected. In the case of $SO(3, 1)$, one gets:

- $K \sim SO(3)$, is the maximal compact subgroup.
- $A \sim SO_0(1, 1) \sim \mathbb{R}_*^+ \sim \mathbb{R}$ is the subgroup of the Lorentz boosts in the x_3 -direction.
- $N \sim \mathbb{C}$ is two-dimensional and nilpotent.

Thus one obtains, respectively,

$$SO_0(3, 1) = SO(3) \cdot \mathbb{R}_*^+ \cdot \mathbb{C}, \quad (2.28)$$

$$SL(2, \mathbb{C}) = SU(2) \cdot \mathbb{R}_*^+ \cdot \mathbb{C}. \quad (2.29)$$

Now, let again $G = KAN$ be the Iwasawa decomposition of a connected semi-simple Lie group G , with finite center. Let M be the centralizer of A in K ; that is, $M = \gamma \in K : \gamma a = a\gamma, \forall a \in A$. Then $P = MAN$ is a closed subgroup of G , called the *minimal parabolic subgroup*. The subgroup P is not invariant, but it is the stability subgroup of the North Pole, and the quotient G/P , which is isomorphic to K/M , is simply

$$S^2 \simeq SO_0(3, 1)/P \simeq SO(3)/SO(2), \text{ and} \quad (2.30)$$

$$S^2 \simeq SL(2, \mathbb{C})/P \simeq SU(2)/SU(1). \quad (2.31)$$

This shows that both $SO_0(3, 1)$ and $SL(2, \mathbb{C})$ act transitively on S^2 . As K was previously identified with the Euclidean motions on S^2 and A with dilations, which constitute the basic operations on the sphere, the parameter space of this theory is the homogeneous space

$$X \equiv SO_0(3, 1)/N \simeq SO(3) \cdot A. \quad (2.32)$$

The next step is the derivation of the action of dilations on the sphere. We will proceed in a purely algebraic way, starting from the Iwasawa decomposition of an element $g = \gamma an \in SL(2, \mathbb{C})$:

$$\begin{pmatrix} a & b \\ c & d \end{pmatrix} = \begin{pmatrix} \alpha & \beta \\ -\bar{\beta} & \bar{\alpha} \end{pmatrix} \begin{pmatrix} \delta^{-1/2} & 0 \\ 0 & \delta^{1/2} \end{pmatrix} \begin{pmatrix} 1 & \zeta \\ 0 & 1 \end{pmatrix}, \quad (2.33)$$

with $\alpha, \beta, \zeta \in \mathbb{C}, \delta \in \mathbb{R}_*^+$. The elements of $SU(2)$ are expressed in Euler parameterizations:

$$\alpha = \cos \frac{\theta}{2} \cdot e^{-\frac{i(\varphi+\psi)}{2}}, \quad (2.34)$$

$$\beta = -i \sin \frac{\theta}{2} \cdot e^{\frac{i(\psi-\varphi)}{2}}. \quad (2.35)$$

On the other hand $SU(2)$ has the following Euler decomposition:

$$\begin{pmatrix} \alpha & \beta \\ -\bar{\beta} & \bar{\alpha} \end{pmatrix} = \begin{pmatrix} e^{-i\psi/2} & 0 \\ 0 & e^{i\psi/2} \end{pmatrix} \begin{pmatrix} \cos \frac{\theta}{2} & -i \sin \frac{\theta}{2} \\ -i \sin \frac{\theta}{2} & \cos \frac{\theta}{2} \end{pmatrix} \begin{pmatrix} e^{-i\varphi/2} & 0 \\ 0 & e^{i\varphi/2} \end{pmatrix} \quad (2.36)$$

$$\equiv m(\psi)u(\theta)m(\varphi). \quad (2.37)$$

Then, for an element $g(a) = \text{diag}(a^{-1/2}, a^{1/2}) \in SL(2, \mathbb{C})$, acting on another $\gamma \in SU(2)$, we have $\gamma_a = g(a)\gamma$. Since $g(a)$ commutes with $m(\psi)$ we can write

$$\gamma_a = m(\psi)g(a)u(\theta)m(\varphi), \quad (2.38)$$

Here of interest is the product $g(a)u(\theta)$ which we decompose using (2.33) and thus we obtain

$$\cos \theta_a = \frac{(1+a^2)\cos\theta + (1-a^2)}{(1-a^2)\cos\theta + (1+a^2)}. \quad (2.39)$$

It is clear that the action of the dilation on $SU(2)$ is of the form

$$\gamma(\varphi, \theta, \psi) \rightarrow \gamma(\varphi, \theta_a, \psi). \quad (2.40)$$

Using (2.39) and applying basic trigonometric relations, it is clear that

$$\tan \frac{\theta_a}{2} = a \cdot \tan \frac{\theta}{2}. \quad (2.41)$$

Finally, in polar spherical coordinates, the dilation operator acting on a point $\omega = (\theta, \varphi)$ is :

$$D_a^{S^2}(\theta, \varphi) = (\theta_a, \varphi), \quad \text{with } \tan \frac{\theta_a}{2} = a \cdot \tan \frac{\theta}{2}. \quad (2.42)$$

Thus, the transformation corresponding to a pure dilation is the usual Euclidean dilation lifted on S^2 by inverse stereographic projection:

$$D_a^{S^2} : \omega \mapsto (\Phi^{-1} \cdot D_a^{\mathbb{C}} \cdot \Phi)(\omega), \quad \omega = (\theta, \varphi). \quad (2.43)$$

Consider the space of finite energy signals $\mathcal{H} = L^2(S^2, d\mu)$, where $d\mu(\omega) = \sin\theta d\theta d\varphi$ is the usual rotation invariant measure on S^2 . In this space, the basic transformations are represented by the following unitary operators:

- rotation R_ρ

$$(R_\rho f)(\omega) = f(\rho^{-1}\omega), \omega \equiv (\theta, \varphi). \quad (2.44)$$

where $\rho \in SO(3)$ is a 3×3 rotation matrix acting on a unit vector in \mathbb{R}^3 and may be parameterized in terms of Euler angles.

- dilation D_a

$$(D_a f)(\omega) = \lambda^{1/2}(a, \theta) f(\omega_{1/a}), \text{ with } \omega_a \equiv (\theta_a, \varphi), \quad (2.45)$$

where the Radon-Nikodým derivative $\lambda(a, \theta)$ is given by

$$\lambda(a, \theta) = \frac{4a^2}{[(a^2 - 1)\cos\theta + (a^2 + 1)]^2}. \quad (2.46)$$

Thus the spherical wavelet function becomes

$$\psi_{a,\rho}(\omega) = R_\rho D_a \psi(\omega) = R_\rho \lambda^{1/2}(a, \theta) \psi(\omega_{1/a}). \quad (2.47)$$

2.3.2 The continuous wavelet transform on the sphere

On the two-dimensional sphere S^2 , embedded in \mathbb{R}^3 , the basic transformations consist of rotations, defined by elements ρ of the group $SO(3)$, and dilations, parameterized by the scale $a \in SO_0(1,1) \in \mathbb{R}_*^+$. Thus, it remains to find a suitable unitary irreducible representation of the Lorentz group $SO_0(3,1)$ in the Hilbert space $L^2(S^2, d\mu)$, that is the space of square integrable functions on S^2 , with the rotation invariant Lebesgue measure $d\mu(\theta, \varphi) = \sin \theta d\theta d\varphi$. As it was already mentioned, it is not the whole group $SO(3,1)$ which is of interest here but a section $\sigma := X = KAN/N \rightarrow KAN$ in the principle fibre bundle defined by the Iwasawa decomposition. The points on the space X are written as pairs $x \equiv (\gamma, a)$, with $\gamma \in SO(3)$ and $a \in A \simeq SO(1,1)$ and thus the natural section is choosen:

$$\sigma_I(\gamma, a) = \gamma a. \quad (2.48)$$

Spherical admissibility condition

It is clear that not all dilated and rotated spherical functions can be wavelets. Only those which fulfill the following condition are admissible.

Theorem 12. (*Antoine and Vandergheynst [11]*) *The representation*

$$[U(\sigma(x))f](\omega) = \lambda^{1/2}(\sigma(x), \omega) f(\sigma^{-1}(x)\omega) \quad (2.49)$$

is square-integrable modulo the subgroup N and the section σ_I ; that is, the representation space $L^2(S^2, d\mu)$ contains a nonzero vector ψ admissible mod(N, σ_I), which means that there exists a constant $c > 0$, independent of l , such that

$$C_\psi(l) = \frac{8\pi^2}{2l+1} \sum_{|m| \leq l} \int_0^\infty \frac{da}{a^3} |\hat{\psi}_a(l, m)|^2 < c, \quad (2.50)$$

where $\hat{\psi}(l, m) = \langle Y_l^m | \psi \rangle$ stands for the Fourier coefficient of ψ and

$$\psi_a(\omega) = [U(\sigma_I(e, a))\psi](\omega) \equiv (D_a\psi)(\omega) = \lambda^{1/2}(a, \theta)\psi(\omega_{1/a}). \quad (2.51)$$

The proof consists in an explicit calculation, using the properties of the Fourier analysis on the sphere. So, according this proposition, any admissible ψ generates a continuous family $\{\psi_{a,g} \equiv U(\sigma(\rho, a))\psi, (\rho, a) \in X\}$ of spherical wavelets, but in fact there is more:

Proposition 13. (*Antoine and Vandergheynst [11]*)

For any admissible vector ψ such that $\int_0^{2\pi} d\varphi \psi(\theta, \varphi) \neq 0$, the family $\{\psi_{\sigma_I(x)}, x \in X\}$ is a continuous frame; that is, there exist constants $A > 0$ and $B < \infty$ such that

$$A\|\phi\|^2 \leq \int_X d\nu(x) |\langle \psi_{\sigma_I(x)} | \phi \rangle|^2 \leq B\|\phi\|^2, \forall \phi \in L^2(S^2, d\mu). \quad (2.52)$$

Thus, for any admissible vector ψ , we get a continuous frame, but not necessarily a tight one. The condition (2.50) is necessary and sufficient for the admissibility of ψ , but it is somewhat complicated to use in practice, since it requires the evaluation of nontrivial Fourier coefficients. Instead, there is a simpler, although only necessary, condition.

Proposition 14. (*Antoine and Vandergheynst [11]*)

A function $\psi \in L^2(S^2, d\mu)$ is admissible only if it satisfies the condition

$$\int_{S^2} d\mu(\theta, \varphi) \frac{\psi(\theta, \varphi)}{1 + \cos \theta} = 0. \quad (2.53)$$

This necessary condition is the exact equivalent of the usual necessary condition for wavelets in the Euclidean plane, $\int d^2x\psi(x) = 0$. The interesting about it is that is zero mean condition, as in the flat case. As such, it plays the same role, i.e. it ensures that the CWT on S^2 act as a local filter.

Theorem 12 yields the basic ingredient for writing the CWT on S^2 . Given an admissible wavelet $\psi \in L^2(S^2, d\mu)$, the wavelets on the sphere are the functions $\psi_{\gamma,a} = U(\sigma_I(\gamma, a))\psi$, and the CWT reads:

$$\mathcal{W}_f(\rho, a) = \langle \psi_{\rho,a} | f \rangle \quad (2.54)$$

$$= \int_{S^2} d\mu(\omega) \overline{R_\rho D_a \psi(\omega)} f(\omega) \quad (2.55)$$

$$= \int_{S^2} d\mu(\omega) \overline{\psi_a(\rho^{-1}\omega)} f(\omega), \quad (2.56)$$

where $\overline{(\cdot)}$ denotes the complex conjugate. This last expression is nothing but a spherical correlation, i.e.,

$$\mathcal{W}_f(\rho, a) = (\psi_a \star f)(\rho) \equiv \int_{S^2} d\mu(\omega') \overline{[R_\rho \psi_a](\omega')} f(\omega'). \quad (2.57)$$

The following proposition shows that the family of rotated and translated wavelets constitutes a (continuous) frame in $L^2(S^2)$, from which the reconstruction formula can be derived.

Proposition 15. (*Antoine et al. [7]*)

Let $f \in L^2(S^2)$. If ψ is an admissible wavelet such that $\int_0^{2\pi} d\varphi \psi(\theta, \varphi) \neq 0$, then

$$f(\omega) = \int_{\mathbb{R}_*^+} \int_{SO(3)} \frac{d\alpha d\nu(\rho)}{a^3} \mathcal{W}_f(\rho, a) [R_\rho L_\psi^{-1} D_a \psi](\omega), \quad (2.58)$$

where $d\nu(\rho)$ is the left Haar measure on $SO(3)$ and the coefficients are given by (2.55). The frame operator L_ψ is defined by

$$\widehat{[L_\psi h]}(l, m) = C_\psi(l) \hat{h}(l, m), \quad \forall h \in L^2(S^2), \quad (2.59)$$

where $C_\psi(l)$ is given in (2.50).

The frame operator so obtained is probably not tight, in general. As a consequence, the spherical CWT does not define an isometry. However, one has the following result, which immediately follows from (2.58):

Corollary 16. (*Antoine et al. [7]*) Under the conditions of Proposition 15, the following Plancherel relation is satisfied

$$\|f\|^2 = \int_{\mathbb{R}_*^+} \int_{SO(3)} \frac{d\alpha d\nu(\rho)}{a^3} \overline{\widetilde{\mathcal{W}}_f(\rho, a)} \mathcal{W}_f(\rho, a) \quad (2.60)$$

with

$$\widetilde{\mathcal{W}}_f(\rho, a) = \langle \tilde{\psi}_{\rho,a} | f \rangle = \langle R_\rho L_\psi^{-1} D_a \psi | f \rangle. \quad (2.61)$$

Before giving a concrete example of an wavelet on the 2-sphere, we will mention one last interesting result concerning the SCWT. It states that the inverse stereographic projection of a wavelet on the Euclidean plane leads to a wavelet on the sphere. The related technical proofs can be found in [75]. Beyond its pure theoretical interest, this new correspondence principle between the wavelet formalisms on the plane and on the sphere is of great practical use. Indeed, it enables to construct wavelets on the sphere by simple projection of wavelets on the plane.

2.3.3 An example of wavelets on the sphere

Example 5. (The "difference-of-Gaussian" (DOG) spherical wavelet) Given a square-integrable function $\phi(\theta, \varphi) = \exp\left(-\tan^2 \frac{\theta}{2}\right)$, we define

$$\psi_\phi^\alpha(\theta, \varphi) = \phi(\theta, \varphi) - \frac{1}{\alpha} D^\alpha \phi(\theta, \varphi), \quad (\alpha > 1). \quad (2.62)$$

This particular wavelet is depicted on Figure 2.2.

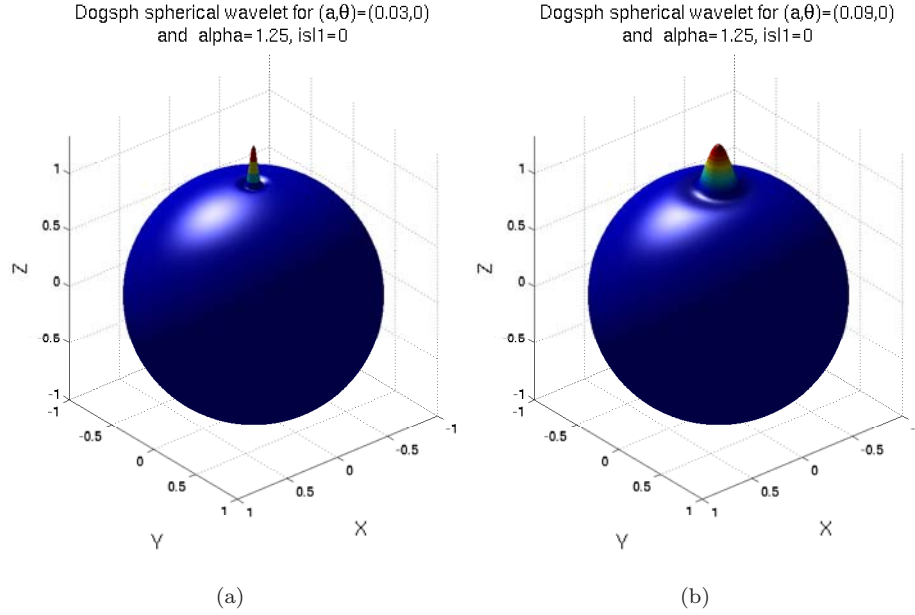


Figure 2.2: Spherical DOG wavelet for $\alpha = 1.25$: (a) $a = 0.03$, (b) $a = 0.09$.

Corresponding to the axisymmetric function on the sphere, the wavelet build using it will be an *axisymmetric spherical wavelet*. Given $[\omega] = \rho(\varphi, \theta, 0) \in SO(3)$, we define the correlation $\tilde{\star} : L^2(S^2) \times L^2(S^2) \rightarrow L^2(S^2)$ as

$$(g\tilde{\star}h)(\omega) = \int_{S^2} d\mu(\omega') \overline{R_{[\omega]}g(\omega')} h(\omega'), \quad (2.63)$$

to distinguish it from the complete correlation \star in equation (2.57). Since the stereographic dilation is radial around the North Pole, an axisymmetric wavelet ψ on S^2 remains axisymmetric after dilation. Consequently, the CWT is redefined on $S^2 \times \mathbb{R}_+^*$ by

$$\mathcal{W}_f(\omega, a) = (\psi_a \star f)([\omega]) = (\psi_a \tilde{\star} f)(\omega), \quad a \in \mathbb{R}_+^*. \quad (2.64)$$

In this particular case, the reconstruction formula (2.58), becomes

$$f(\omega) = \int_{\mathbb{R}_+^*} \int_{S^2} \frac{dad\mu(\omega')}{a^3} \mathcal{W}_f(\omega', a) [R_{[\omega]} L_\psi^{-1} D_a \psi](\omega'), \quad (2.65)$$

where L_ψ is the frame operator defined in equation (2.59) with G_ψ reducing to

$$G_\psi(l) = \frac{4\pi}{2l+1} \int_{\mathbb{R}_+^*} \frac{da}{a^3} |\hat{\psi}_a(l, 0)|^2. \quad (2.66)$$

In the general set-up for wavelet construction, we pointed out that a good wavelet transform on the sphere should be asymptotically Euclidean, in other words, the spherical WT should match the usual CWT in the Euclidean plane at small scales or, what amounts to the same, for large values of the radius of curvature. To this statement may be given a precise mathematical meaning, using the technique of group contractions, as it was derived in [10].

2.3.4 Wavelets on the sphere based on convolution

Before proceeding toward discretization of the continuous wavelet transform on the sphere we need to point out one more general result: it is possible to construct wavelets on the sphere, independently of the group theoretical approach. Since there exist a convolution theorem on the sphere in the sense of spherical harmonics, it is equivalently possible to do a derivation through spherical convolution. This aspects of the wavelets on the sphere, together with some basic implementations (concerning directional wavelets on the sphere), were performed in [7].

2.4 Discrete wavelet transform on the sphere

As in the Euclidean case, the WT on the sphere has two branches: the continuous wavelet transform and the discrete wavelet transform.

Various alternative constructions of discrete spherical wavelets have been proposed. For example, spherical wavelets based on the lifting scheme were introduced in [70]. They yield a multiresolution analysis on the sphere based on a particular parametrization of the latter.

W. Freeden [31] defines also a transformation on S^2 using a special dilation operator defined in the Fourier domain. Polynomial spherical frames have also been introduced in [58] where the order of the polynomials plays the role of the dilation. The drawbacks of these methods is that they focus on the frequential aspect of the transformations. In consequence, the spatial localization of these wavelets is either not guaranteed or precisely controlled.

T. Bülow did succeed in getting good localization properties by using the evolution of a spherical Gaussian governed by the heat equation on S^2 [18]. Then he gets a set of wavelet filters by differentiation of this Gaussian. However, this approach is restricted to the Gaussian function and thus it not as general as the one based on a stereographic dilation applied to an arbitrary admissible wavelet on S^2 .

In the following discussion, we describe under which conditions the parameters of the spherical continuous wavelet transform can be discretized without losing the reconstruction property. We assume all wavelets to be axisymmetric. This construction also appears in [14] and [44].

2.4.1 Half-continuous spherical frames

First approach

We propose to discretize the scale of the CWT but we let the position vary continuously. We choose therefore

$$\omega \in S^2, \quad a \in \alpha = \{a_j \in \mathbb{R}_+^* : j \in \mathbb{Z}, a_j > a_{j+1}\}, \quad (2.67)$$

which generates the half-continuous grid

$$\Lambda(\alpha) = \{(\omega, a_j) : \omega \in S^2, j \in \mathbb{Z}\}. \quad (2.68)$$

To simplify these notations, we will replace in the sequel each occurrence of a_j by j , $\psi_{a_j} = D_{a_j}\psi$ becoming for instance $\psi_j = D_j\psi$, and similarly $\mathcal{W}_j(\omega) = \langle \psi_{\omega,j} | f \rangle$.

In order to have a reconstruction of every function $f \in L^2(S^2)$, a first possible approach would be to impose

$$A\|f\|^2 \leq \sum_{j \in \mathbb{Z}} \nu_j \int_{S^2} d\mu(\omega) |\mathcal{W}_j(\omega)|^2 \leq B\|f\|^2, \quad (2.69)$$

with $A, B \in \mathbb{R}_+^*$ independent of f , and for some weights $\nu_j > 0$ taking into account the discretization of the continuous measure da/a^3 . In this case, the family

$$\Psi = \{\psi_{\omega,j} = R_{[\omega]}D_j\psi : \omega \in S^2, j \in \mathbb{Z}\} \quad (2.70)$$

constitutes a half-continuous frame in $L^2(S^2)$. The following proposition transposes the last condition in the Fourier domain (as identified by spherical harmonics).

Proposition 17. *Let ψ be an admissible wavelet. If there are two constants $A, B \in \mathbb{R}_+^*$ such that*

$$A \leq \frac{4\pi}{2l+1} \sum_{j \in \mathbb{Z}} \nu_j |\widehat{\psi}_j(l, 0)|^2 \leq B, \quad \text{for all } l \in \mathbb{N}, \quad (2.71)$$

then (2.69) is satisfied.

Proof : The SCWT of a function $f \in L^2(S^2)$ in the Fourier domain is given by

$$\mathcal{W}_f(\omega, a) = \sum_{(l,m) \in \mathcal{N}} \sqrt{\frac{4\pi}{2l+1}} \widehat{f}(l, m) \overline{\widehat{\psi}_a(l, 0)} Y_l^m(\omega).$$

Using this expression, we obtain

$$\begin{aligned} \sum_{j \in \mathbb{Z}} \nu_j \int_{S^2} d\mu(\omega) |\mathcal{W}_j(\omega)|^2 &= \sum_{j \in \mathbb{Z}} \nu_j \sum_{(l,k) \in \mathcal{N}} \sum_{(l',k') \in \mathcal{N}} \frac{4\pi}{\sqrt{(2l+1)(2l'+1)}} \widehat{f}(l, k) \overline{\widehat{f}(l', k')} \\ &\quad \overline{\widehat{\psi}_j(l, 0)} \widehat{\psi}_j(l', 0) \int_{S^2} d\mu(\omega) Y_l^k(\omega) \overline{Y_{l'}^{k'}(\omega)} \\ &= \sum_{j \in \mathbb{Z}} \nu_j \sum_{(l,k) \in \mathcal{N}} \frac{4\pi}{2l+1} |\widehat{f}(l, k)|^2 |\widehat{\psi}_j(l, 0)|^2 \\ &= \sum_{(l,k) \in \mathcal{N}} |\widehat{f}(l, k)|^2 \sum_{j \in \mathbb{Z}} \frac{4\pi}{2l+1} \nu_j |\widehat{\psi}_j(l, 0)|^2, \end{aligned}$$

where we have used the orthonormality of the spherical harmonics. The lower and upper bounds in (2.69) are well defined if there are two constants $A, B \in \mathbb{R}_+^*$ such that

$$A \leq \frac{4\pi}{2l+1} \sum_{j \in \mathbb{Z}} \nu_j |\widehat{\psi}_j(l, 0)|^2 \leq B, \quad \text{for all } l \in \mathbb{N}.$$

■

In order to illustrate this result, let us choose a DOG wavelet ($\alpha = 1.25$) and a discretized dyadic scale with a certain number of voices $K \in \mathbb{N}^0$ per octave, namely,

$$a_j = a_0 2^{-j/K}, \quad j \in \mathbb{Z}. \quad (2.72)$$

Once again, for the sake of simplicity, we replace the indices a_j by j . Moreover we choose weights ν_j that take into account the discretization of the continuous measure da/a^3 , which means

$$\nu_j = \frac{a_j - a_{j+1}}{a_j^3} = \frac{2^{1/K} - 1}{2^{1/K} a_j^2}. \quad (2.73)$$

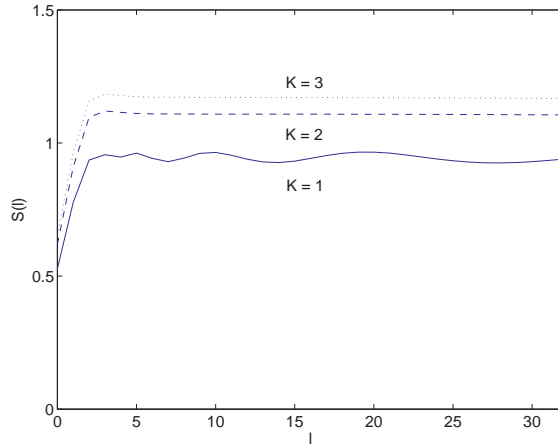


Figure 2.3: The function $S(l)$ for $l \in [0, 31)$ and $K = 1, 2, 3$. First Approach.

| K | A | B | B/A |
|-----|--------|--------|--------|
| 1 | 0.5281 | 0.9658 | 1.8288 |
| 2 | 0.6817 | 1.1203 | 1.8107 |
| 3 | 0.6537 | 1.1836 | 1.8107 |
| 4 | 0.6722 | 1.2171 | 1.8107 |

Table 2.1: Estimation of the bounds A and B as a function of the extremum of $S(l)$ for some values of K . First approach.

We have estimated the bounds A and B , respectively, by the minimum and the maximum of the quantity

$$S(l) = \frac{4\pi}{2l+1} \sum_{j \in \mathbb{Z}} \nu_j |\widehat{\psi}_j(l, 0)|^2, \quad (2.74)$$

over $l \in [0, 31]$ and for $K = 1, 2, 3$. The function $S(l)$ is represented on Figure 2.3 and the results are shown in Table 2.1. We see that for $K > 2$, the ratio B/A converges towards the value 1.8107. We thus do not obtain a tight frame, for which we should have $A = B$. As can be checked on the graph, however, $S(l)$ quickly tends to a constant for $l \geq 5$. The problem mostly comes from a severe “dip” in the graph of $S(l)$ (Figure 2.3) for small values of l ($l \leq 3$).

Second approach

Trying to converge to a tight frame, we adopt now a second approach for our half-continuous discretization. We start from the Plancherel relation defined in Corollary 16 and determine under which conditions we can obtain a *controlled* frame. That is, for two frame bounds $A, B \in \mathbb{R}_+^*$, we want

$$A\|f\|^2 \leq \sum_{j \in \mathbb{Z}} \nu_j \int_{S^2} d\mu(\omega) \mathcal{W}_j(\omega) \overline{\widehat{\mathcal{W}}_j(\omega)} \leq B\|f\|^2, \quad (2.75)$$

where $f \in L^2(S^2)$ and $\widehat{\mathcal{W}}_j(\omega) = \langle R_{[\omega]} L_\psi^{-1} D_j \psi | f \rangle$. The operator L_ψ^{-1} controlling the frame is the continuous frame operator defined in the Fourier domain by

$$\widehat{L_\psi^{-1} f}(l, m) = G_\psi^{-1}(l) \widehat{f}(l, m),$$

where G_ψ is given in (2.66). It is bounded with bounded inverse, i.e., $L_\psi \in GL(\mathfrak{H})$, if and only if the wavelet ψ is admissible.

Proposition 18. *If there exist two constants $A, B \in \mathbb{R}_+^*$ such that*

$$A \leq \frac{4\pi}{2l+1} G_\psi(l)^{-1} \sum_{j \in \mathbb{Z}} \nu_j |\widehat{\psi}_j(l, 0)|^2 \leq B, \quad \text{for all } l \in \mathbb{N}, \quad (2.76)$$

then (2.75) is satisfied.

Proof : As in the previous proposition, we start from the Fourier coefficients

$$\mathcal{W}_f(\omega, a) = \sum_{(l,m) \in \mathcal{N}} \sqrt{\frac{4\pi}{2l+1}} \widehat{f}(l, m) \overline{\widehat{\psi}_a(l, 0)} Y_l^m(\omega).$$

Then $\widetilde{\mathcal{W}}_f(\omega, a) = \langle R_{[\omega]} L_\psi^{-1} D_a \psi | f \rangle$ reads

$$\widetilde{\mathcal{W}}_f(\omega, a) = \sum_{(l,m) \in \mathcal{N}} \sqrt{\frac{4\pi}{2l+1}} G_\psi(l)^{-1} \widehat{f}(l, m) \overline{\widehat{\psi}_a(l, 0)} Y_l^m(\omega),$$

since the frame operator depends only on l and commutes with rotations.

Using these expressions for the coefficients and the fact that spherical harmonics are orthonormal, we find

$$\sum_{j \in \mathbb{Z}} \nu_j \int_{S^2} d\mu(\omega) \mathcal{W}_j(\omega) \overline{\widetilde{\mathcal{W}}_j(\omega)} = \sum_{(l,k) \in \mathcal{N}} |\widehat{f}(l, k)|^2 \sum_{j \in \mathbb{Z}} \frac{4\pi}{2l+1} G_\psi(l)^{-1} \nu_j |\widehat{\psi}_j(l, 0)|^2.$$

Then, inequalities in (2.75) are verified if there exist two constants $A, B \in \mathbb{R}_+^*$, such that

$$A \leq \frac{4\pi}{2l+1} G_\psi(l)^{-1} \sum_{j \in \mathbb{Z}} \nu_j |\widehat{\psi}_j(l, 0)|^2 \leq B, \quad \text{for all } l \in \mathbb{N}.$$

■

Note that, for $a_j = a_0 2^{-j/K}$,

$$G_\psi(l) = \lim_{K \rightarrow \infty} \frac{4\pi}{2l+1} \sum_{j \in \mathbb{Z}} \nu_j |\widehat{\psi}_j(l, 0)|^2, \quad (2.77)$$

since the weights ν_j discretize the continuous measure da/a^3 (in other words, G_ψ is well approximated by Riemann sums). Therefore, we obtain a good approximation of G_ψ by taking a large K in the previous equation. We will set $K = 10$.

Given this scale discretization and using the same wavelet and the same weights ν_j as in the first approach, the new quantity

$$S(l) = \frac{4\pi}{2l+1} G_\psi(l)^{-1} \sum_{j \in \mathbb{Z}} \nu_j |\widehat{\psi}_j(l, 0)|^2 \quad (2.78)$$

has been evaluated. It is drawn on Figure 2.4 for several values of K . The previous ‘‘dip’’ at small l has disappeared and the oscillations occurring at $K = 1$ are almost inexistent for $K = 3$. This is confirmed in Table 2.2, where the values of A and B have been estimated by the infimum and the supremum of $S(l)$ on $l \in [0, 31]$, respectively. We see that the ratio B/A tends quickly to 1 as K increases. A tight frame is thus reachable using the controlled frame approach.

Before proceeding toward the spherical frame reconstruction, we first expose some explicit discussion on the scale range of the spherical continuous wavelet transform associated to an axisymmetric wavelets.

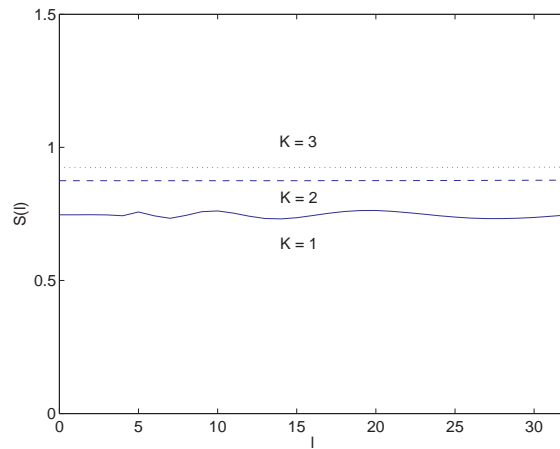


Figure 2.4: The function $S(l)$ for $l \in [0, 31[$ and $K = 1, 2, 3$. Second Approach.

| K | A | B | B/A |
|-----|--------|--------|--------|
| 1 | 0.7313 | 0.7628 | 1.0431 |
| 2 | 0.8747 | 0.8766 | 1.0021 |
| 3 | 0.9242 | 0.9254 | 1.0014 |
| 4 | 0.9503 | 0.9512 | 1.0009 |

Table 2.2: Estimation of the bounds A and B as a function of the extremum of $S(l)$ for some values of K . Second approach.

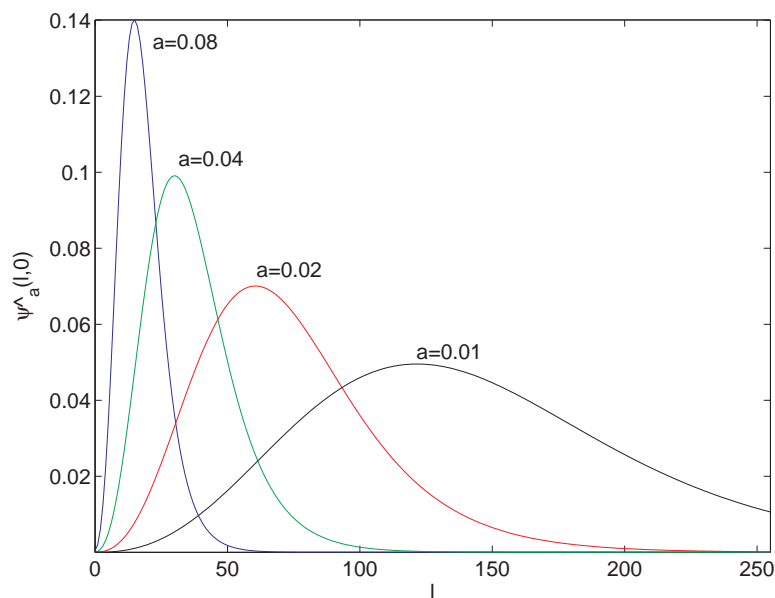


Figure 2.5: Behavior of $\hat{\psi}_a(l, 0)$ as a function of the scale a . If $a = 0.01$, the bandwidth of the dilated wavelet exceeds the limit fixed by the discretization.

The scale range

The range of the scale parameter in the continuous wavelet transform seems arbitrary. However, this is not the case in practice. For fixing ideas, let us recall the situation for classical wavelets on \mathbb{R} . Even if the wavelet transform of a signal is obtained by integration over the whole real line, in practice, data are discretized and have finite length. Hence the possible values of the scale parameter are constrained on one side by the sampling frequency (this gives a lower bound: the wavelet cannot oscillate more than permitted by the Nyquist frequency) and on the other side by the length of the interval where the signal is defined (upper bound: the wavelet should “live” inside that interval).

In the case of the spherical continuous wavelet transform, the smallest a is also constrained by the sampling frequency of the spherical grid. This phenomenon is displayed on Figure 2.5, where $\widehat{\psi}_a(l, 0)$ is drawn for several values of a . On this graph, we discretize ψ_a on a 512×512 spherical grid according to the previous section, for a maximal permitted bandwidth $\beta = 256$. One clearly sees that $\widehat{\psi}(l, 0)$ is *not* numerically negligible for $l = 255$ with the choice $a \leq 0.01$. Therefore $\psi_a \notin \mathcal{B}_\beta$ and it cannot be defined on \mathcal{G}_{256} . As a matter of fact, the upper limit of the scales is also constrained by the high frequencies of the dilated wavelet. Actually, the nature of the dilation produces an accumulation of points around the South Pole, so the oscillating tails of the wavelet are compelled to oscillate faster as a increases, even if the amplitude is negligible. The following discussion roughly formalizes this behavior.

We are going to estimate the highest non-negligible frequency $l_M(a)$ reached by the dilated wavelet ψ_a , which determines its bandwidth. We will see that it increases not only for small values of the scale (as expected because that corresponds to high frequencies), but also for large ones. Our argument rests upon the fact that the bandwidth of an oscillatory function may be estimated from the distance between its zero crossings.

Given two latitudes α and β in $[0, \pi]$, let us first study the evolution of the (angular) distance between the dilated angles α_a and β_a as a function of a . We get

$$\begin{aligned} \Delta_{\alpha\beta}(a) &:= \tan \frac{(\alpha_a - \beta_a)}{2} \\ &= \frac{\tan \frac{\alpha_a}{2} - \tan \frac{\beta_a}{2}}{1 + \tan \frac{\alpha_a}{2} \tan \frac{\beta_a}{2}} \\ &= \frac{a(\tan \frac{\alpha}{2} - \tan \frac{\beta}{2})}{1 + a^2 \tan \frac{\alpha}{2} \tan \frac{\beta}{2}} \\ &= \frac{a(1 + \tan \frac{\alpha}{2} \tan \frac{\beta}{2})}{(1 + a^2 \tan \frac{\alpha}{2} \tan \frac{\beta}{2})} \frac{(\tan \frac{\alpha}{2} - \tan \frac{\beta}{2})}{(1 + \tan \frac{\alpha}{2} \tan \frac{\beta}{2})} \\ &= \Xi_{\alpha\beta}(a) \Delta_{\alpha\beta}(1), \end{aligned}$$

where we have denoted

$$\Xi_{\alpha\beta}(a) = \frac{a(1 + \tan \frac{\alpha}{2} \tan \frac{\beta}{2})}{1 + a^2 \tan \frac{\alpha}{2} \tan \frac{\beta}{2}}. \quad (2.79)$$

If α and β are not zero, the function $\Xi_{\alpha\beta}$ has a unique maximum in

$$\tilde{a}(\alpha, \beta) = \frac{1}{\sqrt{\tan \frac{\alpha}{2} \tan \frac{\beta}{2}}}. \quad (2.80)$$

We also have that $\Xi_{\alpha\beta}(0) = \lim_{a \rightarrow +\infty} \Xi_{\alpha\beta}(a) = 0$. In other words, the distance $\Delta_{\alpha\beta}(a)$ increases in $(0, \tilde{a}]$ and decreases in $[\tilde{a}, +\infty)$.

If the bandwidth of the wavelet is l_0 , the minimal distance between two of its zeros is of the order of $\frac{\pi}{l_0}$. Let us label those points as α and $\beta = \alpha + \frac{\pi}{l_0}$.

From the relation $\Delta_{\alpha\beta}(a) = \Xi_{\alpha\beta}(a)\Delta_{\alpha\beta}(1)$, we can see that the bandwidth $l_M(a)$ of the dilated wavelet ψ_a is approximately related to l_0 by

$$\tan \frac{\pi}{2l_M(a)} \simeq \Xi_{\alpha\beta}(a) \tan \frac{\pi}{2l_0},$$

that is to say,

$$l_M(a) \simeq \frac{\pi}{2 \tan^{-1}(\Xi_{\alpha\beta}(a) \tan(\frac{\pi}{2l_0}))}. \quad (2.81)$$

Knowing the behavior of $\Xi_{\alpha\beta}(a)$, from (2.81), we can roughly say that $l_M(a)$ decreases in the interval $(0, \tilde{a}]$ and increases in $[\tilde{a}, +\infty)$. A minimum $l_M = 3$ is in a neighborhood of $a = 0.8$. This means that the DOG wavelet should be discretized on an equi-angular spherical grid of 8×8 points at least and for values of a near 0.8 only. Besides, if we take for example a 256×256 grid ($\beta = 128$), the dilated wavelet ψ_a will not be correctly discretized for a outside of the interval $[a_{\min} = 0.0204, a_M = 45.83]$ because $l_M(a)$ is strictly bigger than $l = 127$ for those values.

Having this specific issues on the spherical wavelet scale range, we proceed towards the spherical frames reconstruction.

Reconstruction

A function $f \in L^2(S^2)$ can be reconstructed from its coefficients $\mathcal{W}_j(\omega)$ as soon as the family $\Psi = \{\psi_{\omega,j} : \omega \in S^2, j \in \mathbb{Z}\}$ constitutes a (classical) half-continuous frame.

Proposition 19. *Let $\alpha = \{a_j : j \in \mathbb{Z}, a_j > a_{j+1}\}$ be a sequence of scales. If ψ is an axisymmetric wavelet such that, for two constants $A, B \in \mathbb{R}_+^*$,*

$$A \leq g_\psi(l) = \frac{4\pi}{2l+1} \sum_{j \in \mathbb{Z}} \nu_j |\widehat{\psi}_j(l, 0)|^2 \leq B, \quad \forall l \in \mathbb{N}, \quad (2.82)$$

then,

$$\begin{aligned} f(\omega) &= \sum_{j \in \mathbb{Z}} \nu_j \int_{S^2} d\mu(\omega') \left[R_{[\omega]} \ell_\psi^{-1} D_{a_j} \psi \right] (\omega') \mathcal{W}_f(\omega', a_j) \\ &= \sum_{j \in \mathbb{Z}} \nu_j [\underline{\psi}_j \star \mathcal{W}_j](\omega), \end{aligned}$$

where ℓ_ψ is the operator defined in the Fourier domain by

$$[\widehat{\ell_\psi^{-1} h}](l, m) = g_\psi^{-1}(l) h(l, m). \quad (2.83)$$

and $\underline{\psi}_j = \ell_\psi^{-1} \psi_j$ is the dual function of ψ_j .

The proof is similar to the proof of Proposition 18, replacing G_ψ by g_ψ . The new operator ℓ_ψ is nothing but the discretization of L_ψ defined in (2.66). According to this proposition, the family Ψ can be interpreted as a tight frame controlled by the operator ℓ_ψ^{-1} .

We have seen, in our discussion on the wavelet scale range, that there exists a limit scale $\tilde{a} \in \mathbb{R}_+^*$ such that, for increasing $a \in [\tilde{a}, +\infty[$, the support of $\tilde{\psi}_a$ stops contracting towards low frequencies and starts growing again towards high frequencies. We will lump together all wavelets having this behavior into a single scaling function ζ defined by

$$|\widehat{\zeta}(l, m)|^2 = \delta_{m,0} \sum_{j=-\infty}^{-1} \nu_j |\widehat{\psi}_j(l, 0)|^2. \quad (2.84)$$

We have estimated the angular distance between two dilated angles on the sphere to have a maximum for $\tilde{a} \simeq 0.8$. Thus we can safely take $\tilde{a} = 1$, corresponding to $j = 0$. This justifies the upper bound in the sum (2.84). However, the weights $\nu_j \propto a_j^{-2}$ decrease rapidly for $j \rightarrow -\infty$ (large scales), so that only the last few terms, with $|j|$ small, will contribute significantly to the sum, which entails that the function ζ is mainly concentrated at low frequencies.

In addition, if the analyzed signal f is band-limited, i.e., there is a bandwidth $\beta \in \mathbb{N}^0$ such that $f \in \mathcal{B}_\beta$ (a frequent situation for signals on the sphere), we may define a *residual* function with

$$|\widehat{\eta}(l, m)|^2 = \mathbb{1}_{[0, \beta)}(l) \delta_{m, 0} \sum_{j=J+1}^{\infty} \nu_j |\widehat{\psi}_j(l, 0)|^2, \quad (2.85)$$

where J is the maximal resolution such that the support of $\widehat{\psi}_j(l, 0)$ is contained in $[0, \beta[$.

This function will catch the high frequency components of f omitted by $\widehat{\psi}_j$ for $j \in [0, J]$. With these two functions, the reconstruction formula reads

$$f(\omega) = [\bar{\zeta} \star S](\omega) + \sum_{j=0}^J \nu_j [\bar{\psi}_j \star \mathcal{W}_j](\omega) + [\bar{\eta} \star H](\omega), \quad (2.86)$$

with $S(\omega) = \langle R_{[\omega]} \zeta | f \rangle$, $\zeta = \ell_\psi^{-1} \zeta$, $H(\omega) = \langle R_{[\omega]} \eta | f \rangle$ and $\eta = \ell_\psi^{-1} \eta$.

2.4.2 Discrete spherical frames

As a last step, we will now completely discretize the CWT on the sphere. First, the scales are discretized as previously, namely

$$a \in \alpha := \{a_j \in \mathbb{R}_+^* : a_j > a_{j+1}, j \in \mathbb{Z}\}.$$

Then we choose the positions on an equi-angular grid of resolution j and of size $2\beta_j \times 2\beta_j$ ($\beta_j \in \mathbb{N}$), i.e.,

$$\omega \in \mathcal{G}_j := \{\omega_{jpq} = (\theta_{jp}, \varphi_{jq}) \in S^2 : \theta_{jp} = \frac{(2p+1)\pi}{4\beta_j}, \varphi_{jq} = \frac{q\pi}{\beta_j}, p, q \in \mathbb{Z}[2\beta_j]\}. \quad (2.87)$$

As explained in Section 2.2.4, the grid \mathcal{G}_j allows to sample perfectly any function of bandwidth β_j .

The complete grid finally reads as follows :

$$\Lambda(\alpha, \beta) = \{(a_j, \omega_{jpq}) : j \in \mathbb{Z}, p, q \in \mathbb{Z}[2\beta_j]\}, \quad (2.88)$$

for a set of bandwidths $\beta = \{\beta_j \in \mathbb{N} : j \in \mathbb{Z}\}$. In this case, for an axisymmetric admissible mother wavelet $\psi \in S^2$, the family

$$\Psi = \{\psi_{jpq} = R_{[\omega_{jpq}]} D_j \psi : j \in \mathbb{Z}, p, q \in \mathbb{Z}[2\beta_j]\} \quad (2.89)$$

constitutes a weighted frame controlled by the operator L_ψ^{-1} , if there are two constants $A, B \in \mathbb{R}_+^*$ such that, for any $f \in L^2(S^2)$,

$$A \|f\|^2 \leq \sum_{j \in \mathbb{Z}} \sum_{p, q \in \mathbb{Z}[2\beta_j]} \nu_j w_{jp} \mathcal{W}_j[p, q] \overline{\widetilde{\mathcal{W}}_j[p, q]} \leq B \|f\|^2, \quad (2.90)$$

with $\mathcal{W}_j[p, q] = \langle \psi_{jpq} | f \rangle$, $\widetilde{\mathcal{W}}_j[p, q] = \langle L_\psi^{-1} \psi_{jpq} | f \rangle$, and where the quadrature weights $w_{jp} = w_p^{\beta_j}$ are defined in (2.23). The product $\nu_j w_{jp}$ replaces the continuous measure $a^{-3} da d\mu(\theta, \varphi)$ of the continuous framework.

Proposition 20. Consider the discretization grid $\Lambda(\alpha, \beta)$ defined in (2.88). Given an axisymmetric admissible wavelet ψ on S^2 , define the quantities

$$S'(l) = \sum_{j \in \mathbb{Z}} \frac{4\pi\nu_j}{2l+1} \mathbb{1}_{[0, \beta)}(l) G_\psi^{-1}(l) |\widehat{\psi}_j(l, 0)|^2, \quad (2.91)$$

$$\delta = \|\mathcal{X}\| \equiv \sup_{(H_l)_{l \in \mathbb{N}}} \frac{\|\mathcal{X}H\|}{\|H\|}, \quad (2.92)$$

where the infinite matrix $(\mathcal{X}_{ll'})_{l, l' \in \mathbb{N}}$ is given by

$$\mathcal{X}_{ll'} = \sum_{j \in \mathbb{N}} \frac{2\pi\nu_j c_j(l, l')}{\beta_j} \mathbb{1}_{[2\beta_j, +\infty)}(l+l') G_\psi^{-1}(l) |\widehat{\psi}_j(l, 0)| |\widehat{\psi}_j(l', 0)| \quad (2.93)$$

and $c_j(l, l') = (2(l + \beta_j) + 1)^{1/2} (2(l' + \beta_j) + 1)^{1/2}$. If we have

$$0 \leq \delta < K_0 \leq K_1 < \infty, \quad (2.94)$$

where $K_0 = \inf_{l \in \mathbb{N}} S'(l)$ and $K_1 = \sup_{l \in \mathbb{N}} S'(l)$, then the family (2.89) is a weighted spherical frame controlled by the operator L_ψ^{-1} , with frames bounds $K_0 - \delta$, $K_0 + \delta$.

The technical proof of this result is placed in Appendix A.

The evaluation of $\|\mathcal{X}\|$ could be complex when the size of \mathcal{X} is infinite. In practice, however, we work with band-limited functions $f \in L^2(S^2)$ of bandwidth $\beta_M \in \mathbb{N}^0$. In this case $\|\mathcal{X}\|$ can be replaced by the norm of the finite matrix $(\mathcal{X}_{l, l'})_{0 \leq l, l' < \beta_M}$.

We have estimated the bounds of a spherical DOG wavelet frame in the case $\beta_M = 128$, using a dyadically discretized scale (with $K = a_0 = 1$ in (2.72)), while the bandwidth associated to the grid size supporting each resolution j was fixed to

$$\beta_j = \beta_0 2^{|j|}, \quad \beta_0 \in \mathbb{N}, \quad (2.95)$$

where β_0 is the minimal bandwidth associated to ψ_1 . The last equation takes into account the particular nature of the stereographic dilation on S^2 . Indeed, for the DOG wavelet, the (numerical) support of $\widehat{\psi}_j$ increases roughly with $2^{|j|}$. Table 2.3 presents the results of the evaluation of K_0 , K_1

| | K_0 | K_1 | δ | $A = K_0 - \delta$ | $B = K_1 + \delta$ | B/A |
|---------------|--------|--------|----------|--------------------|--------------------|--------|
| $\beta_0 = 2$ | 0.6691 | 0.7644 | 344.2417 | — | — | — |
| $\beta_0 = 4$ | 0.7313 | 0.7736 | 0.0607 | 0.6707 | 0.8343 | 1.2440 |
| $\beta_0 = 8$ | 0.7313 | 0.7736 | 0.0014 | 0.7299 | 0.7751 | 1.0618 |

Table 2.3: Evaluation of K_0 , K_1 and δ on the functions $f \in L^2(S^2)$ at bandwidth 128.

and δ as well as the bounds of the associated frames. One can see that condition (2.94) is satisfied for $\beta_0 \geq 4$. However, a tight frame cannot be obtained by increasing β_0 . Indeed if β_0 tends to infinity, the spherical grids at each resolution become finer and finer and we approach half-continuous frames. But, as seen in the previous section, this single voice discretization of the scale is not sufficient for producing a tight frame.

Approximate reconstruction

As explained in Section 1.8.3, the frame $\Psi = \{\psi_{jpq}\}$ controlled by L_ψ^{-1} provides a simple approximate reconstruction formula if the bounds A and B are sufficiently close. In this case, indeed, we have

$$f(\omega) \simeq \frac{2}{A+B} \sum_{j \in \mathbb{Z}} \sum_{p, q \in \mathbb{Z}[2\beta_j]} \nu_j w_{jp} \mathcal{W}_j[p, q] [L_\psi^{-1} \psi_{jpq}](\omega). \quad (2.96)$$

Let us assume that f is a band-limited function, i.e., $f \in \mathcal{B}_{\beta_M}$, for a certain $\beta_M \in \mathbb{N}$. Therefore, f may be discretized without loss of information on a grid \mathcal{G}_J , where $J \in \mathbb{N}^0$ is the maximal resolution of the grid such that $\beta_J = \beta_M$. As in the half-continuous case, the residual function η defined in (2.85) can be used to catch the high frequencies left over by the restriction $j \leq J$.

This leads to the approximate reconstruction formula

$$\begin{aligned} \frac{A+B}{2}f(\omega) &\simeq \sum_{j=-J}^J \sum_{p,q \in \mathbb{Z}[2\beta_j]} \nu_j w_{jp} \mathcal{W}_j[p, q] [L_\psi^{-1} \psi_{jpq}](\omega) + \dots \\ &+ \sum_{p,q \in \mathbb{Z}[2\beta_M]} H[p, q] [L_\psi^{-1} \eta_{pq}](\omega), \end{aligned} \quad (2.97)$$

where $H[p, q] = \langle \eta_{pq} | f \rangle$ and $\eta_{pq}(\omega) = [R_{[\omega_{Jpq}]} \eta](\omega)$.

Notice that a scaling function could be defined to gather wavelets in the range $j < -J$. However, wavelet coefficients at these resolutions are practically negligible since the weights ν_j decrease with j as 2^{2j} . The approximation of f by the new frame operator

$$\begin{aligned} L'_\psi f &= \frac{2}{A+B} \sum_{j=-J}^J \sum_{p,q \in \mathbb{Z}[2\beta_j]} \nu_j w_{jp} \mathcal{W}_j[p, q] L_\psi^{-1} \psi_{jpq} + \dots \\ &+ \frac{2}{A+B} \sum_{p,q \in \mathbb{Z}[2\beta_M]} H[p, q] L_\psi^{-1} \eta_{pq}, \end{aligned} \quad (2.98)$$

may be largely improved by using the *conjugate gradient algorithm* [54], which computes iteratively, from L'_ψ , the reconstruction of f that we would obtain with the dual wavelets of ψ_n . Note the latter cannot be obtained explicitly, because we cannot control the effect in Fourier space of the undersampling implied by the successive grids.

An example of spherical wavelet frame

We will now decompose and reconstruct a particular example of spherical data. The spherical data to be processed, s , represents the planet Mars. It is recorded to an equi-angular grid of 512×512 points and therefore bandwidth $\beta_M = 256$. For this frame decomposition a spherical DOG with $\alpha = 1.25$ is the mother wavelet. The parameters of the multi-scale grid are $\alpha_0 = 1$ and $\beta_0 = 4$. First, we note that there is no subgrid imbedded in the maximum one, i.e $\mathcal{G}_j \not\subseteq \mathcal{G}_J$ and thus we compute $\mathcal{W}_s[\omega, a_j]$ on the maximum grid \mathcal{G}_J . Next, a linear interpolation of the coefficients $W_s(\omega_{jpq}, a_j)$ on the sub-grid \mathcal{G}_j from the coefficients $W_s(\omega_{Jp'q'}, a_j)$ is performed. From this two operations, the values $\mathcal{W}_s[p, q]$ have been obtained. Figures 2.6(b), 2.6(c), 2.6(d), 2.6(e), 2.6(f) show respectively wavelet coefficients $\mathcal{W}_2[p, q]$, $\mathcal{W}_3[p, q]$, $\mathcal{W}_5[p, q]$, $\mathcal{W}_7[p, q]$ and $\mathcal{W}_8[p, q]$.

For the purpose of reconstruction of Mars the function $G_\psi(l)$ from equation (2.77) has been estimated for $K = 10$. The ratio $\frac{2}{A+B}$ from equation (2.96) is set to 1.3289, according the results in Table 2.3. On Figures 2.7(a) and 2.7(b) we can see the the reconstructed signal and the deference between the signal and its reconstruction $s - L'_\psi s$, respectively. The amplitude of this difference is calculated, and we can see that the reconstruction $L'_\psi s$ is very close to s :

$$\frac{\|s - L'_\psi s\|}{\|s\|} \simeq 0.8846. \quad (2.99)$$

A better reconstruction is obtained with the conjugate gradient algorithm. The amplitude of difference $s - s^{(2)}$ reconstructed by this algorithm is respectively:

$$\frac{\|s - s^{(2)}\|}{\|s\|} \simeq 0.3586. \quad (2.100)$$

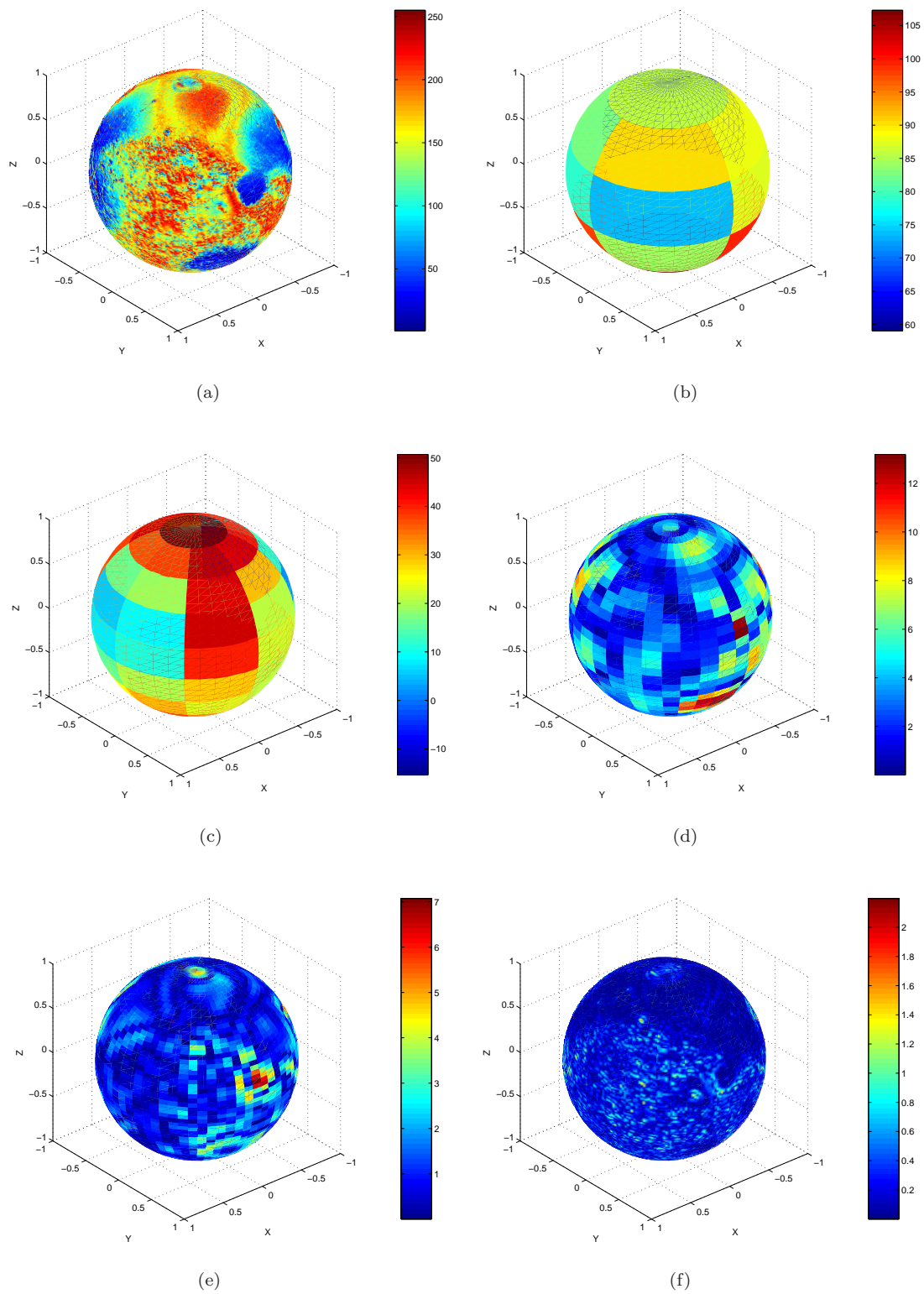


Figure 2.6: Spherical frame decomposition of Mars map: (a) original data (Mars map) (512×512 equi-angular grid), (b) $\mathcal{W}_2[p, q]$, (c) $\mathcal{W}_3[p, q]$, (d) $\mathcal{W}_5[p, q]$, (e) $\mathcal{W}_7[p, q]$, (f) $\mathcal{W}_8[p, q]$.

The reconstructed signal and the amplitude of the error of it is shown on Figures 2.7(c) and 2.7(d), respectively.

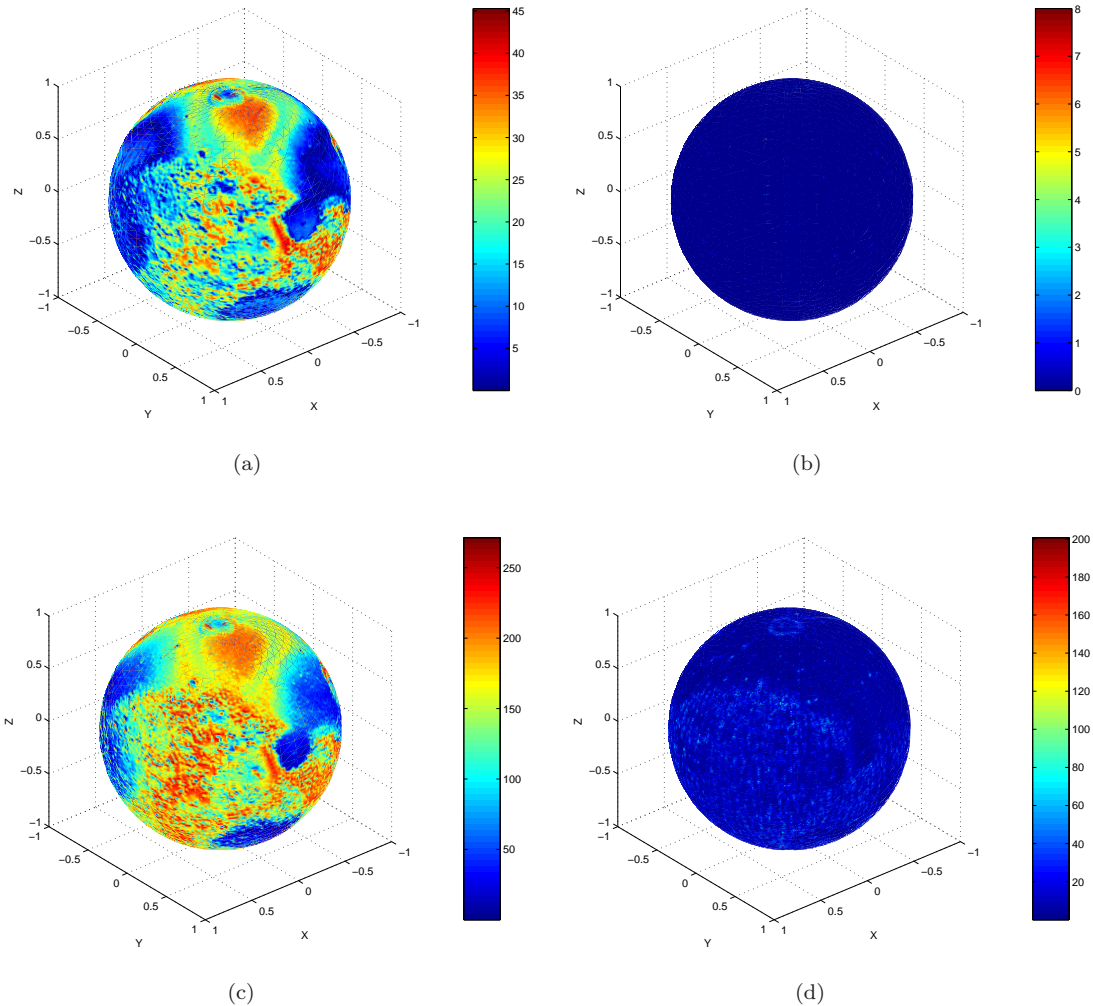


Figure 2.7: Spherical frame reconstruction of the Mars map: (a) approximate reconstruction (by inverse spherical wavelet frames), (b) amplitude of the error of the reconstruction, (c) by spherical conjugate algorithm, (d) difference between the original and reconstructed signal $s^{(2)}$ obtained by 2 iterations of the conjugate gradient algorithm.

2.5 Laplacian pyramid on the sphere

One of the simple ancestors of the wavelet transform is the *Laplacian Pyramid* (LP). It is a versatile data structure with many attractive features and approaches the wavelet analysis by representing the signal at different scales.

2.5.1 Euclidean Laplacian pyramid

Burt and Adelson introduced it first for Euclidean images in [19]. They implemented a technique for image encoding in which local operators of many scales but identical shape serve as the basis functions. The resulting code elements, which form a self-similar structure, are localized in both space and spatial frequency. We use the term *Euclidean Laplacian Pyramid* for it and briefly sketch it here.

The first step in it is to low-pass the original image I_0 and so obtain the image I_1 . Filtering is performed by a procedure equivalent to convolution with one of a family of local, symmetric weighted functions. An important member of this family resembles the Gaussian probability distribution, so the sequence of images I_0, I_1, \dots, I_n is called *Gaussian pyramid*. The image I_0 is the bottom or zero level of the Gaussian pyramid. Pyramid level 1 contains image I_1 , which is a reduced (or low-pass filtered) version of I_0 . Each value within level 1 is computed as a weighted average of values in level 0 within a $n \times n$ window. The size of this window is not crucial but must be selected so that it provides adequate filtering at low computational cost. Each value within level 2, representing I_2 , is then obtained from values within level 1 by applying the same pattern of weights:

$$I_l(i, j) = \sum_{m=-2}^2 \sum_{n=-2}^2 w(m, n) I_{l-1}(2i + m, 2j + n), \quad (2.101)$$

where $0 < l < N$, $0 \leq i < C_l$ and $0 \leq j < R_l$. The pyramid is of level N . Note that the same $n \times n$ pattern of weights w is used to generate each pyramid array from its predecessor. This weighting pattern, called *generating kernel*, is chosen for simplicity to be separable: $w(m, n) = \hat{w}(m)\hat{w}(n)$. The one-dimensional function, length n , \hat{w} is normalized $\sum_{m=-2}^2 \hat{w}(m) = 1$ and symmetric $\hat{w}(i) = \hat{w}(-i)$ for $i = 0, 1, \dots, \frac{n-1}{2}$.

Iterative pyramid generation is equivalent to convolving the Image I_0 with a set of "equivalent weighting functions" H_l :

$$I_l = H_l \oplus I_0 \quad (2.102)$$

or

$$I_l(i, j) = \sum_{m=-M_l}^{M_l} \sum_{n=-M_l}^{M_l} H_l(m, n) I_0(i2^l + m \cdot j2^l + n). \quad (2.103)$$

The effect of convolving an image with one of the equivalent weighted functions H_l is to blur, or low-pass, the image. The pyramid algorithm reduces the filter band limit by an octave from level to level, and reduces the sample interval by the same factor.

The purpose for constructing the reduced image I_i is that it might serve as a prediction for pixel values in the original image I_0 . To obtain a compressed representation, we encode the error image E_0 which remains when an expanded (low-passed) I_1 is subtracted from I_0 . This image becomes a bottom level of the Laplacian pyramid. The next level is generated by encoding I_1 in the same way. Thus the LP is a sequence of error images E_0, E_1, \dots, E_N . Each is the difference between two levels of the Gaussian pyramid and for $0 \leq l < N$:

$$E_l = I_l - I_{l+1}. \quad (2.104)$$

It is clear that just as we may view the Gaussian pyramid as a set of low-pass filtered copies of the original image, we may view the LP as a set of band-pass filtered copies of the image. The scale of the Laplacian operator doubles from level to level of the pyramid, while the center frequency of the pass-band is reduced by an octave.

The original image can be recovered by expanding and then summing all the levels of the Laplacian pyramid: expand E_N once and add it to E_{N-1} , then expand this image once and add it to

E_{N-2} and so on until level 0 is reached and I_0 is recovered. Actually, this procedure is just reversing the steps in LP generation.

Laplacian pyramid from the Euclidean to the spherical case

Now we will define the LP for a spherical signal. Following the classical (Euclidean) technique and supported by already existing spherical sampling theorem (by the means of Proposition 11) and the spherical correlation theorem (as in Proposition 10), we thus initiate the *Spherical Laplacian Pyramid (SLP)*.

The input spherical signal is defined on an equi-angular grid $\omega \in \mathcal{G}_j$ (equation (2.87)). These grids allow us to perfectly sample any band-limited function $f \in L^2(S^2)$ of bandwidth β_j , i.e. such that $\hat{f}(m, n) = 0$ for all $m > \beta_j$. Moreover, this class of sampling grids is associated to a Fast Spherical Fourier Transform [38]. In general the SLP consists of two operations:

- low-pass filtering - convolution of the spherical data with a Gaussian, and
- down-sampling - reducing the data by 2,

from whose combination we build the LP on the sphere.

2.5.2 Analysis spherical Laplacian pyramid

The forward 2-level Laplacian Pyramid is shown for Mars surface map and depicted on Figure 2.8. The input data is on 512×512 -grid. The first step in the SLP is to low-pass filter the original spherical signal f_0 and thus obtain f_1 . Obviously, f_1 is reduced version of f_0 . In the similar way we form f_2 , as a reduced version of f_1 , and so on. For performing this step we use an axisymmetric low pass filter defined by its Fourier coefficients:

$$\hat{H}_{\sigma_0}(m) = e^{-\sigma_0 m_0}. \quad (2.105)$$

This operation is performed in the Fourier domain for speeding up the computations. Suppose the original data f_0 is bandlimited, i.e. $\hat{f}_0(m, n) = 0, \forall n > B_0$ and sampled on \mathcal{G}_0 . The bandwidth parameter σ_0 is chosen so that the filter is numerically close to a perfect half-band filter $\hat{H}_{\sigma_0}(m) = 0, \forall m > B_0/2$. The sequence of spheres $f_0, f_1, f_2 \dots f_l$ is called *spherical Gaussian pyramid*.

The low pass filtered data is then down-sampled on the nested sub-grid \mathcal{G}_1 , which gives the low-pass channel of our pyramid f_1 . The high-pass channel of the pyramid is computed as usual, that is, by first up-sampling f_1 on the finer grid \mathcal{G}_0 , low-pass filtering it with h_{σ_0} and taking the difference with f_0 . Coarser resolutions are computed by iterating this algorithm on the low-pass channel f_l and scaling the filter bandwidth accordingly, i.e. $\sigma_l = 2^l \sigma_0$.

The spherical Laplacian pyramid is the sequence of "error spheres" $h_0, h_1 \dots h_l$, and each is the difference between two levels of the spherical Gaussian pyramid.

2.5.3 Synthesis spherical Laplacian pyramid

The synthesis of so decomposed Mars surface is a reversion of the steps in the Laplacian pyramid generation. It is represented on Figure 2.9. Actually, the input spherical data can be reconstructed by expanding and summing all the levels of the Laplacian pyramid. Expanding consists of low-pass filtering and up-sampling. In the case of 2-levels SLP, we expand first h_1 and add it to h_0 .

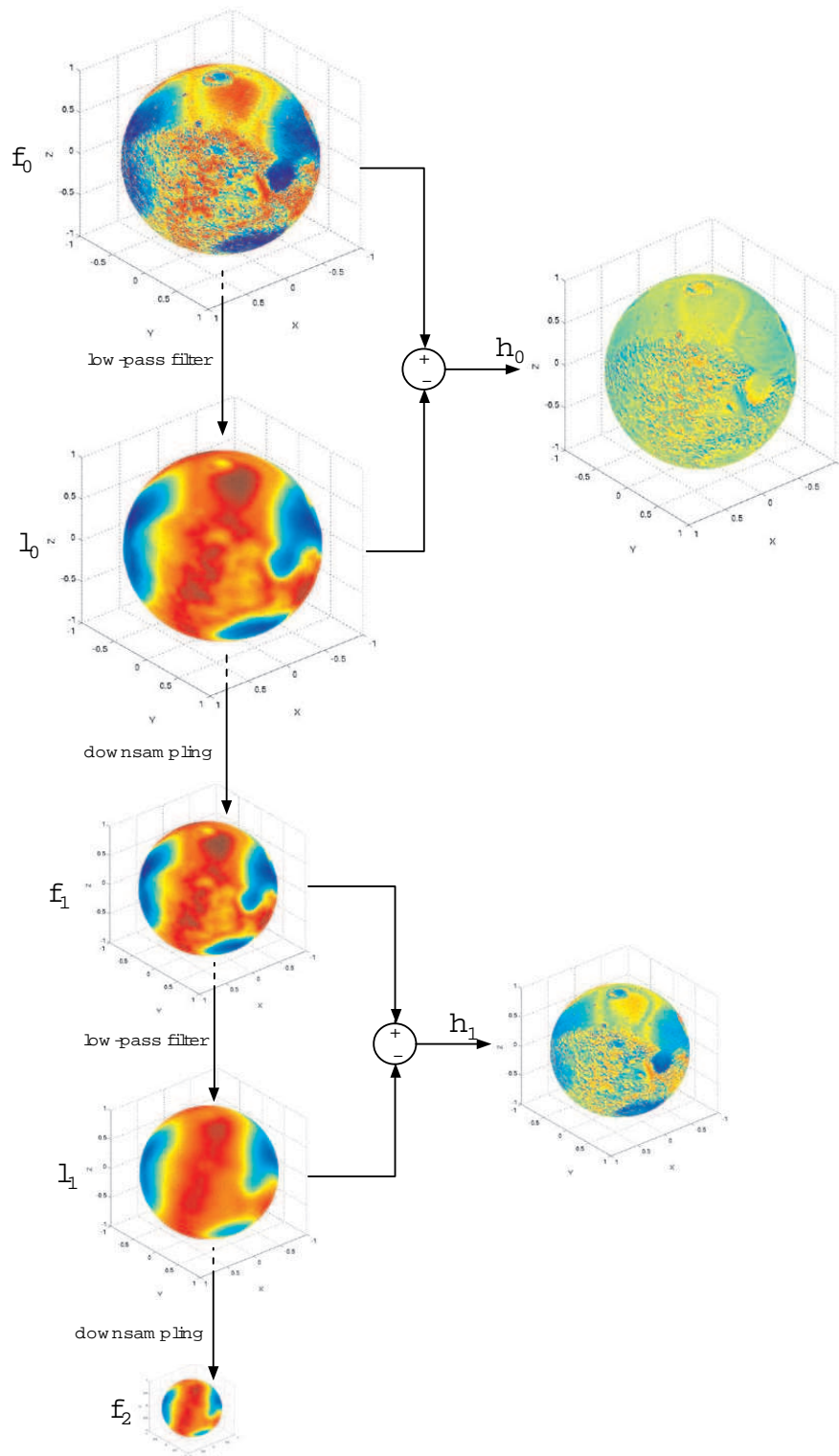


Figure 2.8: Decomposition step of 2 level Spherical Laplacian Pyramid, 512×512 -Mars surface map. The finished pyramid consists of two high-pass bands (h_0, h_1) and the low-pass band (f_2).

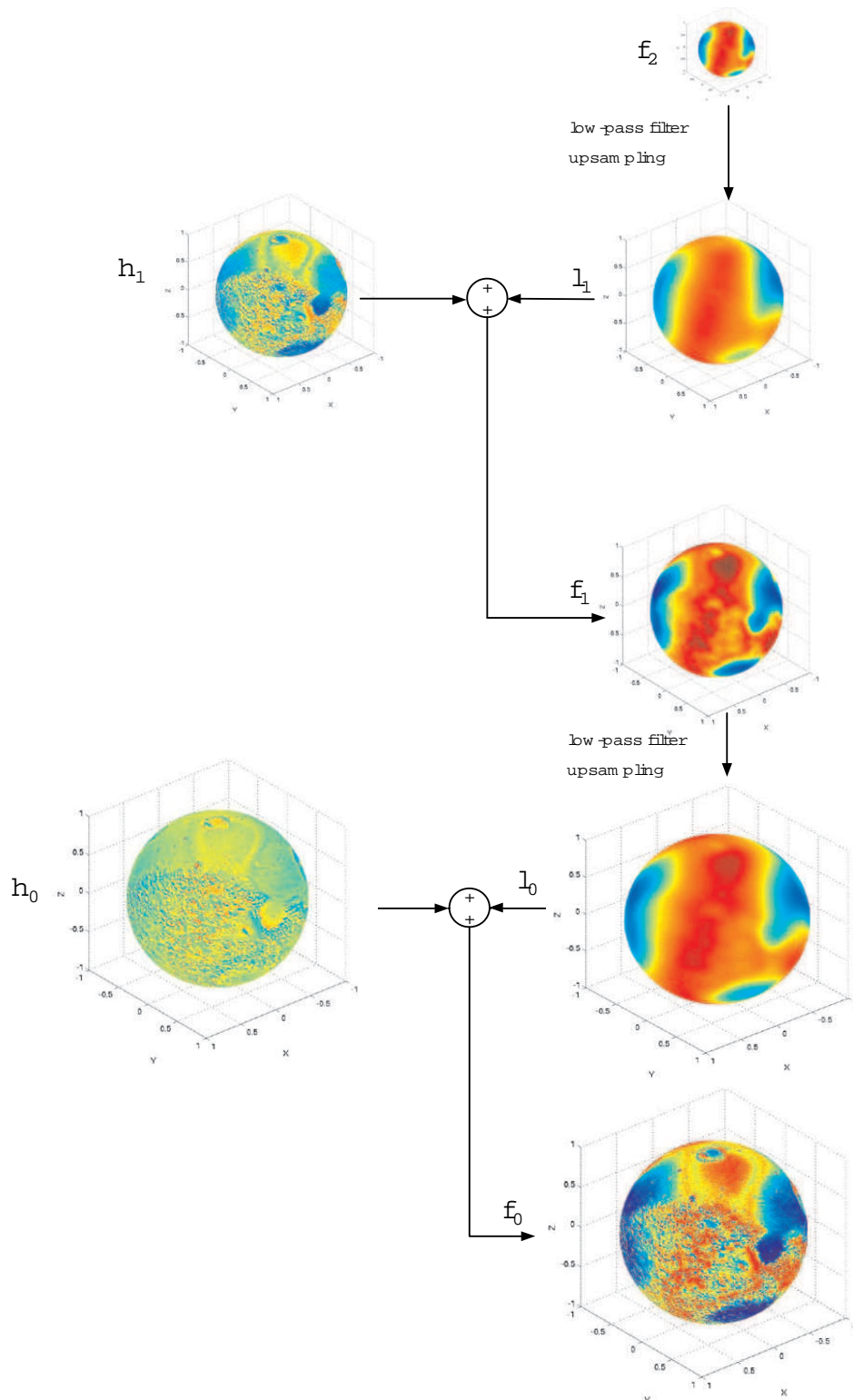


Figure 2.9: Reconstruction step for 2 level Spherical Laplacian Pyramid. The process begins with the two high-pass bands (h_0, h_1) and the low-pass band (f_2), and then perfectly reconstructs the starting sphere f_0 .

2.6 Summary

- The continuous wavelet transform on the sphere has been recalled.
- Half-continuous spherical frames $\mathcal{W}_j(\omega)$ have been derived. They are based on a half-continuous grid, where only the scale is discretized and the position vary continuously. It has been proved that a function $f \in L^2(S^2)$ can be reconstructed from its coefficients $\mathcal{W}_j(\omega)$.
- Complete discretization of the CWT on the sphere has been done. In this case both the scale and the position on the sphere are discretized. It is based on a equi-angular grid of resolution j and of size $2\beta_j \times 2\beta_j$ ($\beta_j \in \mathbb{N}$). The frame $\Psi = \{\psi_{j pq}\}$ controlled by L_ψ^{-1} provides a simple approximate reconstruction formula if the bounds A and B are sufficiently close. An example of spherical wavelet frame decomposition and reconstruction has been provided, where the planet Mars has been used as spherical data.
- A spherical Laplacian pyramid has been proposed. Two main operations are used in this spherical encoding technique: low-pass filtering (smoothing) and down-sampling of a bandlimited spherical signal. The spherical Laplacian pyramid is a sequence of "error spheres" as each is a difference between two levels of low-passed spheres. The original sphere can be recovered by expanding and then summing all the levels of the analyzing spherical Laplacian pyramid. A concrete example of spherical Laplacian pyramid decomposition and reconstruction has been performed on the Mars surface map.

Wavelets on the Hyperboloid

3

In this chapter we enter deeper into the non-Euclidean world. Here we focus on the hyperboloid - a non-Euclidean manifold of negative curvature. We work only in the continuous time-domain and we construct a family of hyperbolic wavelets. For doing this, first we define hyperbolic rotations, motions and a generalized hyperbolic dilation. The latter consists of conic projection and flattening. Then, the continuous wavelet transform on the hyperboloid is obtained by convolution of the scaled wavelets with the signal. This wavelet transform is proved to be invertible whenever the hyperbolic wavelets satisfy a particular admissibility condition. We give illustrative examples for both the hyperbolic wavelet and the hyperbolic wavelet transform. Finally, we discuss the limit at big curvature radiuses.

3.1 Motivation

Although the sphere is a manifold most desirable for applications, the mathematical analysis made so far invites us to consider other manifolds with similar geometrical properties. Among them, the two-sheeted hyperboloid H^2 stands as a very interesting case.

In fact, the negatively curved geometries, of which the hyperbolic non-Euclidean geometry is the prototype, have profound applications to the study of complex variables, to the topology of two- and three-dimensional manifolds, to the study of finitely presented infinite groups, to physics,... For instance, in quantum mechanics such a manifold may be a particular example of a phase space [33, 34]. Other examples come from physical systems constrained on a hyperbolic manifold, for instance, an open expanding model of the universe; or it can be viewed as the phase-space for the motion of a free particle in 1 + 1-anti de Sitter space-time. A completely different example of application is provided by the emerging field of catadioptric image processing [53, 24]. In this case, a normal (flat) sensor is overlooking a curved mirror in order to obtain an omnidirectional picture of the physical scene. An efficient system is obtained using a hyperbolic mirror, since it has a single effective viewpoint. Finally, from a purely conceptual point of view, having already built the CWT for data analysis in Euclidean spaces and on the sphere, it is natural to raise the question of its

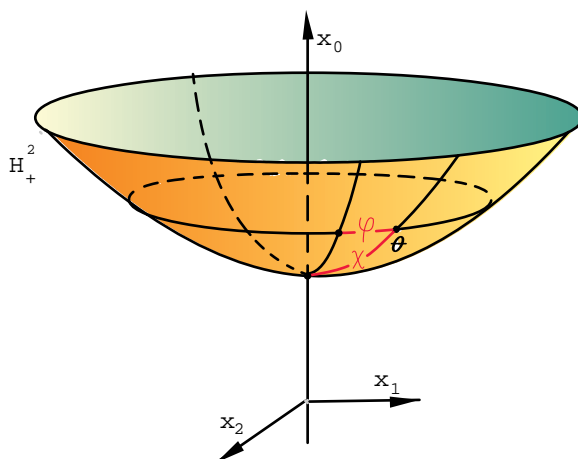


Figure 3.1: Geometry of the 2-hyperboloid.

existence and form on the dual manifold.

3.2 Geometry of the two-sheeted hyperboloid

The non-Euclidean geometry of Gauss, Lobachevsky and Bolyai is usually called hyperbolic geometry because of one of its natural analytic models: the two-sheeted hyperboloid.

3.2.1 Hyperbolic coordinates

We start by recalling basic facts about the upper sheet of the two-sheeted 2-hyperboloid ($H^2 \in \mathbb{R}^3$) of radius ρ , $H_{+\rho}^2$. Let χ, φ be a system of polar coordinates for $H_{+\rho}^2$. To each point $\theta = (\chi, \varphi)$ we shall associate the vector $x = (x_0, x_1, x_2)$ of \mathbb{R}^3 given by

$$\begin{aligned} x_0 &= \rho \cosh \chi, \\ x_1 &= \rho \sinh \chi \cos \varphi, \quad \rho > 0, \quad \chi \geq 0, \quad 0 \leq \varphi < 2\pi, \\ x_2 &= \rho \sinh \chi \sin \varphi, \end{aligned}$$

where $\chi \geq 0$ is the arc length from the pole to the given point on the hyperboloid, while φ is the arc length over the equator, as shown in Figure 3.1. The meridians ($\varphi = \text{const}$) are geodesics. The squared metric element in hyperbolic coordinates is:

$$(ds)^2 = -\rho^2 \left((d\chi)^2 + \sinh^2 \chi (d\varphi)^2 \right), \quad (3.1)$$

called *Lobachevskian metric*, whereas the measure element on the hyperboloid is

$$d\mu = \rho^2 \sinh \chi d\chi d\varphi. \quad (3.2)$$

In the sequel, we shall designate the unit hyperboloid $H_{+\rho=1}^2$ by H_+^2 .

3.2.2 Projective structures

Various projections can be used to endow H_+^2 with a local Euclidean structure. One of them is immediate. It suffices to *flatten* the hyperboloid onto $\mathbb{R}^2 \simeq \mathbb{C}$.

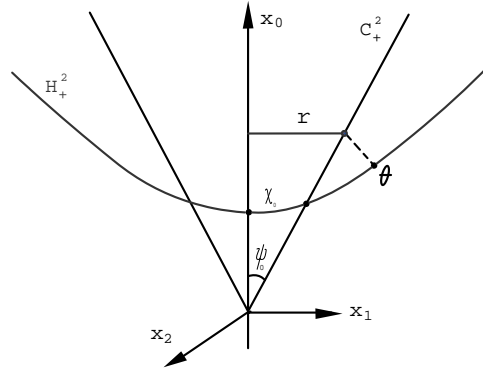


Figure 3.2: Projective structure on the hyperboloid: conic projection

Another possibility is to project the hyperboloid onto a cone. Let us consider a half null cone $C_+^2 \in \mathbb{R}^3$ of equation $(x_0)^2 - \frac{1}{\tan^2 \psi_0}((x_1)^2 + (x_2)^2) = 0, x_0 \geq 0$. This cone C_+^2 has Euclidean nature (metric (3.1) vanishes). The cone surface unrolled is a circular sector. All points of H_+^2 will be mapped onto C_+^2 using a specific conic projection. The characteristic parameter of this conic projection is the constant of the cone $m = \cos \psi_0$, where ψ_0 is the Euclidean angle of inclination of the generatrix of the cone as shown in Figure 3.2. The relation with the hyperbolic angle χ_0 of the parallel intersecting the cone and ψ_0 is :

$$\cos \psi_0 = \frac{1}{\sqrt{1 + \tanh^2 \chi_0}} \equiv m.$$

Considering the radial conic projection, it is more convenient to use a radius r defined by the Euclidean distance between the point on the cone, conic projection of the point $(\chi, \varphi) \in H_+^2$, and the x_0 -axis:

$$r = f(\chi), \quad dr = f'(\chi)d\chi \quad \text{with} \quad \left. \frac{dr}{d\chi} \right|_{\chi=0} = 1. \quad (3.3)$$

Each suitable projection is determined by a specific choice of $f(\chi)$. It is clear that dilation of the cone $C_+^2 \mapsto aC_+^2 = C_+^2$ entails $r \mapsto ar$. Consequently, the resulting map $\chi \mapsto \chi_a$ is determined by $f(\chi_a) = a \cdot f(\chi)$. This is precisely the point at the heart of our approach for constructing wavelets on the hyperboloid and we shall discuss this in more details in Section 3.3.2.

3.3 Affine transformations on the 2-hyperboloid

We recall that our purpose is to build a total family of functions in $L^2(H_+^2, d\mu)$ by picking a wavelet or probe $\psi(\chi)$ with suitable localization properties and applying on it hyperbolic motions, belonging to the group $SO_0(1, 2)$, supplemented by appropriate dilations

$$\psi(x) \rightarrow \lambda(a, x)\psi(d_{1/a}g^{-1}x) \equiv \psi_{a,g}(x), \quad g \in SO_0(1, 2). \quad (3.4)$$

Dilations d_a will be studied in section 3.3.2. We first start by the hyperbolic rotations and motions

3.3.1 Rotations and motions on the hyperboloid

Hyperbolic rotations and motions, $g \in SO_0(1, 2)$, act on x in the following way. A motion $g \in SO_0(1, 2)$ can be factorized as $g = k_1 h k_2$, where $k_1, k_2 \in SO(2)$, $h \in SO_0(1, 1)$, and the respective

action of k and h are the following

$$k(\varphi_0).x(\chi, \varphi) = \begin{pmatrix} 1 & 0 & 0 \\ 0 & \cos \varphi_0 & -\sin \varphi_0 \\ 0 & \sin \varphi_0 & \cos \varphi_0 \end{pmatrix} \begin{pmatrix} \cosh \chi \\ \sinh \chi \cos \varphi \\ \sinh \chi \sin \varphi \end{pmatrix} \quad (3.5)$$

$$= x(\chi, \varphi + \varphi_0), \quad (3.6)$$

$$h(\chi_0).x(\chi, \varphi) = \begin{pmatrix} \cosh \chi_0 & \sinh \chi_0 & 0 \\ \sinh \chi_0 & \cosh \chi_0 & 0 \\ 0 & 0 & 1 \end{pmatrix} \begin{pmatrix} \cosh \chi \\ \sinh \chi \cos \varphi \\ \sinh \chi \sin \varphi \end{pmatrix} \quad (3.7)$$

$$= x(\chi + \chi_0, \varphi) \quad (3.8)$$

The action of a motion on a point $x \in H_+^2$ is trivial: it displaces (rotates) by an hyperbolic angle $\chi \in \mathbb{R}_+$ (respectively by an angle φ).

3.3.2 Dilations on the hyperboloid

The dilation is a homeomorphism $d_a : H_+^2 \rightarrow H_+^2$ and we require that d_a fulfills the two conditions:

Requirements on the hyperbolic dilation

(i) it monotonically dilates the azimuthal distance between two points on H_+^2 :

$$\text{dist}(d_a(x), d_a(x')), \quad (3.9)$$

where $\text{dist}(x, x')$ is defined by

$$\text{dist}(x, x') = \cosh^{-1}(x \cdot x'), \quad (3.10)$$

and the dot product is the Minkowski product in \mathbb{R}^3 . Note that $\text{dist}(x, x')$ reduces to $|\chi - \chi'|$ when $\varphi = \varphi'$.

(ii) it is homomorphic to the group \mathbb{R}_*^+ :

$$\mathbb{R}_*^+ \ni a \rightarrow d_a, \quad d_{ab} = d_a d_b, \quad d_{a^{-1}} = d_a^{-1}, \quad d_1 = \mathbb{I}_d.$$

It has to be noted that, as opposed to the case of the sphere, attempting to use the conformal group $SO_0(1, 3)$ for describing dilation, our requirements are not satisfied. Here we adopt an alternative procedure that describes different maps for dilating the hyperboloid.

To dilate the hyperboloid we must endow it with Euclidean structure so that the Euclidean dilation can be applied on it. There are different possibilities for projections of the hyperboloid. To each of them corresponds a specific scheme for hyperbolic dilation.

Dilation on hyperboloid through conic projection

Considering the half null-cone of equation

$$C_+^2 = \left\{ \xi \in \mathbb{R}^3 : \xi \cdot \xi = \xi_0^2 - \xi_1^2 - \xi_2^2 = 0, \quad \xi_0 > 0 \right\}, \quad (3.11)$$

there exist the $SO_0(1, 2)$ -motions and the obvious Euclidean dilations

$$\xi \in C_+^2 \rightarrow a\xi \in C_+^2 \equiv d_a^{C_+^2}(\xi), \quad (3.12)$$

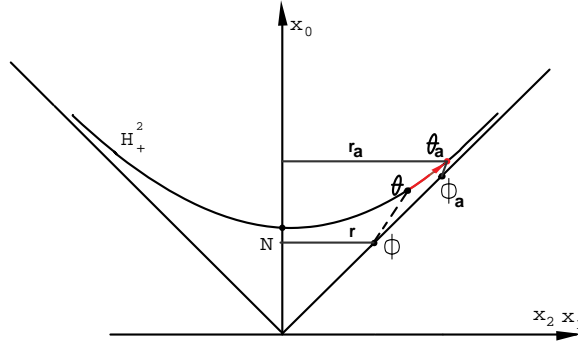


Figure 3.3: Cross-section of a conic projection of the hyperboloid and the action of the dilation through it.

which form a multiplicative one parameter group isomorphic to \mathbb{R}_*^+ .

In order to lift the dilation (3.12) back to H_+^2 , it is natural to use possible *conic projections* of H_+^2 onto C_+^2

$$H_+^2 \ni x \rightarrow \Phi(x) \in C_+^2, \quad (3.13)$$

as it was previously mentioned. Then, we might wish to find a form of the radial conic projection (initially defined in (3.3)), Φ , such that expressed in polar coordinates, the measure is

$$d\mu = r dr d\varphi. \quad (3.14)$$

In this way, dilating r will quadratically dilate the measure $d\mu$ as well. By expressing the measure (3.14) with the radius defined in (3.3) we obtain

$$f(\chi)f'(\chi) = \sinh \chi \implies f(\chi) = 2 \sinh \frac{\chi}{2}. \quad (3.15)$$

Consequently, the radius of the conic projection is

$$r = 2 \sinh \frac{\chi}{2} \quad (3.16)$$

Thus, the conic projection $\Phi : H_+^2 \rightarrow C_+^2$ is a bijection given by

$$\Phi(x) = 2 \sinh \frac{\chi}{2} e^{i\varphi},$$

with $x \equiv (\chi, \varphi)$, $\chi \in \mathbb{R}_+$, $0 \leq \varphi < 2\pi$. The action of Φ is depicted in Figure 3.3. Then, the lifted dilation is of the form

$$\sinh \frac{\chi_a}{2} = a \sinh \frac{\chi}{2}. \quad (3.17)$$

Dilation through flattening

If we chose to use flattening as projective structure, then we have

$$H_+^2 \ni x = x(\chi, \varphi) \rightarrow \Pi_0 \Phi(x) = \sinh \chi e^{i\varphi} \in \mathbb{C}, \quad (3.18)$$

where Π_0 stands for flattening defined by

$$\Pi_0 \Phi(x) : x(r, \varphi) \in C_+^2 \mapsto r \cdot e^{i\varphi} \in \mathbb{C}. \quad (3.19)$$

The invariant metric and measure on H_+^2 , respectively (3.1) and (3.2), are then transformed into

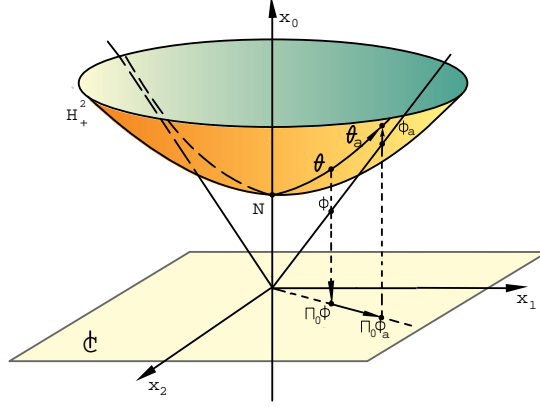


Figure 3.4: Action of a dilation a on the hyperboloid H_+^2 by “flattening”.

$$(ds)^2 \rightarrow \cosh^2 \chi (d\chi)^2 - \sinh^2 \chi (d\varphi)^2, \quad (3.20)$$

$$d\mu(\chi, \varphi) \rightarrow \frac{\sinh \chi \cosh \chi}{\sqrt{1 + \sinh^2 \chi}} d\chi d\varphi. \quad (3.21)$$

In polar coordinates r, φ , the measure (3.14) reads

$$d\mu(r, \varphi) = \frac{r}{\sqrt{1 + r^2}} dr d\varphi. \quad (3.22)$$

The action of dilation by flattening is depicted in Figure 3.4 and it is of the form

$$\sinh \chi_a = a \sinh \chi. \quad (3.23)$$

Generalized hyperbolic dilation: conic projection and flattening

The two preceding situations lead us to consider one generalization, namely, we consider the following family of projections indexed by a positive parameter p :

$$H_+^2 \ni x = x(\chi, \varphi) \rightarrow \Pi_0 \Phi(x) = \frac{1}{p} \sinh p\chi e^{i\varphi} = r e^{i\varphi} \in \mathbb{C}. \quad (3.24)$$

Flattening reveals the Euclidean nature of the conic projection and the full action of (3.24) is depicted on Figure 3.5. Thus, for one particular case $p = \frac{1}{2}$, the conic projection $\Phi : H_+^2 \rightarrow \mathbb{C}_+^2$ is a bijection which, after flattening, is given by

$$\Pi_0 \Phi(x) = 2 \sinh \frac{\chi}{2} e^{i\varphi}. \quad (3.25)$$

The action of Φ for different values of the parameter p is depicted on Figure 3.6. The invariant metric and measure on H_+^2 , respectively (3.1) and (3.2), are then transformed into

$$(ds)^2 \rightarrow - \left(\frac{1}{1 + p^2 r^2} (dr)^2 + \frac{1}{4} (\varpi(r)^2 + (\varpi(r))^{-2} - 2) (d\varphi)^2 \right), \quad (3.26)$$

$$d\mu(\chi, \varphi) \rightarrow \frac{1}{2} \frac{\varpi(r) - (\varpi(r))^{-1}}{\sqrt{1 + p^2 r^2}} dr d\varphi, \quad (3.27)$$

where $\varpi(r) = \sqrt[1/p]{pr + \sqrt{1 + p^2 r^2}}$. This also shows that so defined class of dilations is not conformal. The action of dilation in this general case is given by

$$\sinh p\chi_a = a \sinh p\chi \quad (3.28)$$

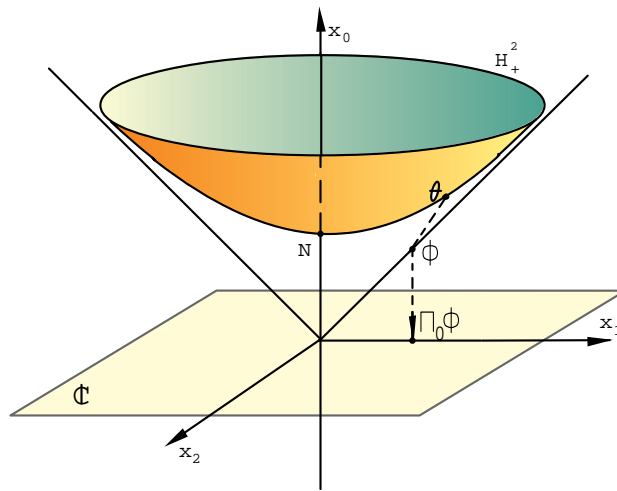


Figure 3.5: Conic projection and flattening.

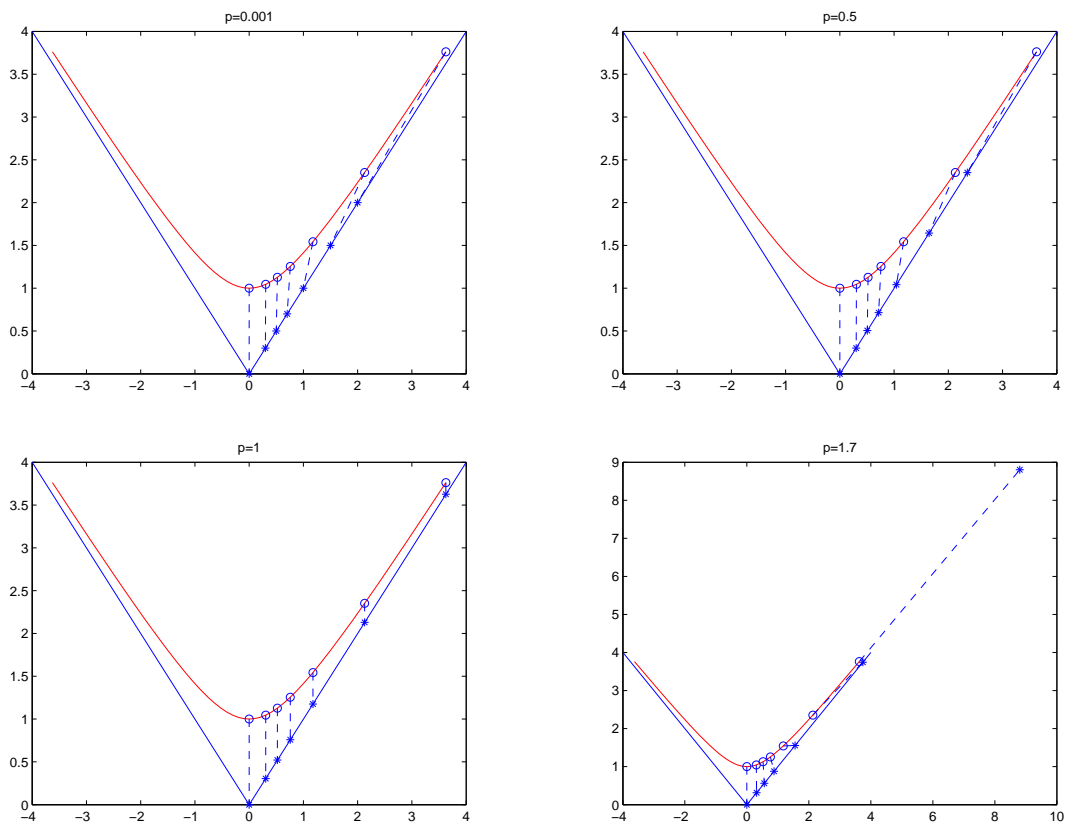


Figure 3.6: Cross-section of conic projection for different parameter p .

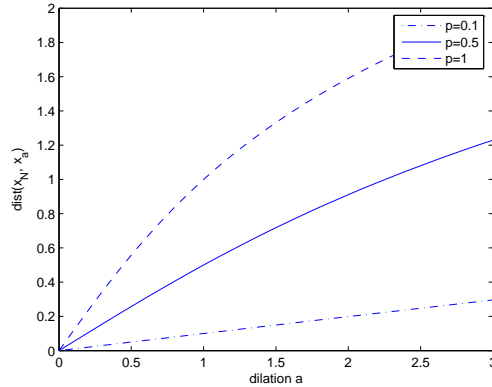


Figure 3.7: Analysis of the distance (3.9) as a function of dilation a , with x_N being the North Pole and using conic projection for different parameter p .

For any of the values of parameter p the dilated point $x_a \in H_+^2$ is

$$x_a = (\cosh \chi_a, \sinh \chi_a \cos \varphi, \sinh \chi_a \sin \varphi), \quad (3.29)$$

with polar coordinates $\theta_a \equiv (\chi_a, \varphi)$. The behavior of $\text{dist}(x_N, x_a)$ with x_N being the North Pole, in the case $p = 0.1$, $p = 0.5$ and $p = 1$, is shown in Figure 3.7. We can immediately see that in all cases this is an increasing function with respect to the dilation a .

Dilation through stereographic projection

It is also interesting to compute the action of dilations in the bounded version of H_+^2 . The latter is obtained by applying the stereographic projection from the South Pole of H^2 and it maps the upper sheet H_+^2 onto the open unit disc in the equatorial plane:

$$x = x(\chi, \varphi) \rightarrow \Phi(x) = \tanh \frac{\chi}{2} e^{i\varphi}. \quad (3.30)$$

In the case $p = 0.5$, using (3.17) and basic trigonometric relations we obtain

$$\tanh \frac{\chi_a}{2} = \sqrt{\frac{a^2 \tanh^2 \frac{\chi}{2}}{1 + (a^2 - 1) \tanh^2 \frac{\chi}{2}}} \equiv \zeta. \quad (3.31)$$

In this case, the dilation leaves invariant both $\zeta = 0$ and $\zeta = 1$, the center and the border of the disc, respectively. Figure 3.8 depicts the action of this transformation on a point $x \in H_+^2$. A hyperbolic dilation from the North Pole (D_N) is considered as a dilation in the unit disc in equatorial plane and lifted back to H_+^2 by inverse stereographic projection from the South Pole. A dilation from any other point $x \in H_+^2$ is obtained by moving $x \in H_+^2$ to the North Pole by a rotation $g \in SO_0(1, 2)$, performing dilation D_N and going back by inverse rotation:

$$D_x = g^{-1} D_N g.$$

The visualization of the dilation on the hyperboloid H_+^2 with $p = 0.5$ is provided in Figure 3.9. There, each circle represents points on the hyperboloid at constant χ and is dilated by the scale factor $a = 0.75$.

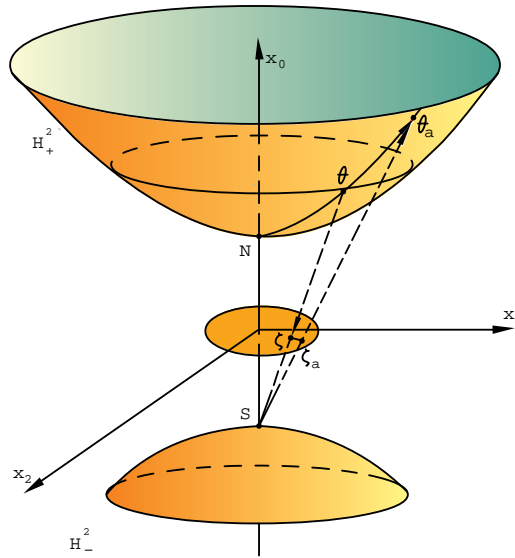


Figure 3.8: Action of a dilation a on the hyperboloid H_{\pm}^2 through a stereographic projection.

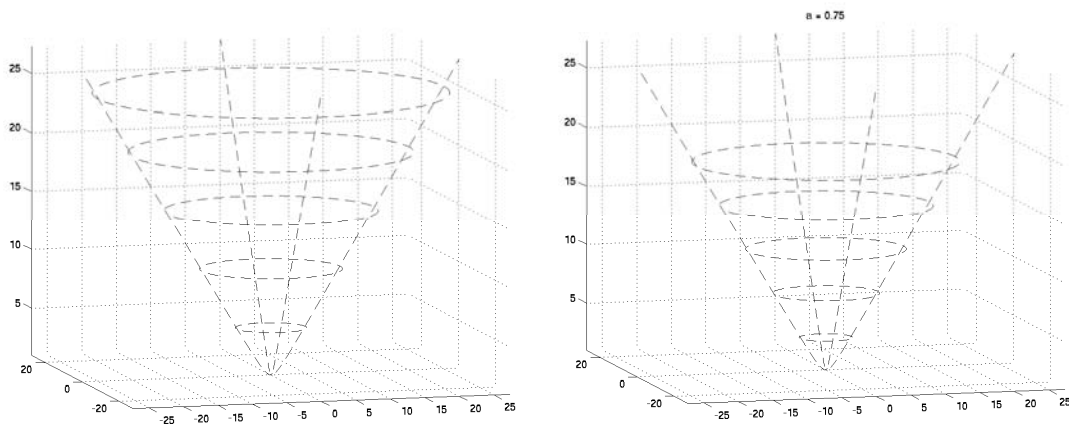


Figure 3.9: Visualization of the dilation on a hyperboloid H_+^2 .

3.4 Harmonic analysis on the 2-hyperboloid

3.4.1 Fourier-Helgason Transform

This integral transform is the precise analog of the Fourier-Plancherel transform on \mathbb{R}^n [5]. It consists of an isometry between two Hilbert spaces

$$\mathcal{FH} : L^2(H_+^2, d\mu) \longrightarrow L^2(\mathcal{L}, d\eta), \quad (3.32)$$

where the measure $d\mu$ is the $SO_0(1, 2)$ -invariant measure on H_+^2 and $L^2(\mathcal{L}, d\eta)$ denotes the Hilbert space of sections of a line-bundle \mathcal{L} over another suitably defined manifold, the so-called Helgason-dual of H_+^2 and denoted by Ξ . We note here that the Helgason-dual of \mathbb{R}^n is just its own dual.

Let us see what is the concrete realization of the dual space Ξ . In fact Ξ can be realized as the *projective half null-cone*, as defined in (3.11) and asymptotic to H_+^2 , times the positive real line. The space Ξ is given by

$$\Xi = \mathbb{R}_+ \times \mathbb{PC}_+ \equiv \{k = (\nu, \vec{\xi})\}, \quad (3.33)$$

where \mathbb{PC}_+ denotes the projective forward cone $\{\xi \in C_+^2 \mid \lambda\xi \equiv \xi, \lambda > 0, \xi_0 > 0\}$ (the set of ‘‘rays’’ on the cone). A convenient realization of \mathbb{PC}_+ makes it diffeomorphic to the 1-sphere S^1 as follows

$$\mathbb{PC}_+ \simeq \{\vec{\xi} \in \mathbb{R}^2 : \|\vec{\xi}\| = 1\} \sim S^1 \quad (3.34)$$

$$\xi \equiv (\xi_0, \vec{\xi}) = (\xi_0, \xi_1, \xi_2) \mapsto \frac{1}{\xi_0} \vec{\xi}. \quad (3.35)$$

The Fourier - Helgason transform, is defined in an way similar to the ordinary Fourier transform by using the eigenfunctions of the invariant differential operator of second order, i.e. the Laplacian on H_+^2 . In our case, the functions of the (unique) invariant differential operator (the Laplacian) are named *hyperbolic plane waves* [16]

$$\mathcal{E}_{\nu, \xi}(x) = (\xi \cdot x)^{-\frac{1}{2} - i\nu}, \quad \xi \in C_+^2, \nu \in \mathbb{R}_+. \quad (3.36)$$

These waves are not parameterized by points of $\mathbb{R}_+ \times \mathbb{PC}_+$ but rather by points of $\mathbb{R}_+ \times C_+^2$; however the action of \mathbb{R}_+ on C_+^2 just rescales them by a factor which is constant in $x \in H_+^2$. In other words, they are sections of an appropriate line bundles over Ξ , which we denote by \mathcal{L} and C_+^2 is thought of as total space of \mathbb{R}_+ over \mathbb{PC}_+ . As well, we note that the inner product $\xi \cdot x$ is positive on the product space $C_+^2 \times H_+^2$, so that the complex exponential is uniquely defined.

Let us express the plane waves in polar coordinates for a point $x \equiv (x_0, \vec{x}) \in H_+^2$

$$\mathcal{E}_{\nu, \xi}(x) = (\xi \cdot x)^{-\frac{1}{2} - i\nu} \quad (3.37)$$

$$\equiv \left(\cosh \chi - \frac{\vec{\xi} \cdot \vec{x}}{\xi_0} \right)^{-\frac{1}{2} - i\nu} \quad (3.38)$$

$$= (\cosh \chi - (\hat{n} \cdot \hat{x}) \sinh \chi)^{-\frac{1}{2} - i\nu}, \quad (3.39)$$

where $\hat{n} \in S^1$ is a unit vector in the direction of $\vec{\xi}$ and $\hat{x} \in S^1$ is the unit vector in the direction of \vec{x} . Applying any rotation $\varrho \in SO(2) \subset SO_0(1, 2)$ on this wave, it immediately follows

$$R(\varrho) : \mathcal{E}_{\nu, \xi}(x) \rightarrow \mathcal{E}_{\nu, \xi}(\varrho^{-1} \cdot x) = \mathcal{E}_{\nu, \varrho \cdot \xi}(x). \quad (3.40)$$

Finally, the Fourier - Helgason transform \mathcal{FH} and its inverse \mathcal{FH}^{-1} are defined as

$$\hat{f}(\nu, \xi) \equiv \mathcal{FH}[f](\nu, \xi) = \int_{H_+^2} f(x) (x \cdot \xi)^{-\frac{1}{2} + i\nu} d\mu(x), \quad \forall f \in \mathcal{C}_0^\infty(H_+^2), \quad (3.41)$$

$$\mathcal{FH}^{-1}[g](x) = \int_{\mathbf{j}\Xi} g(\nu, \xi) (x \cdot \xi)^{-\frac{1}{2} - i\nu} d\eta(\nu, \xi), \quad \forall g \in \mathcal{C}_0^\infty(\mathcal{L}), \quad (3.42)$$

where $C_0^\infty(\mathcal{L})$ denotes the space of compactly supported smooth sections of the line-bundle \mathcal{L} . The integration in (3.42) is performed along any smooth embedding $\mathbf{j}\Xi$ into the total space of the line-bundle \mathcal{L} and the measure $d\eta$ is given by

$$d\eta(\nu, \xi) = \frac{d\nu}{|\mathbf{c}(\nu)|^2} d\sigma_0, \quad (3.43)$$

with $\mathbf{c}(\nu)$ being the Harish-Chandra \mathbf{c} -function [41]

$$\mathbf{c}(\nu) = \frac{2^{i\nu}\Gamma(1)\Gamma(i\nu)}{\sqrt{\pi}\Gamma(\frac{1}{2} + i\nu)}. \quad (3.44)$$

The factor $|\mathbf{c}(\nu)|^{-2}$ can be simplified to

$$|\mathbf{c}(\nu)|^{-2} = \nu \sinh(\pi\nu) |\Gamma(\frac{1}{2} + i\nu)|^2. \quad (3.45)$$

The 1-form $d\sigma_0$ in the measure (3.43) is defined on the null cone C_+^2 , it is closed on it and hence the integration is independent of the particular embedding of Ξ . Thus, such an embedding can be the following

$$\mathbf{j} : \Xi \longrightarrow \mathbb{R}_+ \times C_+^2 \quad (3.46)$$

$$(\nu, \xi) \longmapsto (\nu, (1, \frac{\xi_1}{\xi_0}, \frac{\xi_2}{\xi_0})) = (\nu, (1, \hat{\xi})) \quad (3.47)$$

Note that the transform \mathcal{FH} maps functions on H_+^2 to sections of \mathcal{L} and the inverse transform maps sections to functions. Thus, we have

Proposition 21. [41] *The Fourier - Helgason transform defined in equations (3.41, 3.42) extends to an isometry of $L^2(H_+^2, d\mu)$ onto $L^2(\mathcal{L}, d\eta)$ so that we have*

$$\int_{H_+^2} |f(x)|^2 d\mu(x) = \int_{\mathbf{j}\Xi} |\hat{f}(\xi, \nu)|^2 d\eta(\xi, \nu). \quad (3.48)$$

3.5 Continuous Wavelet Transform on the Hyperboloid

One way of constructing the CWT on the hyperboloid H_+^2 would be to find a suitable group containing both $SO_0(1, 2)$ and the group of dilations, and then find its square-integrable representations in the Hilbert space $\psi \in L^2(H_+^2, d\mu)$, where $d\mu$ is the normalized $SO_0(1, 2)$ -invariant measure on H_+^2 . We will take another approach by directly studying the following wavelet transform

$$\int \overline{\psi_{a,g}(x)} f(x) d\mu(x) = \langle \psi_{a,g} | f \rangle,$$

where the notation $\psi_{a,g}$ has been introduced in (3.4) and will be now made more precise in terms of group representation. Looking at pseudo-rotations (motions) only, we have the unitary action :

$$[\mathcal{U}_g \psi](x) = f(g^{-1}x), \quad g \in SO_0(1, 2), \quad \psi \in L^2(H_+^2, d\mu), \quad (3.49)$$

where \mathcal{U}_g is a quasi-regular representation of $SO_0(1, 2)$ on $L^2(H_+^2)$.

We now have to incorporate the dilation. However, the measure $d\mu$ is not dilation invariant, so that a Radon-Nikodym derivative $\lambda(g, x)$ must be inserted, namely:

$$\lambda(a, x) = \frac{d\mu(a^{-1}x)}{d\mu(x)}, \quad a \in \mathbb{R}_*^+. \quad (3.50)$$

The function λ is a 1-cocycle and satisfies the equation

$$\lambda(a_1 a_2, x) = \lambda(a_1, x) \lambda(a_2, a_1^{-1} x). \quad (3.51)$$

In the case of dilating the hyperboloid through generalized projection with parameter $p > 0$, we have

$$\lambda(a, \chi) = \frac{d \cosh \chi_{1/a}}{d \cosh \chi} = \frac{1}{a} \frac{\sinh \chi_{1/a}}{\sinh \chi} \frac{\cosh p\chi}{\cosh p\chi_{1/a}}, \quad (3.52)$$

with $\sinh p\chi_{1/a} = \frac{1}{a} \sinh p\chi$. Note here that the case $p = \frac{1}{2}$ is unique in the sense that $\lambda(a, \chi)$ does not depend on χ : $\lambda(a, \chi) = a^{-2}$. In the case $p = 1$, we get the more elaborate expression

$$\lambda(a, \chi) = \frac{d \cosh \chi_{1/a}}{d \cosh \chi} = \frac{\cosh \chi}{a^2 \sqrt{1 + a^{-2} \sinh^2 \chi}}. \quad (3.53)$$

Thus, the action of the dilation operator on the function is

$$D_a \psi(x) \equiv \psi_a(x) = \lambda^{\frac{1}{2}}(a, \chi) \psi(d_a^{-1} x) = \lambda^{\frac{1}{2}}(a, \chi) \psi(x_{\frac{1}{a}}) \quad (3.54)$$

with $x_a \equiv (\chi_a, \varphi) \in H_+^2$ and it reads

$$\psi_a(x) = \sqrt{\frac{1}{a} \frac{\sinh \chi_{1/a}}{\sinh \chi} \frac{\cosh p\chi}{\cosh p\chi_{1/a}}} \psi(x_{\frac{1}{a}}). \quad (3.55)$$

Finally, the *hyperbolic wavelet function* can be written as

$$\psi_{a,g}(x) = \mathcal{U}_g D_a \psi(x) = \mathcal{U}_g \psi_a(x).$$

Accordingly, the *hyperbolic continuous wavelet transform* of a signal (function) $f \in L^2(H_+^2)$ is defined as:

$$W_f(a, g) = \langle \psi_{a,g} | f \rangle \quad (3.56)$$

$$= \int_{H_+^2} \overline{[\mathcal{U}_g D_a \psi](x)} f(x) d\mu(x) \quad (3.57)$$

$$= \int_{H_+^2} \overline{\psi_a(g^{-1}x)} f(x) d\mu(x) \quad (3.58)$$

where $x \equiv (\chi, \varphi) \in H_+^2$ and $g \in SO_0(1, 2)$.

In the next section, we show that this expression can be conveniently interpreted and studied as a hyperbolic convolution.

3.5.1 Convolution on the hyperboloid

Since H_+^2 is a homogeneous space of $SO_0(1, 2)$, one can easily define a convolution. Indeed, let $f \in L^2(H_+^2)$ and $s \in L^1(H_+^2)$, their *hyperbolic convolution* is the function of $g \in SO_0(1, 2)$ defined as

$$(f * s)(g) = \int_{H_+^2} f(g^{-1}x) s(x) d\mu(x). \quad (3.59)$$

Then $f * s \in L^2(SO_0(1, 2), dg)$, where dg stands for the left Haar measure on the group and

$$\|f * s\|_2 \leq \|f\|_2 \|s\|_1, \quad (3.60)$$

by the Young convolution inequality.

Let us deal with a simpler definition where the convolution is a function defined on H_+^2 . Let $[\cdot] : H_+^2 \longrightarrow SO_0(1, 2)$ be a section in the fiber bundle defined by the group and its homogeneous space. In the following we will make use of the *Euler section*, whose construction is now presented. Recall from Section 3.3.1 that any $g \in SO_0(1, 2)$ can be uniquely decomposed as a product of three elements $g = k(\varphi)h(\chi)k(\psi)$. Using this parametrization, we thus define :

$$\begin{aligned} [\cdot] & : H_+^2 \longrightarrow SO_0(1, 2) \\ [\cdot] & : x(\chi, \varphi) \mapsto g = k(\varphi)h(\chi) \end{aligned}$$

The hyperbolic convolution, restricted to H_+^2 , thus takes the following form:

$$(f * s)(y) = \int_{H_+^2} f([y]^{-1}x)s(x)d\mu(x), \quad y \in H_+^2$$

We will mostly deal with convolution kernels that are axisymmetric (or rotation invariant) functions on H_+^2 (i.e. functions of the variable χ alone). The Fourier-Helgason transform of such an element has a simpler form as shown by the following proposition.

Proposition 22. *If f is a rotation invariant function, i.e. $f(\varrho^{-1}x) = f(x), \forall \varrho \in SO(2)$, its Fourier-Helgason transform $\hat{f}(\xi, \nu)$ is a function of ν alone, i.e. $\hat{f}(\nu)$.*

Proof : Applying the Fourier-Helgason transform on a rotation-invariant function we write:

$$\hat{f}(\xi, \nu) = \int_{H_+^2} f(x) \mathcal{E}_{\xi, \nu}(x) d\mu(x) \quad (3.61)$$

$$= \int_{H_+^2} f(\varrho^{-1}x)(\xi \cdot x)^{-\frac{1}{2}+i\nu} d\mu(x), \quad \xi \in \mathbb{P}C_+, \rho \in SO(2) \quad (3.62)$$

$$= \int_{H_+^2} f(x')(\xi \cdot \varrho x')^{-\frac{1}{2}+i\nu} d\mu(x') \quad (3.63)$$

$$= \hat{f}(\varrho^{-1}\xi, \nu), \quad (3.64)$$

and so $\hat{f}(\xi, \nu)$ does not depend on ξ . ■

We now have all the basic ingredients for formulating a useful convolution theorem in the Fourier - Helgason domain. As we will see now, the Fourier-Helgason transform of a convolution takes a simple form, provided one of the kernels is rotation invariant.

Theorem 23. (Convolution) *Let f and s be two measurable functions with $f, s \in L^2(H_+^2)$ and s be rotation invariant. The convolution $(s * f)(y)$ is in $L^1(H_+^2)$ and its Fourier-Helgason transform satisfies*

$$\widehat{(s * f)}(\nu, \xi) = \hat{f}(\nu, \xi) \hat{s}(\nu). \quad (3.65)$$

Proof : The convolution of s and f is given by:

$$(s * f)(y) = \int_{H_+^2} s([y]^{-1}x)f(x)d\mu(x).$$

Since s is $SO(2)$ -invariant, we write its argument in this equation in the following way :

$$\begin{pmatrix} \cosh \chi & \sinh \chi & 0 \\ \sinh \chi & \cosh \chi & 0 \\ 0 & 0 & 1 \end{pmatrix} \begin{pmatrix} x_0 \\ x_1 \\ 0 \end{pmatrix} = \begin{pmatrix} x_0 \cosh \chi + x_1 \sinh \chi \\ x_0 \sinh \chi + x_1 \cosh \chi \\ 0 \end{pmatrix}, \quad (3.66)$$

where $x = (x_0, x_1, x_2)$ and we used polar coordinates for $y = y(\chi, \varphi)$. On the other hand we can alternatively write this equation in the form :

$$\begin{pmatrix} x_0 \cosh \chi + x_1 \sinh \chi \\ x_0 \sinh \chi + x_1 \cosh \chi \\ 0 \end{pmatrix} = \begin{pmatrix} x_0 & x_1 & 0 \\ x_1 & x_0 & 0 \\ 0 & 0 & 1 \end{pmatrix} \begin{pmatrix} \cosh \chi \\ \sinh \chi \\ 0 \end{pmatrix}. \quad (3.67)$$

Thus we have

$$s([y]^{-1}x) = s([x]^{-1}y). \quad (3.68)$$

Therefore, the convolution with a rotation invariant function is given by

$$(s * f)(y) = \int_{H_+^2} f(x) s([y]^{-1}x) d\mu(x) \quad (3.69)$$

$$= \int_{H_+^2} f(x) s([x]^{-1} \cdot y) d\mu(x). \quad (3.70)$$

On the other hand, applying the Fourier-Helgason transform on $s * f$ we get

$$\begin{aligned} \widehat{(s * f)}(\nu, \xi) &= \int_{H_+^2} (s * f)(y) (y \cdot \xi)^{-\frac{1}{2} + i\nu} d\mu(y) \\ &= \int_{H_+^2} d\mu(y) \int_{H_+^2} d\mu(x) s([y]^{-1}x) f(x) (y \cdot \xi)^{-\frac{1}{2} + i\nu} \\ &= \int_{H_+^2} d\mu(x) f(x) \int_{H_+^2} d\mu(y) s([y]^{-1}x) (y \cdot \xi)^{-\frac{1}{2} + i\nu} \\ &= \int_{H_+^2} d\mu(x) f(x) \int_{H_+^2} d\mu(y) s([x]^{-1}y) (y \cdot \xi)^{-\frac{1}{2} + i\nu} \\ &= \int_{H_+^2} d\mu(x) f(x) \int_{H_+^2} d\mu(y) s(y) ([x]y \cdot \xi)^{-\frac{1}{2} + i\nu} \\ &= \int_{H_+^2} d\mu(x) f(x) \int_{H_+^2} d\mu(y) s(y) (y \cdot [x]^{-1}\xi)^{-\frac{1}{2} + i\nu}. \end{aligned}$$

Since ξ belong to the projective null cone, we can write

$$(y \cdot [x]^{-1}\xi) = ([x]^{-1}\xi)_0 \left(y \cdot \frac{[x]^{-1}\xi}{([x]^{-1}\xi)_0} \right), \quad (3.71)$$

and using $([x]^{-1}\xi)_0 = (x \cdot \xi)$, we finally obtain

$$\begin{aligned} \widehat{(s * f)}(\nu, \xi) &= \int_{H_+^2} d\mu(x) f(x) (x \cdot \xi)^{-\frac{1}{2} + i\nu} \int_{H_+^2} d\mu(y) s(y) \left(y \cdot \frac{[x]^{-1}\xi}{([x]^{-1}\xi)_0} \right)^{-\frac{1}{2} + i\nu} \\ &= \hat{f}(\nu, \xi) \hat{s}(\nu) \end{aligned}$$

where we have used the rotation invariance of s . ■

Based on Theorem 23, we can write the hyperbolic continuous wavelet transform of a function f with respect to an axisymmetric wavelet ψ as

$$W_f(a, g) \equiv W_f(a, [x]) = (\bar{\psi}_a * f)(x). \quad (3.72)$$

3.6 Wavelets on the 2-hyperboloid

We now come to the heart of the theory of wavelets on the hyperboloid : we prove that the hyperbolic wavelet transform is a well-defined invertible map, provided the wavelet satisfy an admissibility condition.

3.6.1 The hyperbolic wavelet admissibility condition

Theorem 24. (Admissibility condition) *Let $\psi \in L^1(H_+^2)$ be an axisymmetric function, $a \mapsto \alpha(a)$ a positive function on \mathbb{R}_*^+ and m, M two constants such that*

$$0 < m \leq \mathcal{A}_\psi(\nu) = \int_0^\infty |\hat{\psi}_a(\nu)|^2 \alpha(a) da \leq M < +\infty. \quad (3.73)$$

Then the linear operator A_ψ defined by :

$$A_\psi f(x') = \int_{\mathbb{R}_*^+} \int_{H_+^2} W_f(a, x) \psi_{a,x}(x') dx \alpha(a) da, \quad (3.74)$$

where $\psi_{a,x} = \psi_{a,[x]}$, is bounded and with bounded inverse. More precisely A_ψ is univocally characterized by the following Fourier - Helgason multiplier :

$$\widehat{A_\psi f}(\nu, \varphi) \equiv \widehat{A_\psi} f(\nu, \varphi) = \hat{f}(\nu, \varphi) \int_0^\infty |\hat{\psi}_a(\nu)|^2 \alpha(a) da = \mathcal{A}_\psi(\nu) \hat{f}(\nu, \varphi).$$

Proof : Let the wavelet transform W_f be defined as in equation (3.72) and consider the following quantity :

$$\Delta_a(x') = \int_{H_+^2} W_f(a, x) \psi_{a,x}(x') dx. \quad (3.75)$$

A close inspection reveals that $\Delta_a(x')$ is itself a convolution. Taking the Fourier - Helgason transform on both sides of (3.75) and applying Theorem 23 twice, we thus obtain:

$$\widehat{\Delta}_a(\nu, \varphi) = |\hat{\psi}_a(\nu)|^2 \hat{f}(\nu, \varphi).$$

Finally, integrating over all scales we obtain :

$$\int_{\mathbb{R}_*^+} \alpha(a) da \widehat{\Delta}_a(\nu, \varphi) = \hat{f}(\nu, \varphi) \int_{\mathbb{R}_*^+} \alpha(a) da |\hat{\psi}_a(\nu)|^2 \quad (3.76)$$

which is the expected result. ■

There are three important remarks concerning this result. First, Theorem 24 shows that the wavelet family $\{\psi_{a,x}, a \in \mathbb{R}_*^+, x \in H_+^2\}$ forms a continuous frame provided the admissibility condition (3.73) is satisfied (in the sense of [3]). In this case, the wavelet transform W_f of any f can be inverted in the following way. Let $\widetilde{\psi}_{a,x}$ be a *reconstruction wavelet* defined by :

$$\widetilde{\psi}_{a,x}(\nu) = \mathcal{A}_\psi^{-1}(\nu) \widehat{\psi}_{a,x}(\nu).$$

As a direct consequence of Theorem 24, the inversion formula, to be understood in the strong sense in $L^2(H_+^2)$, reads :

$$f(x') = \int_{\mathbb{R}_*^+} \int_{H_+^2} W_f(a, x) \widetilde{\psi}_{a,x}(x') dx \alpha(a) da. \quad (3.77)$$

As a second remark, one could check that Theorem 24 does not depend on choice of dilation! This is not exactly true, actually. The *architecture* of the proof does not depend on the explicit form of the dilation operator, but the admissibility condition explicitly depends on it. As we shall see later, it will be of crucial importance when trying to construct admissible wavelets. Finally the third remark concerns the somewhat arbitrary choice of measure $\alpha(a)$ in the formulas. Again, one may easily check that the usual 1-D wavelet theory can be formulated along the same lines, keeping an arbitrary scale measure. In that case though, the choice $\alpha = a^{-2}$ leads to a tight continuous frame, i.e. the frame operator A_ψ is a constant. The situation here is more complicated in the sense that no choice of measure would yield to a tight frame, a particularity shared by the continuous wavelet transform on the sphere [10]. Some choices of measure though lead to simplified admissibility conditions as we will now discuss.

Theorem 25. *Let $a \mapsto \alpha(a)$ be a positive continuous function on \mathbb{R}_*^+ which for large a behaves like $a^{-\beta}$, $\beta > 0$. If D_a is the hyperbolic dilation with parameter p defined by equations (3.24), (3.52) and (3.54), then an axisymmetric, compactly supported, continuous function $\psi \in L^2(H_+^2, d\mu(\chi, \varphi))$ is admissible for all $p > 0$ and $\beta > \frac{2}{p} + 1$. Moreover, if $\alpha(a)da$ is a homogeneous measure of the form $a^{-\beta}da$, then the following zero-mean condition has to be satisfied :*

$$\int_{H_+^2} \psi(\chi, \varphi) \left[\frac{\sinh 2p\chi}{\sinh \chi} \right]^{\frac{1}{2}} d\mu(\chi, \varphi) = 0. \quad (3.78)$$

Proof : Let us assume $\psi(x)$ belongs to $\mathcal{C}_0(H_+^2)$, i.e. it is continuous and compactly supported

$$\psi(x) = 0 \quad \text{if } \chi > \tilde{\chi}, \quad \tilde{\chi} < \text{const.}$$

We wish to prove that

$$\int_0^\infty |(\mathcal{E}_{\xi, \nu} | D_a \psi)|^2 \alpha(a) da < \infty. \quad (3.79)$$

First, we compute the Fourier-Helgason coefficients of the dilated function ψ :

$$\begin{aligned} \langle \mathcal{E}_{\xi, \nu} | D_a \psi \rangle &= \int_{H_+^2} D_a \psi(\chi, \varphi) \overline{\mathcal{E}_{\xi, \nu}(\chi, \varphi)} d\mu(\chi, \varphi) \\ &= \int_0^{2\pi} \int_0^{\tilde{\chi}_1/a} \lambda^{\frac{1}{2}}(a, \chi) \psi(\chi_{\frac{1}{a}}, \varphi) \overline{\mathcal{E}_{\xi, \nu}(\chi, \varphi)} \sinh \chi d\chi d\varphi. \end{aligned}$$

By performing the change of variable $\chi' = \chi_{\frac{1}{a}}$, we get $\chi = \chi'_a$ and $d \cosh \chi = d \cosh \chi'_a = \lambda(a^{-1}, \chi') d \cosh \chi'$. The Fourier-Helgason coefficients become

$$\langle \mathcal{E}_{\xi, \nu} | D_a \psi \rangle = \int_0^{2\pi} \int_0^{\tilde{\chi}} \lambda^{\frac{1}{2}}(a, \chi'_a) \psi(\chi', \varphi) \overline{\mathcal{E}_{\xi, \nu}(\chi'_a, \varphi)} \lambda(a^{-1}, \chi') \sinh \chi' d\chi' d\varphi. \quad (3.80)$$

From the cocycle property

$$\lambda^{\frac{1}{2}}(a^{-1}, \chi') = \frac{1}{\lambda^{\frac{1}{2}}(a, \chi'_a)} = \left[a \frac{\sinh \chi_a}{\sinh \chi} \frac{\cosh p\chi}{\cosh p\chi_a} \right]^{\frac{1}{2}}, \quad (3.81)$$

we get

$$\langle \mathcal{E}_{\xi, \nu} | D_a \psi \rangle = \int_0^{2\pi} \int_0^{\tilde{\chi}} \lambda^{\frac{1}{2}}(a^{-1}, \chi') \psi(\chi', \varphi) \overline{\mathcal{E}_{\xi, \nu}(\chi'_a, \varphi)} \sinh \chi' d\chi' d\varphi. \quad (3.82)$$

Then, we split (3.79) in three parts:

$$\int_0^\infty (\cdot) \alpha(a) da = \underbrace{\int_0^\sigma (\cdot) \alpha(a) da}_{I_1} + \underbrace{\int_\sigma^{\frac{1}{\sigma}} (\cdot) \alpha(a) da}_{I_2} + \underbrace{\int_{\frac{1}{\sigma}}^\infty (\cdot) \alpha(a) da}_{I_3}. \quad (3.83)$$

Let us focus on the first integral. Developing the Fourier-Helgason kernel $\mathcal{E}_{\xi, \nu}$ in (3.82), we obtain :

$$I_1 = \int_0^\sigma \alpha(a) da \times \\ \times \left| \int_0^{\bar{\chi}} \int_0^{2\pi} d\mu(\chi', \varphi) \lambda^{\frac{1}{2}}(a^{-1}, \chi') \psi(\chi') (\cosh \chi'_a - \sinh \chi'_a \cos \varphi)^{-\frac{1}{2} + i\nu} \right|^2.$$

Using the explicit form of χ'_a , we have for the various involved quantities the following asymptotic behaviors at small scale $a \approx 0$:

$$\begin{aligned} \cosh p\chi_a &\sim 1 + o(a), \\ \cosh \chi_a &\sim 1 + o(a), \\ \sinh \chi_a &\sim \frac{a}{p} \sinh p\chi + o(a), \\ (\cosh \chi'_a - \sinh \chi'_a \cos \varphi)^{-\frac{1}{2} + i\nu} &\sim 1 - \left(-\frac{1}{2} + i\nu\right) \frac{a}{p} \cos \varphi. \end{aligned}$$

So we have the approximation

$$\begin{aligned} &\int_0^{\bar{\chi}} \int_0^{2\pi} d\mu(\chi', \varphi) \lambda^{\frac{1}{2}}(a^{-1}, \chi') \psi(\chi') (\cosh \chi'_a - \sinh \chi'_a \cos \varphi)^{-\frac{1}{2} + i\nu} \\ &\sim \frac{a}{\sqrt{2p}} \int_0^{\bar{\chi}} \int_0^{2\pi} d\mu(\chi', \varphi) \left[\frac{\sinh 2p\chi}{\sinh \chi} \right]^{\frac{1}{2}} \left(1 - \left(-\frac{1}{2} + i\nu\right) \frac{a}{p} \cos \varphi \right). \end{aligned}$$

Integrating over φ and using the rotation invariance of ψ , we obtain the following approximation for I_1 :

$$I_1 \sim \int_0^\sigma \alpha(a) a^2 da \left| \int_0^{\bar{\chi}} \sinh \chi' d\chi' \left[\frac{\sinh 2p\chi}{\sinh \chi} \right]^{\frac{1}{2}} \psi(\chi') \right|^2. \quad (3.84)$$

The second sub-integral (I_2) is straightforward, since the operator D_a is strongly continuous and thus the integrand is bounded on $[\sigma, \frac{1}{\sigma}]$.

Consider now the inequality :

$$I_3 \leq \int_{\frac{1}{\sigma}}^{+\infty} \alpha(a) da \left(\int_0^{\bar{\chi}} \int_0^{2\pi} d\mu(\chi', \varphi) \lambda^{\frac{1}{2}}(a^{-1}, \chi') |\psi(\chi')| |\cosh \chi'_a - \sinh \chi'_a \cos \varphi|^{-1/2} \right)^2. \quad (3.85)$$

The term $|\cosh \chi'_a - \sinh \chi'_a \cos \varphi|^{-1/2}$ is bounded from above and from below by :

$$e^{-\frac{\chi'_a}{2}} \leq |\cosh \chi'_a - \sinh \chi'_a \cos \varphi|^{-1/2} \leq e^{\frac{\chi'_a}{2}}. \quad (3.86)$$

Now, we have

$$e^{\frac{\chi'_a}{2}} = \left(e^{p\chi'_a} \right)^{\frac{1}{2p}} = \left[\sqrt{1 + a^2 \sinh^2 p\chi' + a \sinh p\chi'} \right]^{\frac{1}{2p}},$$

and so we get the asymptotic behavior of this upper bound at large scale:

$$e^{\frac{\chi'_a}{2}} \sim a^{\frac{1}{2p}} (\sinh p\chi')^{\frac{1}{2p}}.$$

Again using the explicit form of χ'_a and the following asymptotic behaviors at large scale $a \rightarrow \infty$:

$$\begin{aligned} \cosh p\chi_a &\sim a \sinh p\chi, \\ \sinh \chi_a &\sim a^{\frac{1}{p}} (\sinh p\chi)^{\frac{1}{p}}, \end{aligned}$$

we reach the following majoration of I_3 :

$$I_3 \leq \int_{\frac{1}{\sigma}}^{+\infty} \alpha(a) a^{\frac{2}{p}} da \left(\int_0^{\tilde{\chi}} d\chi' (\sinh \chi')^{\frac{1}{2}} (\sinh p\chi')^{\frac{1}{p}-\frac{1}{2}} (\cosh p\chi')^{\frac{1}{2}} |\psi(\chi')| \right)^2.$$

Since the hyperbolic functions involved in the integration on the χ' variable are increasing, we finally end up with the estimate :

$$I_3 \leq \sim (\sinh \tilde{\chi})^{\frac{1}{2}} (\sinh p\tilde{\chi})^{\left(\frac{1}{p}-\frac{1}{2}\right)} (\cosh p\tilde{\chi})^{\frac{1}{2}} \|\psi\|_1^2 \int_{\frac{1}{\sigma}}^{+\infty} \alpha(a) a^{\frac{2}{p}} da.$$

and so $\alpha(a)$ should behave at least like $a^{-\beta}$ with $\beta > \frac{2}{p} + 1$ for $a \rightarrow \infty$.

The convergence of I_1 and I_3 clearly depends on the choice of measure in the integral over scales. Restricting ourselves to homogeneous measures $\alpha(a) = a^{-\beta}$ and to the range $0 < p \leq 2$, one can distinguish the following cases :

- $\beta \leq \frac{2}{p} + 1$: in this case I_3 does not converge and there are no admissible wavelets.
- $\beta > \frac{2}{p} + 1$: In this case I_1 diverges except when $\int_{H_+^2} \psi \left[\frac{\sinh 2p\chi}{\sinh \chi} \right]^{\frac{1}{2}} = 0$. ■

Let us look at the two particular cases. In the first one we use a pure conic dilation ($p = \frac{1}{2}$):

Corollary 26. *Let $\alpha(a)da$ be a homogeneous measure of the form $a^{-\beta}da$, $\beta > 0$. If D_a is the conic dilation defined by equations (3.17) and (3.54) with $\lambda(a, \chi) = a^{-2}$, then an axisymmetric function $\psi \in L^2(H_+^2, d\mu(\chi, \varphi))$ is admissible if $\beta > 5$ and the following zero-mean condition is satisfied :*

$$\int_{H_+^2} \psi(\chi, \varphi) d\mu(\chi, \varphi) = 0. \quad (3.87)$$

Proof : We follow the same arguments as in the proof of Theorem 25 and thus perform the same change of variable while looking for the Fourier-Helgason coefficients of the dilated wavelet function through pure conic dilation ($p = 0.5$).

By performing the change of variable $\chi' = \chi \frac{1}{a}$, we get $\chi = \chi'_a$ and $d \cosh \chi = d \cosh \chi'_a = \lambda(a^{-1}, \chi') d \cosh \chi'$. The Fourier-Helgason coefficients become

$$\langle \mathcal{E}_{\xi, \nu} | D_a \psi \rangle = \int_0^{2\pi} \int_0^{\tilde{\chi}} \lambda^{\frac{1}{2}}(a, \chi'_a) \psi(\chi', \varphi) \overline{\mathcal{E}_{\xi, \nu}(\chi'_a, \varphi)} \lambda(a^{-1}, \chi') \sinh \chi' d\chi' d\varphi. \quad (3.88)$$

From the cocycle property

$$\lambda^{\frac{1}{2}}(a, \chi'_a) = \frac{1}{\lambda^{\frac{1}{2}}(a^{-1}, \chi')} = \frac{1}{a}, \quad (3.89)$$

we get

$$\langle \mathcal{E}_{\xi, \nu} | D_a \psi \rangle = a \int_0^{2\pi} \int_0^{\tilde{\chi}} \psi(\chi', \varphi) \overline{\mathcal{E}_{\xi, \nu}(\chi'_a, \varphi)} \sinh \chi' d\chi' d\varphi. \quad (3.90)$$

Once again, the central point is to prove that

$$\int_0^{\infty} |\langle \mathcal{E}_{\xi, \nu} | D_a \psi \rangle|^2 \alpha(a) da < \infty. \quad (3.91)$$

We split it in three parts:

$$\int_0^{\infty} (\cdot) \alpha(a) da = \underbrace{\int_0^{\sigma} (\cdot) \alpha(a) da}_{I_1} + \underbrace{\int_{\sigma}^{\frac{1}{\sigma}} (\cdot) \alpha(a) da}_{I_2} + \underbrace{\int_{\frac{1}{\sigma}}^{\infty} (\cdot) \alpha(a) da}_{I_3}. \quad (3.92)$$

Let us focus on the first integral. Developing the Fourier-Helgason kernel $\mathcal{E}_{\xi,\nu}$ in (3.90), we obtain :

$$I_1 = \int_0^\sigma \alpha(a) a^2 da \left| \int_0^{\tilde{\chi}} \int_0^{2\pi} d\mu(\chi', \varphi) \psi(\chi') (\cosh \chi'_a - \sinh \chi'_a \cos \varphi)^{-\frac{1}{2}+i\nu} \right|^2.$$

Using the explicit form of χ'_a , we have :

$$I_1 = \int_0^\sigma \alpha(a) a^2 da \left| \int_0^{\tilde{\chi}} \int_0^{2\pi} d\mu(\chi', \varphi) \psi(\chi') \left(1 + 2a^2 \sinh^2 \frac{\chi'}{2} - 2a \sqrt{1 + a^2 \sinh^2 \frac{\chi'}{2}} \sinh \frac{\chi'}{2} \cos \varphi\right)^{-\frac{1}{2}+i\nu} \right|^2. \quad (3.93)$$

Since we are interested in the small scale behavior of this quantity, we can focus on the leading term in the expansion in powers of a , which yields :

$$\begin{aligned} I_1 &\sim \int_0^\sigma \alpha(a) a^2 da \left| \int_0^{\tilde{\chi}} \int_0^{2\pi} d\mu(\chi', \varphi) \psi(\chi') (1 - 2a \sinh \frac{\chi'}{2} \cos \varphi)^{-\frac{1}{2}+i\nu} \right|^2 \\ &\sim \int_0^\sigma \alpha(a) a^2 da \left| \int_0^{\tilde{\chi}} \int_0^{2\pi} d\mu(\chi', \varphi) \psi(\chi') (1 - (-1 + 2i\nu)a \sinh \frac{\chi'}{2} \cos \varphi) \right|^2. \end{aligned}$$

Finally, integrating over φ and using the rotation invariance of ψ , we obtain :

$$I_1 \sim \int_0^\sigma \alpha(a) a^2 da \left| \int_0^{\tilde{\chi}} \sinh \chi' d\chi' \psi(\chi') \right|^2. \quad (3.94)$$

The second subintegral (I_2) is straightforward, since the operator D_a is strongly continuous and thus the integrand is bounded on $[\sigma, \frac{1}{\sigma}]$.

Consider now the inequality :

$$I_3 \leq \int_{\frac{1}{\sigma}}^{+\infty} \alpha(a) a^2 da \left(\int_0^{\tilde{\chi}} \int_0^{2\pi} d\mu(\chi', \varphi) |\psi(\chi')| |\cosh \chi'_a - \sinh \chi'_a \cos \varphi|^{-1/2} \right)^2.$$

The term $|\cosh \chi'_a - \sinh \chi'_a \cos \varphi|^{-1/2}$ is bounded from above and from below by :

$$e^{-\frac{\chi'_a}{2}} \leq |\cosh \chi'_a - \sinh \chi'_a \cos \varphi|^{-1/2} \leq e^{\frac{\chi'_a}{2}}. \quad (3.95)$$

Now, we have

$$e^{\frac{\chi'_a}{2}} = \cosh \frac{\chi'_a}{2} + \sinh \frac{\chi'_a}{2} = a \sinh \frac{\chi'}{2} \left[\sqrt{1 + \frac{1}{a^2 \sinh^2 \frac{\chi'}{2}}} + 1 \right] \sim 2a \sinh \frac{\chi'}{2}.$$

Since the hyperbolic functions involved in the integration on the χ' variable are increasing, we reach the following majoration of I_3 :

$$I_3 \leq \sim 8\pi \sinh^2 \frac{\tilde{\chi}}{2} \sinh^2 \tilde{\chi} \|\psi\|_1^2 \int_{\frac{1}{\sigma}}^{+\infty} \alpha(a) a^4 da,$$

and so $\alpha(a)$ should behave at least like $a^{-\beta}$ with $\beta > 5$ for $a \rightarrow \infty$.

The convergence of I_1 and I_3 clearly depends on the choice of measure in the integral over scales. Restricting ourselves to homogeneous measures $\alpha(a) = a^{-\beta}$, we can distinguish the following cases :

- $\beta \leq 5$: In this case I_3 does not converge and there are no admissible wavelets.

- $\beta > 5$: In this case I_1 diverges except when $\int_{H_+^2} \psi = 0$. ■

In the second case we chose to use flattening as projective structure for obtaining hyperbolic wavelets, and thus we obtain even a simpler version of the admissibility condition:

Corollary 27. *Let $\alpha(a)da$ be a homogeneous measure of the form $a^{-\beta}da$, $\beta > 0$. If D_a is the dilation operator defined through flattening, as by equations (3.23), (3.53) and (3.54), then an axisymmetric function $\psi \in L^2(H_+^2, d\mu(\chi, \varphi))$ is admissible if $\beta > 3$ and the following zero-mean condition is satisfied :*

$$\int_{H_+^2} d\mu(\chi, \varphi) \cosh^{1/2} \chi \psi(\chi, \varphi) = 0. \quad (3.96)$$

Proof: For proving this corollary we use the same technique as in Corollary 26, namely we assume that $\psi(x)$ is compactly supported and we wish to prove that the Fourier-Helgason coefficients of the hyperbolic wavelet function are square-integrable with respect to the dilation.

After the same change of variable and using the cocycle property, the Fourier-Helgason coefficients are computed as follows

$$\langle \mathcal{E}_{\xi, \nu} | D_a \psi \rangle = \int_0^{2\pi} \int_0^{\tilde{\chi}} \lambda^{1/2} (a^{-1}, \chi') \psi(\chi', \varphi) \overline{\mathcal{E}_{\xi, \nu}(\chi'_a, \varphi)} \sinh \chi' d\chi' d\varphi \quad (3.97)$$

$$= \int_0^{2\pi} \int_0^{\tilde{\chi}} \frac{a(\cosh \chi)^{1/2}}{(1 + a^2 \sinh^2 \chi)^{1/4}} \psi(\chi', \varphi) \overline{\mathcal{E}_{\xi, \nu}(\chi'_a, \varphi)} \sinh \chi' d\chi' d\varphi. \quad (3.98)$$

Splitting (3.91) as in (3.92), we start by studying the integral at small scales I_1 .

$$I_1 = \int_0^\sigma \alpha(a) a^2 da \left| \int_0^{\tilde{\chi}} \int_0^{2\pi} d\mu(\chi', \varphi) \frac{(\cosh \chi')^{1/2}}{(1 + a^2 \sinh^2 \chi')^{1/4}} \psi(\chi') \right. \\ \left. \left(\sqrt{1 + a^2 \sinh^2 \chi'} - a \sinh \chi' \cos \varphi \right)^{-\frac{1}{2} + i\nu} \right|^2. \quad (3.99)$$

In this case we are interested in small scale behavior of this quantity and we focus on the leading term in the expansion in powers of a , which leads to

$$I_1 \sim \int_0^\sigma \alpha(a) a^2 da \left| \int_0^{\tilde{\chi}} \int_0^{2\pi} d\mu(\chi', \varphi) (\cosh \chi')^{1/2} \psi(\chi') (1 - a \sinh \chi' \cos \varphi)^{-\frac{1}{2} + i\nu} \right|^2 \\ \sim \int_0^\sigma \alpha(a) a^2 da \left| \int_0^{\tilde{\chi}} \int_0^{2\pi} d\mu(\chi', \varphi) (\cosh \chi')^{1/2} \psi(\chi') \left(1 - \left(-\frac{1}{2} + i\nu \right) a \sinh \chi' \cos \varphi \right) \right|^2 \\ \sim \int_0^\sigma \alpha(a) a^2 da \left| \int_0^{\tilde{\chi}} \int_0^{2\pi} d\mu(\chi', \varphi) (\cosh \chi')^{1/2} \psi(\chi') \right|^2.$$

The integral I_2 is bounded on $[\sigma, \frac{1}{\sigma}]$ because it is strongly continuous.

For calculating the integral I_3 , we first note that the term $|\cosh \chi'_a - \sinh \chi'_a \cos \varphi|^{-1/2}$ is bounded from above and below as in (3.95). We express

$$e^{\chi'_a/2} = (\cosh \chi'_a + \sinh \chi'_a)^{1/2} \quad (3.100)$$

$$= (\sqrt{1 + a^2 \sinh^2 \chi'} + a \sinh \chi')^{1/2} \quad (3.101)$$

$$\sim \sqrt{2a \sinh \chi'}. \quad (3.102)$$

Consider now the inequality

$$I_3 \leq \int_{\frac{1}{\sigma}}^{+\infty} \alpha(a) a^2 da \left(\int_0^{\tilde{\chi}} \int_0^{2\pi} d\mu(\chi', \varphi) \left| \frac{(\cosh \chi')^{1/2}}{(1 + a^2 \sinh^2 \chi')^{1/4}} \right| \right. \\ \left. |\psi(\chi')| |\cosh \chi'_a - \sinh \chi'_a \cos \varphi|^{-1/2} \right)^2.$$

Using (3.102), this inequality becomes

$$\begin{aligned}
I_3 &\leq \int_{\frac{1}{\sigma}}^{+\infty} \alpha(a) a^2 da \left(\int_0^{\tilde{\chi}} \int_0^{2\pi} d\mu(\chi', \varphi) \left| \frac{(\cosh \chi')^{1/2}}{(1 + a^2 \sinh^2 \chi')^{1/4}} \right| |\psi(\chi')| \sqrt{2} a^{1/2} \sinh^{1/2} \chi' \right)^2 \\
&\leq \int_{\frac{1}{\sigma}}^{+\infty} \alpha(a) a^2 da \left(\int_0^{\tilde{\chi}} \int_0^{2\pi} d\mu(\chi', \varphi) \sqrt{2} |\psi(\chi')| \cosh^{1/2} \chi' \right)^2 \\
&\leq C \int_{\frac{1}{\sigma}}^{+\infty} \alpha(a) a^2 da.
\end{aligned}$$

Since $\psi(\chi)$ is assumed to be with compact support and $\cosh \chi \geq 1$, then C is bounded. In this case, in order I_3 to converge, we need to have at least $\alpha(a) = \frac{1}{a^4}$. ■

3.6.2 An example of hyperbolic wavelet

For concluding our theory of the wavelets on the hyperboloid, let us present here a class of admissible vectors, which satisfy the admissibility condition. We restrict ourself to the case $p = 0.5$ but let first state a preliminary result

Proposition 28. *Let $\psi \in L^2(H_+^2, d\mu)$. Then*

$$\int_{H_+^2} D_a \psi(\chi, \varphi) d\mu(\chi, \varphi) = a \int_{H_+^2} \psi(\chi, \varphi) d\mu(\chi, \varphi). \quad (3.103)$$

Proof: We have to compute the following integral

$$I = \int_{H_+^2} D_a \psi(\chi, \varphi) d\mu(\chi, \varphi) = \int_{H_+^2} \lambda^{\frac{1}{2}}(a, \chi) \psi(\chi_{\frac{1}{a}}, \varphi) d\mu(\chi, \varphi).$$

By change of variable $\chi_{\frac{1}{a}} = \chi'$, we get

$$\begin{aligned}
I &= \int_{H_+^2} \lambda^{\frac{1}{2}}(a, \chi'_a) \psi(\chi', \varphi) \lambda(a^{-1}, \chi') d\mu(\chi', \varphi) \\
&= \int_{H_+^2} \lambda^{\frac{1}{2}}(a^{-1}, \chi') \psi(\chi', \varphi) d\mu(\chi', \varphi),
\end{aligned}$$

and having $\lambda^{\frac{1}{2}}(a^{-1}, \chi') = a$, which follows directly from (3.52), we get

$$I = a \int_{H_+^2} \psi(\chi', \varphi) d\mu(\chi', \varphi),$$

which proves the proposition. ■

Using this result, we can build the hyperbolic DOG wavelet. Thus, given a square-integrable function ψ , we define

$$f_{\psi}^{\beta}(\chi, \varphi) = \psi(\chi, \varphi) - \frac{1}{\beta} D_{\beta} \psi(\chi, \varphi), \quad \beta > 1. \quad (3.104)$$

More precisely, using the hyperbolic function $\psi = e^{-\sinh^2 \frac{\chi}{2}}$, we dilate it through the conic projection and thus obtain

$$D_{\beta} \psi = \frac{1}{\beta} e^{-\frac{1}{\beta^2} \sinh^2 \frac{\chi}{2}}. \quad (3.105)$$

Then we write (3.104) and get:

$$f_{\psi}^{\beta}(\chi, \varphi) = e^{-\sinh^2 \frac{\chi}{2}} - \frac{1}{\beta^2} e^{-\frac{1}{\beta^2} \sinh^2 \frac{\chi}{2}}. \quad (3.106)$$

Now, applying a dilation operator on (3.106) we get

$$D_a f^\beta = \frac{1}{a} e^{-\frac{1}{a^2} \sinh^2 \frac{\chi}{2}} - \frac{1}{a\beta^2} e^{-\frac{1}{a^2\beta^2} \sinh^2 \frac{\chi}{2}}. \quad (3.107)$$

One particular example of *hyperbolic DOG wavelet* at $\beta = 2$ is:

$$f_\psi^2(\chi, \varphi) = \frac{1}{a} e^{-\frac{1}{a^2} \sinh^2 \frac{\chi}{2}} - \frac{1}{4a} e^{-\frac{1}{4a^2} \sinh^2 \frac{\chi}{2}}.$$

The resulting hyperbolic DOG wavelet is shown in Figure 3.10 for different values of the scale a and the position (χ, φ) on the hyperboloid.

Of course, similar admissible hyperbolic DOG wavelets can be constructed for generic $p > 0$, but let us discuss some specific features of this one. On Figure 3.11 we can see the same DOG wavelet but viewed on the open unit disk. The action of the dilation a in this particular case is trivial: it dilates the wavelet toward the border of the disk as it never reaches it and it remains centered.

More interesting is the behavior of the wavelet when different hyperbolic translations are applied on it. This is equivalent to variation of the hyperbolic angle χ . The more it is increased, the closer to the disk's border the wavelet moves but it never reaches it. Actually, seen on the disk it behaves as different functions though it is just the same wavelet but hyperbolically translated. We can see this on Figure 3.12.

The action of the rotations on the same wavelet are trivial, it just rotates it in the disk by $\varphi \in [0, 2\pi)$. This is shown on Figure 3.13.

3.6.3 An example of continuous wavelet transform on the hyperboloid

For concluding this section we provide an example of the continuous wavelet transform applied on a synthetic signal - a hyperbolic triangle. The signal is projected on the unit disc and the visualization of its CWT at different scale a is depicted on Figure 3.14.

3.7 The hyperbolic wavelet L^1 -normalized transform

We should emphasize here that the choice of the normalization factor

$$\lambda^{1/2}(a, \chi) = \sqrt{\frac{1}{a} \frac{\sinh \chi_{1/a}}{\sinh \chi} \frac{\cosh p\chi}{\cosh p\chi_{1/a}}}$$

in (3.55) is not essential. This choice makes the transform unitary : $\|\psi_a(x)\|_2 = \|\psi\|_2$ and also $\|\mathcal{W}_f\|_2 = \|f\|_2$, where $\|\cdot\|_2$ denotes the L^2 norm in the appropriate variables (the square norm is interpreted as the total energy of the signal). Instead, in practice one often uses a factor $\lambda(a, \chi)$, which has the advantage of giving more weight to the small scales, i.e. the high frequency part (which contains the singularities of the signal, if any).

Thus, when constructing hyperbolic wavelets through flattening ($p = 1$), we define the action of the dilation operator as

$$(D_a \psi)(x) \equiv \psi_a(x) = \lambda(a, \chi) = \frac{\cosh \chi}{a^2 \sqrt{1 + a^{-2} \sinh^2 \chi}} \psi(\chi_{1/a}), \quad (3.108)$$

and obtain the so called L^1 -normalized transform, which preserves the L^1 -norm of the hyperbolic signal. The same development is valid for any other projection parameter p .

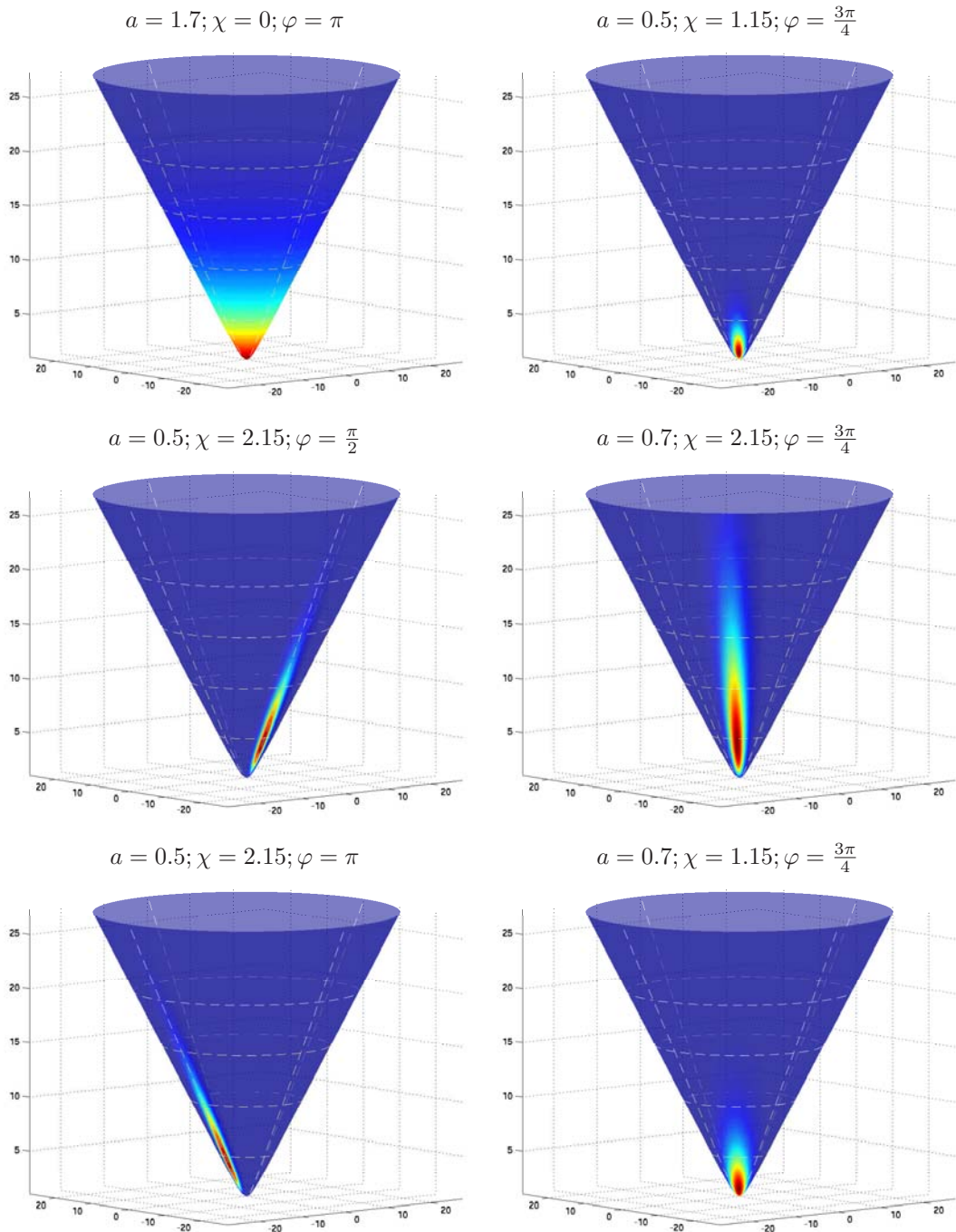


Figure 3.10: The hyperbolic DOG wavelet f_{ψ}^{β} , for $\beta = 2$ at different scales a and positions (χ, φ) .

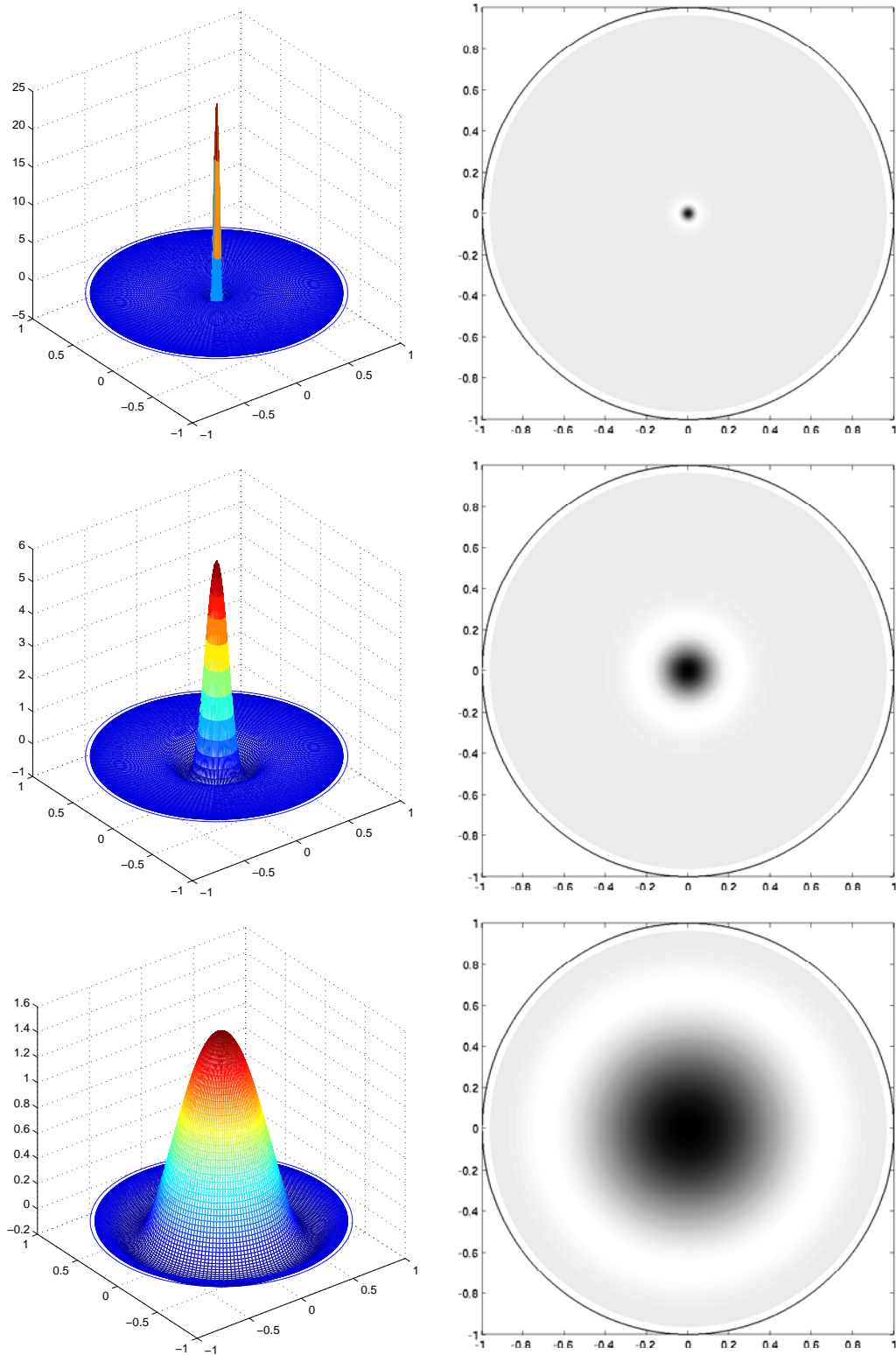


Figure 3.11: Action of a dilation on the hyperbolic DOG wavelet f_{ψ}^{β} , for $\beta = 2$ at $\chi = 0, \varphi = 0$; up: $a = 0.01$, middle: $a = 0.125$, bottom: $a = 0.5$.

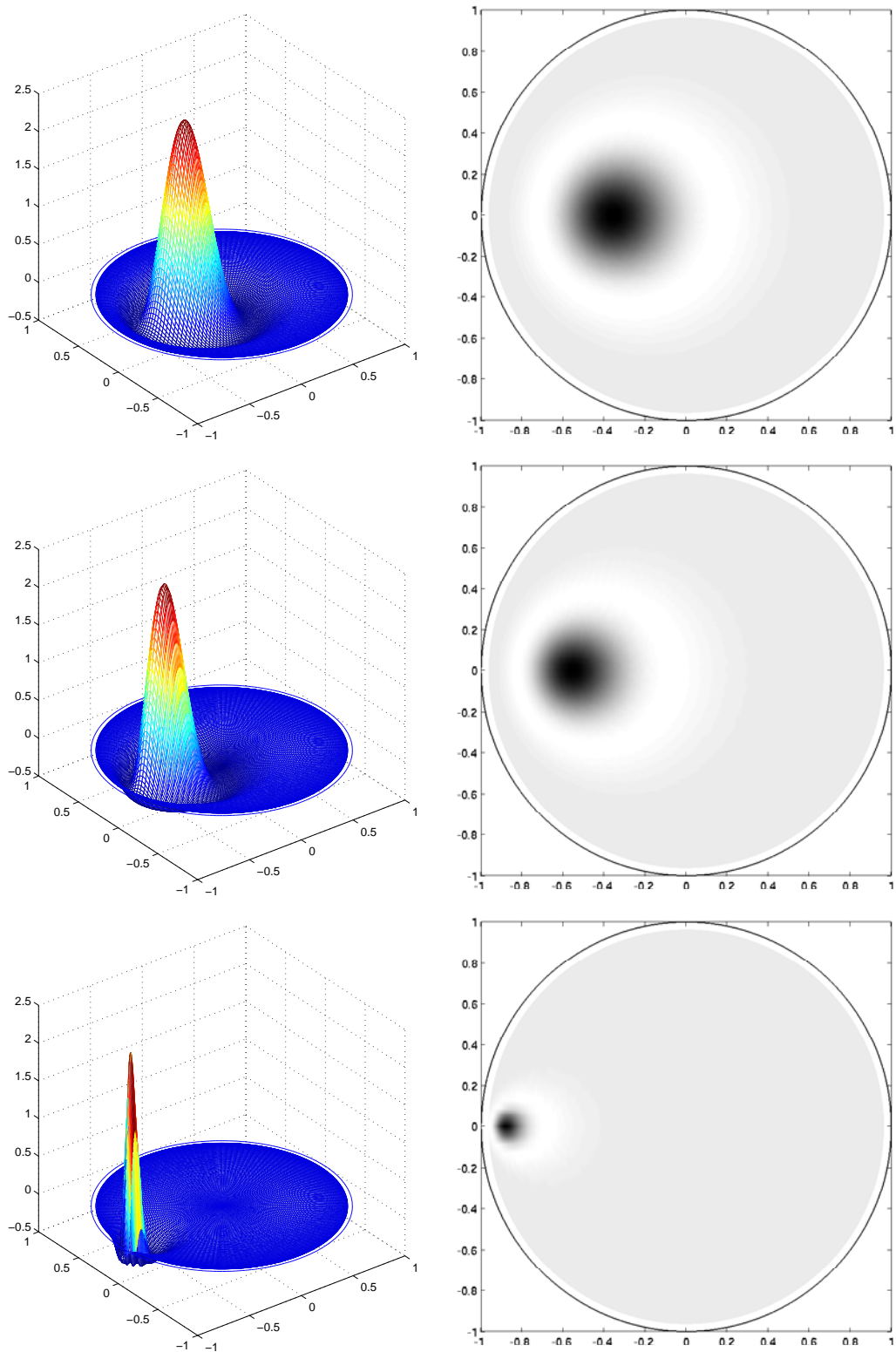


Figure 3.12: Action of a hyperbolic translation on the hyperbolic DOG wavelet f_{ψ}^{β} , for $\beta = 2$ at $a = 0.3, \varphi = \pi$; up: $\chi = 0.75$, middle: $\chi = 1.25$, bottom: $\chi = 2.75$.

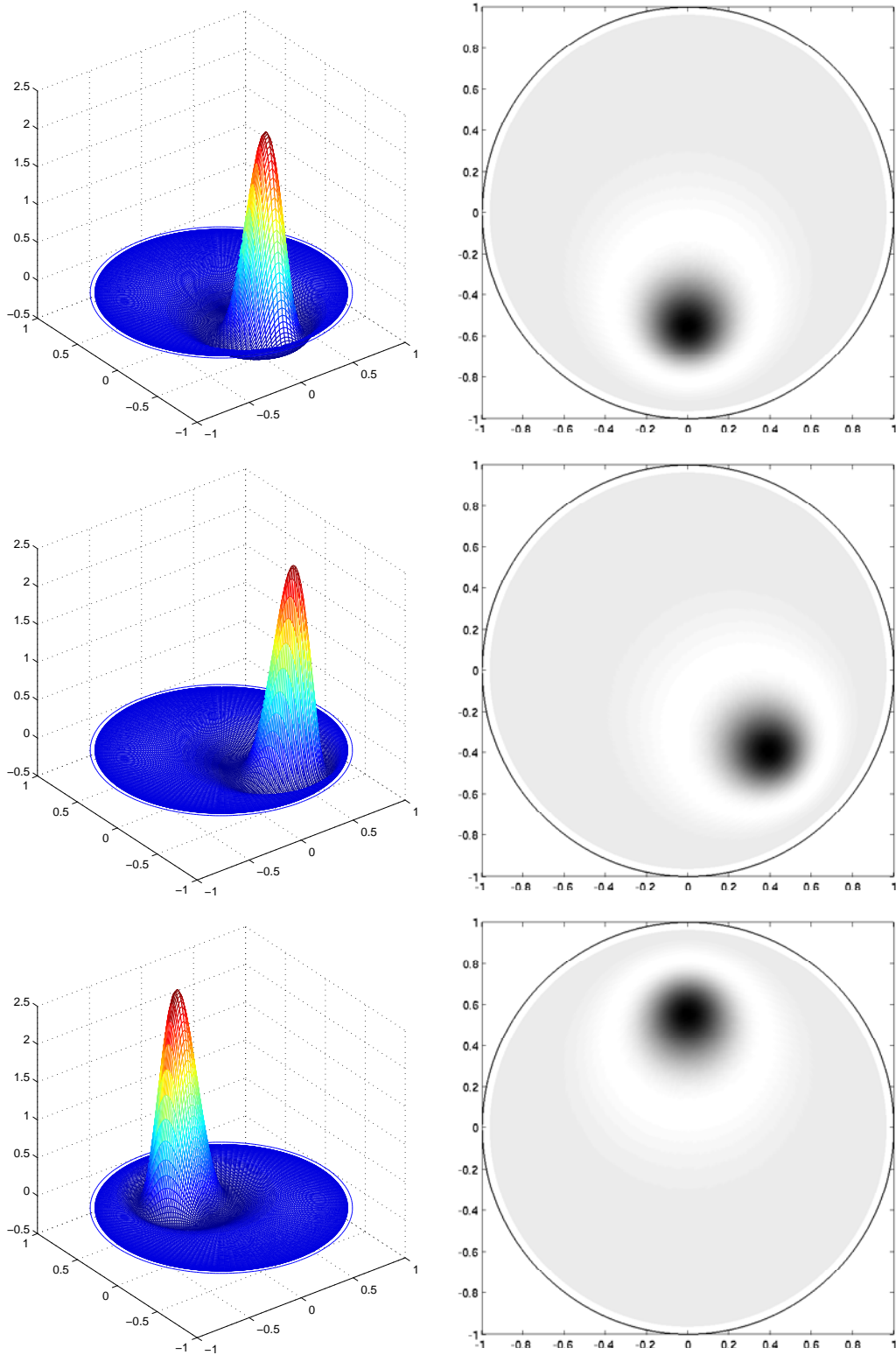


Figure 3.13: Action of a rotation on the hyperbolic DOG wavelet f_{ψ}^{β} , for $\beta = 2$ at $a = 0.3$, $\chi = 1.25$; up: $\varphi = \pi/2$, middle: $\varphi = \pi/4$, bottom: $\varphi = 3\pi/2$.

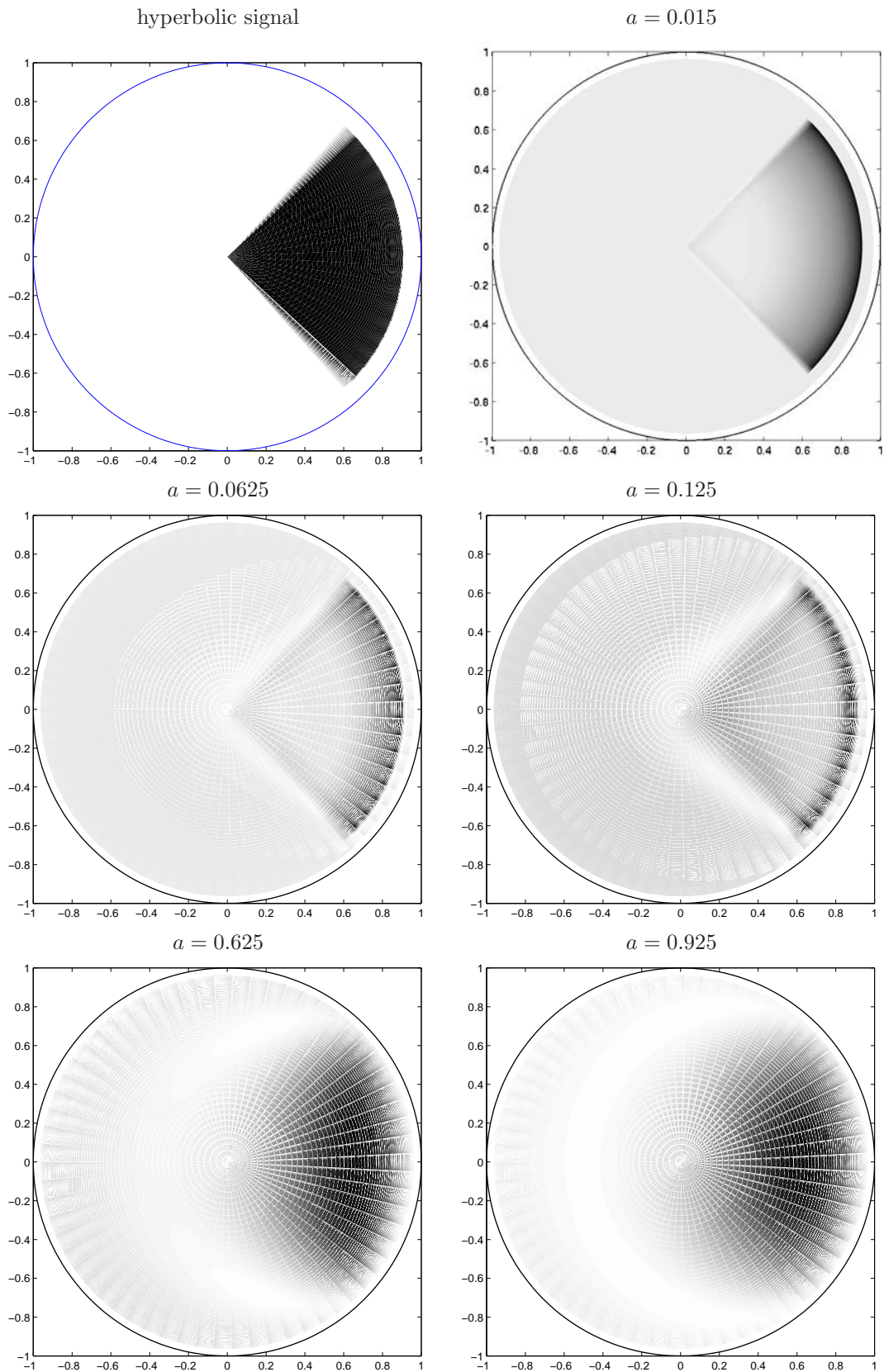


Figure 3.14: Continuous wavelet transform of a hyperbolic triangle at different scales a , using hyperbolic DOG wavelet with $\beta = 2$.

3.7.1 L^1 -normalized hyperbolic admissibility condition

We must note that changing the dilation operator from L^2 to L^1 norm amounts to replacing the factor $\lambda(a, \chi)^{1/2}$ by its square $\lambda(a, \chi)$, but this modifies the admissibility condition in a nontrivial way and is expressed in the following proposition, we develop the admissibility condition for $p = 1$, but the other cases are analogues.

Proposition 29. *Let $\alpha(a)da$ be a homogeneous measure of the form $a^{-\beta}da$, $\beta > 0$. If D_a is the dilation operator defined for $p = 1$, as by equations (3.23), (3.54) and (3.53), then an axisymmetric function $\psi \in L^1(H_+^2, d\mu(\chi, \varphi))$ is admissible if $\beta \geq 3$ and the following zero-mean condition is satisfied :*

$$\int_{H_+^2} d\mu(\chi, \varphi) \psi(\chi, \varphi) = 0. \quad (3.109)$$

Proof: First we start with FH coefficients

$$\langle \mathcal{E}_{\xi, \nu} | D_a \psi \rangle = \int_0^{2\pi} \int_0^{\bar{\chi}} \lambda(a, \chi'_a) \psi(\chi') \overline{\mathcal{E}_{\xi, \nu}(\chi'_a, \varphi)} \lambda(a^{-1}, \chi') \sinh \chi' d\chi' d\varphi \quad (3.110)$$

$$= \int_0^{2\pi} \int_0^{\bar{\chi}} \psi(\chi') \overline{\mathcal{E}_{\xi, \nu}(\chi'_a, \varphi)} \sinh \chi' d\chi' d\varphi \quad (3.111)$$

where was taken the cocycle property

$$\lambda(a, \chi'_a) = \frac{1}{\lambda(a^{-1}, \chi')}.$$

$$I_1 = \int_0^\sigma \alpha(a) da \left| \int_0^{2\pi} \int_0^{\bar{\chi}} d\mu(\chi', \varphi) \psi(\chi') (\cosh \chi'_a - \sinh \chi'_a \cos \varphi)^{-\frac{1}{2} + i\nu} \right|^2 \quad (3.112)$$

$$= \int_0^\sigma \alpha(a) da \left| \int_0^{2\pi} \int_0^{\bar{\chi}} d\mu(\chi', \varphi) \psi(\chi') (\sqrt{1 + a^2 \sinh^2 \chi'} - a \sinh \chi' \cos \varphi)^{-\frac{1}{2} + i\nu} \right|^2 \quad (3.113)$$

$$\sim \int_0^\sigma \alpha(a) da \left| \int_0^{2\pi} \int_0^{\bar{\chi}} d\mu(\chi', \varphi) \psi(\chi') (1 - a \sinh \chi' \cos \varphi)^{-\frac{1}{2} + i\nu} \right|^2 \quad (3.114)$$

$$\sim \int_0^\sigma \alpha(a) da \left| \int_0^{2\pi} \int_0^{\bar{\chi}} d\mu(\chi', \varphi) \psi(\chi') \left(1 - \left(-\frac{1}{2} + i\nu\right) a \sinh \chi' \cos \varphi\right) \right|^2 \quad (3.115)$$

$$\sim \int_0^\sigma \alpha(a) da \left| \int_0^{2\pi} \int_0^{\bar{\chi}} d\mu(\chi', \varphi) \psi(\chi') \right|^2 \quad (3.116)$$

The integral I_2 converges because ψ is defined to be with compact support.

It remains to see what is the behavior of I_3 .

$$I_3 \leq \int_{1/\sigma}^{+\infty} \alpha(a) da \left(\int_0^{2\pi} \int_0^{\bar{\chi}} d\mu(\chi', \varphi) |\psi(\chi')|^2 \sqrt{2a \sinh \chi'} \right)^2 \quad (3.117)$$

$$\leq \int_{1/\sigma}^{+\infty} \alpha(a) 2a da \left(\int_0^{2\pi} \int_0^{\bar{\chi}} d\mu(\chi', \varphi) |\psi(\chi')|^2 \sinh^{1/2} \chi' \right)^2 \quad (3.118)$$

This integral converges for all $\alpha(a) \geq \frac{1}{a^3}$. In this case, in order the integral I to converge we need the subintegral I_1 to converge and this happens when is fulfilled

$$\int_{H_+^2} \psi(\chi) d\mu(\chi, \varphi) = 0. \quad (3.119)$$

■

3.8 Euclidean limit

Since the hyperboloid is locally flat, the associated wavelet transform should match the usual 2-D CWT in the Euclidean plane at small scales, i.e. for large radiuses of curvature. In this section we recall some basic facts emphasizing those notions.

Let $\mathcal{H}_\rho \equiv L^2(H_{+\rho}^2, d\mu_\rho)$ be the Hilbert space of square integrable functions on a hyperboloid of radius ρ ,

$$\int_{H_\rho^2} |f(\chi, \varphi)|^2 \rho^2 \sinh \chi d\chi d\varphi < \infty, \quad (3.120)$$

and $\mathcal{H} = L^2(\mathbb{R}^2, d^2\vec{x})$ be the Hilbert space of square integrable functions on the plane.

One can easily adapt the Fourier-Helgason transform by updating $\mathcal{E}_{\nu, \xi}(x)$ for any ρ [6]:

$$\mathcal{E}_{\nu, \xi}^\rho(x) = \left(\frac{x_0 - \hat{n}\vec{x}}{\rho} \right)^{-\frac{1}{2} - i\nu\rho}, \quad (3.121)$$

for $x \in H_{+\rho}^2$, ($x^2 = \rho^2$). The Inönü-Wigner contraction limit of the Lorentz to the Euclidean group $SO(2, 1)_+ \rightarrow ISO(2)_+$ is the limit at $\rho \rightarrow \infty$ for (3.121) with $x_0 \approx \rho$, $\vec{x}^2 \ll \rho^2$, i.e

$$\lim_{\rho \rightarrow \infty} \mathcal{E}_{\nu, \xi}^\rho(x) = \lim_{\rho \rightarrow \infty} \left(\frac{x_0 - \hat{n}\vec{x}}{\rho} \right)^{-\frac{1}{2} - i\nu\rho} \quad (3.122)$$

$$\approx \lim_{\rho \rightarrow \infty} \left(1 - \frac{\hat{n}\vec{x}}{\rho} \right)^{-i\nu\rho} = \exp(i\nu\hat{n}\vec{x}). \quad (3.123)$$

The Fourier-Helgason transform on the hyperboloid of radius ρ reads :

$$\hat{\psi}^\rho(\nu, \xi) = \frac{\rho}{2\pi} \int_{\vec{x}} \psi(\vec{x}) \mathcal{E}_{\nu, \xi}^\rho(\vec{x}) \frac{d^2\vec{x}}{x_0} \quad (3.124)$$

and since $x_0 \approx \rho$ for $\rho \rightarrow \infty$, we obtain

$$\lim_{\rho \rightarrow \infty} \hat{\psi}^\rho(\nu, \xi) = \frac{1}{2\pi} \int_{\vec{x}} \psi(\vec{x}) \exp(i\nu\hat{n}\vec{x}) d^2\vec{x} \quad (3.125)$$

$$= \hat{\psi}(\vec{k}), \quad (3.126)$$

which is the Fourier transform in the Euclidean plane.

This relation shows that the geometric and algebraic breakdown $SO(2, 1)_+ \rightarrow ISO(2)_+$ is mirrored at the functional level. Consequently, the necessary condition of the hyperbolic wavelet contracts to the 2-D Euclidean one is:

$$\lim_{\rho \rightarrow \infty} \int_{H^2} \psi^\rho(\chi, \varphi) d\mu(\chi, \varphi) \rightarrow \int_{\mathbb{R}^2} \psi(\vec{x}) d^2\vec{x}. \quad (3.127)$$

A much finer analysis would be necessary to understand if this association holds at the level of the necessary and sufficient condition (3.73).

3.9 Summary

In this chapter a constructive theory for the continuous wavelet transform on the hyperboloid $H_+^2 \in \mathbb{R}_+^3$ has been developed.

- Affine transformations on the hyperboloid have been defined and different schemes for dilating H_+^2 have been proposed.

- Hyperbolic convolution has been proved by the means of Fourier-Helgason transform.
- The hyperbolic continuous wavelet transform together with the corresponding admissibility condition have been derived. Two particular cases of the admissibility condition have been presented: through conic projection and through flattening.
- An example of hyperbolic DOG wavelet has been given and some details on the action of the zoom, translation and rotation on the hyperbolic DOG wavelet have been shown.
- Finally, we have used the Inönü-Wigner contraction limit of the Lorentz to the Euclidean group $SO_0(2,1)_+ \rightarrow ISO(2)_+$ to check the consistency of the CWT on the hyperboloid with that one on the Euclidean plane.

On Processing Non-Euclidean Images

4

In this chapter we concentrate on one possible application of non-Euclidean wavelets-processing of non-Euclidean images. These images are closely related to the plenoptic function, a concept that embodies all visual information in a scene. The plenoptic function is represented in spherical coordinates and is in a tight relation with projection of the scene onto a sphere. Thus one efficient way for processing is by mapping the scene on the sphere, and then applying spherical frames. But depending on the curved mirror used for capturing the scene, it can be processed directly in the geometry of the mirror, for instance we could apply hyperbolic wavelets for processing a non-Euclidean image reflected by a hyperbolic mirror. For completing the set of processing tools for non-Euclidean images, we develop scale-space and active contour for the case of the sphere and hyperboloid. This is supplemented by a multiresolution motion estimation algorithm on the sphere.

4.1 Plenoptic function

The plenoptic function is a parameterized function for describing everything that is visible from a given point in space. Adelson and Bergen [1] assigned the name *plenoptic function* to the pencil of rays visible from any point in space, at any time, and over any range of wavelengths. This function describes all of the radiant energy that can be perceived from the point of view of the observer rather than the point of view of the source (Figure 4.1(a)).

It is interesting to note the parameter space over which this function is valid. Let an observer stand at any point in space (X, Y, Z) , from which one selects any of the viewable rays by choosing an azimuth and elevation angle $(\theta_{pl}, \varphi_{pl})$, as on Figure 4.1(b), as well as a band of wavelength λ which one wishes to consider. In addition, if this is a dynamic scene, one can choose the time t , at which the light field to be evaluated. This results in the following form for the plenoptic function

$$p = P(\theta_{pl}, \varphi_{pl}, \lambda, X, Y, Z, t). \quad (4.1)$$

For the purpose of visualization, one can consider this function as a scene representation. In

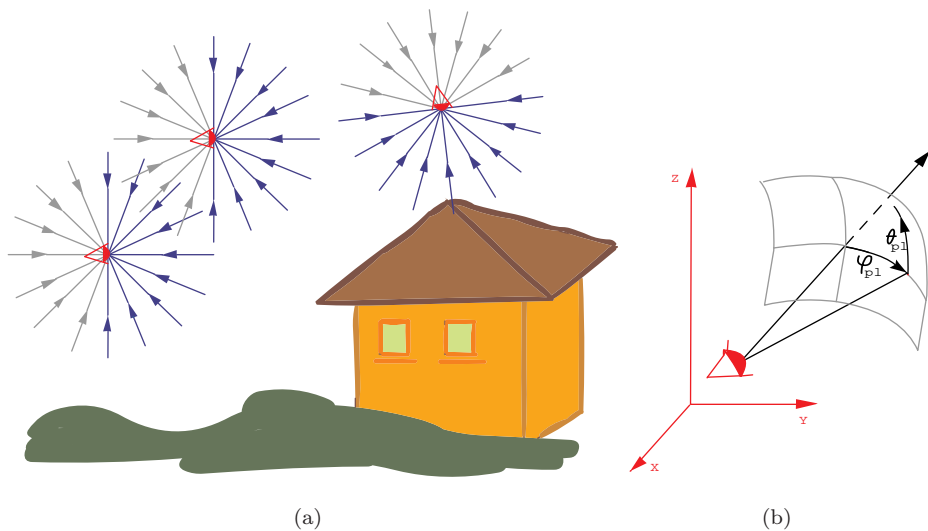


Figure 4.1: Notion of plenoptic function: (a) The plenoptic function describes the information available to an observer at any point in space and time, (b) the image information available from a single viewing point is described by the pencil of light rays passing through the eye; the rays are parameterized in spherical coordinates and so is represented the full sphere of optical information impinging on a point in space.

order to generate a view from a given point in a particular direction we would need to merely plug in appropriate values for (X, Y, Z) and select from a range of $(\theta_{pl}, \varphi_{pl})$ for some constant t . We define a complete sample of the plenoptic function as a full spherical map for a given viewpoint and time value, and an incomplete sample as some solid angle subset of this spherical map.

One can measure any of the variables but an important case is where $\vec{P} = (X, Y, Z)$ is fixed and one records $I_{\vec{P}}(\theta, \varphi)$, that is the light incoming on a perfect punctual observer located at \vec{P} . Measuring $I_{\vec{P}}(\theta, \varphi)$ is equivalent to observing the scene in any direction (θ, φ) from a fixed viewpoint \vec{P} . This can be achieved by a catadioptric sensor as we now explain.

4.1.1 Catadioptric sensors and omni-directional images

Catadioptric sensors have direct applications in a variety of fields—video conferences, computer vision, virtual reality and robotics. The original idea of the catadioptric vision sensors has been initially proposed by Rees [67]. Later this concept was extended [77, 42, 78].

Obviously, the conventional imaging systems (photographic or video) are severely limited in their fields of view. Thus for obtaining an image of entire (360°) scene, either multiple or rotating cameras may be used. But in many cases the rotating camera is not suitable. For instance, it can not simultaneously cover actions in all directions of a dynamic scene. On the other hand, the highest spatial resolution is given with multiple cameras pointing outwards but it is technically difficult to achieve a single effective viewpoint (center of projection) with it. To use mirrors in conjunction with lenses tends out to be an effective way to enhance the field of view. The *catadioptric sensor* is an imaging sensor based on combination of a mirror (catoptrics) and a lens (dioptrics) to form a projection onto the image plane of a (video) camera. The mirror itself presents virtually no chromatic aberration while its surface can provide for a complex remapping of the scene. A catadioptric sensor offers the potential for simultaneously capturing an image with a high resolution on target as well

as a wide-field-of-view periphery. In fact, these are the main advantages of such imaging sensors over the classical ones. These sensors are capable of viewing the world in all directions from the center of projection, i.e. the entire sphere of view around a single point. Consequently, the images obtained from such a sensor are omni-directional because they contain the information from a scene in all directions. Some examples of such images are provided on Figure 4.2:

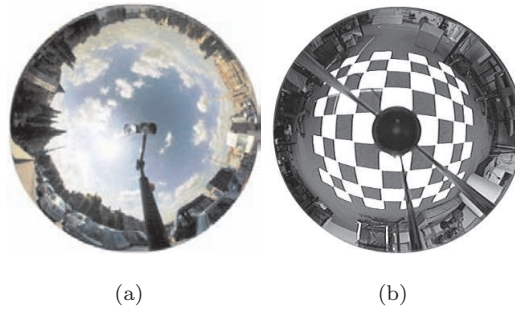


Figure 4.2: Examples of non-Euclidean images: (a) hyperbolic, (b) parabolic.

Depending on the curved mirror used, we can clearly distinguish some particular examples of catadioptric sensors. The images obtained from each one can be defined as *non-Euclidean images* since they result from a reflection of the scene by a non-Euclidean (curved) mirror. The design and properties of these sensors have already been studied [12].

The fixed viewpoint constraint is the requirement that a catadioptric camera only measures the intensity of light passing through a single point in 3-D (Euclidean) space. The direction of the light passing through this point may vary, but that is all. In other words, the catadioptric sensor must sample the 5-D plenoptic function at a single point in 3-D space. The fixed 3-D point at which a catadioptric sensor samples the plenoptic function is known as the *effective viewpoint*.

It is highly desirable that a catadioptric sensor has a single effective viewpoint, i.e. center of projection. The reason for this is obvious: having a unique center of projection permits to warp geometrically correct images from the images captured by the catadioptric sensors. Such a generation is possible because under the single effective viewpoint constraint, every pixel in the captured image measures the irradiance of the light passing through the viewpoint in one particular direction. Since one knows the geometry of the catadioptric sensor, it is possible to precompute this direction for each pixel. Therefore, we can map the irradiance value measured by each pixel onto a plane at any distance from the viewpoint to form a Euclidean (planar) images. Actually, so warping gives a, so called, perspective image, which is more natural to inspect (when presented to a human).

In this chapter, we deal only with non-Euclidean images obtained from catadioptric sensors where all rays intersect in a single point, i.e. sensor that have a single effective viewpoint.

4.1.2 Central catadioptric sensors

The sensors with a single effective viewpoint are called *central catadioptric sensors*. In general, a conic* reflects any ray of light incident with one of its foci (F_M in Figure 4.3) to a ray of light incident with its other focus (F_C). Central catadioptric devices utilize this property and achieve a single effective viewpoint at one of the foci of a conic (F_M). Therefore, sensors fulfilling the single effective viewpoint are, for instance, with hyperbolic and parabolic mirror. We recall some basic facts on both for better understanding the geometry of the images obtained.

*The four mathematical curves that can be found in a cone: circle, ellipse, parabola, hyperbola.

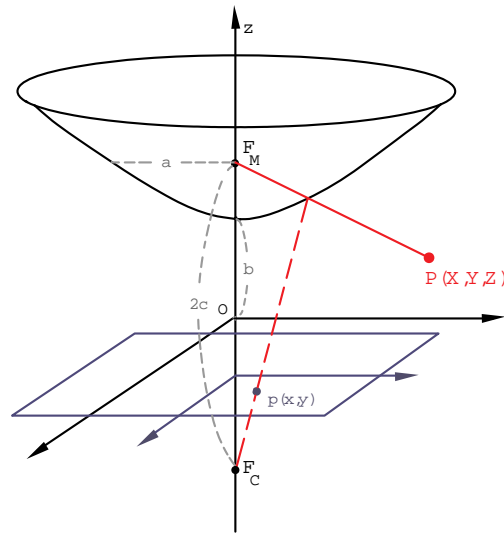


Figure 4.3: Geometric configuration of catadioptric sensor with hyperbolic mirror: the camera center coincides with the focal point of the mirror F_C and the rays reflected from the mirror intersect in F_M .

Hyperbolic catadioptric sensor

In this kind of sensor, an image reflected by a hyperboloidal mirror is taken by a (video) camera. The mirror features a two sheeted hyperboloid with two focuses, F_M and F_C as shown in Figure 4.3. The camera is fixed so that its lens center coincides with the external focus F_C of the hyperbolic mirror. In terms of 3D-world coordinates (X, Y, Z) , the mirror surface is expressed as

$$\frac{X^2 + Y^2}{a^2} - \frac{Z^2}{b^2} = -1, \quad Z > 0. \quad (4.2)$$

The mirror focus F_M is the point $(0, 0, c)$ and the lens center is $(0, 0, -c)$, where $c = \sqrt{a^2 + b^2}$. Here, a, b and c are parameters of the hyperboloidal mirror.

The hyperboloidal mirror has a focal point, which makes possible easy generation of any desired image projected on any designated image plane, such a perspective image or a panoramic image, from an omnidirectional input. It also allows a human user to see familiar perspective images or panorama images instead of an unfamiliar omnidirectional input image deformed by the hyperboloidal mirror. On the other hand, with a hyperbolic projection, the vertical edges in the environment appear radially in the image and the azimuth angles are invariant to changes in distance and height.

Parabolic catadioptric sensor

The paraboloid is the limiting case of the hyperboloid when the focal point F_C goes to infinity. A parabolic catadioptric sensor is shown on Figure 4.4. The mirror, an elliptic paraboloid, is placed at the parabolic focus. It is reflective on its outer surface. All rays from the environment reflect at the parabolic mirror and run parallel to its rotating axis. In this way they reach the image plane which is perpendicular to the direction of the projection. There is a single effective viewpoint in the focus of the paraboloid if the mirror is imaged by an orthographic camera*.

*A camera that uses parallel projection to generate a two-dimensional image of the objects in a three-dimensional model. In particular, an orthographic camera uses orthographic projection, in which the view plane is perpendicular to the viewing direction.

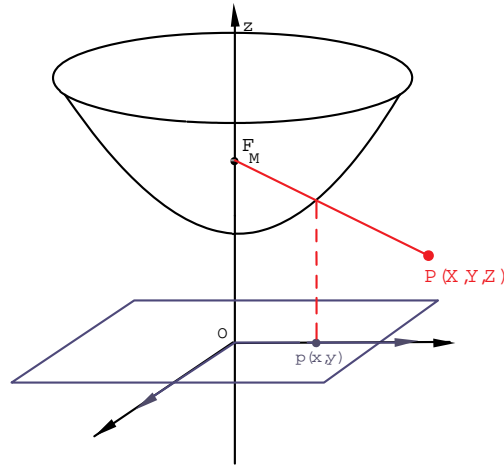


Figure 4.4: Geometric configuration of catadioptric sensor with parabolic mirror: an (orthographic) camera with a parabolic mirror assembled so that rays of the camera are parallel to the mirror symmetry axis and the reflected rays intersect in F_M .

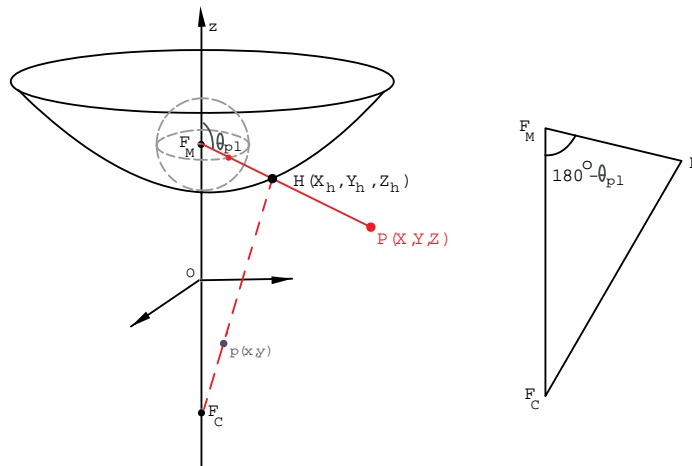


Figure 4.5: Plenoptic sphere centered at the hyperbolic mirror focus F_M .

Actually, a central catadioptric projection is equivalent to a two-step mapping via a sphere. All that can be seen from a single viewpoint can be represented by a non-Euclidean image mapped on a sphere of view. In the case of parabolic mirror, the second step is equivalent to a stereographic projection, while the hyperbolic case is more complicated. In the following two sections, we briefly sketch these equivalencies. In both cases our goal is to recover the spherical coordinates, $\theta = [0, \pi]$ and $\varphi = [0, 2\pi)$, of incoming rays of light at the parabola/hyperbola focus F_M , which locates our ideal observer.

4.1.3 Mapping of a hyperbolic image onto the sphere

Let us consider a sphere with a center in the mirror focus F_M as shown on Figure 4.5. Through the focal projection a point of the hyperboloid (χ, φ) is sent onto the plenoptic sphere with coordinates $(\theta_{pl}, \varphi_{pl})$. Let us assume the mirror is the upper sheet of a unit two-sheeted hyperboloid. Then we have that the parameters $a = b = 1$ and consequently $c = \sqrt{2}$. The meaning of this parameters was

given on Figure 4.3. For deriving the angle θ_{pl} , we consider $\triangle F_M F_C H$, for which it holds:

$$\sphericalangle H F_M F_C = 180^\circ - \theta \quad (4.3)$$

$$F_M F_C = 2\sqrt{2}, \quad (4.4)$$

$$F_C H = \sqrt{X_h^2 + Y_h^2 + (Z_h + \sqrt{2})^2}, \quad (4.5)$$

$$F_M H = \sqrt{X_h^2 + Y_h^2 + (Z_h - \sqrt{2})^2}. \quad (4.6)$$

Applying the law of cosines for $\triangle F_M F_C H$, we write

$$(F_C H)^2 = (F_M F_C)^2 + (F_M H)^2 - 2(F_M F_C)(F_M H) \cos(\sphericalangle H F_M F_C), \quad (4.7)$$

from where we easily derive

$$\cos(\sphericalangle H F_M F_C) = \frac{(F_M F_C)^2 + (F_M H)^2 - (F_C H)^2}{2(F_M F_C)(F_M H)}. \quad (4.8)$$

Substituting the sides with their values as in (4.6) we get

$$\cos(180^\circ - \theta_{pl}) = \frac{2 - Z_h \sqrt{2}}{\sqrt{2(X_h^2 + Y_h^2 + (Z_h - \sqrt{2})^2)}}. \quad (4.9)$$

Then

$$180^\circ - \theta_{pl} = \arccos \frac{2 - Z_h \sqrt{2}}{\sqrt{2(X_h^2 + Y_h^2 + (Z_h - \sqrt{2})^2)}}, \quad (4.10)$$

from where follows

$$\theta_{pl} = 180^\circ - \arccos \frac{2 - Z_h \sqrt{2}}{\sqrt{2(X_h^2 + Y_h^2 + (Z_h - \sqrt{2})^2)}}. \quad (4.11)$$

In other words, an object in the three-dimensional Euclidean space captured by a hyperbolic catadioptric sensor can be represented on the plenoptic sphere with the θ_{pl} derived in (4.11) knowing its special coordinates (X, Y, Z) .

4.1.4 Mapping of a parabolic image onto the sphere

In order to see how a parabolic image is mapped on the sphere, we first consider a cross-section of the paraboloid as shown on Figure 4.6 [35]. All points on the parabola are equidistant to the focus F_M and the directrix d . Let l pass through F_M and be perpendicular to the parabolic axis. If a circle has center F_M and radius equal to twice the focal length of the paraboloid, then the circle and parabola intersect twice the line l and the directrix is tangent to the circle. The North Pole N of the circle is the point diametrically opposite to the intersection of the circle and the directrix. Point P is projected on the circle from its center, which gives Π_1 . This is equivalent to a projective representation, where the projective space (set of rays) is represented as a circle here. One easily sees that Π_2 is the stereographic projection of the point Π_1 to the line l from the North Pole N , where Π_1 is the intersection of the ray $F_M P$ and the circle. We can thus conclude that the parabolic projection of the point P , yields point Π_2 which is collinear with Π_1 and N . Extending this reasoning to three dimensions, the projection by a parabolic mirror is equivalent to projection on the sphere (Π_1) followed by stereographic projection (Π_2).

Therefore, a projection by a parabolic mirror is equivalent to the composition of normalization to the unit sphere followed by stereographic projection. We can thus recover the spherical coordinates of incoming light rays through a simple inverse stereographic projection of the parabolic omnidirectional images.

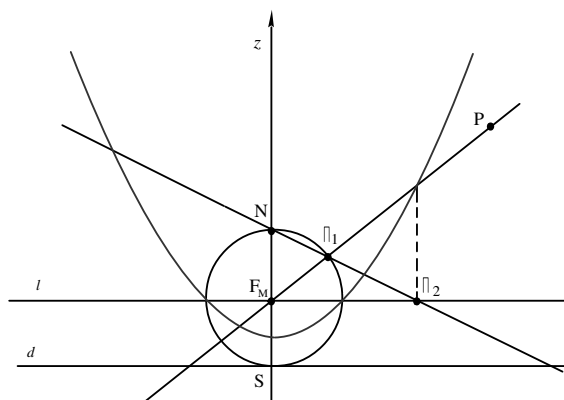


Figure 4.6: Cross-section of mapping the parabolic image on the sphere [35].

4.2 Processing of non-Euclidean images

Considering the discussion on obtaining non-Euclidean images from central catadioptric sensors, we therefore distinguish two main ways toward their processing:

- (i) projecting the non-Euclidean image onto the sphere: In this case, the hyperbolic or parabolic image is mapped on the sphere and the processing is performed on the sphere. It can then be processed by spherical frames (as developed in Section 2.4);
- (ii) direct processing of the non-Euclidean image (this is the image as viewed from the camera pointing into the mirror): In this case, the particular geometry of the reflecting mirror is taken into consideration and the non-Euclidean image is directly processed as it comes in its disk-like form. For instance, for processing such a hyperbolic image we could apply hyperbolic wavelets.

For completing the set of processing techniques for non-Euclidean images, we develop some basic but highly practical techniques. In the following section we develop the scale-space analysis for the spherical and hyperbolic cases. This is followed by derivation of the active contour on the sphere and the hyperboloid. Then we propose an algorithm for local motion estimation on the sphere, which can be applied on both hyperbolic or parabolic images, once they are mapped on the sphere.

4.2.1 Scale-space analysis for non-Euclidean images

It was observed that objects in the world appear in different ways depending on the scale of observation [52]. Besides this multi-scale properties of real-world objects, it is necessary to cope with the complexity of unknown scenes and noise. This brings us to the conclusion that for a deep understanding of the image structure, multi-resolution image representation is necessary. One such representation is to embed the image in a one-parameter family of images. Starting from the data $I(\vec{x})$, one creates a family of images $I(\vec{x}, t)$, where t measures the *scale* or the *time* by setting $I(\vec{x}, t = 0) = I(\vec{x})$. This method derives, from one image, a whole stack of images as it is shown in Figure 4.7. It is interesting to see how one-parameter set of images can be generated. Actually, it is possible on the basis of many different principles. One way is by progressively blurring an image using heat flow/ partial differential equation:

$$\frac{\partial}{\partial t} I(\vec{x}, t) = \Delta I(\vec{x}, t), \quad (4.12)$$

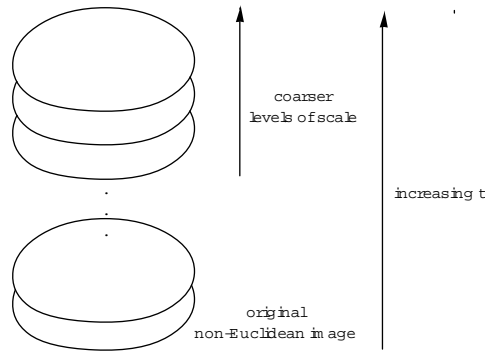


Figure 4.7: Scale-space stack of non-Euclidean images.

where I stands for the luminance of the image which depends on the position \vec{x} and scale t and Δ is the Laplacian operator. Generating images at coarser and coarser resolution is very much like in the wavelet approximation scheme. In fact, generating coarser resolution images can be done by a convolution with a Gaussian kernel at scale t , $I(\vec{x}, t) = I * G(\vec{x}, t)$, where

$$G(x, y, t) = \frac{1}{2\pi t} e^{-\frac{|x|}{4t}}. \quad (4.13)$$

The resulting structure is known as *Gaussian scale-space* and this is another strong link between scale-space and wavelet analysis.

In order to generalize the scale-space analysis to a non-Euclidean manifold, one needs a generalization of the Laplacian operator. On a smooth manifold, the differential df encodes all the first derivative information of a function f in a coordinate-free manner; equivalently, on a Riemannian manifold, the gradient ∇f encodes this information. To keep track of second derivative information, d^2f certainly will not do, and Δf is a complicated combination of second derivative information (and lower order terms). Therefore, Laplacian may be defined on non-Euclidean manifolds with a metric (Riemannian manifolds). In this case, it is still defined as the divergence of the gradient; however, the definitions of the divergence and gradient are modified in order to take into account the curvature. When derived in this way, i.e. taking into account the Riemannian metric, the Laplacian operator is known as *Laplace-Beltrami operator*.

Laplace-Beltrami operator

First, we need to define a Hilbert space of real valued functions on M , i.e. $L^2(M)$, by setting $\langle f, g \rangle = \int_M f(x)g(x)$. Then, let us define the Laplacian $\Delta : L^2(M, g) \rightarrow L^2(M, g)$. We want the Laplacian to agree with the standard Laplacian $-\left(\frac{\partial^2}{\partial(x^1)^2} + \dots + \frac{\partial^2}{\partial(x^n)^2}\right)$ on \mathbb{R}^n . However, this expression depends on the standard coordinates for \mathbb{R}^n , and we need a coordinate-free expression for our realization. This is provided by the classical equation

$$-\left(\frac{\partial^2}{\partial(x^1)^2} + \dots + \frac{\partial^2}{\partial(x^n)^2}\right) = -\text{div} \circ \nabla. \quad (4.14)$$

In local coordinates we have

$$\nabla f = g^{ij} \partial_i f \partial_j, \quad (4.15)$$

where $\partial_j = \frac{\partial}{\partial x^j}$, and g^{ij} is the inverse matrix of g_{ij} .

As for div , integration by parts applied to $f \in C^\infty(\mathbb{R}^n)$ gives

$$-\int_{\mathbb{R}^n} \partial_i X^i \cdot f = \int_{\mathbb{R}^n} \partial_i f \cdot X^i, \quad (4.16)$$

for functions X^i , which shows that the divergence $\partial_i X^i$ of a vector field $X = X^i \partial_i$ on \mathbb{R}^n is characterized by the equation

$$\langle -\text{div} X, f \rangle = \langle X, \nabla f \rangle, \quad (4.17)$$

where the inner products are the global inner products on functions and vector fields induced by the standard dot product.

We are interested in what does the operator $\text{div} X$ look like in local coordinates.

If g denotes the metric tensor on the manifold, the volume form in local coordinates is given by [69]:

$$d\text{vol} = \sqrt{\det g} \, dx^1 \wedge \cdots \wedge dx^n,$$

whenever $(\partial_{x^1}, \dots, \partial_{x^n})$ is a positively oriented basis of $T_x M$.

Finally, for any function $f \in C^\infty(U)$ and vector field $X = X^i \partial_i \in TM$, we have

$$\langle X, \nabla f \rangle = \int_M \langle X, \nabla f \rangle d\text{vol} \quad (4.18)$$

$$= \int_U \langle X^i \partial_i, g^{kj} \partial_k f \partial_j \rangle d\text{vol} \quad (4.19)$$

$$= \int_U X^i (\partial_k f) g^{kj} g_{ij} \sqrt{\det g} \, dx^1 \cdots dx^n \quad (4.20)$$

$$= \int_U X^i (\partial_i f) \sqrt{\det g} \, dx^1 \cdots dx^n \quad (4.21)$$

$$= - \int_U \frac{1}{\sqrt{\det g}} f \cdot \partial_i (X^i \sqrt{\det g}) \sqrt{\det g} \, dx^1 \cdots dx^n \quad (4.22)$$

$$= \langle f, -\frac{1}{\sqrt{\det g}} \partial_i (X^i \sqrt{\det g}) \rangle. \quad (4.23)$$

From here we can see that it must be satisfied

$$\text{div} X = \frac{1}{\sqrt{\det g}} \partial_i (X^i \sqrt{\det g}). \quad (4.24)$$

Here, once again, the Einstein notation is used, so the above is actually a sum in i .

Assuming this expression is independent of choice of coordinates, we can then define the Laplacian on functions to be $\Delta = -\text{div} \circ \nabla$, a second order differential operator. In local coordinates, we get

$$\Delta f = -\frac{1}{\sqrt{\det g}} \partial_j (g^{ij} \sqrt{\det g} \partial_i f) \quad (4.25)$$

$$= -g^{ij} \partial_i \partial_j f + (\text{lower order terms}). \quad (4.26)$$

We must note that this reduces to the usual expression for the Laplacian on \mathbb{R}^n . The last expression shows that not only is the Laplacian determined by the Riemannian metric, but the Laplacian also determines the metric. In other words, by evaluating Δ on a function which is locally $x^i x^j$, we recover g^{ij} and hence g_{ij} . We expect the spectral theory of the Laplacian to be intimately connected with the geometry of (M, g) .

Laplace-Beltrami operator on the hyperboloid

Consider the 2-hyperboloid in \mathbb{R}^3 , with coordinates (x_0, x_1, x_2) , in terms of which the Lobachevskian metric has the form

$$dl^2 = dx_0^2 - dx_1^2 - dx_2^2. \quad (4.27)$$

Let us recall that 2-hyperboloid of radius R is the set of points satisfying the equation

$$x_0^2 - x_1^2 - x_2^2 = R^2. \quad (4.28)$$

In spherical coordinates (ρ, χ, φ) , the metric (4.27) takes the form

$$dl^2 = -\rho^2(d\chi^2 + \sinh^2 \chi d\varphi^2) + d\rho^2. \quad (4.29)$$

For $\rho = R$ we distinguish the upper sheet of the hyperboloid, and for $\rho = -R$, the lower one. Since ρ is constant on the hyperboloid, the metric can be written as

$$-dl^2 = R^2(d\chi^2 + \sinh^2 \chi d\varphi^2). \quad (4.30)$$

We can define a stereographic projection of the hyperboloid onto the plane. It maps the upper sheet of the hyperboloid onto the open disc $x_1^2 + x_2^2 < R^2$. If a point $P \in H_+^2$ has coordinates (x_0, x_1, x_2) , and its projection on the plane has coordinates (u, v) , then

$$\frac{x_1}{u} = \frac{x_0 + R}{R}, \quad \frac{x_2}{v} = \frac{x_0 + R}{R}, \quad (4.31)$$

whence

$$x_1 = u \left(1 + \frac{x_0}{R}\right), \quad x_2 = v \left(1 + \frac{x_0}{R}\right). \quad (4.32)$$

Substituting these in (4.28) and solving the resulting equation for $x_0 > 0$, we get

$$x_0 = -R \left(1 + \frac{2R^2}{u^2 + v^2 - R^2}\right), \quad (4.33)$$

from where we obtain

$$x_1 = \frac{2R^2 u}{R^2 - u^2 - v^2}, \quad x_2 = \frac{2R^2 v}{R^2 - u^2 - v^2}. \quad (4.34)$$

Thus, we can express the induced metric in terms of the coordinates (u, v) . But first, let us recall the hyperbolic coordinates:

$$x_0 = R \cosh \chi \quad (4.35)$$

$$x_1 = R \sinh \chi \cos \varphi \quad (4.36)$$

$$x_2 = R \sinh \chi \sin \varphi \quad (4.37)$$

From the equivalence of (4.35) and (4.33), and putting $u^2 + v^2 = r^2$, we get

$$\cosh \chi = - \left(1 + \frac{2R^2}{r^2 - R^2}\right), \quad (4.38)$$

which, after differentiation, leads to

$$\sinh \chi d\chi = \frac{4R^2 r}{(r^2 - R^2)^2} dr. \quad (4.39)$$

On the other hand, from (4.34), (4.36) and (4.37) we get

$$\sinh^2 \chi = \frac{x_1^2 + x_2^2}{R^2} = \frac{4R^2 r^2}{(R^2 - r^2)^2}. \quad (4.40)$$

From (4.30) and using (4.39) and (4.40) we obtain

$$-dl^2 = \frac{4R^4}{(R^2 - r^2)^2} (dr^2 + r^2 d\varphi^2), \quad (4.41)$$

that is

$$-dl^2 = \frac{4R^4}{(R^2 - u^2 - v^2)^2} (du^2 + dv^2). \quad (4.42)$$

We can see that the metric on the hyperboloid is obtained from the metric on the Euclidean plane by multiplying the latter of a function, i.e. these two metric are "proportional".

If we take out the minus sign in (4.30) we obtain

$$dl^2 = R^2 (d\chi^2 + \sinh^2 \chi d\varphi^2), \quad (4.43)$$

which is the metric on the upper sheet of the hyperboloid.

In terms of the coordinates in the disk (x, y) , the metric on the upper sheet of the unit hyperboloid, i.e $R = 1$, takes the form

$$dl^2 = \frac{4}{(1 - x^2 - y^2)^2} (dx^2 + dy^2), \quad (4.44)$$

where $x^2 + y^2 < 1$. The open disc with the metric (4.44) is the Poincaré model of Lobachevsky's geometry. Taking into account that $dl^2 = g_{ij} dx^i dx^j$ with $x^1 = x$ and $x^2 = y$, we directly obtain the metric tensor :

$$(g)_{ij} = \begin{pmatrix} \frac{4}{(1-x^2-y^2)^2} & 0 \\ 0 & \frac{4}{(1-x^2-y^2)^2} \end{pmatrix} = \begin{pmatrix} g_{xx} & g_{xy} \\ g_{yx} & g_{yy} \end{pmatrix}, \quad (4.45)$$

and accordingly its contra-variant (inverse) metric:

$$(g)^{ij} = \begin{pmatrix} \frac{(1-x^2-y^2)^2}{4} & 0 \\ 0 & \frac{(1-x^2-y^2)^2}{4} \end{pmatrix}. \quad (4.46)$$

Developing the Laplacian operator (4.25) for this particular case we write

$$\Delta_{D_+} f = \frac{1}{\sqrt{\det g}} \left(\frac{\partial}{\partial x} \sqrt{\det g} g^{xx} \frac{\partial f}{\partial x} + \frac{\partial}{\partial y} \sqrt{\det g} g^{yy} \frac{\partial f}{\partial y} \right) \quad (4.47)$$

$$= \frac{(1 - x^2 - y^2)^2}{4} \left(\frac{\partial^2 f}{\partial x^2} + \frac{\partial^2 f}{\partial y^2} \right) \quad (4.48)$$

$$= \frac{(1 - x^2 - y^2)^2}{4} \Delta_{\mathbb{R}^2} f. \quad (4.49)$$

The last result shows that the Laplacian operator on the hyperboloid (or the open disk) is a scaled version of the Laplacian operator on the plane.

We apply this theory on a synthetic hyperbolic image, which is shown on Figure 4.8(a). This is an Escher tiling of the hyperbolic plane. The equivalence between the hyperboloid and the disk is by the stereographic projection through the South Pole.

Obviously, it is straightforward to be numerically implemented the scale-space of hyperbolic image and it is suggested by the linear diffusion equation (4.12). If we denote the original hyperbolic image as $h(x, y, t = 0)$, then it holds $h_t = \Delta h$. As t increases, we approach to a blurred version of the original hyperbolic image as shown on Figure 4.8

Accordingly, for the gradient of a hyperbolic image we have:

$$(\nabla_{D_+} f)_x = g^{xx} \frac{\partial f}{\partial x} + g^{xy} \frac{\partial f}{\partial y} = g^{xx} \frac{\partial f}{\partial x} \quad (4.50)$$

$$(\nabla_{D_+} f)_y = g^{yx} \frac{\partial f}{\partial x} + g^{yy} \frac{\partial f}{\partial y} = g^{yy} \frac{\partial f}{\partial y} \quad (4.51)$$

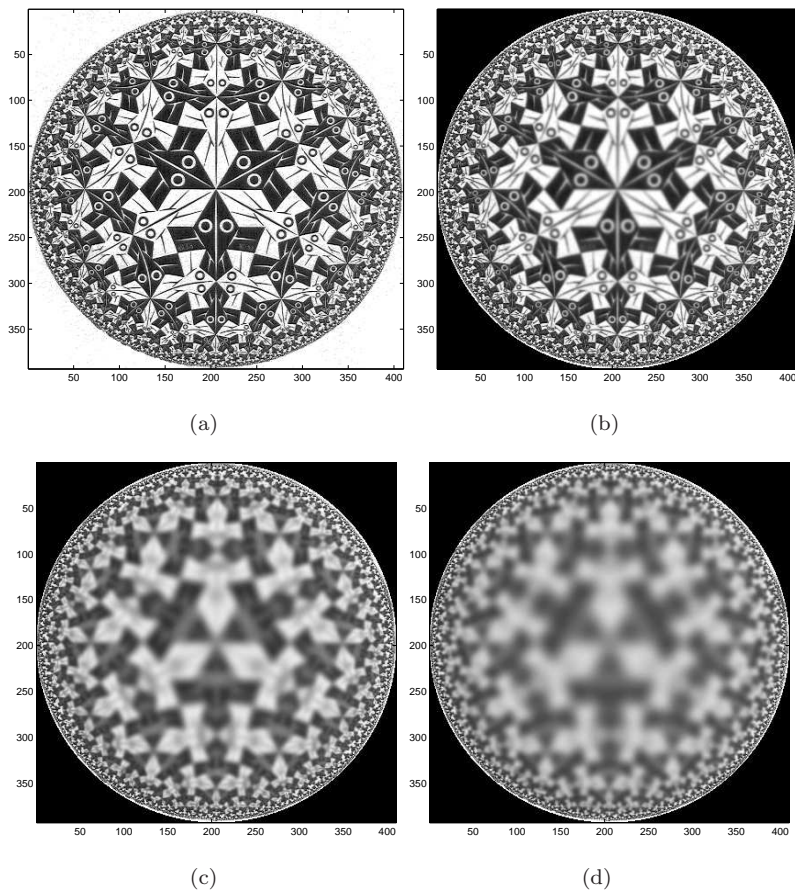


Figure 4.8: Scale-space on a hyperbolic image: (a) original, (b) $t = 10$, (c) $t = 100$, (d) $t = 300$.

We can easily see that

$$\nabla_{D_+} f = \frac{(1 - x^2 - y^2)^2}{4} \nabla_{\mathbb{R}^2} f. \quad (4.52)$$

Therefore, the gradient on the hyperboloid is proportional to the gradient of the Euclidean plane. What concerns a hyperbolic disk image, its gradient is a scaled gradient of the plane. From an image processing point of view, the gradient operator is used to localize contours, as shown on Figure 4.9.

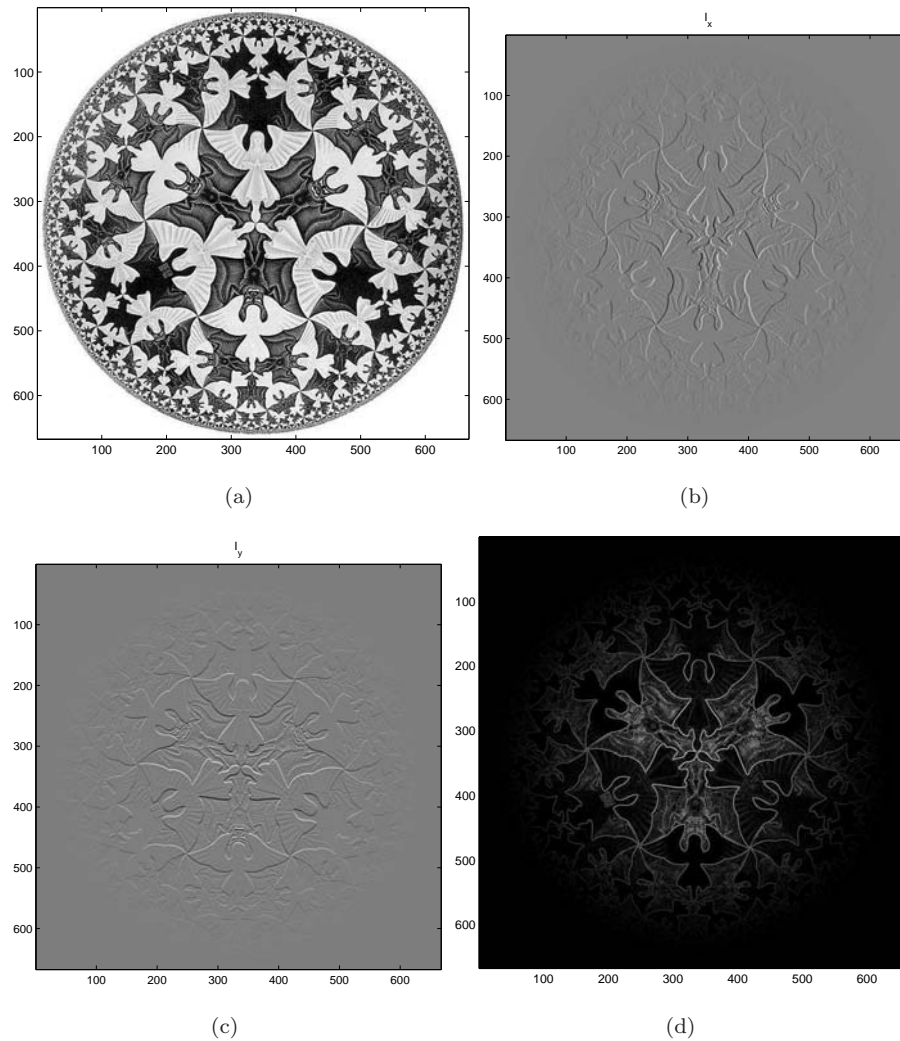


Figure 4.9: Gradient of a hyperbolic image: (a) original image, (b) gradient in direction of x , (c) gradient in direction of y , (d) magnitude of the gradient.

Laplace-Beltrami operator on the sphere

Consider the sphere as introduced in Section 2.1.1. A point on the sphere is the vector (x_0, x_1, x_2) . In terms of spacial coordinates, the Euclidean metric takes the form

$$dl^2 = dx_0^2 + dx_1^2 + dx_2^2 = dr^2 + r^2(d\theta^2 + \sin^2 \theta d\varphi^2). \quad (4.53)$$

On the surface $R = r$, the differential $dr = 0$, so the metric induced on the sphere is given by

$$dl^2 = r^2(d\theta^2 + \sin^2 \theta d\varphi^2) \quad (4.54)$$

The stereographic projection of the sphere sends a point (θ, φ) on the sphere to the point with polar coordinates (R, φ) in the plane, for which we have that $\varphi = \varphi, R = r \cot \theta/2$. In terms of these new coordinates the metric becomes

$$dl^2 = \frac{4r^4}{(r^2 + R^2)^2}(dR^2 + R^2 d\varphi^2). \quad (4.55)$$

Let us proceed toward (Euclidean) coordinates in the disc: $(x_1, x_2) \equiv (x, y) \in \mathbb{R}^2$, where $R^2 = x^2 + y^2$. We obtain

$$dl^2 = \frac{4r^4}{(r^2 + x^2 + y^2)^2}(dx^2 + dy^2). \quad (4.56)$$

We can see that in this case as well, the metric on the sphere is obtained from the Euclidean metric on the plane by multiplying the latter by the function $\frac{4r^4}{(r^2 + x^2 + y^2)^2}$:

$$dl_{S^2}^2 = \frac{4r^4}{(r^2 + x^2 + y^2)^2} dl_{\mathbb{R}^2}^2. \quad (4.57)$$

Accordingly, the metric on the unit sphere, i.e. $R = 1$, is derived as

$$(g)_{ij} = \begin{pmatrix} \frac{4}{(1+x^2+y^2)^2} & 0 \\ 0 & \frac{4}{(1+x^2+y^2)^2} \end{pmatrix}, \quad (4.58)$$

and accordingly

$$(g)^{ij} = \begin{pmatrix} \frac{(1+x^2+y^2)^2}{4} & 0 \\ 0 & \frac{(1+x^2+y^2)^2}{4} \end{pmatrix}. \quad (4.59)$$

Developing the Laplacian operator (4.25) on the sphere, we obtain

$$\Delta_{S^2} f = \frac{1}{\sqrt{\det g}} \left(\frac{\partial}{\partial x} \sqrt{\det g} g^{xx} \frac{\partial f}{\partial x} + \frac{\partial}{\partial y} \sqrt{\det g} g^{yy} \frac{\partial f}{\partial y} \right) \quad (4.60)$$

$$= \frac{(1+x^2+y^2)^2}{4} \left(\frac{\partial^2 f}{\partial x^2} + \frac{\partial^2 f}{\partial y^2} \right) \quad (4.61)$$

$$= \frac{(1+x^2+y^2)^2}{4} \Delta_{\mathbb{R}^2} f. \quad (4.62)$$

The gradient of a spherical image is

$$\nabla_{S^2} f = \frac{(1+x^2+y^2)^2}{4} \nabla_{\mathbb{R}^2} f, \quad (4.63)$$

It is clear that both the Laplace-Beltrami operator and the gradient of a spherical non-Euclidean image are proportional to the Euclidean image, as it turned out to be in the hyperbolic case. Implementing the scale-space for spherical image is analogous to the hyperbolic one. The stack of images forming the spherical scale-space is shown on Figure 4.10. Looking at the spherical gradient on Figure 4.11, we can clearly distinguish the main difference in gradient's action for the hyperbolic and the spherical case. In the first case the gradient acts as it never reaches the border of the disk. This is a natural consequence of the hyperbolic geometry. In the case of sphere, the action is stronger toward and including the border of the disk.

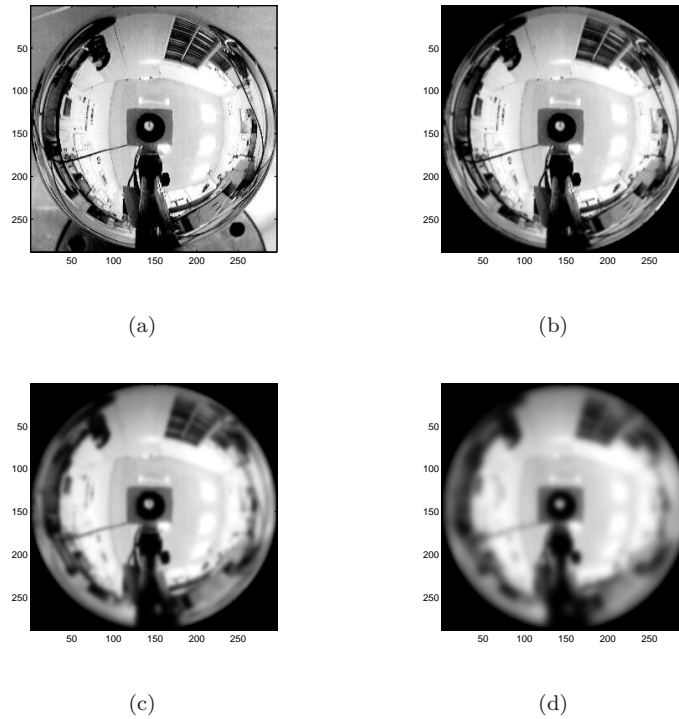


Figure 4.10: Scale-space on a spherical image: (a) original image, (b) $t = 10$, (c) $t = 100$, (d) $t = 300$.

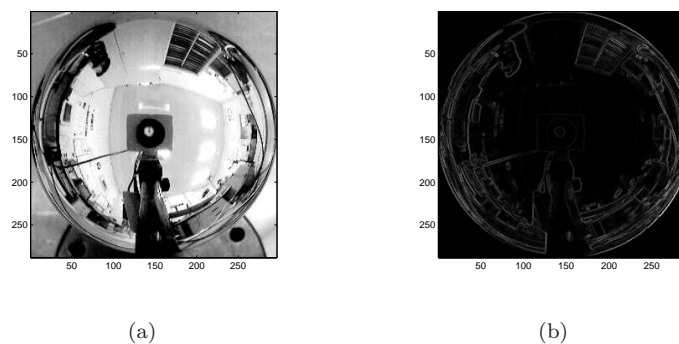


Figure 4.11: Gradient of a real spherical image: (a) original image, (b) spherical gradient.

4.2.2 Active contours on non-Euclidean manifolds

The notion of active contour model

In classical (Euclidean) image analysis, image segmentation is a fundamental component and its main objective consists in determine the semantically important parts of images. When it is needed to detect objects in an image, the *active contour* segmentation model is used. It proposes to detect the closest contours from an initial position and was introduced in [45]. This model detects sharp image intensity variations by deforming (like a snake) a curve \mathcal{C} toward the edges of objects. The evolution equation of the parametric Euclidean curve $\mathcal{C}(p) = (x(p), y(p)) \in \Omega, p \in [0, 1]$ is given by the minimization of the following energy functional defined for any observed Euclidean image $I_0 \in L^1(\Omega)$ and any positive parameters α, β, λ :

$$F(\mathcal{C}) = \alpha \int_0^1 \left| \frac{\partial \mathcal{C}(p)}{\partial p} \right|^2 dp + \beta \int_0^1 \left| \frac{\partial^2 \mathcal{C}}{\partial p^2} \right|^2 dp + \lambda \int_0^1 f^2(I_0(\mathcal{C})) dp, \quad (4.64)$$

where the first two terms are physics based smoothness constraints on the geometry of the curve since the first term makes the snake act like a membrane and the second term makes it act like a thin plate. The sum of both terms is called the *internal energy*. The third term, called the *external energy*, attracts the curve toward the boundaries of objects using an edge detecting function f vanishing at infinity such as the function:

$$f(I_0) = \frac{1}{1 + \gamma |\nabla(I_0 \star G_\sigma)|^2}, \quad (4.65)$$

where G_σ is the Gaussian function with standard deviation σ , $I_0 \star G_\sigma$ is the low-passed image I_0 and γ is an arbitrary positive constant. With this method it is not possible to detect more than one object, since the final curve has the same topology as the initial one as shown on Figure 4.12. From Figure 4.12(d) we can clearly see that this model cannot naturally change its topology during the evolution process since the final contour has captured only one object. To overcome the limitation

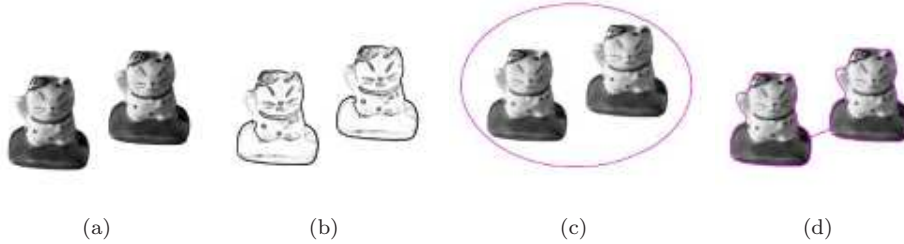


Figure 4.12: Active contour on a Euclidean image: (a) original image (b) associated edge detecting function $f(I_0)$, (c) the contour at the beginning of the evolution process, (d) the contour at the end of the evolution process.

of the changes of topology, a powerful level-set method was proposed in [64, 71]. The curve \mathcal{C} is then implicitly represented by a function of higher dimension, called the level-set function, and the curve evolution equation can be re-written in a level set formulation.

Based on energy functional in (4.64), a new one was proposed in [21, 47, 46]:

$$E(\mathcal{C}) = \int_0^1 f(|\nabla I_0(\mathcal{C}(p))|) |\mathcal{C}'(p)| dp = \int_0^{L(\mathcal{C})} f(|\nabla I_0(\mathcal{C}(s))|) ds, \quad (4.66)$$

where ds is the Euclidean element of length and $L(\mathcal{C})$ is the Euclidean length of the curve \mathcal{C} defined by $L(\mathcal{C}) = \int_0^1 |\mathcal{C}'(p)| dp = \int_0^{L(\mathcal{C})} ds$ and $|\mathcal{C}'(p)|$ is the length of tangent vector in Euclidean geometry.

Hence, the functional (4.66) is actually a new length obtained by weighting the Euclidean element of length ds by the function f which contains information concerning the boundaries of objects. The function f is the edge detecting function as defined in equation (4.65). The equivalence between (4.64) and (4.66) was shown in [21].

Geometric active contour model on non-Euclidean manifold

The active contours in non-Euclidean spaces follows the theory of its counterpart in Euclidean spaces. Actually, the curve minimizing $E(\mathcal{C})$ in (4.66) is a geodesic in a Riemannian space with metric tensor $g_{ij} = f(|\nabla I_0|)\delta_{ij}$, where f is the edge detecting function.

Once again, the goal is to minimize E for \mathcal{C} in a certain allowed space of curves. Following the classical model, we need to minimize the energy functional

$$\int_0^1 f(|\nabla I(\mathcal{C}(h))|)|\mathcal{C}'(h)|dh, \quad (4.67)$$

where f is an edge-detecting function, disk-curve $\mathcal{C}(h) = (x(h), y(h)) \in \Omega, h \in [0, 1]$ and $|\mathcal{C}'(h)|$ is the length of tangent vector in Euclidean geometry. This functional is not intrinsic since it depends on the parametrization h , which for the moment is arbitrary.

In other words, the solution to the energy problem is given by a curve of minimal "weighted distance" between given points. Distance is measured in a given Riemannian space with the first fundamental form g_{ij} .

$$|\mathcal{C}'(h)| = \sqrt{g_{ij}\mathcal{C}'_i\mathcal{C}'_j}dh, \quad (i, j = 1, 2), \quad (4.68)$$

Since $\mathcal{C} = (\mathcal{C}_1, \mathcal{C}_2)$, we can write

$$|\mathcal{C}'(h)| = \sqrt{g_{11}\mathcal{C}'_1{}^2 + 2g_{12}\mathcal{C}'_1\mathcal{C}'_2 + g_{22}\mathcal{C}'_2{}^2}dh. \quad (4.69)$$

The geodesic is computed by the calculus of variations. Thus we are brought to minimizing the following functional:

$$\mathcal{E}(\mathcal{C}) = \int_0^1 f(|\nabla I(\mathcal{C}(h))|)\sqrt{(g)_{ij}\mathcal{C}'_i\mathcal{C}'_j}dh. \quad (4.70)$$

Taking our two specific examples, sphere and hyperboloid, with tensor metrics derived in (4.58) and (4.45), respectively, we could even simplify it. Both metrics are diagonal; $g_{12} = g_{21} = 0, g_{11} = g_{22}$ and thus $\sqrt{(g)_{ij}\mathcal{C}'_i\mathcal{C}'_j} = \sqrt{g^{1/2}\delta_{ij}\mathcal{C}'_i\mathcal{C}'_j}$. The energy functional becomes:

$$\begin{aligned} \mathcal{E}(\mathcal{C}) &= \int_0^1 f(|\nabla I(\mathcal{C}(h))|)\sqrt{g^{1/2}\delta_{ij}\mathcal{C}'_i\mathcal{C}'_j}dh \\ &= \int_0^1 g^{1/4}f(|\nabla I(\mathcal{C}(h))|)\left|\frac{\partial\mathcal{C}}{\partial h}\right|, \end{aligned}$$

where g denotes the determinant of $(g)_{ij}$. We denote the edge detector function for the spherical/hyperbolic (non-Euclidean) image as $f_D = g^{1/4}f(|\nabla I(\mathcal{C})|)$, where f is the edge detector in Euclidean case. Let us introduce an artificial time t and consider the family of curves $\mathcal{C}(t)$ in the disk D . The first variation of the energy $\mathcal{E}(\mathcal{C})$ is then $\frac{d\mathcal{E}(\mathcal{C})}{dt}$, and it reads :

$$\frac{d\mathcal{E}(\mathcal{C})}{dt} = \int_0^1 \frac{df_D(|\nabla I(\mathcal{C})|)}{dt}\left|\frac{\partial\mathcal{C}}{\partial h}\right|dh + \int_0^1 f_D(|\nabla I(\mathcal{C})|)\frac{d}{dt}\left|\frac{\partial\mathcal{C}}{\partial h}\right|dh. \quad (4.71)$$

Let us first develop the derivatives separately. We start by the term

$$\frac{df_D(|\nabla I(\mathcal{C})|)}{dt} = \frac{d}{dt}f_D(\mathcal{C}_1, \mathcal{C}_2) = \frac{\partial f_D}{\partial u_1}\frac{\partial\mathcal{C}_1}{\partial t} + \frac{\partial f_D}{\partial u_2}\frac{\partial\mathcal{C}_2}{\partial t} = \langle \nabla f_D, \frac{\partial\mathcal{C}}{\partial t} \rangle, \quad (4.72)$$

where the contour was considered as a vector $\mathcal{C} \equiv (\mathcal{C}_1, \mathcal{C}_2)$ and for obtaining its derivative the chain rule was applied.

Next, we look at the term:

$$\frac{d}{dt} \left| \frac{\partial \mathcal{C}}{\partial h} \right| = \frac{d}{dt} \sqrt{\left(\frac{\partial \mathcal{C}_1}{\partial h} \right)^2 + \left(\frac{\partial \mathcal{C}_2}{\partial h} \right)^2} \quad (4.73)$$

$$= \frac{1}{2\sqrt{\left(\frac{\partial \mathcal{C}_1}{\partial h} \right)^2 + \left(\frac{\partial \mathcal{C}_2}{\partial h} \right)^2}} 2 \left(\frac{\partial \mathcal{C}_1}{\partial h} \frac{\partial^2 \mathcal{C}_1}{\partial t \partial h} + \frac{\partial \mathcal{C}_2}{\partial h} \frac{\partial^2 \mathcal{C}_2}{\partial t \partial h} \right) \quad (4.74)$$

$$= \left\langle \frac{\frac{\partial \mathcal{C}}{\partial h}}{\left| \frac{\partial \mathcal{C}}{\partial h} \right|}, \frac{\partial^2 \mathcal{C}}{\partial t \partial h} \right\rangle \quad (4.75)$$

Then the energy variation in (4.71) becomes

$$\frac{d\mathcal{E}(\mathcal{C})}{dt} = \int_0^1 \langle \nabla f_D, \frac{\partial \mathcal{C}}{\partial t} \rangle \left| \frac{\partial \mathcal{C}}{\partial h} \right| dh + \int_0^1 f_D \left\langle \frac{\frac{\partial \mathcal{C}}{\partial h}}{\left| \frac{\partial \mathcal{C}}{\partial h} \right|}, \frac{\partial^2 \mathcal{C}}{\partial t \partial h} \right\rangle dh \quad (4.76)$$

We integrate by parts with respect to h the second integral and thus obtain

$$\frac{d\mathcal{E}(\mathcal{C})}{dt} = \int_0^1 \langle \nabla f_D, \frac{\partial \mathcal{C}}{\partial t} \rangle \left| \frac{\partial \mathcal{C}}{\partial h} \right| dh - \int_0^1 \left\langle \frac{\partial \mathcal{C}}{\partial t}, f_D \frac{\partial}{\partial h} \left(\frac{\frac{\partial \mathcal{C}}{\partial h}}{\left| \frac{\partial \mathcal{C}}{\partial h} \right|} \right) + \frac{\frac{\partial \mathcal{C}}{\partial h}}{\left| \frac{\partial \mathcal{C}}{\partial h} \right|} \langle \nabla f_D, \frac{\partial \mathcal{C}}{\partial h} \rangle \right\rangle dh.$$

This equation can be rewritten as

$$\frac{d\mathcal{E}(\mathcal{C})}{dt} = \int_0^1 \left| \frac{\partial \mathcal{C}}{\partial h} \right| \left\langle \frac{\partial \mathcal{C}}{\partial t}, \nabla f_D - \frac{f_D}{\left| \frac{\partial \mathcal{C}}{\partial h} \right|} \frac{\partial}{\partial h} \left(\frac{\frac{\partial \mathcal{C}}{\partial h}}{\left| \frac{\partial \mathcal{C}}{\partial h} \right|} \right) - \frac{\frac{\partial \mathcal{C}}{\partial h}}{\left| \frac{\partial \mathcal{C}}{\partial h} \right|} \langle \nabla f_D, \frac{\frac{\partial \mathcal{C}}{\partial h}}{\left| \frac{\partial \mathcal{C}}{\partial h} \right|} \rangle \right\rangle dh \quad (4.77)$$

By definition, for the tangent vector we have:

$$\mathcal{T} = \frac{\frac{\partial \mathcal{C}}{\partial h}}{\left| \frac{\partial \mathcal{C}}{\partial h} \right|}. \quad (4.78)$$

The normal vector \mathcal{N} is perpendicular to the tangent and by its definition it reads

$$\frac{1}{\left| \frac{\partial \mathcal{C}}{\partial h} \right|} \frac{\partial}{\partial h} \mathcal{T} = \kappa \mathcal{N}, \quad (4.79)$$

with κ being the curvature. Using these two definitions, the energy variation becomes:

$$\frac{d\mathcal{E}(\mathcal{C})}{dt} = \int_0^1 \left| \frac{\partial \mathcal{C}}{\partial h} \right| \left\langle \frac{\partial \mathcal{C}}{\partial t}, \nabla f_D - \kappa f_D \mathcal{N} - \langle \mathcal{T}, \nabla f_D \rangle \mathcal{T} \right\rangle dh. \quad (4.80)$$

Decomposing the vector $\nabla f_D = \langle \nabla f_D, \mathcal{N} \rangle \mathcal{N} + \langle \nabla f_D, \mathcal{T} \rangle \mathcal{T}$, we obtain:

$$\frac{d\mathcal{E}(\mathcal{C})}{dt} = \int_0^1 \left| \frac{\partial \mathcal{C}}{\partial h} \right| \left\langle \frac{\partial \mathcal{C}}{\partial t}, \langle \nabla f_D, \mathcal{N} \rangle \mathcal{N} - \kappa f_D \mathcal{N} \right\rangle dh. \quad (4.81)$$

From here it is obvious that the direction of the strongest energy variations correspond to

$$\frac{\partial \mathcal{C}}{\partial t} = (\kappa f_D - \langle \nabla f_D, \mathcal{N} \rangle) \mathcal{N}, \quad (4.82)$$

which is the equation of the active geodesic contour, representing an evolving curve in the direction of its normal vector and under the action of a force \mathcal{F} :

$$\frac{\partial \mathcal{C}}{\partial t} = \mathcal{F}\mathcal{N}. \quad (4.83)$$

In the specific case $f_D = 1 \Rightarrow f = \frac{1}{g^{1/4}}$, we get an evolving curve which minimizes the mean curvature:

$$\frac{\partial \mathcal{C}}{\partial t} = \kappa \mathcal{N}. \quad (4.84)$$

Active contour on the hyperboloid

The specific evolution of the active contour on the hyperboloid is shown on Figure 4.13. The initial contour has an oval form and it is preserved on the hyperbolic image. Its evolution is analogical to that in the Euclidean plane: the given initial contour shrinks towards its center, while the geometry of contour seen on the hyperboloid does not have the same form as seen on the disk-image.

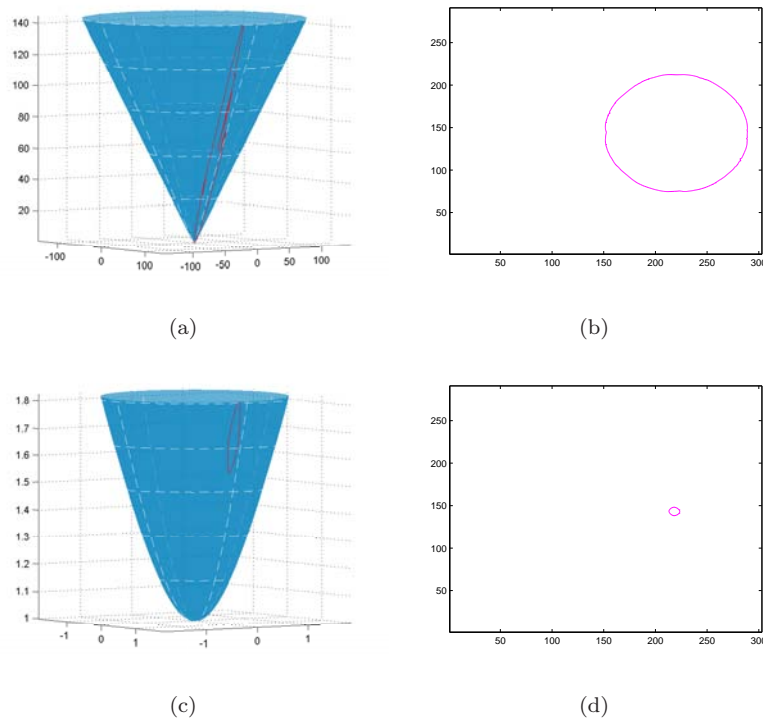


Figure 4.13: Evolution of geometric active contour on the hyperboloid: (a) initial contour on the hyperboloid, (b) initial contour viewed on the unit disk, (c) the contour at final state of evolution on the hyperboloid, (d) the contour at final state of evolution, viewed on the unit disk .

We use a synthetic hyperbolic image to perform a hyperbolic segmentation using active contour. The image consists of a set of three hyperbolic triangles and is shown on Figure 4.14(a). Applying the hyperbolic gradient on it, we obtain the edge detecting function as shown on Figure 4.14(b). After evolution of the contour toward the objects of interest, it stops at their border and thus they are segmented from the background.

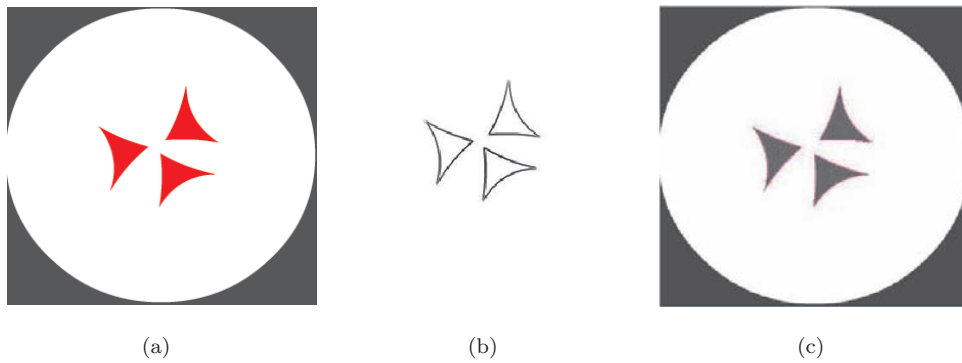


Figure 4.14: Segmentation in a synthetic hyperbolic image: (a) original image, (b) edge detection function, (c) segmented image .

Active contour on the sphere

On Figure 4.15 is shown the evolution of a contour on the sphere. It is interesting to notice that opposite to the hyperbolic case, here the contour evolves towards the border of the disk. Such a behavior is natural and it comes directly from the action of the spherical geometry on the contour.

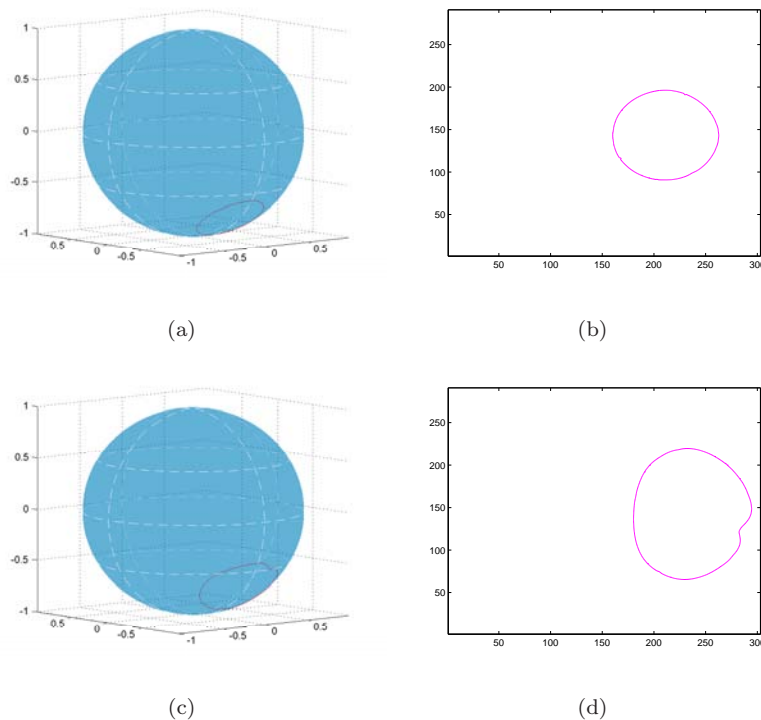


Figure 4.15: Evolution of the geometric active contour on the sphere: (a) the initial state of the contour on the sphere, (b) the initial state of the contour projected on the disk, (c) the contour in a further state of its evolution on the sphere, (d) the contour in a further state of its evolution projected on the disk .

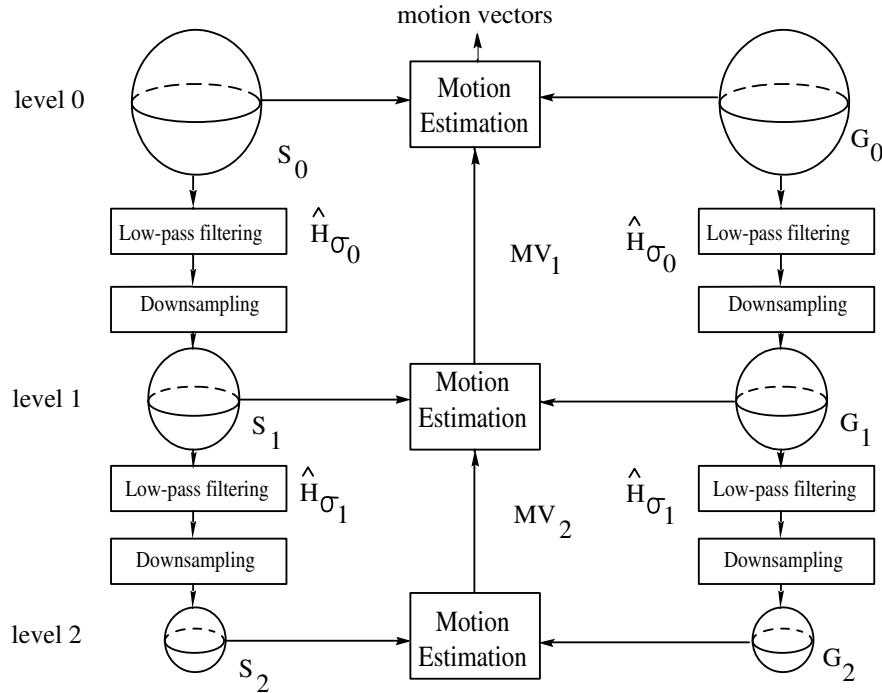


Figure 4.16: Algorithm for local motion estimation on the sphere.

4.2.3 Motion estimation in spherical omnidirectional images

In Section 4.1 we have seen that the plenoptic function can be represented directly in the spherical domain. Let us suppose that we have several central catadioptric sensors capturing a static 3-D scene from arbitrary viewpoints. According Sections 4.1.3 and 4.1.4, each of these sensors outputs an omnidirectional image that can be mapped on a sphere. However the output images from multiple cameras are obviously correlated, and a rate efficient representation of the overall 3-D scene first requires the removal of redundancy between the different views. Thus a local motion estimation algorithm that captures the correlation between omnidirectional images, taken from arbitrary view point, is needed. The choice of local motion estimation is driven by the perspective of an efficient coding of the plenoptic function.

Multiresolution motion estimation algorithm

Due to the distortion introduced in the unwrapped images, we choose to implement the local motion estimation algorithm directly in the spherical domain. The algorithm is based on L -level multiresolution approach, that pairs solid angles from two spherical images. This is depicted on Figure 4.16. Assume that the motion estimation aims at computing a prediction \widetilde{G}_0 of the spherical image G_0 from S_0 , that is an image scene, but captured from a different (arbitrary) viewpoint. Both spherical images are first filtered and down-sampled, to generate a multiresolution representation of the scene, as described in Section 2.5.2 for analysis spherical Laplacian pyramid. The multiresolution approach clearly limits the complexity of the motion estimation, and improves the consistency of the motion field.

The local motion estimation consists in the following. The lowest resolution spherical image G_{L-1} is divided into uniform solid angles, of size $M\delta_\theta^{L-1} \times N\delta_\varphi^{L-1}$. The predicted blocks g_{L-1}^i in

G_{L-1} are then paired with the best matching blocs with the same size in the reference image S_{L-1} with a search window of $W\delta_\theta^{L-1} \times W\delta_\varphi^{L-1}$, around the location of the g_{L-1}^i . A full search for each block g_{L-1}^i determines the best prediction in a MSE sense, s_{L-1}^i , and the corresponding motion vectors. Note that, even if the blocks g_{L-1}^i are all distinct, the blocks s_{L-1}^i may be overlapping. The implemented block-matching algorithm also takes into account the periodicity in the azimuthal direction.

The motion estimation is then iteratively redefined as successive resolution levels. The blocks at resolution l , b_l^i , are divided into four sub-blocks of size $M^{l-1}\delta_\theta^{l-1} \times N^{l-1}\delta_\varphi^{l-1}$ at the next resolution level $l-1$, with $2\delta_\theta^{l-1} = \delta_\theta^l$ and $2\delta_\varphi^{l-1} = \delta_\varphi^l$, due to the change in the resolution level. The motion vector from lower resolution level l serve as initial estimations of the motion vectors of the four sub-block b_l^i . These estimations are then refined based on the spherical images at resolution $l-1$, with a full search in a window of size $W^{l-1}\delta_\theta^{l-1} \times W^{l-1}\delta_\varphi^{l-1}$ around the location specified by the motion vector from the lower resolution l , that has been up-sampled accordingly. The same process is applied iteratively up to the fines resolution, and eventually outputs the field of motion vectors. These motion vectors, along with the spherical image s_0 are used to form the prediction \widetilde{G}_0 of G_0 . The prediction error is finally denoted $E_0 = G_0 - \widetilde{G}_0$.

Algorithm 4.1: Multiresolution local motion estimation on the sphere

$l = L - 1. MV_L^i = [0, 0], \forall i, \delta_\theta^0 = \frac{\pi}{2B_0}, \delta_\varphi^0 = \frac{2\pi}{2B_0}, B_0 \equiv$ full resolution

repeat

$\delta_\theta^l = 2^l \delta_\theta^0, \delta_\varphi^l = 2^l \delta_\varphi^0;$

divide G_l into I uniform blocks of size $M^l \delta_\theta^l \times N^l \delta_\varphi^l;$

$i = 0;$

repeat

$(p_i, q_i) \leftarrow$ position of $g_l^i;$

$MV_l^i \leftarrow$ up-sample $MV_{l+1}^i;$

$\Omega \leftarrow \{(p, q)\}$ such that

$p \in [p_i + MV_l^i(1) - \frac{W^l \delta_\theta^l}{2} + 1, p_i + MV_l^i(1) + \frac{W^l \delta_\theta^l}{2}]$ and

$q \in [q_i + MV_l^i(1) - \frac{W^l \delta_\varphi^l}{2} + 1, q_i + MV_l^i(1) + \frac{W^l \delta_\varphi^l}{2}];$

$f_l^i = \arg \min_{\Omega} MSE(g_l^i, s_l^i);$

$(w_i, t_i) \leftarrow$ position of $s_l^i;$

$MV_l^i \leftarrow [p_i + w_i, q_i + t_i];$

$i \leftarrow i + 1;$

until $i > I$

$l \leftarrow l - 1;$

until $l < 0$

This algorithm is built on a multiresolution representation of spherical images, in order to provide a consistent motion field even with images captured at very different viewpoints. The multiresolution coarse-to-fine motion estimation method used for classical images [22] has been adapted to the spherical framework, in order to report similarities between solid angles, instead of blocks of pixels.

Experimental results

Here we present the results of the algorithm proposed above. Figure 4.17 shows one image captured by a parabolic catadioptric sensor, i.e. parabolic image, after it has been mapped on the sphere at the second finest resolution level ($l = 1$). Figures 4.18(a) and 4.18(b) show the original unfolded images



Figure 4.17: Parabolic image mapped on the sphere of view, level $l = 1$.



(a)

(b)

Figure 4.18: Level 0 of the motion estimation algorithm: (a) first original unfolded sphere S_0 , (b) second original unfolded sphere G_0 .

of a static scene captured from two different viewpoints. These images represent real parabolic images mapped on the sphere, but shown here as Euclidean images in the θ, φ - plane, to provide visibility of all image's features. Figure 4.19 represents the prediction \tilde{G}_0 of the second frame, with the local motion estimation algorithm, and Figure 4.20 shows the corresponding prediction error E_0 , that has been inverted to highlight the distribution of the residual error (a white pixel corresponds to no error). The number of decomposition levels is $L = 5$. The size of the blocks has been set to 4×4 . The size of the search window can vary from one resolution to another. We have chosen the window size for the lowest level to be 32×32 and for all higher levels 8×8 . In this way, the proposed algorithm can capture big motions with low search complexity. It can be seen that the motion estimation is quite efficient, since the predicted image provides a very good approximation of G_0 . Also, the prediction error is almost exclusively located along high frequency components, as expected from the high-pass characteristics of motion estimation. Figure 4.21 represents the motion field that corresponds to the third level of resolution. It can be seen that the motion field is mostly consistent with the spherical image information. For example, motion vectors are very small in



Figure 4.19: Motion predicted image \tilde{G}_0 .



Figure 4.20: Motion predicted error E_0 .

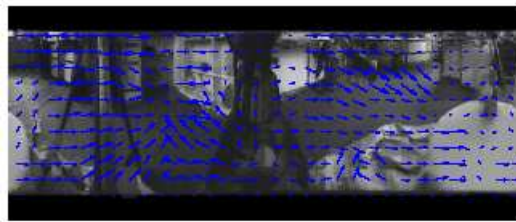


Figure 4.21: Motion field at resolution level 3.

uniform and static areas like the table (on the right-hand side of the predicted image). As expected from local motion estimation algorithm driven by MSE criteria, the motion vectors do not however necessarily follow semantic objects, but rather pair areas with similar luminance information. This behavior can be encountered for large motions where the change of lighting conditions can induce discrepancies. On the other side, the obtained motion field precisely depicts smaller movements.

Figure 4.22 presents the evolution of the residual energy relative to the original image energy, as a function of the size of the solid angle, and the size of the search window. It can be seen that a larger search window at the coarsest resolution level generally improves the quality of the motion estimation. In the same time, smaller block size provides also a better prediction, since details can be better approximated. In a coding perspective however, a trade-off needs to be found between the accuracy of the motion estimation, and the coding cost, which generally increases with the number of motion vectors.

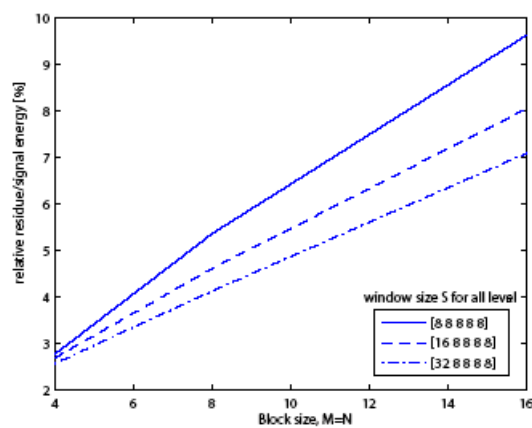


Figure 4.22: Relative energy of the prediction error, for different block and search window sizes ($L = 5$).

4.3 Summary

- One possible way to measure the plenoptic function is by using catadioptric sensor for capturing a given scene. The images obtained by them are termed as non-Euclidean since they carry the geometry of the sensor's curved mirror.
- One way to process non-Euclidean images, obtained from both hyperbolic or parabolic catadioptric sensors, is to map them on the sphere and then process the data on the sphere. Or, for directly working in the geometry of the mirror, the processing is performed on the corresponding image.
- For completing the set of processing techniques for non-Euclidean images, the following have been proposed:
 - Scale-space analysis of non-Euclidean images. Laplace-Beltrami operator and gradient for the hyperbolic and spherical cases are somehow "proportional" to the Euclidean one.
 - Geometric active contour on non-Euclidean images. Its derivation comes from minimization of a contour but solved for the specific geometry: hyperbolic, spherical.
 - A local motion estimation algorithm that captures the correlation between non-Euclidean images obtained from central catadioptric sensors but taken from arbitrary viewpoints in the space. A multiresolution approach has been used for improving the motion field accuracy, while limiting the computational complexity of the motion estimation scheme. The local motion estimation algorithm has been shown to be quite efficient since the residual error is kept small and mostly located around edges or high frequency components in the predicted image. The proposed scheme can certainly represent an important building block in a rate distortion efficient encoder for distributed omnidirectional images.

Conclusions

The central theme of this dissertation is how to process scalar data on non-Euclidean manifold, with a twist toward multiresolution techniques.

First, we derive discrete spherical frames based on the existing continuous wavelet transform on the sphere. We started with half-continuous spherical wavelet frames where the scale of the continuous wavelet transform has been discretized but the position kept varying continuously. Then it had been shown that a controlled frame may be constructed in order to get an easy reconstruction of functions from their decomposition coefficients. Second, the complete discretization of the continuous spherical wavelets has been performed. Thus both scale and position have been discretized. A numerical implementation of so derived spherical discrete frames has been done based on existing FFTs on the sphere and we gave several illustrative examples.

Second, we dealt with the hyperboloid and a family of wavelets on this non-Euclidean manifold of constant negative curvature have been derived. Even though the conformal group of the 2-hyperboloid is identified, $SO(1, 3)$, the group theoretical approach for construction wavelets on the hyperboloid does not give a dilation which acts only on one sheet of the two-sheeted hyperboloid. In contrary, the dilation operator acting on a point on the upper sheet of the hyperboloid sends it on the down and vice versa. An approach toward hyperbolic wavelets based on a convolution theorem for square-integrable functions on the hyperboloid has been applied. This theorem has been derived by the means of the Fourier-Helgason transform. The continuous wavelet transform on the hyperboloid has been obtained by convolution of the scaled wavelets with the signal. The wavelet transform has been proved to be invertible whenever the hyperbolic wavelets satisfy a particular admissibility condition.

We then focused on potential applications: processing non-Euclidean images. These images are closely related to the plenoptic function, which is represented in spherical coordinates and turns out to be in a tight relation with projection of the scene onto a sphere. Mapping of the hyperbolic and parabolic images on the sphere has been shown. Thus for non-Euclidean image coding, spherical frames are suggested to be applied. Another possibility for processing is directly in the geometry of the mirror used for obtaining the non-Euclidean image. As an efficient tool for processing a non-Euclidean image reflected by a hyperbolic mirror, hyperbolic wavelets stand. The set of processing tools for non-Euclidean images has been extended to scale-space analysis and active contours for the case of the sphere and hyperboloid. Finally, a multiresolution motion estimation algorithm on the sphere has been proposed as an application of the multiresolution paradigm.

As a future work, it is interesting to check the existence of wavelets on another non-Euclidean manifolds. One interesting case is the ellipsoid. Actually, the sphere is a particular version of the ellipsoid. Another case is the paraboloid(elliptic or hyperbolic). It seems logical to get desired wavelets if the construction technique is based on the convolution. One could then think to extend these constructions by performing well-behaved deformations of the manifold.

Appendix A

In this Appendix we prove Proposition 20 from Chapter 2.

Proof:

Let us define

$$S = \sum_{j \in \mathbb{Z}} \sum_{p, q \in \mathbb{Z}[2\beta_j]} \nu_j w_{jp} \mathcal{W}_f(\omega_{jppq}, a_j) \overline{\widetilde{\mathcal{W}}_f(\omega_{jppq}, a_j)}.$$

Since

$$\mathcal{W}_f(\omega, a) = \sum_{(l, m) \in \mathcal{N}} \sqrt{\frac{4\pi}{2l+1}} \widehat{f}(l, m) \overline{\widehat{\psi}_a(l, 0)} Y_l^m(\omega)$$

and

$$\widetilde{\mathcal{W}}_f(\omega, a) = \sum_{(l, m) \in \mathcal{N}} \sqrt{\frac{4\pi}{2l+1}} G_\psi(l)^{-1} \widehat{f}(l, m) \overline{\widehat{\psi}_a(l, 0)} Y_l^m(\omega),$$

we have

$$\begin{aligned} S &= \sum_{j \in \mathbb{N}} \sum_{p, q \in \mathbb{Z}[2\beta_j]} \sum_{(l, m) \in \mathcal{N}} \sum_{(l', m') \in \mathcal{N}} \frac{4\pi}{\sqrt{(2l+1)(2l'+1)}} \widehat{f}(l, m) \overline{\widehat{f}(l', m')} \\ &\quad \nu_j w_{jp} G_\psi^{-1}(l) \overline{\widehat{\psi}_{a_j}(l, 0)} \widehat{\psi}_{a_j}(l', 0) Y_l^m(\omega_{jppq}) \overline{Y_{l'}^{m'}(\omega_{jppq})} \\ &= \sum_{j \in \mathbb{N}} 4\pi \nu_j \sum_{(l, m) \in \mathcal{N}} \sum_{(l', m') \in \mathcal{N}} \frac{\widehat{f}(l, m) \overline{\widehat{f}(l', m')}}{\sqrt{(2l+1)(2l'+1)}} G_\psi^{-1}(l) \overline{\widehat{\psi}_{a_j}(l, 0)} \widehat{\psi}_{a_j}(l', 0) \\ &\quad \sum_{p, q \in \mathbb{Z}[2\beta_j]} w_{jp} Y_l^k(\omega_{jppq}) \overline{Y_{l'}^{k'}(\omega_{jppq})}. \end{aligned}$$

If $l + l' < \beta_j$, the product $Y_l^m \overline{Y_{l'}^{m'}}$ having order $l + l'$ [74], the weight w_{jp} provides the quadrature formula [15, 29]

$$\sum_{p, q \in \mathbb{Z}[2\beta_j]} w_{jp} Y_l^m(\omega_{jppq}) \overline{Y_{l'}^{m'}(\omega_{jppq})} = \int_{S^2} d\mu(\omega) Y_l^m(\omega) \overline{Y_{l'}^{m'}(\omega)} = \delta_{ll'} \delta_{mm'}, \quad (6.1)$$

for all $|m| \leq l$ and all $|m'| \leq l'$. Therefore, the sum S splits in two parts

$$\begin{aligned} S &= \sum_{j \in \mathbb{N}} \sum_{p, q \in \mathbb{Z}[2\beta_j]} \sum_{\substack{(l, m) \in \mathcal{N} \\ (l', m') \in \mathcal{N} \\ l+l' < 2\beta_j}} \dots + \sum_{j \in \mathbb{N}} \sum_{p, q \in \mathbb{Z}[2\beta_j]} \sum_{\substack{(l, k) \in \mathcal{N} \\ (l', m') \in \mathcal{N} \\ l+l' \geq 2\beta_j}} \dots \\ &= C + D. \end{aligned}$$

The first term C , where (6.1) is valid, reduces to

$$\begin{aligned} C &= \sum_{j \in \mathbb{N}} 4\pi\nu_j \sum_{\substack{(l,m) \in \mathcal{N} \\ l < \beta_j}} \frac{1}{(2l+1)} |\widehat{f}(l, m)|^2 G_\psi^{-1}(l) |\widehat{\psi}_{a_j}(l, 0)|^2 \\ &= \sum_{(l,m) \in \mathcal{N}} |\widehat{f}(l, m)|^2 \sum_{j \in \mathbb{N}} \frac{4\pi\nu_j}{(2l+1)} \mathbb{1}_{[0, \beta_j[}(l) G_\psi^{-1}(l) |\widehat{\psi}_{a_j}(l, 0)|^2. \end{aligned}$$

If (2.94) is verified, then

$$K_0 \|f\|^2 \leq C \leq K_1 \|f\|^2. \quad (6.2)$$

Let us analyze the part D . Since $Y_l^m(\omega_{j p q}) = Y_l^m(\theta_{j p}, 0) e^{i m \varphi_{j q}}$, with $\theta_{j p} = \frac{2p+1}{4\beta_j} \pi$ et $\varphi_{j q} = \frac{q\pi}{\beta_j}$, we find

$$\begin{aligned} & \sum_{q \in \mathbb{Z}[2\beta_j]} Y_l^m(\omega_{j p q}) \overline{Y_{l'}^{m'}(\omega_{j p q})} \\ &= Y_l^m(\theta_{j p}, 0) \overline{Y_{l'}^{m'}(\theta_{j p}, 0)} \sum_{q \in \mathbb{Z}[2\beta_j]} e^{i(m-m') \frac{q\pi}{\beta_j}} \\ &= 2\beta_j Y_l^m(\theta_{j p}, 0) \overline{Y_{l'}^{m'}(\theta_{j p}, 0)} \sum_{\substack{t \in \mathbb{Z} \\ |m+2t\beta_j| \leq l'}} \delta_{m', m+2t\beta_j} \\ &= 2\beta_j \sum_{\substack{t \in \mathbb{Z} \\ |m+2t\beta_j| \leq l'}} Y_l^m(\theta_{j p}, 0) \overline{Y_{l'}^{m+2t\beta_j}(\theta_{j p}, 0)} \delta_{m', m+2t\beta_j} \\ &= 2\beta_j \sum_{t \in \mathbb{Z}} \mathbb{1}_{[-l', l']}(m+2t\beta_j) Y_l^m(\theta_{j p}, 0) \overline{Y_{l'}^{m+2t\beta_j}(\theta_{j p}, 0)} \delta_{m', m+2t\beta_j} \end{aligned}$$

So,

$$\begin{aligned} D &= \sum_{j \in \mathbb{N}} 8\pi\nu_j \beta_j \sum_{(l,m) \in \mathcal{N}} \sum_{l' \in \mathbb{N}} \sum_{t \in \mathbb{Z}} \frac{\mathbb{1}_{[2\beta_j, +\infty[}(l+l') \mathbb{1}_{[-l', l']}(m+2t\beta_j)}{\sqrt{(2l+1)(2l'+1)}} \widehat{f}(l, m) \overline{\widehat{f}(l', m+2t\beta_j)} \\ & \quad G_\psi^{-1}(l) \widehat{\psi}_{a_j}(l, 0) \widehat{\psi}_{a_j}(l', 0) \sum_{p \in \mathbb{Z}[2\beta_j]} w_{j p} Y_l^m(\theta_{j p}, 0) \overline{Y_{l'}^{m+2t\beta_j}(\theta_{j p}, 0)}. \end{aligned}$$

Therefore,

$$\begin{aligned} |D| &\leq \sum_{j \in \mathbb{N}} 8\pi\nu_j \beta_j \sum_{(l,m) \in \mathcal{N}} \sum_{l' \in \mathbb{N}} \sum_{t \in \mathbb{Z}} \frac{\mathbb{1}_{[2\beta_j, +\infty[}(l+l') \mathbb{1}_{[-l', l']}(m+2t\beta_j)}{\sqrt{(2l+1)(2l'+1)}} |\widehat{f}(l, m)| |\widehat{f}(l', m+2t\beta_j)| \\ & \quad G_\psi(l)^{-1} |\widehat{\psi}_{a_j}(l, 0)| |\widehat{\psi}_{a_j}(l', 0)| \sum_{p \in \mathbb{Z}[2\beta_j]} w_{j p} |Y_l^m(\theta_{j p}, 0)| |Y_{l'}^{m+2t\beta_j}(\theta_{j p}, 0)| \\ &\leq \sum_{j \in \mathbb{N}} 4\pi\nu_j \sum_{(l,m) \in \mathcal{N}} \sum_{l' \in \mathbb{N}} \sum_{t \in \mathbb{Z}} |\widehat{f}(l, m)| |\widehat{f}(l', m+2t\beta_j)| \mathbb{1}_{[-l', l']}(m+2t\beta_j) \\ & \quad \mathbb{1}_{[\beta_j, +\infty[}(l+l') G_\psi^{-1}(l) |\widehat{\psi}_{a_j}(l, 0)| |\widehat{\psi}_{a_j}(l', 0)| \end{aligned}$$

where we used the fact that $|Y_l^m| \leq \sqrt{\frac{2l+1}{4\pi}}$ for all $(l, m) \in \mathcal{N}$, and $\sum_{p \in \mathbb{Z}[2\beta_j]} w_{j p} = \frac{4\pi}{2\beta_j}$.

The sums on m and t can be bounded since

$$\begin{aligned}
& \sum_{t \in \mathbb{Z}} \sum_{|m| \leq l} |\widehat{f}(l, m)| |\widehat{f}(l', m + 2t\beta_j)| \mathbb{1}_{[-l', l']}(m + 2t\beta_j) \\
& \leq \sum_{t \in \mathbb{Z}} \left[\sum_{|m| \leq l} |\widehat{f}(l, m)|^2 \mathbb{1}_{[-l', l']}(m + 2t\beta_j) \right]^{1/2} \left[\sum_{|m| \leq l} |\widehat{f}(l', m + 2t\beta_j)|^2 \mathbb{1}_{[-l', l']}(m + 2t\beta_j) \right]^{1/2} \\
& \leq \left[\sum_{t \in \mathbb{Z}} \sum_{|m| \leq l} |\widehat{f}(l, m)|^2 \mathbb{1}_{[-l', l']}(m + 2t\beta_j) \right]^{1/2} \left[\sum_{t \in \mathbb{Z}} \sum_{|m| \leq l} |\widehat{f}(l', m + 2t\beta_j)|^2 \mathbb{1}_{[-l', l']}(m + 2t\beta_j) \right]^{1/2} \\
& \leq \left[\sum_{|m| \leq l} |\widehat{f}(l, m)|^2 \left[\frac{2l' + 1}{2\beta_j} + 1 \right] \right]^{1/2} \left[\sum_{t \in \mathbb{Z}} \sum_{m' = -l + 2t\beta_j}^{l + 2t\beta_j} |\widehat{f}(l', m')|^2 \mathbb{1}_{[-l', l']}(m') \right]^{1/2} \\
& \leq \left[\sum_{|m| \leq l} |\widehat{f}(l, m)|^2 \left[\frac{2l' + 1}{2\beta_j} + 1 \right] \right]^{1/2} \left[\sum_{t \in \mathbb{Z}} \sum_{m' \in \mathbb{Z}} |\widehat{f}(l', m')|^2 \mathbb{1}_{[-l, l]}(m' - 2t\beta_j) \mathbb{1}_{[-l', l']}(m') \right]^{1/2} \\
& \leq \left[\sum_{|m| \leq l} |\widehat{f}(l, m)|^2 \left[\frac{2l' + 1}{2\beta_j} + 1 \right] \right]^{1/2} \left[\sum_{t \in \mathbb{Z}} \sum_{m' = -l'}^{l'} |\widehat{f}(l', m')|^2 \mathbb{1}_{[-l, l]}(m' - 2t\beta_j) \right]^{1/2} \\
& \leq \left[\sum_{|m| \leq l} |\widehat{f}(l, m)|^2 \left[\frac{2l' + 1}{2\beta_j} + 1 \right] \right]^{1/2} \left[\sum_{|m'| \leq l'} |\widehat{f}(l', m')|^2 \left[\frac{2l + 1}{2\beta_j} + 1 \right] \right]^{1/2} \\
& \leq (2\beta_j)^{-1} (2(l + \beta_j) + 1)^{1/2} (2(l' + \beta_j) + 1)^{1/2} \left[\sum_{|m| \leq l} |\widehat{f}(l, m)|^2 \right]^{1/2} \left[\sum_{|m'| \leq l'} |\widehat{f}(l', m')|^2 \right]^{1/2},
\end{aligned}$$

applying the Cauchy-Schwarz inequality first on the sum over m and then on the sum over t . Therefore,

$$|D| \leq \sum_{l, l' \in \mathbb{N}} \left[\sum_{|m| \leq l} |\widehat{f}(l, m)|^2 \right]^{1/2} \left[\sum_{|m'| \leq l'} |\widehat{f}(l', m')|^2 \right]^{1/2} \chi(l, l')$$

with

$$\chi(l, l') = \sum_{j \in \mathbb{N}} \frac{2\pi\nu_j c_j(l, l')}{\beta_j} \mathbb{1}_{[2\beta_j, +\infty[}(l + l') G_{\psi}^{-1}(l) |\widehat{\psi}_{a_j}(l, 0)| |\widehat{\psi}_{a_j}(l', 0)|.$$

and $c_j(l, l') = (2(l + \beta_j) + 1)^{\frac{1}{2}} (2(l' + \beta_j) + 1)^{\frac{1}{2}}$.

Denoting $F_l^2 = \sum_{|m| \leq l} |\widehat{f}(l, m)|^2$, we obtain with the Cauchy-Schwarz inequality

$$\begin{aligned}
|D| & \leq \sum_{l \in \mathbb{N}} F_l \sum_{l' \in \mathbb{N}} \chi(l, l') F_{l'} \\
& \leq \|F\| \|\mathcal{X}F\| \\
& = \|f\| \|\mathcal{X}F\|,
\end{aligned}$$

with $F = (F_l)_{l \in \mathbb{N}}$, $\|F\|^2 = \sum_{l \in \mathbb{N}} |F_l|^2 = \|f\|^2$, $\mathcal{X} = (\chi(l, l'))_{l, l' \in \mathbb{N}}$ and $(\mathcal{X}F)_l = \sum_{l' \in \mathbb{N}} \chi(l, l') F_{l'}$. If (2.94) is satisfied, we have

$$|D| \leq \|f\| \|\mathcal{X}\| \|f\| = \delta \|f\|^2,$$

with the norm

$$\|\mathcal{X}\| = \sup_{(G_l)_{l \in \mathbb{N}}} \frac{\|\mathcal{X}G\|}{\|G\|}.$$

The proof of the theorem is provided by noting that

$$0 < (K_0 - \delta) \|f\|^2 < C - |D| \leq S \leq C + |D| < (K_1 + \delta) \|f\|^2 < \infty.$$

■

Bibliography

- [1] E. H. Adelson and J. Bergen. The Plenoptic Function and the Elements of Early Vision. *Annals of Physics*, 1:1–37, 1993.
- [2] S. T. Ali, J.-P. Antoine, and J.-P. Gazeau. Continuous frames in Hilbert space. *Computational Models of Visual Processing*, 222:3–20, 1991.
- [3] S. T. Ali, J.-P. Antoine, and J.-P. Gazeau. *Coherent States, Wavelets and Their Generalizations*. Springer-Verlag, Berlin-Heidelberg-New York, 1999.
- [4] S. T. Ali, J.-P. Antoine, J.-P. Gazeau, and U. Mueller. Coherent states and their generalizations: A mathematical overview. *Reviews Math. Phys.*, 7:1013–1104, 1995.
- [5] S. T. Ali and M. Bertola. Symplectic geometry of the Wigner transform on noncompact symmetric spaces. In *XXIV International Conference on Group Theoretical Methods in Physics*, 2002.
- [6] M. A. Alonso, G. S. Pogosyan, and K. B. Wolf. Wigner functions for curved spaces. I. On hyperboloids. *J. Math. Phys.*, 7(12):5857–5871, 2002.
- [7] J.-P. Antoine, L. Demanet, L. Jacques, and P. Vandergheynst. Wavelets on Sphere: Implementation and Approximations. *Appl. Comput. Harmon. Anal.*, 13:177–200, 2002.
- [8] J.-P. Antoine, R. Murenzi, P. Vandergheynst, and S. T. Ali. *Two-dimensional Wavelets and Their Relatives*. University Press, Cambridge, 2004.
- [9] J.-P. Antoine and P. Vandergheynst. Wavelets on n-sphere and related manifolds. *J. Math. Phys.*, 39:3987–4008, 1998.
- [10] J.-P. Antoine and P. Vandergheynst. Wavelets on 2-Sphere: a Group Theoretical Approach. *Appl. Comput. Harmon. Anal.*, 7:1–30, 1999.
- [11] J.-P. Antoine and P. Vandergheynst. Wavelets on 2-Sphere and Related Manifolds. *Reports Math. Phys.*, 43:13–24, 1999.
- [12] R. Benosman and S. B. Kang. *Panoramic Vision: Sensors, Theory and Applications*. Springer, Berlin-Heidelberg-New York, 2001.
- [13] M. Berger. *A Panoramic View of Riemannian Geometry*. Springer, Berlin-Heidelberg-New York, 2003.
- [14] I. Bogdanova, P. Vandergheynst, J.-P. Antoine, L. Jacques, and M. Morvidone. Stereographic frames of wavelets on the sphere. *Appl. Comput. Harmon. Anal.*, 19:223–252, 2005.

-
- [15] J. Boyd. *Chebyshev and Fourier Spectral Methods, Lecture notes in engineering*. Springer-Verlag, New York.
- [16] J. Bros, J.-P. Gazeau, and U. Moschella. Quantum field theory in the de Sitter universe. *Physical Review Letters*, 73(13):1746–1749, 1994.
- [17] A. Brun, C.-F. Westin, M. Herberthson, and H. Knutsson. Fast manifold learning based on Riemannian normal coordinates. In *Proceedings of the SCIA;05*, Joensuu, Finland, June 2005.
- [18] T. Buelow. Multiscale image processing on the sphere. In *DAGM-Symposium*, 2002.
- [19] P. J. Burt and E. H. Adelson. The Laplacian pyramid as a compact image code. *IEEE Transactions on Communications*, COM-31,4:532–540, 1983.
- [20] J. Cannon, W. Floyd, R. Kenyon, and W. Parry. Hyperbolic Geometry. *Flavors of Geometry, MRSI Publications*, 31, 1997.
- [21] V. Caselles, R. Kimmel, and G. Sapiro. Geodesic Active Contours. *International Journal of Computer Vision*, 22(1):61–79, 1997.
- [22] G. Conklin and S. Hemani. Multi-resolution motion estimation. In *Proceedings of the IEEE International Conference on Acoustics, Speech, and Signal Processing*, 1997.
- [23] H. S. M. Coxeter. *Non-Euclidean Geometry*. The mathematical association of America, Washington, D.C.20036, 1998.
- [24] K. Daniilidis, A. Makadia, and T. Bulow. Image processing in catadioptric planes: spatiotemporal derivatives and optical flow computation. In *Proceedings of the Third Workshop on Omnidirectional Vision*, page 3. IEEE Computer Society, 2002.
- [25] I. Daubechies. *Ten Lectures on Wavelets*. SIAM, Philadelphia, PA, 1992.
- [26] I. Daubeshies. Orthogonal bases of compactly supported wavelets. *Comm. Pur. Appl. Math.*, 41:909–996, 1988.
- [27] I. Daubeshies. The wavelet transform, time-frequency localization and signal analysis. *IEEE Transactions on Information Theory*, 36(5):961–1005, 1990.
- [28] I. Daubeshies. Orthonormal bases of compactly supported wavelets ii, variations on a theme. *SIAM Journal of Mathematical Analysis*, 24(3):499–519, 1993.
- [29] J. R. Driscoll and D. M. Healy. Computing Fourier transforms and convolutions on the 2-sphere. *Adv. in Appl. Math.*, 15:202–250, 1994.
- [30] J. R. Duffin and A. C. Schaeffer. A class of nonharmonic Fourier series. In *Trans. Amer. Math. Soc.*, volume 72, pages 341–366, 1952.
- [31] R. J. Freedden, T. Maier, and S. Zimmermann. A survey on wavelet methods for (geo)applications. *Revista Mathematica Complutense*, 8:170–184, 1966.
- [32] D. Gabor. Theory of communication. *Journal of I.E.E.*, 93:429–441, 1946.
- [33] J.-P. Gazeau, R. Balbinot, A. Gradechi, and B. Giorini. Phase space for quantum elementary systems in anti-de-Sitter and Minkowski space-times. *J. Phys. A: Math Gen.*, 25(13):1185–1210, 1989.

-
- [34] J.-P. Gazeau and V. Hussin. Poincaré contraction of $SU(1,1)$ Fock-Bargmann structure. *J. Phys. A: Math Gen.*, (25):1549–1573, 1992.
- [35] C. Geyer and K. Daniilidis. Catadioptric projective geometry. *International Journal of Computer Vision*, 45(3):223–243, 2001.
- [36] A. Grossmann and J. Morlet. Decomposition of Hardy functions into square integrable wavelets of constant shape. *SIAM J. Math. Anal.*, 15:723–736, 1984.
- [37] P. Hagmann. *From diffusion MRI to brain connectomics*. PhD thesis, EPFL, Lausanne, Suisse, 2005.
- [38] D. M. Healy, D. Rockmore, P. J. Kostelec, and S. S. B. Moore. FFTs for the 2-Sphere - Implementations and Variations. volume 9, pages 341–385, 2003.
- [39] D. M. Healy, D. Rockmore, and S. S. B. Moore. An FFT for the 2-sphere and Application. In *Proc. of ICASSP-96*, volume 3, pages 1323–1326, 1996.
- [40] C. Heil and D. Walnut. Continuous and discrete wavelet transforms. *SIAM Review*, pages 628–666, 1989.
- [41] S. Helgason. *Geometric Analysis on Symmetric Spaces*, volume 39. AMS, mathematical surveys and monographs edition, 1994.
- [42] J. Hong and all. Image-based homing. *Proceedings of ICRA*, pages 620–625, 1991.
- [43] L. Jackson. *Signals, Systems, and Transforms*. Addison-Wesley, Massachusetts, 1991.
- [44] L. Jacques. *Ondelettes, repères et couronne solaire*. PhD thesis, Université Catholique de Louvain, Louvain-la-Neuve, Belgique, 2004.
- [45] M. Kass, A. Witkin, and D. Terzopoulos. Snakes: Active Contour Models. *International Journal of Computer Vision*, pages 321–331, 1987.
- [46] S. Kichenassamy, A. Kumar, P. Olver, A. Tannenbaum, and A. Yezzi. Conformal curvature flows: From phase transitions to active vision. *Archive for Rational Mechanics and Analysis*, 134:275–301, 1996.
- [47] S. Kichenassamy, A. Kumar, P. Olver, A. Tannenbaum, and A. Yezzi. Gradient Flows and Geometric Active Contour Models. In *IEEE International Conference on Computer Vision*, pages 810–815, 1999.
- [48] P. Kraniuskas. *Transforms in Signals and Systems*. Addison-wesley, Wokingham, England, 1992.
- [49] H. Kwakernaak and R. Sivan. *Modern Signals and Systems*. Prentice Hall, Englewood Cliffs, NJ 07632, 1991.
- [50] S. Lang. *Differential and Riemannian Manifolds*. Springer-Verlag, New Yourk Inc., 1995.
- [51] L. Li, F. Mao, W. Qian, and L. P. Clarke. Wavelet transform for directional feature extraction in medical imaging. In *IEEE Trans. Pattern Anal. Machine Intell.*, volume 3, page 500, 1997.
- [52] T. Lindeberg. Scale space: A framework for handling image structures at multiple scale. In *CERN School of Computing Egmond and Zee*, 1996.

-
- [53] A. Makadia and K. Daniilidis. Direct 3D-rotation estimation from spherical images via a generalized shift theorem. In *Proc. IEEE CVPR*, 2003.
- [54] S. Mallat. *A Wavelet Tour of Signal Processing*. Academic Press, 1998.
- [55] S. G. Mallat. A theory for multiresolution signal decomposition: the wavelet representation. In *IEEE Trans. Pattern Anal. Machine Intell.*, volume 11, 1981.
- [56] Y. Meyer. *Wavelets*. Springer Verlag, Berlin, 1989.
- [57] Y. Meyer. *Les Ondelettes, Algorithmes et Applications*. Armand Colin, 1992.
- [58] H. N. Mhaskar, F. J. Narcowich, J. Prestin, and J. D. Ward. Polynomial frames on the sphere. *Adv. Comput. Math.*, 13:3873–403, 2000.
- [59] F. Morgan. *Riemannian Geometry, a Beginner's Guide*. A K Peters, Wellesley, Massachusetts, 1998.
- [60] R. Murenzi. Wavelet transforms associated to the n-dimensional Euclidean group with dilations: Signals in more than one dimensions. Springer-Verlag, 1989.
- [61] R. Murenzi. *Ondelettes multidimensionnelles et applications à l'analyse d'images*. PhD thesis, Université Catholique de Louvain, Louvain-la-Neuve, Belgique, 1990.
- [62] A. Oppenheim and R. Schaffer. *Discrete-time signal processing*. Prentice Hall, Englewood Cliffs, New Jersey, 1989.
- [63] A. Oppenheim, A. Willsky, and T. Young. *Signals and Systems*. Prentice Hall, Englewood Cliffs, New Jersey, 1983.
- [64] S. Osher and J. A. Sethian. Fronts Propagating with Curvature-Dependent Speed: Algorithms Based on Hamilton-Jacobi Formulations. *Journal of Computational Physics*, 79(1)(12-49), 1988.
- [65] M. M. Postnikov. *Geometry IV: Riemannian geometry*. Springer-Verlag, Berlin, 2001.
- [66] I. Rahman, I. Drori, V. Stodden, D. Donoho, and P. Schroeder. Multiscale representations for manifold-valued data. Technical Report 2005-3, Dept. of statistics, Stanford Univ., 2005.
- [67] D. W. Rees. Panoramic television viewing system. *United States Patent NO 3,505,465*, 1970.
- [68] A. Reid. *Hyperbolic Manifolds*. lecture notes, University of Texas, 2002.
- [69] S. Rosenberg. *The Laplacian on a Riemannian Manifold*. University press, Cambridge, 1997.
- [70] P. Schroeder and W. Sweldens. Spherical wavelets: efficiently representing functions on the sphere. In *Computer Graphics Proc. (SIG-GRAPH)*, volume 27, pages 161–175, ACM Siggraph, 1995.
- [71] J. A. Sethian. *Level set methods and Fast Marching Methods: Evolving Interfaces in Computational Geometry, Fluid Mechanics, Computer Vision and Material Sciences*. University Press, Cambridge, 1999.
- [72] B. Torrèsani. *Analyse Continue par Ondelettes*. InterEditions/CNRS Editions, Paris, 1995.
- [73] P. Vandergheynst. *Ondelettes bidimensionnelles et ondelettes sur la sphère*. PhD thesis, Université Catholique de Louvain, Louvain-la-Neuve, Belgique, 1998.

-
- [74] N. J. Vilenkin. *Fonction spéciales et théorie de la représentation des groupes*. Dunod, Paris, 1969.
- [75] Y. Wiaux, L. Jacques, and P. Vandergheynst. Correspondence principle between spherical and Euclidean wavelets. *Astrophysical Journal*, 632:15, 2005.
- [76] Y. Wiaux, L. Jacques, and P. Vandergheynst. Fast directional correlation on the sphere with steerable filters [submitted]. *preprint astro-ph/0508516*, 2005.
- [77] Y. Yagi and S. Kawato. Panoramic scene analysis with conic projection. In *Proc. Int. Conf. Robots and Systems*, 1990.
- [78] K. Yamazawa, Y. Yagi, and M. Yachida. Omnidirectional imaging with hyperboloidal projection. In *Proceedings of IROS*, Jokohama, Japan, 1993.

Curriculum Vitae

PERSONAL

| | |
|----------------|-------------------------|
| Full Name | Iva Dimitrova Bogdanova |
| Nationality | Bulgarian |
| Date of Birth | December 4th, 1974 |
| Place of Birth | Varshetz, Bulgaria |
| Civil status | Single |

EDUCATION

| | |
|------------------------------|---|
| October 2003 - December 2005 | Doctorat ès Sciences, Swiss Federal Institute of Technology (EPFL) Lausanne, Switzerland, School of Engineering (STI), Signal Processing Institute (ITS). |
| October 1999 - July 2000 | Swiss Federal Institute of Technology (EPFL), Lausanne, Switzerland, Department of Communication Systems, Graduate School of Communication Systems. |
| September 1997 - July 1999 | Technical University of Sofia, Bulgaria, Institute of Applied Mathematics and Computer Science, grade obtained: <i>M.Sc. in Applied Mathematics</i> . |
| October 1992 - July 1997 | Technical University of Sofia, Bulgaria, Faculty of Communication Systems and Technologies, Department of Telecommunications, grade obtained: <i>M.Sc. in Telecommunication Techniques and Technologies</i> . |

PROFESSIONAL EXPERIENCE

| | |
|-----------------------|---|
| August 2000 - present | Research and teaching assistant at Swiss Federal Institute of Technology (EPFL), Signal Processing Institute (ITS), Lausanne, Switzerland |
|-----------------------|---|

September 1997 - July 1999

"New Television"-Sofia, Bulgaria, Digital Studio,
computer graphics and design, video editing

SKILLS

Languages

| | |
|--------|---|
| Native | Bulgarian |
| Fluent | Russian, Greek, English, French, Spanish, German |

Computer literacy

| | |
|-----------------------|--|
| Operating Systems | Mac, Windows9X/00/NT/XP, Unix, MS-Dos |
| Programming languages | MATLAB, Delphi, C, C++, Pascal, HTML, Java, JavaScript, Action Script, PHP, XML |
| Tools | Microsoft Office, Macromedia Flash, Macromedia Dreamweaver, Macromedia Director, Adobe Photoshop, Adobe Illustrator, Paint Pro Shop, Authorware, Pages, Keynote, Front page |

PUBLICATIONS

Journal Papers

- ◇ I. Bogdanova, P. Vandergheynst, J.-P. Gazeau, "Continuous Wavelet Transform on the Hyperboloid", Applied and Computational Harmonic Analysis [submitted], June 2005
- ◇ I. Bogdanova, P. Vandergheynst, J.-P. Antoine, L. Jacques and M. Morvidone, "Stereographic Frames of Wavelets on the Sphere", Applied and Computational Harmonic Analysis, volume 19, Issue 2, pp. 223-252, September 2005.

Conference Proceedings

- ◇ I. Tasic, I. Bogdanova, P. Frossard and P. Vandergheynst, "Multiresolution Motion Estimation for Omnidirectional Images", In Proc. of EUSIPCO, Antalya, Turkey, September 2005
- ◇ I. Bogdanova, P. Vandergheynst, J.-P. Antoine, L. Jacques, M. Morvidone, "Describe Wavelet Frames on the Sphere", In Proc. of EUSIPCO, Vienna, Austria, September 6-10, 2004
- ◇ I. Bogdanova, P. Vandergheynst and M. Kunt, "Virtual Classroom for Multimedia Teaching on WWW", Proc. ASEE/IEEE 32d Annual Frontiers in Education FIE'02, Boston, MA, November 6-9, 2002, pp. F3E-7 - F3E-11.
- ◇ I. Bogdanova, R. Khan and M. Kunt, "Multimedia Teaching on WWW: a New Approach", Proc. NAISO Networked Learning 2002 NL'02, Berlin, Germany, May 1-4, 2002, (CD)

Technical Reports

- ◇ I. Bogdanova, X. Bresson, J.-Ph. Thiran, P. Vandergheynst, "Laplacian Operator, Difusion Flow and Active Contour on Non-Euclidean Images", TR-ITS-2005.020, August 2005.
- ◇ I. Bogdanova, P. Vandergheynst, J.-P. Gazeau, "Wavelets on the 2-Hyperboloid", TR-ITS-2004.028, November 2004.
- ◇ I. Bogdanova, P. Vandergheynst, J.-P. Antoine, L. Jacques and M. Morvidone, "Stereographic Frames on the Sphere", TR-ITS-2004.001, January 2004.
- ◇ I. Bogdanova, P. Vandergheynst and M. Kunt, "Specification for Digital Image Processing On-line Lab-sessions", TR-ITS-2002.09, November 2002
- ◇ I. Bogdanova, P. Vandergheynst and M. Kunt, "On-line Digital Image Processing Lab-Sessions", TR-ITS-2002.06, April 2002
- ◇ I. Bogdanova, R. Khan and M. Kunt, "Graphical User Interface and MATLAB Web Server for Multimedia Teaching on WWW", TR-ITS-2001.08, 2001

Master Thesis

- ◇ I. Bogdanova, "Transmission of Voice Messages in Corporate Information Systems", Institute of Applied Mathematics and Computer Science, Technical University of Sofia, July 1999
- ◇ I. Bogdanova, "Imitation Modeling of Message Transfer Part in Common Channel Signaling System No7", Telecommunications Department, Technical University of Sofia, July 1997